Colloid and Polymer Science
https://doi.org/10.1007/s00396-023-05187-x

RESEARCH

A green and sustainable approach to the fabrication of ZnO nanoparticles via *Jatropha podagrica* leaf extract for effective dye degradation and antibacterial applications

Venkatesh Golthi[1,2,3] · **Jayarao Kommu**[1,3] · **A. V. Ramesh**[4]

Received: 19 August 2023 / Revised: 13 October 2023 / Accepted: 16 October 2023

Abstract
A robust green synthesis method was employed using *Jatropha podagrica* (Buddha belly plant) leaf extract as a capping agent to prepare ZnO nanoparticles (ZnO NPs). Several analytical techniques such as XRD, SEM, SEM-EDX, HR-TEM, FT-IR, and UV-visible spectroscopy were employed to characterize the green synthesized JP-ZnO NPs. The XRD, SEM, and HR-TEM images proved the presence of spherical nanoparticles having a wurtzite crystalline structure with a size of 12 to 18 nm. The characteristic vibration mode of the Zn-O bond was observed at 430 cm^{-1} in the FT-IR spectrum. The photocatalytic performance of these NPs was evaluated through the degradation of Rhodamine B (RhB), Fluorescein Sodium (FS), and Crystal Violet (CV) dyes in sunlight. Degradation rates of 90–95% were achieved in a time span of 1–2 h. The synthesized ZnO nanoparticles were efficient antimicrobial agents against gram-positive (*Staphylococcus aureus*, *Bacillus coagulans*) and gram-negative (*Klebsiella pneumoniae*, *Escherichia coli*) bacterial strains. Using the well diffusion method, with 150 μL of JP-ZnO nanoparticles, inhibition zones measuring 17, 15, 11, and 10 mm were formed. The current study highlights the efficiency of synthesized JP-ZnO nanoparticles in removing the dyes from aqueous solutions and their efficient antimicrobial properties.

Keywords ZnO nanoparticle · *Jatropha podagrica* plant · Dye degradation · Antioxidant activity

Introduction

In the contemporary world, there has been a continuous increase in industrialization and population growth, leading to the release of various new pollutants into aquatic environments. Specifically, the discharge of noxious dye effluents from industries like textile, paper, leather, and printing poses grave ecological and health hazards [1, 2]. Dyes such as Rhodamine B (RhB), Fluorescein Sodium (FS), and Crystal Violet (CV) pose ingestion risks to humans and animals and induce skin, ocular, and respiratory irritation [3]. In a different context, the recurrence of contagious illnesses and the ongoing evolution of antibiotic resistance in numerous disease-causing bacteria present a significant global public health concern. *Enterococcus*, *Staphylococcus*, and *Streptococcus*, which are closely related species, are harmful microorganisms that are attributed to a diverse range of infections and diseases [4].

In the realm of recent advancements in nanotechnology, nanomaterials play a crucial role due to their significant surface area and volume ratio [5]. This characteristic makes them valuable for applications such as water purification and the creation of novel biocidal substances. Among various types of nanoparticles, zinc oxide nanoparticles (ZnO NPs) possess exceptional optical and electrical characteristics, making them an outstanding choice for *n*-type semiconductor materials [6]. These NPs demonstrate remarkable efficacy in dye degradation [6, 7] and also exhibit antibacterial properties [8, 9], further highlighting their distinctiveness.

✉ Venkatesh Golthi
venkatesh@gdcc.ac.in

[1] Andhra University Trans-Disciplinary Research Hub (A.U. TDR-HUB), Visakhapatnam 530003, AP, India

[2] Department of Chemistry, Government Degree College, Chodavaram 531036, AP, India

[3] Department of Chemistry, Wellfare Institute of Science, Technology and Management, Pinagadi, Pendurthi 531173, AP, India

[4] Department of Chemistry, Dr. V.S. Krishna Govt. Degree College, Visakhapatnam 530003, AP, India

Numerous techniques have been documented for the production of ZnO NPs, including hydrothermal [10], precipitation [11], microwave [12], microemulsion [13], solvothermal [14], supercritical water [15], and sol-gel methods [16]. Recent progress in nanotechnology has spurred the rise of sustainable synthesis approaches for generating ZnO NPs [17, 18]. These environmentally synthesized ZnO NPs have garnered substantial interest for their prospective utilization across diverse domains, encompassing dye degradation and antibacterial functionalities. The utilization of these NPs offers a promising solution for addressing environmental challenges associated with dye pollution and combating the spread of drug-resistant bacteria. By harnessing the unique properties of green-synthesized ZnO NPs, researchers aim to explore their efficacy in degrading dyes and inhibiting the growth of pathogenic bacteria, presenting a sustainable and effective approach for environmental and healthcare applications [17–19]. This article delves into the dye degradation and antibacterial activity of ZnO NPs synthesized through green methods, shedding light on their potential as eco-friendly alternatives in addressing pressing global concerns [20–23].

Jatropha podagrica (JP), a traditional medicinal plant, has a history of being utilized for treating various ailments like fever, scabies, ulcers, and wounds. Additionally, it exhibits several beneficial properties including antitumorigenic, antioxidant, and antibacterial activities [24]. The leaves of *Jatropha podagrica* have been analyzed and found to contain specific phytochemicals, namely, flavonoids (such as apigenin, acacetin, and luteolin), phenolic acids (including vanillic, syringic, P-hydroxybenzoic acid, melilotic, cis-trans ferulic, P-coumaric, and phloretic acids), tannins, proanthocyanidins, and glycol flavones [25, 26]. ZnO NPs were successfully produced using leaf extract from the *Jatropha podagrica* plant for the first time. The phytochemicals found within the extract played a crucial and multifaceted role in the *Jatropha podagrica*-capped ZnO nanoparticle (JP-ZnO NP) synthesis, serving both as capping agents and enhancing stability, surpassing that achieved through conventional chemical synthesis methods [25]. Moreover, the presence of diverse phenolic acids within these phytochemicals contributes to achieving well-defined sizes and shapes of ZnO NPs, outperforming analogous green-synthesized counterparts (as depicted in Table 1). To unlock the full potential of unexplored plant species, the selection of new and unique plants for nanoparticle synthesis is imperative. This approach allows researchers to diversify the spectrum of nanoparticles that can be effectively stabilized, achieved through the discovery of novel proteins and phytochemicals derived from previously uninvestigated plant sources. Additionally, these novel plant species may offer additional advantages such as heightened productivity, reduced costs, or specialized attributes suitable for specific applications. In the present research, JP-ZnO nanoparticles displayed a surface with a negative charge, providing them with outstanding adsorption properties for efficiently eliminating Rhodamine B (RhB), Fluorescein Sodium (FS), and Crystal Violet (CV) dyes. Additionally, the antibacterial effectiveness of these manufactured JP-ZnO NPs was evaluated against both Gram-positive bacteria (*Staphylococcus aureus*, *Bacillus coagulans*) and Gram-negative bacteria (*Klebsiella pneumoniae*, *Escherichia coli*).

Table 1 Comparison of the average size and morphology of ZnO nanoparticles in the present work with previous publications

Plant materials	Precursor name	Average size and morphology	Applications	Reference
Jatropha podagrica leaf extract	$Zn(OOCCH_3)_2.2H2O$	12–18 nm and spherical shape	Dye degradation and antibacterial applications	Present work
Calotropis procera extract	$Zn(NO_3)_2.6H2O$	24 nm and spherical shape	Photodegradation of methyl orange	[17]
Solanum torvum L. leaf extract	$Zn(NO_3)_2.6H2O$	28.24 and spherical shape	Toxicological studies	[27]
Simarouba glauca leaf extract	$Zn(NO_3)_2.6H2O$	17–37 nm and hexagonal shape	Antioxidant and antimitotic properties	[28]
Aegle marmelos fruit juice	$Zn(NO_3)_2.6H2O$	17 nm and hexagonal shape	Photodegradation, antibacterial and antioxidant	[29]
Punica granatum leaf extract	$Zn(NO_3)_2.6H2O$	20 nm and spherical shape	Photocatalytic degradation	[30]
Pelargonium zonale leaf extract	$Zn(NO_3)_2.6H2O$	50–60 nm and spherical in shape	Antibacterial activities	[31]
Azadirachta indica leaf extract	$Zn(NO_3)_2.6H2O$	100–200 nm and triangular shape	Antimicrobial activity	[32]
Tetraselmis indica extract	$Zn(OOCCH_3)_2.2H2O$	20–40 nm and spherical shape	Antibacterial, antioxidant, and hemolytic activity	[33]
Aesculus hippocastanum extract	$Zn(OOCCH_3)_2.2H2O$	40 nm and hexagonal shape	Antibacterial activities	[34]
Sechium edule leaf extract	$Zn(OOCCH_3)_2.2H2O$	36.2 nm and spherical shape	Antibacterial and anticancer studies	[35]

Materials and methods

Materials

Fresh *Jatropha podagrica* leaves were picked from the garden of the Government Degree College in Chodavaram, Andhra Pradesh, India. The initial source, zinc acetate dihydrate $Zn(OOCCH_3)_2.2H_2O$ (98% purity), sodium hydroxide (NaOH), Rhodamine B (RhB), Fluorescein Sodium (FS), and Crystal Violet (CV) were acquired from Merck in India and utilized without purification. Milli-Q water was utilized in all of the experiments.

Jatropha podagrica leaf extract preparation

Fresh JP plant leaves were collected and meticulously cleansed using warm water, followed by thorough rinsing with Milli-Q water. These leaves were then dried under shaded conditions for a duration of 25 days until completely dry. Once dry, the leaves were ground into a fine powder using a grinder. Subsequently, 1 g of the powdered sample was placed in a 250-mL glass beaker, and 100 mL of Milli-Q water was added. The blend was subsequently warmed using a heating mantle at 80 °C for 30 min, yielding a brilliant golden-yellow solution. The solution was meticulously sieved using Whatman grade 1 filter paper to eliminate any particulate matter and subsequently subjected to centrifugation at 8000 rpm for 5–10 min to attain a pristine extract solution. The resultant extract was then carefully stored in a refrigerator at 4 °C for subsequent processing [36].

Synthesis of *Jatropha podagrica*-capped ZnO nanoparticles

In a standard eco-friendly synthesis procedure, 10 mL of the aqueous extract derived from JP leaves was blended with 100 mL of a 2 mM aqueous solution containing zinc acetate dihydrate. The amalgamation was subjected to stirring at 80 °C for 30 min, leading to the creation of a vivid yellow solution. Following this, a 1 M solution of sodium hydroxide was meticulously introduced dropwise into the mixture, with uninterrupted agitation at ambient temperature. As a result, the yellow color of the mixture gradually transformed into a yellowish-white suspension, reaching a pH of 12. To purify the suspended particles, they were dispersed in Milli-Q water and then centrifuged at a speed of 8000 rpm. The resultant white particles underwent repeated washing with Milli-Q water to purge impurities and yield the ultimate product. The white solid was then subjected to vacuum drying at 60 °C for 6 h in an oven. Lastly, the material was finely pulverized using a mortar and pestle, rendering it ready for subsequent characterization [36, 37].

Photocatalytic potential of JP-ZnO NPs for the degradation of RhB, FS, and CV dyes

The photocatalytic effectiveness of JP-ZnO NPs against RhB, FS, and CV dyes was assessed using a readily available source of UV radiation — sunlight. In separate containers, 0.01 g of JP-ZnO NPs was blended with 100 mL of 1 ppm solutions of RhB, FS, and CV dyes. To ensure the stability of the solutions against adsorption–desorption phenomena, the reaction mixtures were gently stirred in the absence of light for a duration of 1 h. After stabilization, the solutions were maintained in the sunshine with constant stirring using magnetic stirrers at pH 10. At regular intervals, constant samples were taken from each dye solution and the NPs were separated in a centrifuge at 8000 rpm. A UV spectrometer was used to measure the color intensities at 555 nm, 495 nm, and 590 nm for the RhB, FS, and CV dyes, respectively. The proportion of photocatalytic degradation and rate constants were calculated using the equation below:

$$\text{Degradation rate (\%)} = \left(\left(\mathrm{A_0} - \mathrm{A}\right)/\mathrm{A_0}\right) \times 100$$

$$\ln A_0/A = kt$$

In the equation, “A_0” symbolizes the initial concentration, while “A” denotes the concentration at the culmination of the degradation process. The degradation constant is denoted by k, and t indicates the duration of sunlight irradiation [38].

Characterization of JP-ZnO NPs

To ascertain the crystalline arrangement of the JP-ZnO NPs, a variety of analytical methodologies were applied. X-ray diffraction (XRD) measurements were carried out across a 2θ range of 0 to 90° using a Bruker Kappa Apex II instrument. The instrument was operated with CuKα radiation ($\lambda = 1.54060$ Å) at settings of 40 kV, 35 mA, and a scanning rate of 0.2 s. Fourier transform infrared spectra (FT-IR) of the samples were captured utilizing a Thermo Nicolet iS50 spectrometer. Spectra were acquired within the frequency span of 4000–400 cm^{-1}, using high-quality KBr pellets in transmission mode. For an in-depth investigation of the optical attributes, UV-Vis diffuse reflectance/absorbance spectroscopy was conducted on the synthesized samples. A Shimadzu (2450 – SHIMADZU) spectrophotometer, equipped with a diffuse reflectance accessory, was deployed under room temperature conditions. $BaSO_4$ was utilized as a reference material, and measurements were executed over the wavelength range of 200–800 nm. The surface topography and elemental composition of the JP-ZnO NPs were scrutinized through scanning electron microscopy (SEM). The specific apparatus employed was the JEOL 6390LA/OXFORD XMX N, which featured energy-dispersive X-ray (EDX) spectroscopy. SEM images were recorded with an acceleration voltage of 20 kV. For a more comprehensive exploration of the microstructure and particle dimensions, high-resolution transmission electron microscopy (HRTEM) was engaged. The JEOL/JEM 2100 instrument was utilized at an operational voltage of 200 kV. Carbon-copper grids were used for sample preparation, enabling the acquisition of micrographs that facilitated particle size determination. Furthermore, selected area electron diffraction (SAED) images were captured utilizing the HRTEM instrument.

Results and discussions

UV-Vis spectroscopy studies

Figure 1 illustrates the UV-Vis absorption spectra of both JP leaf extract and JP-ZnO NPs. The leaf extract comprises a diverse array of phytochemicals, encompassing alkaloids, phenolic acids, flavonoids, tannins, proanthocyanidins, and glycol flavones. These compounds contribute to pronounced absorption bands at 280 and 351 nm [24]. Additionally, a well-defined absorption peak at 372 nm in the spectra signifies the presence of JP-ZnO NPs, predominantly arising from their capacity to absorb and scatter light [39]. Notably, the absence of absorption peaks at 280 and 351 nm in the JP-ZnO NPs spectra, which were originally observed in the JP leaf extract, implies that these phytochemicals play a pivotal role in the reduction and encapsulation of JP-ZnO NPs during the synthesis process [40].

FTIR analysis of the synthesized JP-ZnO NPs

FTIR spectroscopy was employed to discern the specific functional groups existing within the synthesized NPs and to ascertain their molecular composition. To examine the data concerning functional groups found in the plant (as depicted in Fig. 2), it is evident that a wide peak detected at approximately 3500 cm^{-1} signifies the presence of a phenolic group. Additionally, the identification of aromatic compounds is supported by the absorption of a broad peak around 1639 cm^{-1}. Furthermore, the peaks observed at 1178.39 cm^{-1} and 1042.36 cm^{-1} indicate the existence of amide functional groups and carbonated functional group vibrations within the plant. JP-ZnO NPs were analyzed (as shown in Fig. 2), and their absorption peaks were found to be in the range of 400–4000 cm^{-1}. The peak at 429.08 cm^{-1} indicates the stretching frequency of Zn-O bonding [41]. Peaks observed at 917.20, 901.10, and 795 cm^{-1} can be assigned to carbonate moieties. The occurrence of the symmetric stretching of carboxyl side groups within the amino acid residues of protein molecules is potentially ascribed to

Fig. 1 UV-Vis spectra of *Jatropha podagrica* (JP) leaf extract and *Jatropha podagrica* leaf extract-capped ZnO NPs

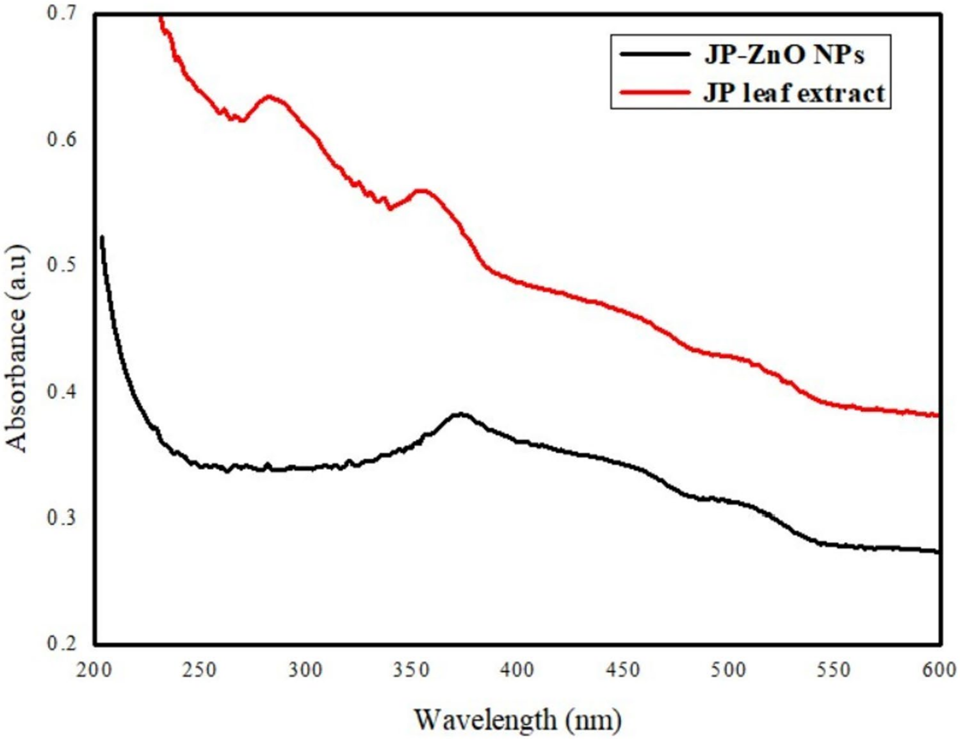

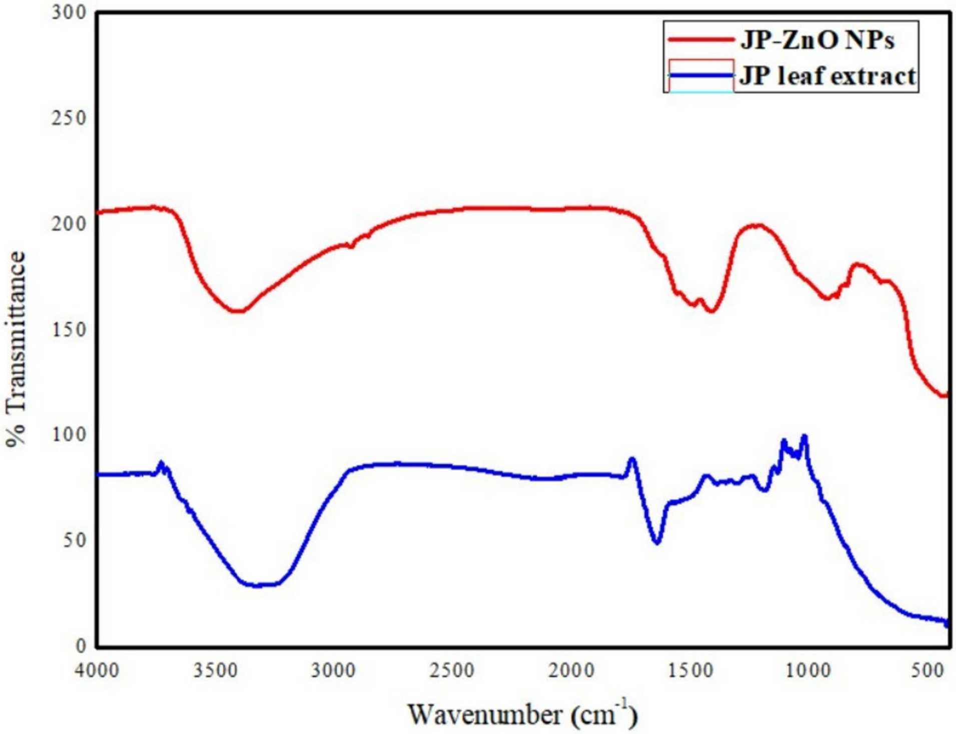

Fig. 2 FTIR spectra of *Jatropha podagrica* leaf extract and *Jatropha podagrica* leaf extract-capped ZnO NPs

the peak at 1410.06 cm^{-1} [42]. The presence of a peak within the 1550- to 1450-cm^{-1} range is likely linked to the C=C stretching of aromatic compounds [43]. Evident and robust absorption bands at 3397.10 and 2923.56 cm^{-1} were identified, signifying the −OH stretching vibration intrinsic to phenolic groups and the −CH stretching vibration characteristic of aldehyde groups [44, 45]. These distinctive peaks within the IR spectrum serve as indicators of the purity and compositional makeup of the biofabricated JP-ZnO NPs.

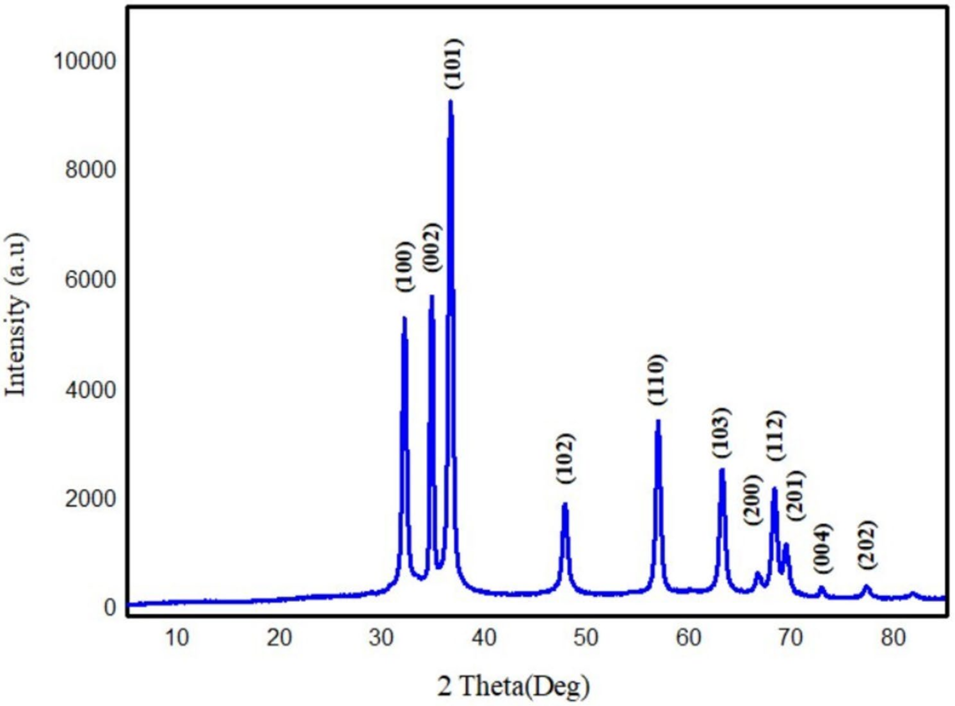

Fig. 3 XRD patterns of ZnO NPs using an aqueous leaf extract of *Jatropha podagrica*

Table 2 The structure and geometric parameters of JP-ZnO NPs

Planes	2*θ*	*β*	cos*θ*	Size (nm)
100	31.98	0.53635	0.96131	14.23869
002	34.63	0.41516	0.954683	18.26832
101	36.47	0.52835	0.949781	14.28094
102	47.75	0.71887	0.914431	10.10545
110	56.82	0.59138	0.879566	11.81562
103	63.07	0.67663	0.852321	10.00707
200	66.68	1.30914	0.835424	5.069625
112	68.17	0.6336	0.828207	10.38434
201	69.28	0.74629	0.82274	8.7581
004	72.76	0.37226	0.805101	17.18142
202	77.18	0.40693	0.781629	15.25936
Average size				**12.30627**

XRD analysis of the synthesized JP-ZnO NPs

The X-ray diffraction analysis, as shown in Fig. 3, revealed distinctive peak characteristic of JP-ZnO at various angles: 31.98°, 34.63°, 36.47°, 47.75°, 56.82°, 63.07°, 66.68°, 68.17°, 69.28°, 72.76°, and 77.18°. These peaks corresponded to different crystal lattice planes, including (100), (002), (101), (102), (110), (103), (200), (112), (201), (004), and (202), respectively. The congruence of these peaks with the established JCPDS Card No. 89–0510 indicated the presence of ZnO NPs in the wurtzite crystalline structure. The well-defined and narrow diffraction peaks attested to a robust crystalline structure, while the absence of other signals verified the purity of the synthesized JP-ZnO NPs. Notably, the intensity of the (002) peak indicated the

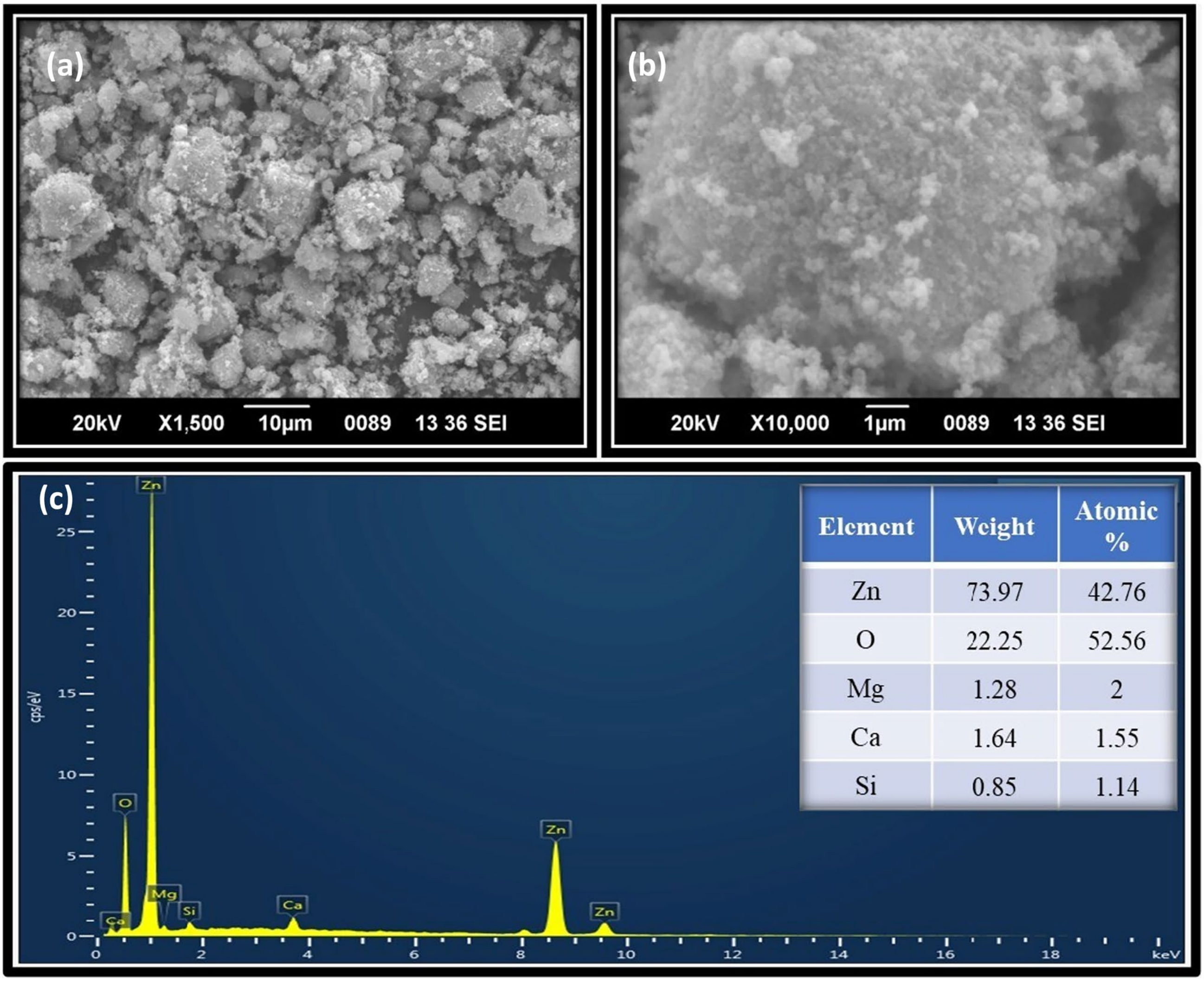

Element	Weight	Atomic %
Zn	73.97	42.76
O	22.25	52.56
Mg	1.28	2
Ca	1.64	1.55
Si	0.85	1.14

Fig. 4 **a** and **b** SEM images ZnO NPs capped with *Jatropha podagrica* leaf extract different magnifications and **c** EDX spectrum of ZnO NPs

spherical morphology of the particles [46]. To calculate the average grain size of the samples, the Debye-Scherer equation was employed: $D = k\lambda/\beta\cos\theta$. Here, D represents the crystal size, λ stands for the wavelength of X-ray radiation ($\lambda = 0.15406$ nm) for Cu Kα, k is the shape factor (typically taken as 0.9), β denotes the full width at half maximum (FWHM), and θ represents the diffraction angle.

Table 2 represents the structure and geometric parameters of JP-ZnO NPs.

Employing the Debye-Scherer equation, the average size of the crystallites within the JP-ZnO NPs was computed to be 12.30627 nm (Table 2), confirming their nanoscale dimensions.

SEM-EDX analysis of synthesized JP-ZnO NPs

The surface characteristics of the produced JP-ZnO NPs were examined using a scanning electron microscope (SEM). As depicted in Fig. 4(a), (b), the particles exhibited predominantly wurtzite crystalline structure and a spherical shape [47]. Some clustering of particles was observed, likely attributed to the presence of phenolic

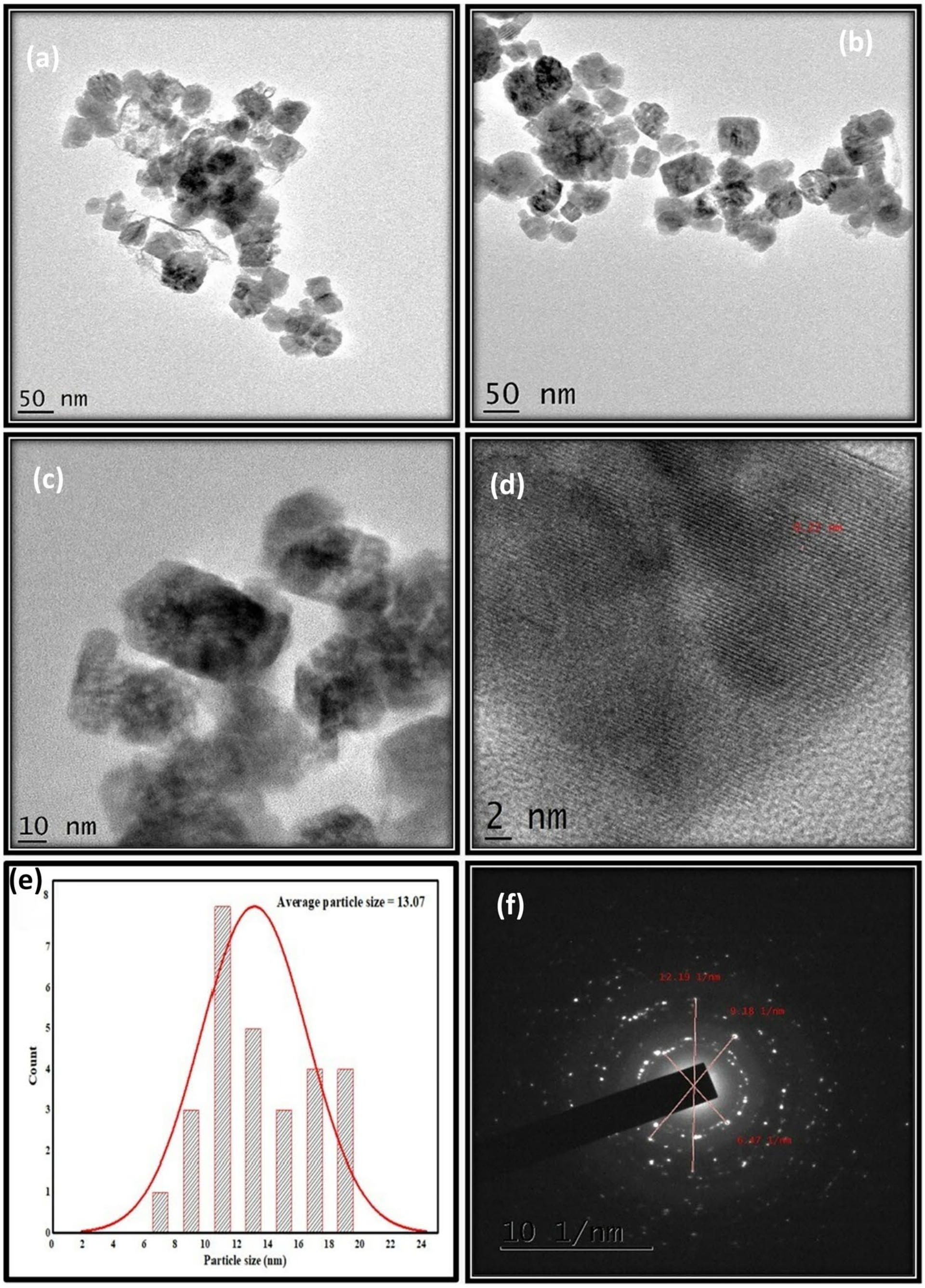

Fig. 5 **a–d** HR-TEM images, **e** size distribution histogram of using aqueous *Jatropha podagrica* leaf extract of ZnO NPs, and **f** SAED patterns

compounds from the JP plant, which acted as a capping agent. To determine the chemical constitution of the ZnO NPs, an energy-dispersive X-ray spectrum (EDX) was obtained from a densely populated region (Fig. 4(c)). The EDX spectrum revealed significant signals from zinc atoms at 1 keV, 8.7 keV, and 9.6 keV, respectively, along with a single peak corresponding to oxygen atoms at 0.5 keV. The presence of a negligible amount of carbon atoms confirmed the high purity of the NPs. Additionally, minor peaks representing calcium (Ca), magnesium (Mg), and silicon (Si) atoms were detected, indicating the contribution of these elements from the biological components.

TEM analysis of synthesized JP-ZnO NPs

The dimensions, arrangement, and architecture of the synthesized JP-ZnO NPs underwent meticulous scrutiny through high-resolution transmission electron microscopy (HR-TEM). HR-TEM images at varying magnifications are showcased in Fig. 5(a–c). Scrutinizing these images unveiled that the average size of the JP-ZnO NPs resides within the range of 12–18 nm. Impressively, a measured "*d*" spacing of 0.22 nm harmonized with the *d* values derived from X-ray diffraction (XRD), thereby affirming the ZnO NPs' wurtzite crystalline structure and spherical morphology [48], as visualized in Fig. 5(d). Significantly, Fig. 5(e) underscores that the particle size deduced from the HR-TEM analysis exhibited commendable concurrence with outcomes from the XRD analysis. The selected area electron diffraction pattern (SAED) of the JP-ZnO NPs is portrayed in Fig. 5(f). The SAED pattern indicated the presence of polycrystalline NPs in the JP-ZnO sample.

Plausible mechanism for fabrication of JP-ZnO NPs

Figure 6 provides an illustrative representation of a potential procedure aimed at producing ZnO NPs utilizing a water-based solution derived from the leaves of

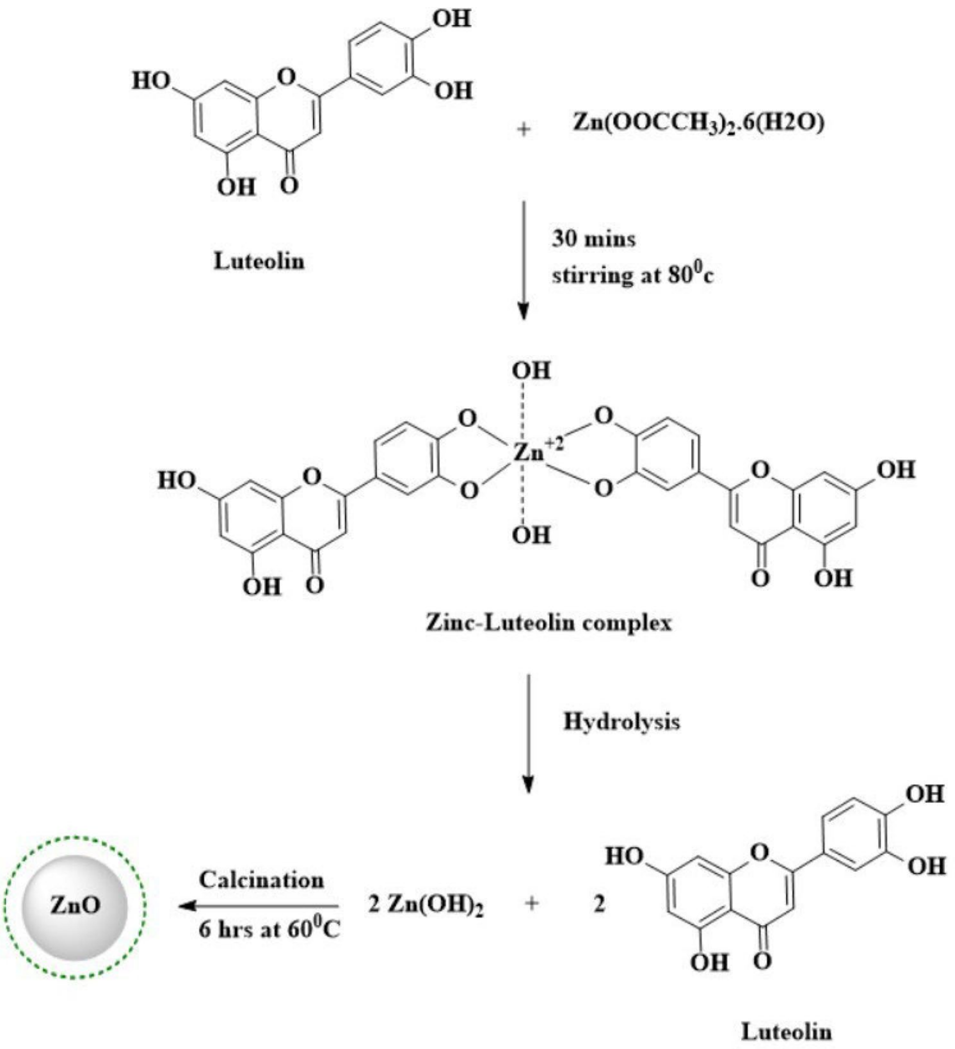

Fig. 6 A proposed mechanism of synthesized ZnO NPs using a *Jatropha podagrica* leaf extract

JP. The procedure involves combining an aqueous leaf extract obtained from JP with zinc acetate hexahydrate ($(Zn(OOCCH_3)_2.6H_2O)$) within a single aqueous phase. The leaf extract from JP contains a range of constituents, including phenolic acids, flavonoids, tannins, terpenoids, and carbohydrates. These components serve a dual purpose as both reducing and capping agents in the reaction. Notably, a remarkable chemical within the leaf extract is luteolin, which complexes with zinc in the form of Zn^{+2} ions.

This initial complexation is followed by the sequential progression of events. First, there is the conception of zinc hydroxide ($Zn(OH)_2$) via hydrolysis. Subsequently, through a process of calcination, the complex undergoes decomposition [49]. This decomposition process strongly favors the generation of JP-ZnO NPs.

A photocatalytic degradation of RhB, FS, and CV dyes by the fabricated JP-ZnO NPs

To evaluate the photocatalytic activity of prepared JP-ZnO NPs, they were employed as catalysts in the photodegradation of RhB, CV, and FS dyes in sunlight. Figures 7, 8, and 9 demonstrate the degradation of the dyes RhB, FS, and CV under sunlight, occurring at time intervals of 180 min, 90 min, and 60 min, respectively. The UV-visible spectrometer was used to measure the RhB, FS, and CV dye degradation at regular intervals of 30 min, 20 min, and 15 min, respectively. Degradation efficiencies of 95%, 94%, and 90% were achieved for RhB, FS, and CV dyes, respectively. The degradation efficiency of the as-prepared JP-ZnO NPs was compared with that of recently reported ZnO NPs in Table 3.

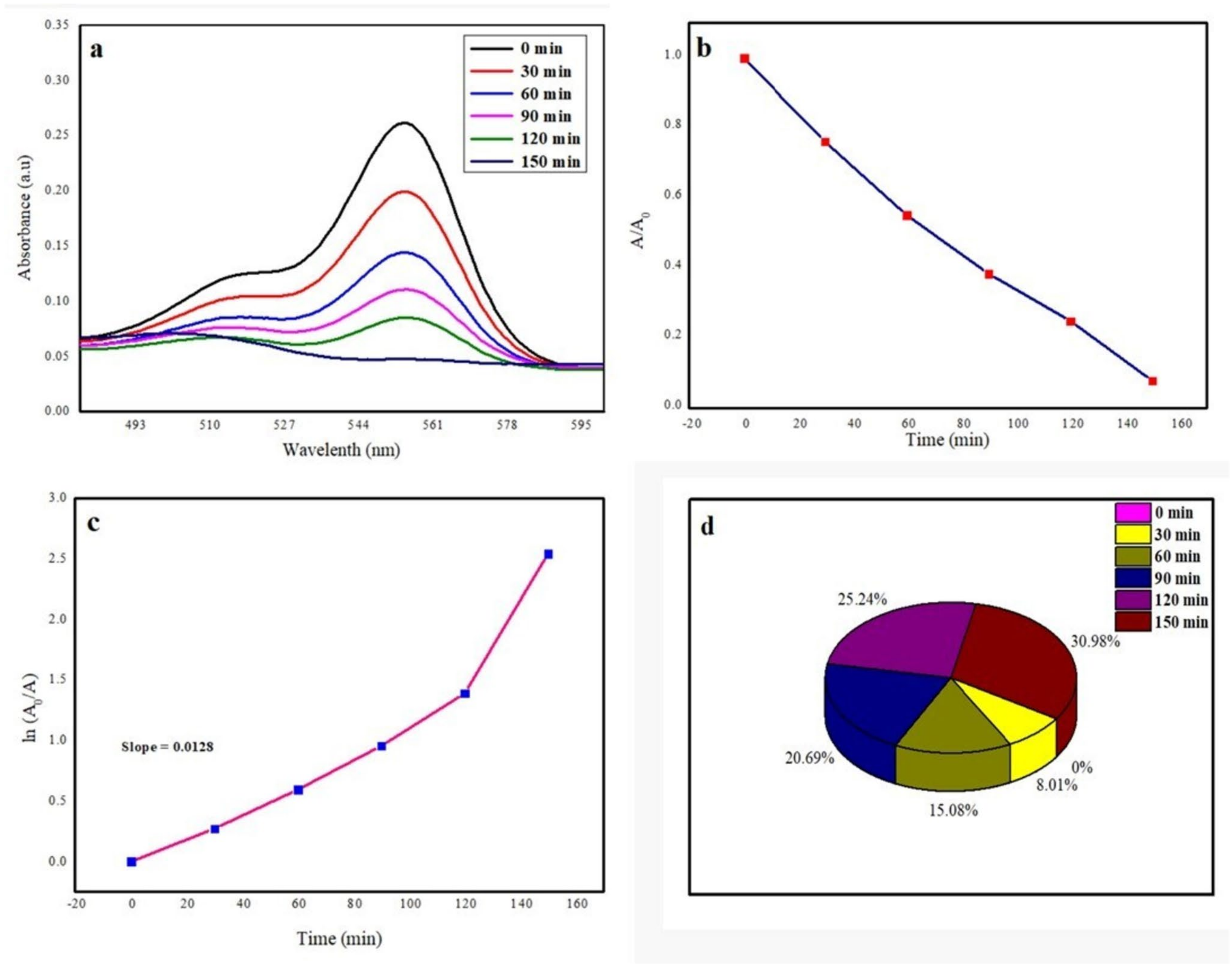

Fig. 7 **a** UV-Vis absorbance spectra of RhB dye under UV (sunlight) illumination over JP-ZnO NPs as a function of time, **b** the progression of RhB dye degradation during consecutive time intervals, **c** the kinetics of RhB dye degradation presented as a first-order linear plot with ln A_0/A as a function of time, and **d** a pie chart representing the distribution of RhB dye degradation across different time intervals

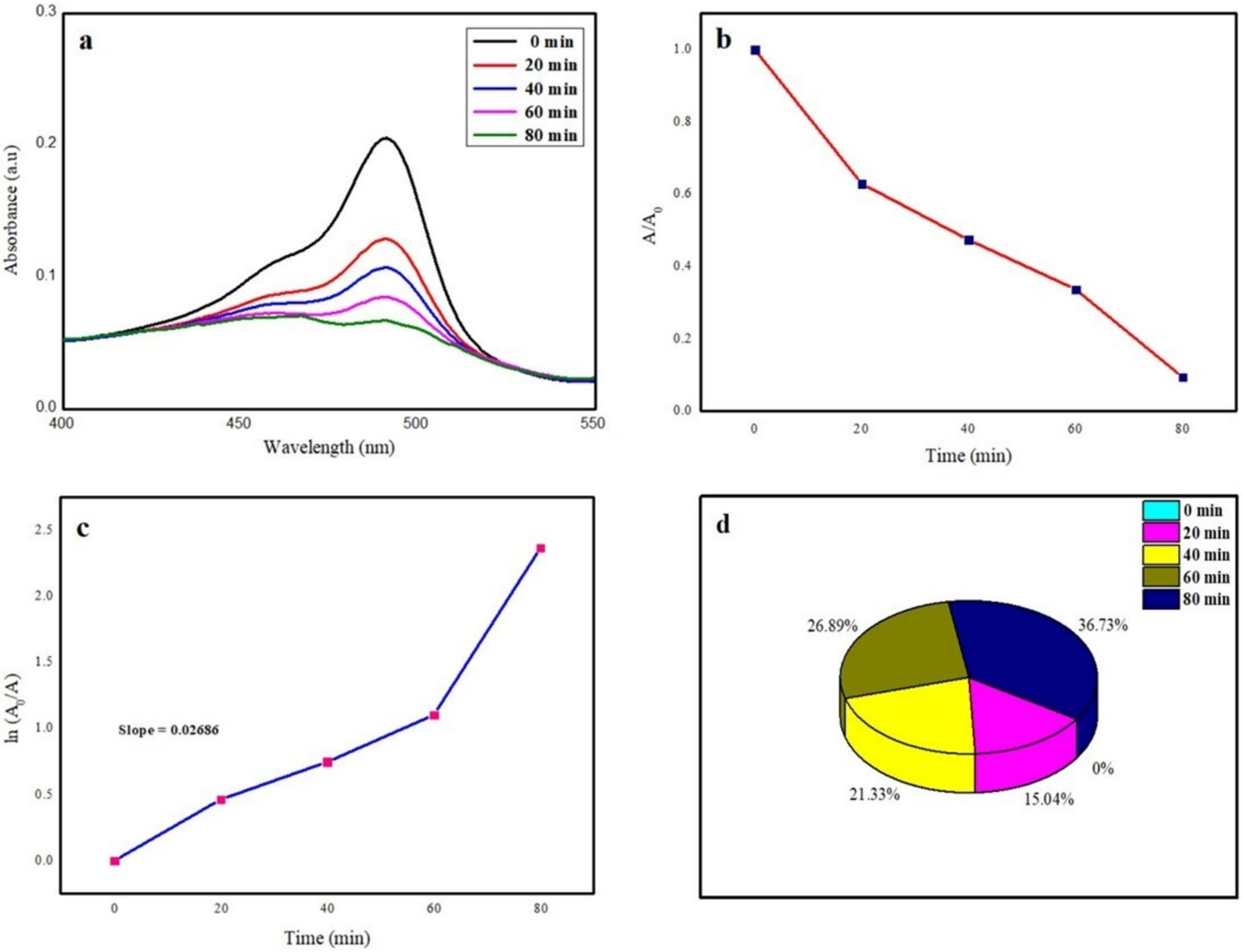

Fig. 8 **a** UV-Vis absorbance spectra of FS dye under UV (sunlight) illumination over JP-ZnO NPs as a function of time, **b** the progression of FS dye degradation during consecutive time intervals, **c** the kinetics of FS dye degradation presented as a first-order linear plot with ln A_0/A as a function of time, and **d** a pie chart representing the distribution of FS dye degradation across different time intervals

The results of this study strongly suggest that JP-ZnO NPs possess significant promise as a material for effectively catalyzing the degradation of organic pollutants through photocatalysis. The remarkable rates of degradation observed, coupled with the observable impact of varying pH conditions on the degradation process, highlight the potential application of JP-ZnO NPs in addressing a wide spectrum of water and wastewater pollution challenges stemming from organic contaminants. These results suggest that JP-ZnO NPs offer promising prospects for addressing environmental pollution challenges.

The following mechanism illustrates how electrons and holes contribute to dye degradation [56]:

$$\mathrm{ZnO} + h\nu \rightarrow e^- + h^+$$

$$\mathrm{O_2\ absorption:}\ O_2 + e^- \rightarrow O_2{}^-$$

$$\mathrm{Ionization\ of\ water:}\ H_2O \rightarrow OH^- + H^+$$

$$\mathrm{Protonation\ of\ superoxide:}\ O_2{}^- + H^+ \rightarrow HOO$$

$$HOO + e^- \rightarrow HO_2{}^-$$

$$HOO^- + H^+ \rightarrow H_2O_2$$

$$H_2O_2 + e^- \rightarrow OH^- + OH$$

$$H_2O + h^+ \rightarrow H^+ + OH$$

$$\mathrm{Dyes} + \mathrm{OH.} \rightarrow \mathrm{Degradant\ product}$$

The aforementioned OH radical is an extremely potent oxidant, highly effective in the degradation of numerous dyes such as RhB, FS, and CV.

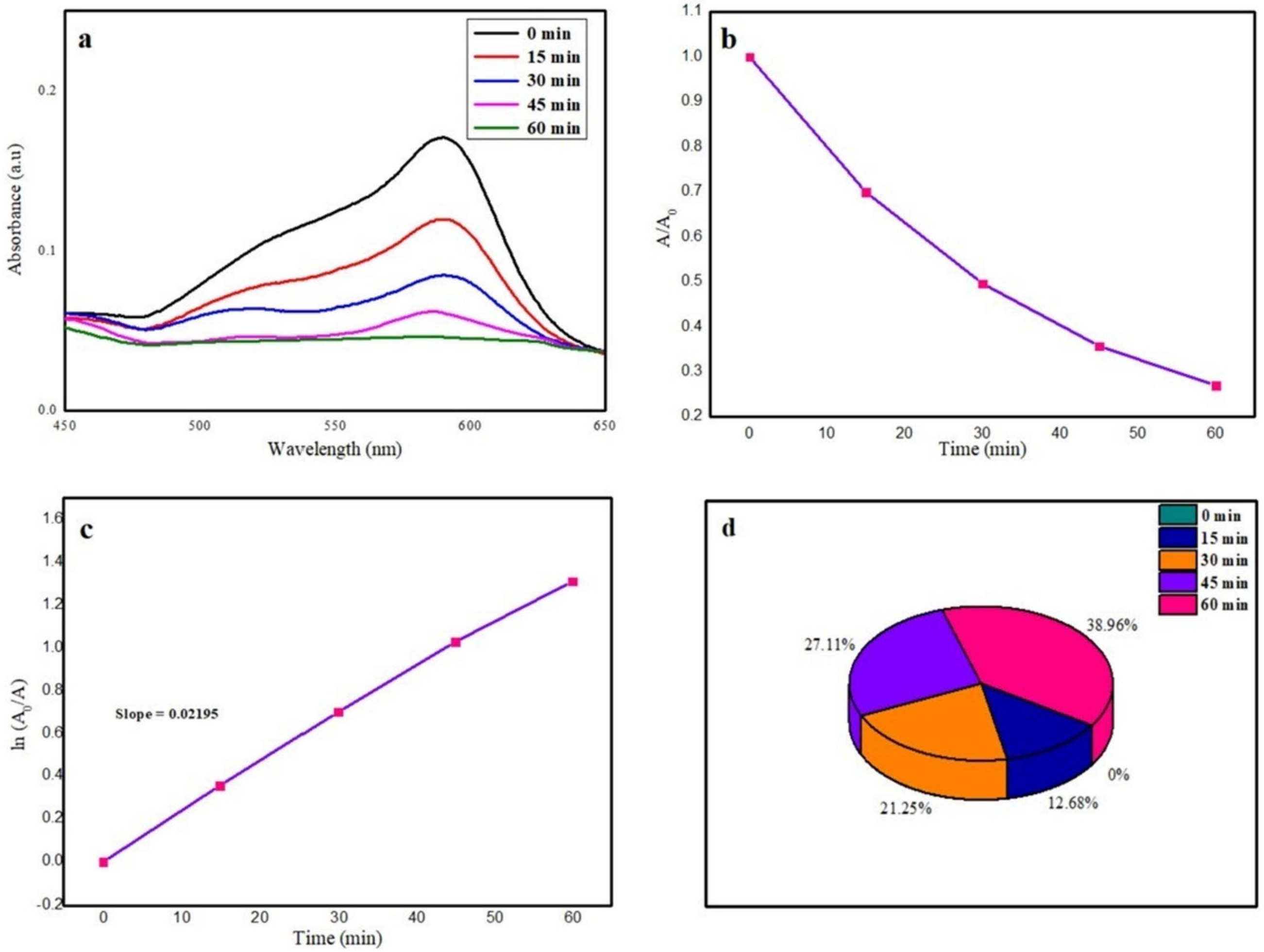

Fig. 9 **a** UV-Vis absorbance spectra of CV dye under UV (sunlight) illumination over JP-ZnO NPs as a function of time, **b** the progression of CV dye degradation during consecutive time intervals, **c** the kinetics of CV dye degradation presented as a first-order linear plot with ln A_0/A as a function of time, and **d** a pie chart representing the distribution of CV dye degradation across different time intervals

Antibacterial activities of synthesized JP-ZnO NPs

The antibacterial effectiveness of JP-ZnO NPs was assessed against both Gram-positive bacteria (*S. aureus*, *B. coagulans*) and Gram-negative bacteria (*K. pneumoniae*, *E. coli*) through the utilization of the well diffusion method. The outcomes of the zone inhibition technique are depicted in Fig. 10, illustrating the diameters of inhibition zones (measured in millimeters) encompassing each well containing the JP-ZnO NP solution. The JP-ZnO NPs prepared for this

Table 3 Comparison of the photocatalytic degradation of ZnO nanoparticles in the present work with previous works

Green materials	Dye	Light source	Irradiation time (min)	Degradation efficiency (%)	Reference
Jatropha podagrica leaf extract	Rhodamine B Crystal Violet Fluorescein Sodium	Sunlight Sunlight Sunlight	150 60 90	95 94 90	Present work
Alchemilla vulgaris leaf extract	Rhodamine B	Sunlight	120	75	[50]
Hibiscus sabdariffa L. petal extract	Rhodamine B	Sunlight	300	80.13	[51]
Paraserianthes lophantha leaf extract	Rhodamine B	UV light	180	83	[52]
Moringa oleifera peel extract	Crystal Violet	UV light	70	94	[53]
Delonix elata leaf extract	Crystal Violet	UV light	90	86	[54]
Sageretia thea aqueous extract	Crystal Violet	UV light	8 h	40.65	[55]

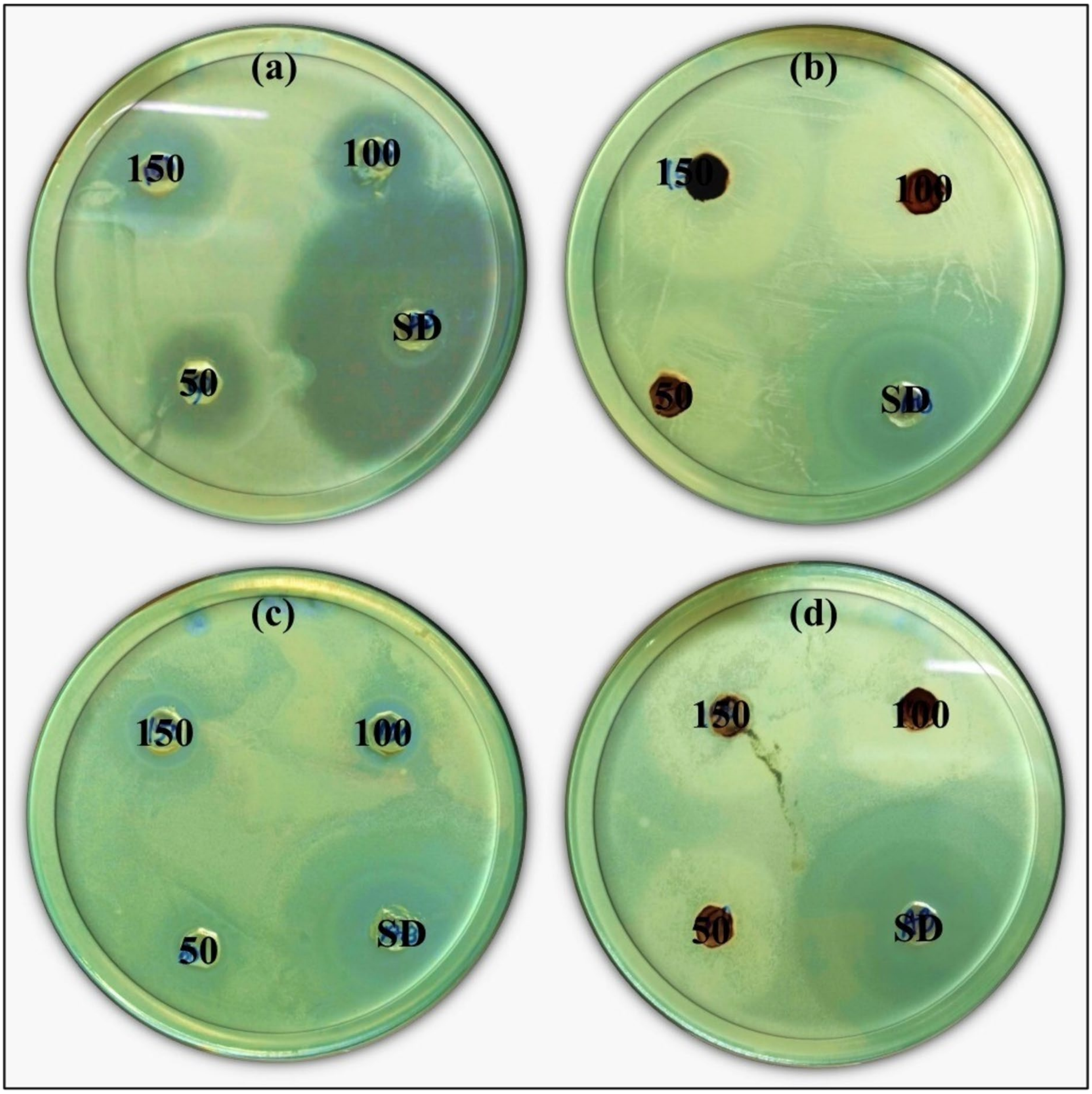

Fig. 10 Antibacterial efficacy of ZnO NPs synthesized using *Jatropha podagrica* leaf extract for **a** *S. aureus*, **b** *B. coagulans*, **c** *K. pneumoniae*, and **d** *E. coli*

study exhibited substantial antibacterial potency against *S. aureus*, *B. coagulans*, *K. pneumoniae*, and *E. coli*. Particularly favorable outcomes were witnessed against *S. aureus* (17 mm), *B. coagulans* (15 mm), *K. pneumoniae* (11 mm), and *E. coli* (10 mm) at a concentration of 150 µL, surpassing the performance of conventional drugs. The plant extract

Table 4 Zone of inhibition at different concentrations of JP-ZnO NPs

Name	*S. aureus*	*B. coagulans*	*K. pneumoniae*	*E. coli*
Shape	Round	Round	Round	Round
Gram reaction	Gram positive	Gram positive	Gram negative	Gram negative
50 µL	15 mm	12 mm	10 mm	10 mm
100 µL	16 mm	13 mm	11 mm	10 mm
150 µL	17 mm	15 mm	13 mm	11 mm
Antibiotic	40 mm	27 mm	40 mm	32 mm

exhibited commendable activity against both Gram-positive and Gram-negative bacteria, resulting in an inhibition zone of 6 mm. At various JP-ZnO NP concentrations, Table 4 shows the zone of inhibition.

From the aforementioned results, the susceptibility of Gram-positive bacteria (*S. aureus*, *B. coagulans*) exhibited a heightened degree of susceptibility to JP-ZnO NPs in contrast to Gram-negative bacteria (*K. pneumoniae*, *E. coli*). This discrepancy in sensitivity can be attributed to the substantial presence of a thick peptidoglycan layer within the cell wall of Gram-positive bacteria, which serves as a robust physical barrier offering shielding and protection. In contrast, Gram-negative bacteria possess both lipopolysaccharide and peptidoglycan, rendering them more resistant to the effects of JP-ZnO NPs [57–59].

Conclusions

In summary, we have successfully employed an eco-friendly method for synthesizing ZnO nanoparticles, using *Jatropha podagrica* leaf extract as a capping agent. Distinct analytical techniques were employed to characterize the nanoparticles which confirmed their wurtzite crystalline structure, spherical shape, and size in the range of 12 to 18 nm. The JP-ZnO nanoparticles have demonstrated a remarkable photocatalytic efficiency, effectively breaking down RhB, FS, and CV dyes under sunlight. The degradation rates of 90–95% were achieved within a time frame of 150, 90, and 60 min for RhB, FS, and CV dyes. We evaluated their antibacterial properties against both gram-positive (*S. aureus*, *B. coagulans*) and gram-negative (*K. pneumoniae*, *E. coli*) bacterial strains. Using 150 µL of nanoparticles, inhibition zones measuring 17, 15, 11, and 10 mm were obtained. These findings highlight the potential applications of JP-ZnO nanoparticles in addressing water pollution challenges and formulating potent antibacterial agents.

Acknowledgements The authors express sincere gratitude to Dr. K. Basavaiah, professor in the Department of Analytical Chemistry at Andhra University, Visakhapatnam, Andhra Pradesh, India, for generously facilitating UV-Vis spectroscopy for the purpose of characterizations.

Author contribution Venkatesh wrote the manuscript and prepared the tables and figures, A. V. Ramesh collected the data, and Jayarao reviewed the manuscript.

Availability of data and materials This declaration is “not applicable” .

Declarations

Ethical approval This declaration is “not applicable”.

Competing interests The authors declare no competing interests.

References

1. Lee KM, Lai CW, Ngai KS, Juan JC (2016) Recent developments of zinc oxide based photocatalyst in water treatment technology: a review. Water Res 88:428–448. https://doi.org/10.1016/j.watres.2015.09.045
2. Weber R, Watson A, Forter M, Oliaei F (2011) Review Article: Persistent organic pollutants and landfills — a review of past experiences and future challenges. Waste Manag Res 29(1):107–121. https://doi.org/10.1177/0734242X10390730
3. Jain R, Mathur M, Sikarwar S, Mittal A (2007) Removal of the hazardous dye rhodamine B through photocatalytic and adsorption treatments. J Environ Manage 85(4):956–964. https://doi.org/10.1016/j.jenvman.2006.11.002
4. Jones N, Ray B, Ranjit KT, Manna AC (2008) Antibacterial activity of ZnO nanoparticle suspensions on a broad spectrum of microorganisms. FEMS Microbiol Lett 279(1):71–76. https://doi.org/10.1111/j.1574-6968.2007.01012.x
5. Emami-Karvani Z, Chehrazi P (2011) Antibacterial activity of ZnO nanoparticle on gram-positive and gram-negative bacteria. Afr J Microbiol Res 5(12):1368–1373. https://doi.org/10.5897/AJMR10.159
6. Golmohammadi M, Honarmand M, Ghanbari S (2020) A green approach to synthesis of ZnO nanoparticles using jujube fruit extract and their application in photocatalytic degradation of organic dyes. Spectrochim Acta Part A Mol Biomol Spectrosc 229:117961. https://doi.org/10.1016/j.saa.2019.117961
7. Davar F, Majedi A, Mirzaei A (2015) Green synthesis of ZnO nanoparticles and its application in the degradation of some dyes. J Am Ceram Soc 98:1739–1746. https://doi.org/10.1111/jace.13467
8. Raghupathi KR, Koodali RT, Manna AC (2011) Size-dependent bacterial growth inhibition and mechanism of antibacterial activity of zinc oxide nanoparticles. Langmuir 27(7):4020–4028. https://doi.org/10.1021/la104825u
9. Sirelkhatim A, Mahmud S, Seeni A et al (2015) Review on zinc oxide nanoparticles: antibacterial activity and toxicity mechanism. Nano-Micro Lett 7:219–242. https://doi.org/10.1007/s40820-015-0040-x
10. Maryanti E, Damayanti D, Gustian I (2014) Synthesis of ZnO nanoparticles by hydrothermal method in aqueous rinds extracts of *Sapindus rarak* DC. Mater Lett 118:96–98. https://doi.org/10.1016/j.matlet.2013.12.044
11. Ghorbani HR, Mehr FP, Pazoki H, Rahmani BM (2015) Synthesis of ZnO nanoparticles by precipitation method. Orient J Chem 31(2). https://doi.org/10.13005/ojc/310281
12. Ahammed KR, Ashaduzzaman M, Paul SC et al (2020) Microwave assisted synthesis of zinc oxide (ZnO) nanoparticles in a noble approach: utilization for antibacterial and photo catalytic activity. SN Appl Sci 2:955. https://doi.org/10.1007/s42452-020-2762-8
13. Yıldırım ÖA, Durucan C (2010) Synthesis of zinc oxide nanoparticles elaborated by microemulsion method. J Alloy Compd 506(2):944–949. https://doi.org/10.1016/j.jallcom.2010.07.125
14. Ghoshal T, Biswas S, Paul M, De SK (2009) Synthesis of ZnO nanoparticles by solvothermal method and their ammonia sensing properties. J Nanosci Nanotechnol 9(10):5973–5980. https://doi.org/10.1166/jnn.2009.1290
15. Leybros A, Piolet R, Ariane M, Muhr H, Bernard F, Demoisson F (2012) CFD simulation of ZnO nanoparticle precipitation in a supercritical water synthesis reactor. J Supercrit Fluids 70:17–26. https://doi.org/10.1016/j.supflu.2012.06.001
16. Hasnidawani JN, Azlina HN, Norita H, Bonnia NN, Ratim S, Ali ES (2016) Synthesis of ZnO nanostructures using sol-gel method. Procedia Chem 19:211–216. https://doi.org/10.1016/j.proche.2016.03.095
17. Gawade VV, Gavade NL, Shinde HM, Babar SB, Kadam AN, Garadkar KM (2017) Green synthesis of ZnO nanoparticles by

using *Calotropis procera* leaves for the photodegradation of methyl orange. J Mater Sci: Mater Electron 28:14033–14039. https://doi.org/10.1007/s10854-017-7254-2

18. Rathnasamy R, Thangasamy P, Thangamuthu R et al (2017) Green synthesis of ZnO nanoparticles using *Carica papaya* leaf extracts for photocatalytic and photovoltaic applications. J Mater Sci: Mater Electron 28:10374–10381. https://doi.org/10.1007/s10854-017-6807-8
19. Batra V, Kaur I, Pathania D, Chaudhary V (2022) Efficient dye degradation strategies using green synthesized ZnO-based nanoplatforms: a review. Appl Surf Sci Adv 11:100314. https://doi.org/10.1016/j.apsadv.2022.100314
20. Thi TUD, Nguyen TT, Thi YD, Thi KHT, Phan BT, Pham KN (2020) Green synthesis of ZnO nanoparticles using orange fruit peel extract for antibacterial activities. RSC Adv 10(40):23899–23907. https://doi.org/10.1039/D0RA04926C
21. Raj A, Lawrence RS, Jalees MOHAMMAD, Lawrence KAPIL (2015) Anti-bacterial activity of zinc oxide nanoparticles prepared from *Brassica oleraceae* leaves extract. Int J Adv Res 3(11):322–328
22. Ramesh M, Anbuvannan M, Viruthagiri GJSAPAM (2015) Green synthesis of ZnO nanoparticles using *Solanum nigrum* leaf extract and their antibacterial activity. Spectrochim Acta Part A Mol Biomol Spectrosc 136:864–870. https://doi.org/10.1016/j.saa.2014.09.105
23. Espenti CS, Rama Krishna AG, Rami Reddy YV (2020) Green biosynthesis of ZnO nanomaterials and their anti-bacterial activity by using *Moringa Oleifera* root aqueous extract. SN Appl Sci 2:1424. https://doi.org/10.1007/s42452-020-2945-3
24. Bhaskarwar BHUSHAN, Itankar PRAKASH, Fulke ABHAY (2008) Evaluation of antimicrobial activity of medicinal plant *Jatropha podagrica* (Hook). Rom Biotechnol Lett 13(5):3873–3877
25. Thomas S (2016) Pharmacognostic and phytochemical constituents of leaves of *Jatropha multifida* Linn. and *Jatropha podagrica* Hook. J Pharmacogn Phytochem 5(2):243–246
26. Panzu NN, Lengbiye EM, Domondo A, Inkoto CL, Muanyishay CL, Gbolo BZ, Mpiana PT (2020) A review on the bioactivity and phytochemistry of *Jatropha podagrica* Hook (Euphorbiaceae). Discov Phytomedicine 7(4):186–194. https://doi.org/10.15562/phytomedicine.2020.150
27. Ezealisiji KM, Siwe-Noundou X, Maduelosi B et al (2019) Green synthesis of zinc oxide nanoparticles using *Solanum torvum* (L) leaf extract and evaluation of the toxicological profile of the ZnO nanoparticles–hydrogel composite in Wistar albino rats. Int Nano Lett 9:99–107. https://doi.org/10.1007/s40089-018-0263-1
28. Hemanth Kumar, N.K., Murali, M., Satish, A et al (2020) Bioactive and biocompatible nature of green synthesized zinc oxide nanoparticles from *Simarouba glauca* DC: An Endemic Plant to Western Ghats, India. J Clust Sci 31:523–534. https://doi.org/10.1007/s10876-019-01669-7
29. Mallikarjunaswamy C, Lakshmi Ranganatha V, Ramu R et al (2020) Facile microwave-assisted green synthesis of ZnO nanoparticles: application to photodegradation, antibacterial and antioxidant. J Mater Sci Mater Electron 31:1004–1021. https://doi.org/10.1007/s10854-019-02612-2
30. Singh K, Singh J, Rawat M (2019) Green synthesis of zinc oxide nanoparticles using *Punica granatum* leaf extract and its application towards photocatalytic degradation of Coomassie brilliant blue R-250 dye. SN Appl Sci 1:624. https://doi.org/10.1007/s42452-019-0610-5
31. Vahidi A, Vaghari H, Najian Y, Najian M, Jafarizadeh-Malmiri H (2019) Evaluation of three different green fabrication methods for the synthesis of crystalline ZnO nanoparticles using *Pelargonium zonale* leaf extract. Green Process Synth 8(1):302–308. https://doi.org/10.1515/gps-2018-0097
32. Sharma BK, Mehta BR, Shah EV et al (2022) Green synthesis of triangular ZnO nanoparticles using *Azadirachta indica* leaf extract and its shape dependency for significant antimicrobial activity: joint experimental and theoretical investigation. J Clust Sci 33:2517–2530. https://doi.org/10.1007/s10876-021-02145-x
33. Thirumoorthy GS, Balasubramaniam O, Kumaresan P et al (2021) *Tetraselmis indica* mediated green synthesis of zinc oxide (ZnO) nanoparticles and evaluating its antibacterial, antioxidant, and hemolytic activity. BioNanoSci 11:172–181. https://doi.org/10.1007/s12668-020-00817-y
34. Çolak H, Karaköse E, Duman F (2017) High optoelectronic and antimicrobial performances of green synthesized ZnO nanoparticles using *Aesculus hippocastanum*. Environ Chem Lett 15:547–552. https://doi.org/10.1007/s10311-017-0629-z
35. Elavarasan N, Kokila K, Inbasekar G et al (2017) Evaluation of photocatalytic activity, antibacterial and cytotoxic effects of green synthesized ZnO nanoparticles by *Sechium edule* leaf extract. Res Chem Intermed 43:3361–3376. https://doi.org/10.1007/s11164-016-2830-2
36. Varadavenkatesan T, Lyubchik E, Pai S, Pugazhendhi A, Vinayagam R, Selvaraj R (2019) Photocatalytic degradation of Rhodamine B by zinc oxide nanoparticles synthesized using the leaf extract of *Cyanometra ramiflora*. J Photochem Photobiol B 199:111621. https://doi.org/10.1016/j.jphotobiol.2019.111621
37. Darvishi D, Kahrizi D, Arkan E (2019) Comparison of different properties of zinc oxide nanoparticles synthesized by the green (using *Juglans regia* L. leaf extract) and chemical methods. J Mol Liq. https://doi.org/10.1016/j.molliq.2019.04.108
38. Hassan SS, El Azab WI, Ali HR, Mansour MS (2015) Green synthesis and characterization of ZnO nanoparticles for photocatalytic degradation of anthracene. Adv Nat Sci: Nanosci Nanotechnol 6(4):045012. https://doi.org/10.1088/2043-6262/6/4/045012
39. Jayappa MD, Ramaiah CK, Kumar MAP et al (2020) Green synthesis of zinc oxide nanoparticles from the leaf, stem and in vitro grown callus of *Mussaenda frondosa* L.: characterization and their applications. Appl Nanosci 10:3057–3074. https://doi.org/10.1007/s13204-020-01382-2
40. Ramesh AV, Pavankumar Y, Lavakusa B, Basavaiah K (2017) A facile green synthesis of ZnO nanorods using leaf extract of *Ficus hispida* L. Int J Eng Appl Sci Technol 2(4):256–260. https://www.ijeast.com/papers/256-260,Tesma204,IJEAST.pdf
41. Rahimi Kalateh Shah Mohammad G, Homayouni Tabrizi M, Ardalan T et al (2019) Green synthesis of zinc oxide nanoparticles and evaluation of anti-angiogenesis, anti-inflammatory and cytotoxicity properties. J Biosci 44:30. https://doi.org/10.1007/s12038-019-9845-y.
42. Sangeetha G, Rajeshwari S, Venckatesh R (2011) Green synthesis of zinc oxide nanoparticles by *Aloe barbadensis* miller leaf extract: structure and optical properties. Mater Res Bull 46(12):2560–2566. https://doi.org/10.1016/j.materresbull.2011.07.046
43. M Awwad A, Albiss B, L Ahmad A (2014) Green synthesis, characterization and optical properties of zinc oxide nanosheets using *Olea europea* leaf extract. Adv Mater Lett 5(9):520–524. https://doi.org/10.5185/amlett.2014.5575
44. El-Khawaga AM, Elsayed MA, Gobara M et al (2023) Green synthesized ZnO nanoparticles by *Saccharomyces cerevisiae* and their antibacterial activity and photocatalytic degradation. Biomass Conv Bioref. https://doi.org/10.1007/s13399-023-04827-0
45. Barzinjy AA, Azeez HH (2020) Green synthesis and characterization of zinc oxide nanoparticles using *Eucalyptus globulus* Labill. leaf extract and zinc nitrate hexahydrate salt. SN Appl Sci 2:991. https://doi.org/10.1007/s42452-020-2813-1
46. Khan AU, Malik N, Singh B et al (2023) Biosynthesis, and characterization of zinc oxide nanoparticles (ZnONPs) obtained from

the extract of waste of strawberry. J Umm Al-Qura Univ Appll Sci 9:268–275. https://doi.org/10.1007/s43994-023-00038-5

47. Rajakumar G, Thiruvengadam M, Mydhili G et al (2018) Green approach for synthesis of zinc oxide nanoparticles from *Andrographis paniculata* leaf extract and evaluation of their antioxidant, anti-diabetic, and anti-inflammatory activities. Bioprocess Biosyst Eng 41:21–30. https://doi.org/10.1007/s00449-017-1840-9
48. Raghavendra VB, Shankar S, Govindappa M et al (2022) Green synthesis of zinc oxide nanoparticles (ZnO NPs) for effective degradation of dye, polyethylene and antibacterial performance in waste water treatment. J Inorg Organomet Polym 32:614–630. https://doi.org/10.1007/s10904-021-02142-7
49. Ambika S, Sundrarajan M (2015) Antibacterial behaviour of *Vitex negundo* extract assisted ZnO nanoparticles against pathogenic bacteria. J Photochem Photobiol, B 146:52–57. https://doi.org/10.1016/j.jphotobiol.2015.02.020
50. Rajendrachari S, Taslimi P, Karaoglanli AC, Uzun O, Alp E, Jayaprakash GK (2021) Photocatalytic degradation of Rhodamine B (RhB) dye in waste water and enzymatic inhibition study using cauliflower shaped ZnO nanoparticles synthesized by a novel one-pot green synthesis method. Arab J Chem 14(6):103180. https://doi.org/10.1016/j.arabjc.2021.103180
51. Alshamsi HA, Jaffer AA (2022, November) New *Hibiscus sabdariffa* L. petals extract based green synthesis of zinc oxide nanoparticles for photocatalytic degradation of Rhodamine B dye under solar light. In AIP Conference Proceedings (Vol. 2394, No. 1). AIP Publishing. https://doi.org/10.1063/5.0121228
52. Hazim K, Hamza Z, Mohamed L (2022) Eco-friendly synthesis, antibacterial activity, and photocatalytic performance of ZnO nanoparticles synthesized via leaves extract of Paraserianthes lophantha. Pak J Med Health Sci 16(03):581–581. https://doi.org/10.53350/pjmhs22163581
53. Surendra TV, Roopan SM, Al-Dhabi NA, Arasu MV, Sarkar G, Suthindhiran K (2016) Vegetable peel waste for the production of ZnO nanoparticles and its toxicological efficiency, antifungal, hemolytic, and antibacterial activities. Nanoscale Res Lett 11:1–10. https://doi.org/10.1186/s11671-016-1750-9
54. Karthik P, Ravichandran S, Mukkannan A, Rajesh J (2022) Plant-mediated biosynthesis of zinc oxide nanoparticles from *Delonix elata*: a promising photocatalyst for crystal violet degradation. Inorg Chem Commun 146:110122. https://doi.org/10.1016/j.inoche.2022.110122
55. Khalil AT, Hameed S, Afridi S, Mohamed HEA, Shinwari ZK (2021) *Sageretia thea* mediated biosynthesis of metal oxide nanoparticles for catalytic degradation of crystal violet dye. Mater Today: Proc 36:397–400. https://doi.org/10.1016/j.matpr.2020.04.687
56. Badma Priya D, Thirumalai D, Asharani IV (2021) Influence of synthetic parameters on the enhanced photocatalytic properties of ZnO nanoparticles for the degradation of organic dyes: a green approach. J Mater Sci: Mater Electron 32:9956–9971. https://doi.org/10.1007/s10854-021-05654-7
57. Jones N, Ray B, Ranjit KT, Manna AC (2008) Antibacterial activity of ZnO nanoparticle suspensions on a broad spectrum of microorganisms. FEMS Microbiol Lett 279(1):71–76.39. https://doi.org/10.1111/j.1574-6968.2007.01012.x
58. da Silva BL, Caetano BL, Chiari-Andreo BG (2019) Linhari Rodrigues Pietro RC, Chiavacci LA, Increased antibacterial activity of ZnO nanoparticles: influence of size and surface modification. Colloids Surf, B. https://doi.org/10.1016/j.colsurfb.2019.02.013
59. Arvanag FM, Bayrami A, Habibi-Yangjeh A, Pouran SR (2019) A comprehensive study on antidiabetic and antibacterial activities of ZnO nanoparticles biosynthesized using *Silybum marianum L* seed extract. Mater Sci Eng, C 97:397–405. https://doi.org/10.1016/j.msec.2018.12.058

ENHANCING CATALYTIC EFFICIENCY: VTIO$_2$ NANOPARTICLES IN THE 1,6 MICHAEL ADDITION OF 3-METHYL-5-PYRAZOLONE TO 3-METHYL-4-NITRO-5-ALKENYL ISOXAZOLES FOR RAPID SYNTHESIS OF 3,3-BIS(INDOLYL)OXINDOLES IN PURE AQUEOUS MEDIUM

T. Appa Rao[a*], B. Prasada Rao[b], Dr. N. Sankara Rao[a], K. Nageswara Rao[a]

Abstract

Herein, we present a report detailing the synthesis of column chromatography-free, heterogeneous vanadium doped titanium dioxide nanoparticles (VTiO$_2$ NPs) for catalysing the 1,6 Michael addition of 3-methyl-5-pyrazolone onto 3-methyl-4-nitro-5-alkenyl isoxazoles. Additionally, we report the swift synthesis of 3,3-di(indolyl)indolin-2-ones through the reaction of indole on isatin at room temperature in water, marking the first instance of such a process. The 1,6 Michael addition reaction yielded moderate to good yields, while the 3,3-bis(indolyl)oxindole products were obtained in quantitative yield.

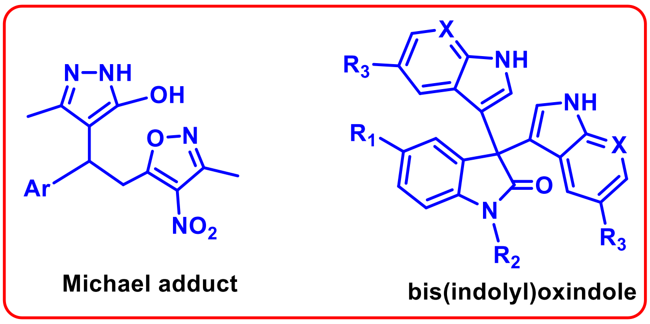

Keywords: Vanadium doped Titanium dioxide nanoparticles (VTiO$_2$ NPs), 1, 6 – Michael addition, 3,3-di(indolyl)indolin-2-ones, green chemistry matrices, 3-methyl-4-nitro-5-alkenyl isoxazoles.

---

[a]Department of Chemistry, Dr. V. S. Krishna Government Degree College (A), Visakhapatnam, Andhra Pradesh.
[b]Department of Physics, SVLNS Govt Degree College, Bheemunipatnam, Andhra Pradesh.

[*]**Corresponding Author:** T. Appa Rao
[*]Department of Chemistry, Dr. V. S. Krishna Government Degree College (A), Visakhapatnam, Andhra Pradesh.

DOI: 10.53555/ecb/2021.10.4.05

Introduction

Heterogeneous catalysis has been instrumental in enabling chemists to develop environmentally friendly and cost-effective chemical processes ever since its inception. The industrial-scale adoption of this approach can be directly attributed to its introduction into chemical processes.[1] However, the pursuit of finding a versatile heterogeneous catalyst that can efficiently catalyse various reactions is often described as the "ideal" scenario, as it promises to reduce input costs and streamline the use of a single catalyst for multiple reactions. Incorporating nanoparticles has proven to be a significant advancement in enhancing the catalytic efficiency of heterogeneous catalysts. This is because the large surface area of nanoparticles promotes greater contact between reactants and catalyst, effectively emulating the performance of homogeneous catalysts.[2]

In this pursuit, researchers have developed a range of materials, including mesoporous materials, nanoparticles, and metal-organic frameworks (MOFs), to address this challenge. Among these materials, transition metal particles, whether in their native state or immobilized on various matrices, have gained recognition for their efficiency and cost-effectiveness as catalysts.[3] Titanium dioxide (TiO_2), in particular, is a well-established additive in the food and cosmetic industries. Both native-state TiO_2 nanoparticles and functionalized variants are known for their ability to catalyse processes such as photodegradation[4] and a variety of other organic reactions.[5] Unfunctionalized TiO_2 nanoparticles (TiO_2 NPs)[6] are characterized by low toxicity.[7] In addition to this, vanadium doped TiO_2 nanoparticles displayed greater catalytic activity for diverse chemical transformations.[8-10] Hence, a comprehensive investigation into the catalytic efficacy of vanadium-doped titanium dioxide nanoparticles ($VTiO_2$ NPs) in facilitating a range of reactions within the established optimal parameters is expected to play a pivotal role in furthering researchers' endeavors towards attaining sustainability objectives.

Conversely, water has gained widespread recognition as a solvent for a broad spectrum of organic reactions, encompassing organometallic reactions,[11] pericyclic reactions,[12] and various other synthetic processes.[13] Existing literature strongly indicates that the utilization of heterogeneous catalytic methods in aqueous media can pave the way for more environmentally friendly, cost-effective, and dependable chemical operations on a larger scale.[14] These observations have guided our research focus toward addressing the challenge of conducting various types of reactions using the same catalyst in an aqueous environment. This work is part of our ongoing research efforts aimed at devising strategies for multicomponent reactions and sustainable protocols for the synthesis of biologically active compounds.[15] Dwivedi and his research team introduced a novel approach by utilizing heterogeneous titanium dioxide nanoparticles (TiO_2 NPs) as a catalyst, eliminating the need for column chromatography. They applied this catalyst to facilitate the 1,6 Michael addition of 3-methyl-5-pyrazolone onto 3-methyl-4-nitro-5-alkenyl isoxazoles and achieved the rapid synthesis of 3,3-di(indolyl)indolin-2-ones through the reaction of indole with isatin. Notably, these reactions were performed in water at room temperature, marking the first time such a method has been demonstrated.[16]

In this context, we present what we believe to be the initial report on the utilization of vanadium doped titanium dioxide nanoparticles ($VTiO_2$ NPs) as a catalyst for the 1,6 Michael addition of 3-Methyl-5-pyrazolone on 3-methyl-4-nitro-5-alkenyl isoxazoles and the rapid synthesis of 3,3-di(indolyl)indolin-2-ones, all conducted in water. Notably, in both cases, the products were obtained in pure form and in quantitative yields without the need for column chromatography.

Results and discussion

Synthesis and characterization of TiO_2 NPs and $VTiO_2$ NPs

20 mL of Tetra-n-Butyl Ortho Titanate and 40 mL of C_2H_5OH should be added to make up of Solution- 1 and agitated for 10 minutes in a 150 mL Pyrex glass beaker. Next, gradually add 3.2 mL of Nitric acid while stirring for 30 minutes. In a 150 ml Pyrex glass beaker, Solution - 2 was made by dissolving the required quantity of 5 wt. % of NH_4VO_3 dopant in a 40 mL of C_2H_5OH and 7.2 mL of H_2O. The mixture was then agitated for 30 minutes. Sol was generated by adding Solution-2 to Solution-1 drop by drop while stirring frequently. The produced sol was kept in dark for 48 hours to form a gelation, which was then dried for 24 hours at 75°C and the crystals were ground for 4 to 6 hours to a fine size. The fine powder that had been obtained was then calcined in a muffle furnace for 5 hours at 450°C. The fine powder was collected and grounded, and placed in airtight amber colour vials. TiO2 was produced using the same process without addition of dopants.[17] Analytical data confirms the TiO_2

NPs and VTiO_2 NPs formation for the study (**Figure 1a-e**). The powder XRD (**Figure 1a**) clearly depicts characteristic peaks at (101), (004), (200), (105), (211), (204), (116), (220) and (215) corresponds to anatase phase of TiO_2 NPs & VTiO_2 NPs and compared with standard (JCPDS card no. 21-1272). FESEM images of TiO_2 NPs and VTiO_2 NPs indicate the uniform size and spherical shape of the particles (**Figure 1b & 1c**) and the EDS (energy dispersive X-ray spectroscopy) spectrum of synthesized TiO_2 NPs and VTiO_2 NPs confirms the presence of Ti and O (**Figure 1d & 1e**).

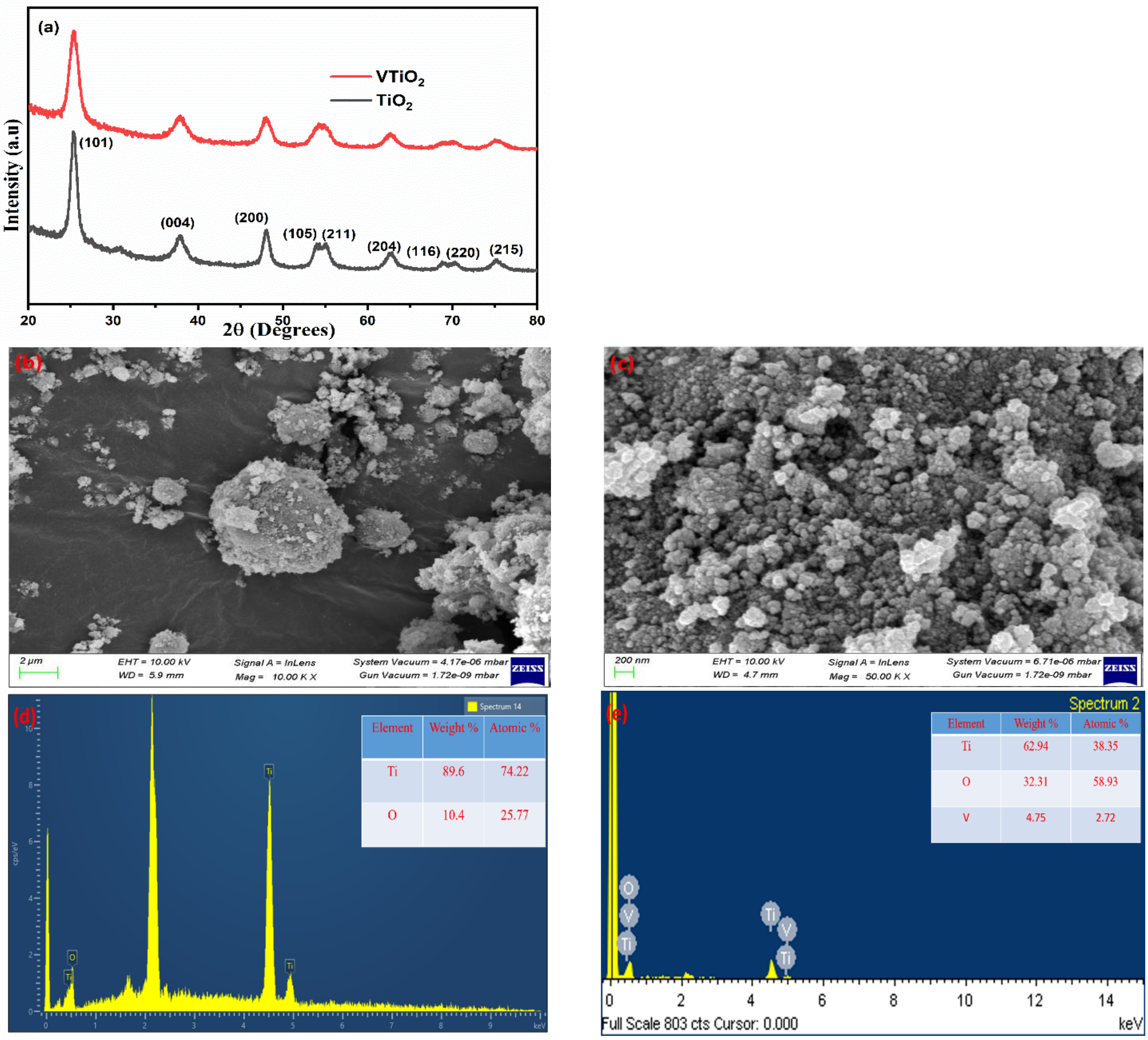

Figure 1; Characterisations of TiO_2 NP and VTiO_2 NP Catalyst; **1a)** powder XRD with the simulated graph (JCPDS Card no. 21-1272). **1b**) FESEM image of TiO_2, **1c**) FESEM image of VTiO_2 **1d**) EDS elemental analysis of TiO_2, **1e**) EDS elemental analysis of VTiO_2

Optimisation and substrate scope studies

Optimization investigations were initially conducted for the 1,6 Michael addition of 3-methyl-5-pyrazolone (2) to 3-methyl-4-nitroisoxazole alkenes (1a). This exploration involved the utilization of different water-stable Lewis acids and EtOH as a solvent. Our aim was to comprehend the efficiencies of catalysts in environmentally friendly conditions under open-air settings (**Figure 2a**).

As evident from the observations, the application of Lewis acid catalysis proved to be productive, yielding 40% with a 10 mol% concentration of $Sc(OTf)_3$ as a catalyst within 90 minutes. The introduction of $Cu(OTf)_2$ during the same timeframe reduced the yield to 21%, while $Fe(OTf)_3$ enhanced it to 51%. Contrarily, the use of 10 mol% commercial TiO_2 solid yielded only 45% within the same time frame. However, employing 10 mol% TiO_2 NPs in ethanol resulted in a significantly improved yield of 82% within the 90-minute duration. The vanadium-doped titanium dioxide nanoparticles (VTiO_2 NPs) catalyst demonstrated a 96% product yield within the anticipated timeframe, surpassing the yield achieved by titanium dioxide nanoparticles (TiO_2 NPs) as a catalyst.

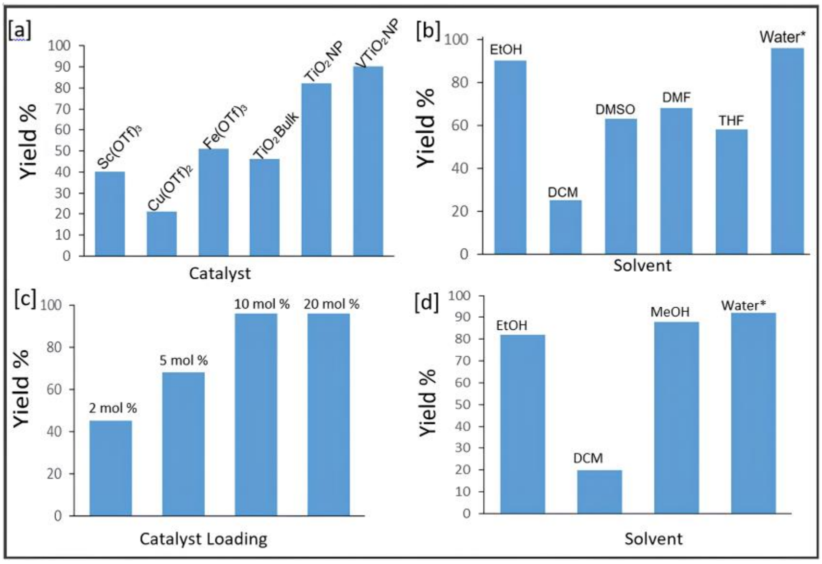

Figure 2: [a]Reaction conditions: unless otherwise specified, **Figure 2a-c** represents the optimization studies are carried out on the reaction with 3-methyl-4-nitroisoxazole alkenes (**1a)** (1.0 mmol), 3-methyl-5-pyrazolone (**2**) (1.0 mmol) at room temperature. **Figure 2d** represents the solvent optimization for 3,3-bis(indolyl)oxindoles synthesis carried out on the reaction with isatin (**4a)** (1.0 mmol), indole (**5a**) (2.0 mmol) and 10 mol% VTiO_2 NPs at room temperature. [b] Isolated yields.

Figure 2a: Catalyst optimization in ethanol solvent with a standard reaction time of 90 min.

Figure 2b: Solvent optimization with 10 mol% VTiO_2 NPs and standard reaction time of 90 min.*Reaction completed in 60 min.

Figure 2c: Catalyst loading optimization in water solvent with a standard reaction time of 60min.

Figure 2d: Solvent optimization for 3,3-bis(indolyl)oxindoles synthesis with 10 mol% VTiO_2 NPs and standard reaction time of 60 min.*Reaction completed in 15 min.

Further optimization studies were conducted to enhance yield and reduce reaction time (**Figure 2b**). Various solvents were explored for the catalytic reaction, revealing that water yielded an impressive 96% within 60 minutes, outperforming all other organic solvents (**Figure 2b**). Subsequent investigations focused on the impact of catalyst loading (**Figure 2c)**, revealing that 10 mol% was the optimal amount for achieving complete reaction in water. Below 10%, the catalyst loading proved inefficient, while an increase to 20 mol% did not significantly improve yield or reduce reaction time. Consequently, we determined that water with a 10 mol% catalyst loading represented the optimized conditions for the 1,6 Michael addition reaction of 5-methylpyrazolone on 3-methyl-4-nitroisoxazole alkenes in pure water. These optimized conditions demonstrated versatility across a broad substrate scope, yielding favorable results (**Table 1**).

Table 1. Substrate scope for 1,6 Michael addition reaction of 3-methyl-4-nitroisoxazole alkenes and 3-methyl-5-pyrazolone

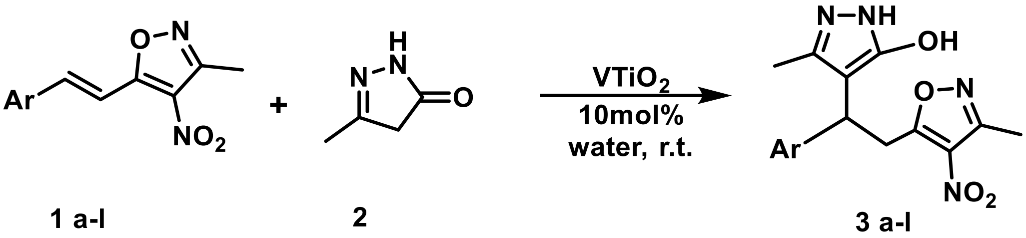

Entry[a]	Ar	2	Product	Time (hrs)	Yield (%)[b]
1	1a= C_6H_5	2a	3a	1.5	86
2	1b: 3-F-C_6H_5	2a	3b	2.0	96
3	1c: 4-F-C_6H_5	2a	3c	1.0	89
4	1d: 2-Cl-C_6H_5	2a	3d	1.2	84
5	1e: 4-Cl-C_6H_5	2a	3e	1.3	88
6	1f: 2-Br-C_6H_5	2a	3f	1.5	87
7	1g: 4-Br-C_6H_5	2a	3g	1.5	84
8	1h: 4-NO_2-C_6H_5	2a	3h	2	89
9	1i: 4-Me-C_6H_5	2a	3i	1	86
10	1j: 4-OMe-C_6H_5	2a	3j	1	89
11	1k= furan	2a	3k	1.5	87
12	1l= thiophene	2a	3l	1	89

[a] Reaction conditions: unless otherwise specified, the reaction was carried out with 3-methyl-4-nitroisoxazole alkenes (**1a-l)** (1.0 mmol), 3-methyl-5-pyrazolone (**2**) (1.0 mmol) and $VTiO_2$ NPs (10 mol%) in 3 mL H_2O. Isolated yields of the product (**3a-l**).

We further explore the diversity of the catalytic application of $VTiO_2$ NPs by synthesizing 3,3-bis(indolyl)oxindoles in neat water. Though bis(indolyl)methane synthesis using aromatic aldehydes and indoles is well established with a range of Lewis acid catalysts[18] 3,3-bis(indolyl)oxindoles synthesis by reacting isatin with indoles in water at room temperature is less explored[19]. As it can be seen from the optimization study (**Figure 2c**), water has given quantitative yield in 15 minutes using **4a** and **5a** as model substrates with 10 mol% of $VTiO_2$ NPs catalyst loading (**Figure 2c**), without any change from previous optimized condition. Other organic solvents performed poorly compared to neat water medium giving less than 80% after 90 minutes (**Figure 2c**). With these optimized conditions in hand, we explored the substrate scope and found that, the developed protocol was efficient and accommodated an array of substrates, giving quantitative yields within a maximum of 20 minutes reaction time (**Table 2**). However, few interesting observations were made; the reaction did not proceed in case of 5-CN indole was used (**Table 2, entry 16**) and Azo indole (Table 2, entry 17). N-methyl Indole too failed to give the desired product (**Table 2, entry 18**).

Table 2. Substrate scope for the 3,3-bis(indolyl)oxindoles

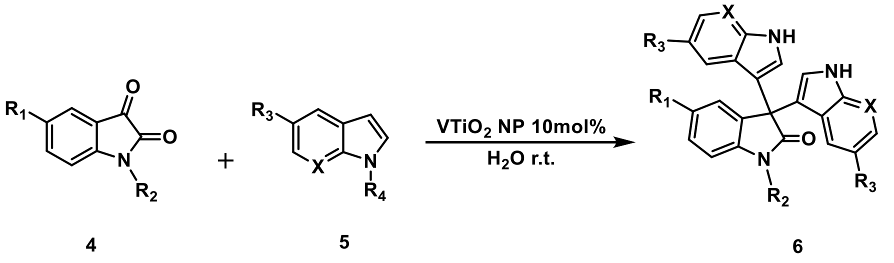

Entry[a]	Product	R_1	R_2	R_3	R_4	X	Time (min)	Yield (%)[b]
1	6a	H	H	H	H	CH	15	98
2	6b	F	H	H	H	CH	10	97
3	6c	Cl	H	H	H	CH	10	96
4	6d	Br	H	H	H	CH	15	98
5	6e	NO_2	H	H	H	CH	20	95
6	6f	H	C_3H_5	H	H	CH	20	96
7	6g	H	CH_2-Ph	H	H	CH	15	97
8	6h	OMe	H	H	H	CH	20	98
9	6i	H	H	Br	H	CH	15	97
10	6j	F	H	Br	H	CH	10	96
11	6k	Cl	H	Br	H	CH	12	96
12	6l	NO_2	H	Br	H	CH	15	98
13	6m	H	C_3H_5	Br	H	CH	18	97

14	6n	H	CH_2-Ph	Br	H	CH	20	96
15	6o	OMe	H	Br	H	CH	20	94
16	6p	H	H	CN	H	CH	60	-*
17	6q	H	H	H	H	N	60	-*
18	6r	H	H	H	Me	CH	60	-*

[a] Reaction condition: unless otherwise specified, the reaction was carried out with isatins (**4a-i)** (1.0 mmol), indole (**5a-d**) (2.0 mmol) and $VTiO_2$ NPs (10 mol%) in 3 mL H_2O was stirred. Isolated yields of the product (**6a-r**).[b] Isolated yield * no product was formed and starting material was recovered.

Plausible Mechanism

Regarding the 1,6 Michael addition, the 3-methyl-5-pyrazolone exhibits keto-enol tautomerism. Notably, the presence of water on the VTiO2 catalyst surface facilitates robust hydrogen bonding with the substrates, immobilizing them and bringing the reactants into close proximity.[16]

For the synthesis of 3,3-bis(indolyl)oxindoles, our rationale involves the stepwise addition of indole to isatin. The initial addition is succeeded by the dehydration of the isatin-indole adduct, leading to the formation of a reactive alkylideneindolenine,[20] and this intermediate promptly undergoes further indole addition, resulting in the formation of the bis indole product.

Experimental section

General experimental details

All commercially available chemicals were used without further purification. ^{1}H NMR spectra were obtained on Bruker 500 MHz FT-NMR spectrometers. ^{13}C NMR spectra were recorded at 125 MHz Chemical shifts are reported in relative to the TMS signal. Multiplicity is indicated as follows: s (singlet); bs (broad singlet); d (doublet); t (triplet); q (quartet); m (multiplet); dd (doublet of doublets), etc. The hydrodynamic sizes of the synthesized TiO_2 NPs were measured using a DLS instrument (MicrotracZetatrac, U2771). FT-IR spectrometer (Shimadzu) in the range of 400–4000 cm^{-1}. Vanadium doped titanium dioxide nanoparticles ($VTiO_2$ NPs) was synthesized as per literature procedure. $VTiO_2$ phase was verified by X-ray diffraction (XRD) analysis were carried out at room temperature using a Bruker D8 Advance X-ray diffractometer. Elemental analysis and imaging were performed using EDS Nova Nano SEM-450 using a scanning electron microscope (SEM) equipped with EDS.

General Procedure for 1, 6 Michael addition of 3-methyl–5–pyrazolone on 3-methyl-4-nitroisoxazole alkenes (3a-l)

To a solution of 3-methyl-4-nitroisoxazole alkenes (**1a-1l**) (1 mmol) in water (3.0 mL) was added 3-methyl-5-pyrazolone (**2**) (1 mmol) and $VTiO_2$NPs (0.1 mmol, 10 mol%) and the resulting mixture was stirred for the specified duration (**Table 1**) at room temperature. Progress of the reaction was determined by thin layer chromatography (TLC). Upon completion, the solid crude product was filtered and dried. The obtained solid was dissolved in ethyl acetate and subjected to centrifugation at 15000 rpm for 1 hour to separate the catalyst nanoparticles. The organic layer was then passed through a celite bed to eliminate any particulate impurities from the product, followed by concentration under reduced pressure. The resulting crude material was recrystallized from methanol to yield the analytically pure product (**3a-l**).

Spectral data for selected compounds of 1, 6 Michael addition reaction (3a, 3b, 3i and 3l):

5-methyl-4-(2-(3-methyl-4-nitroisoxazol-5-yl)-1-phenylethyl)-4H-pyrazol-3-ol, 3a**:** M.P.: 191-193 ^{o}C. IR (KBr) υ_{max} (cm-1) 3412, 2928, 2860, 1604, 1528, 1420, 1221, 832, 749, 651, 525;1H NMR (500 MHz, CDCl3) δ 7.41 (d, J = 7.7 Hz, 2H), 7.30 (t, J = 7.1 Hz, 2H), 7.22 (d, J = 7.6 Hz, 1H), 4.46 (t, J = 8.3 Hz, 1H), 4.19 (dd, J = 15.1, 9.5 Hz, 1H), 3.94 (dd, J = 15.3, 7.0 Hz, 1H), 2.49 (s, 3H), 2.12 (s, 3H). 13C NMR (126 MHz, CDCl3) δ 178.81, 165.40, 159.99, 148.02, 142.50, 134.95, 133.23, 132.10, 131.37, 106.38, 42.72, 37.36, 16.37, 15.05. HRMS (ESI+): *m/z* calculated for $C_{16}H_{16}N_4O_4$ $[M+H]^+$: 329.1250; found: 329.1250.

4-(1-(3-fluorophenyl)-2-(3-methyl-4-nitroisoxazol-5-yl)ethyl)-5-methyl-4H-pyrazol-3-ol, 3b: M.P.: 193-195 ^{o}C. IR (KBr) υ_{max} (cm^{-1}) 3425, 2932, 2877, 1609, 1557, 1420, 1223, 825, 756, 632, 519; ^{1}H NMR (500 MHz, $CDCl_3$) δ 7.26 – 7.21 (m, 1H), 7.15 (d, *J* = 7.7 Hz, 2H), 6.90 (t, *J* = 8.4 Hz, 1H), 4.41 (t, *J* = 8.2 Hz, 1H), 4.15 (dd, *J* = 15.3, 9.3 Hz, 1H), 3.90 (dd, *J* = 15.4, 7.2 Hz, 1H), 2.50 (s, 3H), 2.12 (s, 3H). ^{13}C NMR (126 MHz, $CDCl_3$) δ 179.06, 169.01, 167.16, 165.19, 160.22, 152.12, 150.13, 143.99, 134.89, 127.90, 118.43, 118.26, 105.16, 42.41, 37.29, 17.08, 15.16. HRMS (ESI+):*m/z* calculated for $C_{16}H_{15}FN_4O_4$ $[M+H]^+$: 347.1156; found: 347.1169.

5-methyl-4-(2-(3-methyl-4-nitroisoxazol-5-yl)-1-(p-tolyl)ethyl)-4H-pyrazol-3-ol, 3i: M.P. 203-205 ^{o}C. IR (KBr) υ_{max} (cm^{-1}) 3346, 2931, 2867, 1605, 1498, 1475, 1272, 832, 756, 659, 568; ^{1}HNMR (500 MHz, $CDCl_3$) δ 7.29 (d, *J* = 8.0 Hz, 2H), 7.10 (d, *J* = 7.6 Hz, 2H), 4.40 (t, *J* = 8.1 Hz, 1H), 4.13 (dd, *J* = 15.3, 9.2 Hz, 1H), 3.89 (dd, *J* = 15.4, 7.1 Hz, 1H), 2.49 (s, 3H), 2.30 (s, 3H), 2.09 (s, 3H). ^{13}C NMR (126 MHz, $CDCl_3$) δ 178.78, 165.43, 159.87, 146.08, 143.18, 141.52, 135.87, 133.76, 131.85, 106.45, 42.44, 36.59, 26.17, 16.56, 15.19. HRMS (ESI+): m/z calculated for $C_{17}H_{18}N_4O_4$ $[M+H]^+$: 343.1406; found: 343.1433.

5-methyl-4-(2-(3-methyl-4-nitroisoxazol-5-yl)-1-(thiophen-2-yl)ethyl)-4H-pyrazol-3-ol, 3l: M.P. 228-230 ^{o}C. IR (KBr) υ_{max} (cm^{-1}) 3389, 3012, 2764, 1604, 1525, 1464, 1262, 827, 725, 624, 554; ^{1}HNMR (500 MHz, $CDCl_3$) δ 7.17 (d, *J* = 4.8 Hz, 1H), 6.98 (s, 1H), 6.89 (d, *J* = 3.6 Hz, 1H), 4.74 (s, 1H), 4.13 (d, *J* = 9.2 Hz, 1H), 4.03 (d, *J* = 7.0 Hz, 1H), 2.50 (s, 3H), 2.17 (s, 3H). ^{13}C NMR (126 MHz, $CDCl_3$) δ 179.06, 165.04, 161.32, 153.12, 136.11, 130.65, 129.09, 106.17, 38.28, 37.58, 16.45, 15.34. HRMS (ESI+): m/z calculated for $C_{14}H_{14}N_4O_4S$ $[M+H]^+$: 335.0814; found: 335.0824.

General Procedure for the synthesis 3,3-bis(indolyl)oxindoles (6a-r)

In a water solution containing isatins (1 eq.) and VTiO2 NPs (10 mol%) at a ratio of 3 mL/mmol, indoles (1 eq.) were introduced and stirred for the specified duration at room temperature (see Table 2). The progression of the reaction was monitored through TLC, with the disappearance of isatin color and the formation of white solid serving as visual indicators. Upon completion of the reaction, as evidenced by TLC, the reaction mixture was filtered, yielding a white solid crude product. This solid was then dissolved in ethyl acetate and subjected to centrifugation for 1 hour at 15000 rpm to isolate nanoparticles. The organic layer was subsequently passed through a celite bed to eliminate any particulate impurities, followed by concentration under reduced pressure. The resulting crude material underwent recrystallization from methanol, resulting in the isolation of analytically pure 3,3-di(indolyl)indolin-2-ones products **(6a-r)**.

Spectral data for selected compounds of 3,3-bis(indolyl)oxindoles (6a, 6f, 6k):

[3,3':3',3''-terindolin]-2'-one, 6a: White solid, M.P. 253-255 ^{0}C. IR (KBr, cm^{-1}) 3425, 3427, 3156, 3078, 1703, 1614, 1497, 1017, 813 cm^{-1}; ^{1}H NMR (500 MHz, $CDCl_3$) δ 9.29 (s, 1H), 7.42 (d, *J* = 3.8 Hz, 1H), 7.36 – 7.29 (m, 1H), 7.23 (t, *J* = 7.5 Hz, 1H), 7.09 (t, *J* = 7.4 Hz, 1H), 7.05 – 6.98 (m, 1H), 6.94 – 6.92 (m, 1H), 6.87 (dd, *J* = 14.7, 7.4 Hz, 1H). ^{13}C NMR (126 MHz, $CDCl_3$) δ 182.78, 142.78, 132.12, 130.54, 129.46, 129.47, 126.32, 125.99, 123.41, 119.54, 116.24, 114.61, 56.98. HRMS (ESI+): *m/z* calculated for $C_{24}H_{17}N_3O[M+H]^+$: 364.1450; found: 364.1496.

1'-allyl-[3,3':3',3''-terindolin]-2'-one, 6f: White solid, M.P. 252-254 ^{0}C. IR (KBr, cm^{-1}) 3398, 3371, 3202, 30439, 1664, 1611, 1463, 1110, 767 cm^{-1}; ^{1}H NMR (500 MHz, $CDCl_3$) δ 8.08 (s, 1H), 7.53 (d, J = 7.2 Hz, 1H), 7.38 (t, J = 9.2 Hz, 2H), 7.13 (t, J = 7.6 Hz, 1H), 7.00 (d, J = 7.4 Hz, 2H), 6.89 (t, J = 7.5 Hz, 1H), 5.98 – 5.84 (m, 1H), 5.33 – 5.16 (m, 1H), 4.49 (d, J = 4.5 Hz, 1H).^{13}C NMR (126 MHz, $CDCl_3$) δ 146.90, 141.92, 139.05, 138.95, 136.93, 136.46, 132.59, 130.79, 129.31, 127.17, 126.04, 125.85, 123.52, 123.42, 122.35, 122.26, 119.29, 119.26, 116.39, 116.36, 113.82, 57.44, 47.13. HRMS (ESI+): *m/z* calculated for $C_{27}H_{21}N_3O[M+H]^+$: 404.1763; found: 404.1836.

5,5''-dibromo-5'-chloro-[3,3':3',3''-terindolin]-2'-one, 6k: White solid, M.P. 288-291 ^{0}C. IR (KBr, cm^{-1}) 3647, 3564, 3379, 3032, 1703, 1613, 1605, 1478, 1086, 797, 748 cm^{-1}; ^{1}H NMR (500 MHz, $CDCl_3$) δ 10.76 (s, 2H), 10.55 (s, 1H), 7.45 (s, 2H), 7.28 (d, J = 8.5 Hz, 2H), 7.20 (d, J = 8.2 Hz, 1H), 7.11 (d, J = 8.5 Hz, 2H), 7.09 (s, 2H), 6.99 (d, J = 8.2 Hz, 1H), 6.89 (s, 2H). ^{13}C NMR (126 MHz, $CDCl_3$) δ 183.43, 144.86, 140.92, 140.72, 132.34, 132.28, 131.75, 130.92, 128.84, 129.93, 127.89, 126.89, 127.95, 118.78, 116.77, 116.45, 57.49. HRMS (ESI+): *m/z* calculated for $C_{24}H_{14}Br_2ClN_3O$ $[M+H]^+$: 553.9270; found: 553.9294.

Conclusion

In conclusion, we present the catalytic prowess of $VTiO_2$ NPs in facilitating the 1,6 Michael addition of 3-methyl-5-pyrazolone on 3-methyl-4-nitro-5-alkenyl isoxazoles and the rapid synthesis of 3,3-di(indolyl)indolin-2-ones. Notably, these reactions were conducted in pure water at room temperature, marking a new achievement. The efficacy of this heterogeneous catalytic approach was demonstrated through successful scale-up experimentation (10 mmol), and recyclability trials for both reactions were conducted for up to four cycles.

Acknowledgments

The author extends appreciation to the personnel of the chemistry laboratory, Dr V S Krishna

Government Degree College (A), as well as all those who assisted in gathering materials and conducting this scientific investigation.

Reference

1. (a) U. Dingerdissen, A. Martin, D. Herein, H. J. Wernicke, *The Development of Industrial Heterogeneous Catalysis. In Handbook of Heterogeneous Catalysis; Wiley-VCH Verlag GmbH & Co. K Ga A: Weinheim, Germany,* **2008**, 68–81. (b) J. Heveling, Heterogeneous Catalytic Chemistry by Example of Industrial Applications. *J. Chem. Educ*. **2012**, *89*, 1530–1536. (c) C. Lucarelli, A. Vaccari, Examples of Heterogeneous Catalytic Processes for Fine Chemistry. *Green Chem*. **2011**, *13*, 1941–1949.
2. F. Zaera, Nanostructured Materials for Applications in Heterogeneous Catalysis. *Chem. Soc. Rev.* **2013**, *42*, 2746–2762. Doi:10.1039/C2CS35261C
3. (a) Jiang, W.; Ji, W.; Au, C. T. Surface/Interfacial Catalysis of (Metal)/Oxide System: Structure and Performance Control. *Chem Cat Chem.* ***2018,*** *10,* 2125–2163. (b) G. A. Mutch, S. Shulda, A. J. McCue, M. J. Menart, C. V. Ciobanu, C. Ngo, J. A. Anderson, R. M. Richards, D. Vega-Maza, Facet, Carbon Capture by Metal Oxides: Unleashing the Potential of the (111) Facet. *J. Am. Chem. Soc.* **2018,** *140,* 4736–4742. (c) D. Pla, M. Gomez, Metal and Metal Oxide Nanoparticles: A Lever for C–H Functionalization. *ACS Catal.* **2016,** *6,* 3537–3552. (d) J. Pal, T. Pal, Faceted Metal and Metal Oxide Nanoparticles: Design, Fabrication and Catalysis. *Nanoscale* **2015**, *7,* 14159–14190. Doi:10.1002/ cctc.201701958
4. (a) E. Vulliet, C. Emmelin, J. M. Chovelon, C. Guillard, J. M. Herrmann, Photocatalytic Degradation of the Herbicide Cinosulfuron in Aqueous TiO$_2$ Suspension. *Environ. Chem. Lett.* **2003,** *1,* 62–67. (b) D. Kanakaraju, B. D. Glass, M. Oelgemoller, Titanium Dioxide Photocatalysis for Pharmaceutical Wastewater Treatment. *Environ. Chem. Lett.* **2014,** *12,* 27–47. (c) V. A. Sakkas, A. Dimou, K. Pitarakis, G. Mantis, T. Albanis, TiO$_2$ Photocatalyzed Degradation of Diazinon in an Aqueous Medium. *Environ. Chem. Lett.* **2005,** *3,* 57–61.
5. (a) M. Z. Kassaee, R. Mohammadi, H. F. Masrouri, *Chinese Chem. Lett.* **2011,** *22,* 1203–1206. (b) S. Abdolmohammadi, TiO$_2$ Nanoparticles as an Effective Catalyst for the Synthesis of Hexahydro-2-Quinolinecarboxylic Acids Derivatives. *Chinese Chem. Lett.* **2012,** *23,* 1003–1006. (c) A. Bharathi, S. M. Roopan, A. Kajbafvala, R. D. Padmaja, M. S. Darsana, G. Nandhini Kumari, Catalytic Activity of TiO$_2$ Nanoparticles in the Synthesis of Some 2,3-Disubstituted Dihydroquinazolin-4(1H)-Ones. *Chinese Chem. Lett.* **2014,** *25,* 324–326.
6. S. M. Gupta, M. Tripathi, A Review of TiO$_2$ Nanoparticles. *Chin. Sci. Bull.* **2011,** *56,* 1639–1657. Doi:10.1007/s11434-011-4476-1
7. W. Dudefoi, K. Moniz, E. Allen-Vercoe, M. H. Ropers, V. K. Walker, Impact of Food Grade and nano-TiO$_2$ Particles on a Human Intestinal Community. *Food Chem. Toxicol.* **2017,** *106,* 242–249. Doi:10.1016/j.fct.2017.05.050
8. Wenfang Zhou, Qingju Liu, Zhongqi Zhu and Ji Zhang. Preparation and properties of vanadium-doped TiO$_2$ photocatalysts. *Journal of Physics D: Applied Physics,* **2010,** *43,* 3.
9. Wen-Churng Lin, Yo-Jane Lin, Effect of Vanadium (IV)-Doping on the Visible Light-Induced Catalytic Activity of Titanium Dioxide Catalysts for Methylene Blue Degradation, *Environ Eng Sci.* **2012, *29,*** 6, 447-452. doi: 10.1089/ees.2010.0350.
10. K. Bhattacharyya, S. Varma, A. K. Tripathi, A. Vinu, A. K. Tyagi, Gas-phase photooxidation of alkenes by V-doped TiO2-MCM-41: mechanistic insights of ethylene photooxidation and understanding the structure-activity correlation. *Chemistry,* **2011**, *24, 17,* 12310-25. doi: 10.1002/chem.201001121. Epub 2011 Sep 16.
11. L. Cicco, S. Sblendorio, R. Mansueto, F. M. Perna, A. Salomone, S. Florio, V. Capriati, Water Opens the Door to Organolithiums and Grignard Reagents: exploring and Comparing the Reactivity of Highly Polar Organometallic Compounds in Unconventional Reaction Media towards the Synthesis of Tetrahydrofurans. *Chem. Sci.* **2016,** *7,* 1192–1199. Doi:10.1039/C5SC03436A
12. J. E. Klijn, J. B. F. N. Engberts, Handb. *Green Chem.* **2010,** *5,* 229–271.
13. (a) C. J. Li, Organic Reactions in Aqueous Media with a Focus on Carbon-Carbon Bond Formations: A Decade Update. *Chem. Rev.* **2005**, *105,* 3095–3166. Doi:10.1021/cr030009u
14. (a) C. R. Chang, Z. Q. Huang, J. Li, The Promotional Role of Water in Heterogeneous Catalysis: mechanism Insights from Computational Modeling. Wires. Comput. ***Mol. Sci.*** **2016,** *6,* 679–693. (b) P. R. Davies, On the Role of Water in Heterogeneous Catalysis: A Tribute to Professor M. Wyn Roberts. *Top. Catal.* **2016**, *59,* 671–677. Doi:10.1002/wcms.1272

15. (a) N. S. Kumar, R. N. Kumar, L. C. Rao, N. Muthineni, T. Ramesh, N. J. Babu, H. M. Meshram, Acid-Catalyzed Protocol for the Synthesis of Novel 6-Substituted Tetrahydroquinolines by Highly Regioselective C6-Functionalization of Tetrahydroquinolines with Chromene Hemiacetals or b-Nitrostyrenes. ***Synth.*** **2017,** *49,* 3171–3182. (b) A. M. Akondi, S. Mekala, M. L. Kantam, R. Trivedi, L. R. Chowhan, A. Das, An Expedient Microwave Assisted Regio- and Stereoselective Synthesis of Spiroquinoxaline Pyrrolizine Derivatives and Their AChE Inhibitory Activity. *New J. Chem.* **2017,** *41,* 873–878. (c) M. S. Reddy, L. R. Chowhan, N. Satish Kumar, P. Ramesh, S. B. Mukkamala, An Expedient Regio and Diastereoselective Synthesis of Novel Spiropyrrolidinylindenoquinoxalines via 1,3-Dipolar Cycloaddition Reaction. *Tetrahedron Lett.* **2018,** *59,* 1366–1371. (d) L. R. Chowhan, M. S. Reddy, N. S. Kumar, An Efficient and Rapid Synthesis of 3-Hydroxy-3-Alkyl-2-Oxindoles via Zn-Mediated Barbier-Type Reaction under Aqueous Conditions. *J. Chem. Sci.* **2017,** *129,* 1205–1209.
16. K. D. Dwivedi, S. R. Marri, S. K. Nandigama, L. R. Chowhan, Exploring TiO$_2$ NPs as efficient catalyst for 1,6 Michael addition of 3-methyl-5-pyrazolone on 3-methyl-4-nitro-5-alkenyl isoxazoles and rapid synthesis of 3,3-bis(indolyl)oxindoles in water, *Synthetic Communications,* **2018,** Taylor & Francis.
17. S. A. Alim, T. S. Rao, S. R. Miditana, K. V. D. Lakshmi, Efficient and recyclable visible light-active nickel–phosphorus co-doped TiO$_2$ nanocatalysts for the abatement of methylene blue dye. *J. Nanostruct. Chem.* **2020,** *10,* 211–226. https://doi. org/10.1007/s40097-020-00343-z.
18. P. J. Praveen, P. S. Parameswaran, M. S. Majik, Bis(Indolyl)Methane Alkaloids: Isolation, Bioactivity, and Syntheses. *Synth.* **2015,** *47,* 1827–1837.
19. A. Bahuguna, S. Kumar, V. Sharma, K. L. Reddy, K. Bhattacharyya, P. C. Ravikumar, V. Krishnan, Nanocomposite of MoS 2 -RGO as Facile, Heterogeneous, Recyclable, and Highly Efficient Green Catalyst for One-Pot Synthesis of Indole Alkaloids. *ACS Sustainable Chem. Eng.* **2017,** *5,* 8551–8567. Doi:10.1021/acssuschemeng.7b00648
20. A. Palmieri, M. Petrini, R. Shaikh, Synthesis of 3-Substituted Indoles via Reactive Alkylideneindolenine Intermediates. *Org. Biomol. Chem.* **2010,** *8,* 1259–1270. Doi:10.1039/B919891A

A COMPLETE CLASSIFICATIONAL REVIEW ON ICH GUIDELINES

Dr. Ch. S. Anuradha[1], Dr N Sankara Rao[2], GRDN Lakshmi[3*], Dr.V. Tejeswara Rao[4*]

ABSTRACT
Through industry and regulatory participation, ICH has successfully unified technical guidelines globally. After ICH reform, ICH has transparent governance and membership that is becoming more international. There are five clear steps in the ICH guideline formulation process. The goal of the International Council of Harmonization (ICH) is to secure global harmonization in the development and registration of safe, efficient, and high-quality pharmaceuticals.

Keywords: ICH guidelines; Q- series; harmonization; stability studies; GMP.

---

[1]Lecturer in Chemistry, Dr.V.S.Krishna Government Degree and PG College (A), Visakhapatnam -530013 India
[2]Department of Chemistry, Dr.V.S.Krishna Government Degree College (A), Visakhapatnam.
[3*]Lecturer in Organic Chemistry, Dr.V.S.Krishna Government Degree and PG College (A), Visakhapatnam - 530013 India
[4*]Associate professor, Department of PG Chemistry, MVR Degree and PG College, Visakhapatnam.

***Corresponding Author:** Dr.V.Tejeswara Rao, GRDN Lakshmi
*Associate professor, Department of PG Chemistry, MVR Degree and PG College, Visakhapatnam.
*Lecturer in Organic Chemistry, Dr.V.S.Krishna Government Degree and PG College (A), Visakhapatnam - 530013 India

DOI: - 10.53555/ecb/2022.11.8.103

1. INTRODUCTION

The International Council for Harmonization (ICH), formerly the International Conference on Harmonization (ICH), held its inaugural assembly meetings on October 23, 2015, establishing ICH as an international association and a legal entity under Swiss law. Since its inception in 1990, ICH has gradually evolved to respond to increasingly global developments in the pharmaceutical sector, and these ICH guidelines are being applied by a growing number of regulatory authorities. This step built upon a 25-year track record of successful delivery of harmonized guidelines for global pharmaceutical development as well as their regulation and a longer-standing recognition of the need to harmonize.

1.1 What Does ICH Stand For?

The complete name of ICH is the "International Conference on Harmonization of Technical Requirements for Registration of Pharmaceuticals for Human Use".

1.2 What is ICH?

ICH is a joint initiative involving both regulators and research-based industry representatives of the EU, Japan and the US in scientific and technical discussions of the testing procedures required to assess and ensure the safety, quality and efficacy of medicines. It was established in April, 1990.

ICH is comprised of representative from the six cosponsoring parties as well as three observers and The International federation of pharmaceutical manufactures associations (IFPMA).

Japan: The ministry of health and welfare-**MHW**
The Japan pharmaceutical manufacturer's association-**JPMA**
European: European Commission-**EC**
European federation of pharmaceutical industry association- **EFPIA**
USA: Food and drug administration **–FDA**
The pharmaceutical research and manufacture's of America**-PHRMA**
Observers: WHO, EFTA, Canada

Purpose of ICH: The objective of ICH is to increase international coordination of technical requirements to ensure that safe, effective, and high quality medicines are developed and registered in the most efficient and cost-effective manner.

ICH Guidelines: ICH has developed over 45 harmonized guidelines. The ICH Topics are divided into four major categories:

- **Quality (Q),** i.e., those relating to chemical and Pharmaceutical Quality Assurance.
- **Safety (S),** i.e., those relating to toxicity tests of drugs in preclinical studies.
- **Efficacy (E),** i.e., those relating to clinical studies in human subject.
- **Multidisciplinary topics (M),** i.e., cross-cutting Topics which do not fit uniquely into one of the above categories.

ICH: Quality: The European Medicines Agency publishes scientific guidelines on human medicines that are harmonized by the International Council for Harmonization of Technical Requirements for Registration of Pharmaceuticals for Human Use (ICH).

For a complete list of scientific guidelines [1-6] currently open for consultation, see Public consultations.

- Stability
- Analytical validation
- Impurities
- Regulatory acceptance
- Quality of biotechnological products
- Specifications
- Good manufacturing practice
- Pharmaceutical development
- Lifecycle management

Stability:

- ICH Q1A (R2): Stability testing of new drug substances and drug products: a scientific guideline
- ICH Q1B: Photo stability Testing of New Active Substances and Medicinal Products: A Scientific Guideline
- ICH Q1C Stability Testing: Requirements for New Dosage Forms: A Scientific Guideline
- ICH Q1D Bracketing and Matrixing Designs for Stability Testing of Drug Substances and Drug Products: A Scientific Guideline
- ICH Q1E Evaluation of Stability Data: A Scientific Guideline
- ICH Q1F Stability Data Package for Registration in Climate Zones III and IV: Scientific Guidelines

Analytical validation and development [7-9]:

- ICH Q2(R2) Validation of analytical procedures - Scientific guideline
- ICH Q14 Analytical procedure development - Scientific guideline

Impurities:

- ICH Q3A (R2) Impurities in new drug substances - Scientific guideline
- ICH Q3B (R2) Impurities in new drug products -

Scientific guideline
- ICH Q3C (R8) Residual solvents - Scientific guideline
- ICH Q3D Elemental impurities - Scientific guideline

Regulatory acceptance:
- ICH Q4B Evaluation and recommendation of pharmacopoeia texts for use in the ICH regions - Scientific guideline
- ICH Q4B Annex 1 Residue on ignition/sulphated ash - Scientific guideline
- ICH Q4B Annex 2 Test for extractable volume in parenteral preparations - Scientific guideline
- ICH Q4B Annex 3 Test for particulate contamination: sub-visible particles - Scientific guideline
- ICH Q4B Annex 4A Microbiological examination of non-sterile products: microbial enumeration tests - Scientific guideline
- ICH Q4B Annex 4B Test for microbiological examination of non-sterile products: tests for specified microorganisms - Scientific guideline
- ICH Q4B Annex 4C Test for microbiological examination of non-sterile products: acceptance criteria for pharmaceutical preparations and substances for pharmaceutical use - Scientific guideline
- ICH Q4B Annex 5 Disintegration test - Scientific guideline
- ICH Q4B Annex 6 Uniformity of dosage unites general chapter - Scientific guideline
- ICH Q4B Annex 7 Dissolution test - Scientific guideline
- ICH Q4B Annex 8 Sterility test - Scientific guideline
- ICH 4 QB Annex 9 Tablet friability - Scientific guideline
- ICH Q4B Annex 10 Polyacrylamide gel electrophoresis - Scientific guideline
- ICH Q4B Annex 11 Capillary electrophoresis - Scientific guideline
- ICH Q4B Annex 12 Analytical sieving - Scientific guideline
- ICH Q4B Annex 13 Bulk density and tapped density of powders - Scientific guideline
- ICH Q4B Annex 14 Bacterial end toxins tests - Scientific guideline

Quality of biotechnological products:
- ICH Guideline Q5A(R2) on viral safety evaluation of biotechnology products derived from cell lines of human or animal origin - Scientific guideline
- ICH Q5B Analysis of the expression construct in cell lines used for production of rDNA-derived protein products - Scientific guideline
- ICH Q5C Stability testing of biotechnological/ biological products - Scientific guideline
- ICH Q5D Derivation and characterization of cell substrates used for production of biotechnological/biological products - Scientific guideline
- ICH Q5E Biotechnological/biological products subject to changes in their manufacturing process: Comparability of biotechnological/ biological products
- Scientific guideline

Specifications:
- ICH Q6A specifications: test procedures and acceptance criteria for new drug substances and new drug products: chemical substances - Scientific guideline
- ICH Q6B Specifications: test procedures and acceptance criteria for biotechnological/ biological products - Scientific guideline

Good manufacturing practice
- ICH Q7 Good manufacturing practice for active pharmaceutical ingredients - Scientific guideline

Pharmaceutical development [10]:
- ICH Q8 (R2) Pharmaceutical development - Scientific guideline
- ICH Q9 Quality risk management - Scientific guideline
- ICH Q10 Pharmaceutical quality system - Scientific guideline
- ICH Q8, Q9 and Q10 - questions and answers - Scientific guideline
- ICH Q11 Development and manufacture of drug substances (chemical entities and biotechnological/biological entities) - Scientific guideline
- ICH guideline Q13 on continuous manufacturing of drug substances and drug products - Scientific guideline

Lifecycle management:
- ICH Q12 Technical and regulatory considerations for pharmaceutical product lifecycle management - Scientific guideline

ICH: safety: For a complete list of scientific guidelines [11-12] currently open for consultation, see Public consultations.
- Nonclinical safety in pediatric medicines
- Carcinogenicity studies
- Genotoxicity studies
- Toxic kinetics and pharmacokinetics
- Repeat-dose toxicity
- Reproductive toxicology

- Biotechnological products
- Safety pharmacology studies
- Immunotoxicology studies
- Therapeutic area-specific
- Photo safety evaluation

Nonclinical safety in pediatric medicines
- ICH guideline S11 on nonclinical safety testing in support of development of pediatric pharmaceuticals - Step 5 - Scientific guideline

Carcinogenicity studies:
- ICH S1 Regulatory notice on changes to core guideline on rodent carcinogenicity testing of pharmaceuticals - Scientific guideline
- ICH S1A Need for carcinogenicity studies of pharmaceuticals - Scientific guideline
- ICH guideline S1B(R1) on testing for carcinogenicity of pharmaceuticals - Scientific guideline
- ICH S1C (R2) Dose selection for carcinogenicity studies of pharmaceuticals

- Scientific guideline

Genotoxicity studies:
- ICH S2 (R1) Genotoxicity testing and data interpretation for pharmaceuticals intended for human use - Scientific guideline

Toxic kinetics and pharmacokinetics:
- ICH S3A Toxic kinetics: the assessment of systemic exposure in toxicity studies - Scientific guideline
- ICH S3A Toxic kinetics: the assessment of systemic exposure in toxicity studies - questions and answers - Scientific guideline
- ICH S3B Pharmacokinetics: repeated dose tissue distribution studies - Scientific guideline

Repeat-dose toxicity:
- ICH S4 Duration of chronic toxicity testing in animals (rodent and non-rodent toxicity testing) - Scientific guideline

Reproductive toxicology:
- ICH S5 (R3) Guideline on detection of reproductive and developmental toxicity for human pharmaceuticals - Scientific guideline

Biotechnological products:
- ICH S6 (R1) Preclinical safety evaluation of biotechnology-derived pharmaceuticals - Scientific guideline

Safety pharmacology studies:
- ICH S7A Safety pharmacology studies for human pharmaceuticals - Scientific guideline
- ICH S7B Non-clinical evaluation of the potential for delayed ventricular depolarization (QT interval prolongation) by human pharmaceuticals - Scientific guideline

Immunotoxicology studies:
- ICH S8 Immunotoxicity studies for human pharmaceuticals - Scientific guideline

Therapeutic area-specific:
- ICH S9 Non-clinical evaluation for anticancer pharmaceuticals - Scientific guideline

Photo safety evaluation:
- ICH S10 Photo safety evaluation of pharmaceuticals - Scientific guideline

ICH: efficacy [13,14-15]:
- Clinical safety
- Clinical study reports
- Dose-response studies
- Ethnic factors
- Good clinical practice
- Clinical trials
- Clinical evaluation by therapeutic category
- Clinical evaluation

Clinical safety:
- ICH E1 Population exposure: the extent of population exposure to assess clinical safety - Scientific guideline
- ICH E2A Clinical safety data management: definitions and standards for expedited reporting - Scientific guideline
- ICH E2B (R3) Electronic transmission of individual case safety reports (ICSRs) - data elements and message specification - implementation guide - Scientific guideline
- ICH E2C (R2) Periodic benefit-risk evaluation report - Scientific guideline
- ICH E2D Post-approval safety data management - Scientific guideline
- ICH E2E Pharmacovigilance planning (Pvp) - Scientific guideline
- ICH E2F Development safety update report - Scientific guideline
- ICH guideline E19 on a selective approach to safety data collection in specific late-stage pre-approval or post-approval clinical trials - Scientific guideline

Clinical study report:
- ICH E3 Structure and content of clinical study reports - Scientific guideline

Dose response studies:
- ICH E4 Dose response information to support

drug registration - Scientific guideline

Ethnic factors:

- ICH E5 (R1) Ethnic factors in the acceptability of foreign clinical data - Scientific guideline
- ICH E5(R1) Ethnic factors in the acceptability of foreign clinical data - questions and answers - Scientific guideline

Good clinical practice:

- ICH E6 (R2) Good clinical practice - Scientific guideline

Clinical trials:

- ICH E7 Studies in support of special populations: geriatrics - Scientific guideline
- ICH E7 Studies in support of special populations: geriatrics - questions and answers - Scientific guideline
- ICH E8 General considerations for clinical studies - Scientific guideline
- ICH E9 statistical principles for clinical trials - Scientific guideline
- ICH E10 Choice of control group in clinical trials - Scientific guideline
- ICH E11(R1) step 5 guideline on clinical investigation of medicinal products in the pediatric population - Scientific guideline
- ICH guideline E11A on pediatric extrapolation - Scientific guideline
- ICH guideline E17 on general principles for planning and design of multi- regional clinical trials - Scientific guideline
- ICH E18 Guideline on genomic sampling and management of genomic data

\- Scientific guideline

Clinical evaluation by therapeutic category:

- ICH E12 Principles for clinical evaluation of new antihypertensive drugs - Scientific guideline

Clinical evaluation:

- ICH E14 Clinical evaluation of QT/QTc interval prolongation and proarrhythmic potential for non-ant arrhythmic drugs - Scientific guideline
- ICH E14 (R3) Clinical evaluation of QT/QTc interval prolongation and proarrhythmic potential for non-ant arrhythmic drugs - questions and answers - Scientific guideline
- ICH E15 Definitions for genomic biomarkers, pharmacogenomics, pharmacokinetics, genomic data and sample coding categories - Scientific guideline
- ICH E16 Genomic biomarkers related to drug response: context, structure and format of qualification submissions - Scientific guideline

ICH: multidisciplinary:

- ICH M2 Electronic common technical document (eCTD) - file format criteria - Scientific guideline
- ICH M2 Electronic common technical document (eCTD) - Scientific guideline
- ICH M2 Business requirements - Scientific guideline
- ICH M3 (R2) Non-clinical safety studies for the conduct of human clinical trials for pharmaceuticals - Scientific guideline
- ICH M4 Common technical document (CTD) for the registration of pharmaceuticals for human use - organization of CTD - Scientific guideline
- ICH M4 Common technical document for the registration of pharmaceuticals for human use: questions and answers - Scientific guideline
- ICH M4Q Common technical document for the registration of pharmaceuticals for human use - quality - Scientific guideline
- ICH M4Q Location issues for common technical document for the registration of pharmaceuticals for human use - quality: questions and answers - Scientific guideline
- ICH M4E Common technical document for the registration of pharmaceuticals for human use - efficacy - Scientific guideline
- ICH M4E Common technical document for the registration of pharmaceuticals for human use - efficacy: questions and answers - Scientific guideline
- ICH M4S Common technical document for the registration of pharmaceuticals for human use - safety - Scientific guideline
- ICH M4S Common technical document for the registration of pharmaceuticals for human use - safety: questions and answers - Scientific guideline
- ICH M5 Data elements and standards for drug dictionaries - Scientific guideline
- ICH M5 EWG Routes of administration controlled vocabulary - Scientific guideline
- ICH M5 EWG Units and measurements controlled vocabulary - Scientific guideline
- ICH M7 Assessment and control of DNA reactive (mutagenic) impurities in pharmaceuticals to limit potential carcinogenic risk - Scientific guideline
- ICH M8 Electronic common technical document (eCTD) v4.0 draft ICH implementation guide v2.0 - Scientific guideline
- ICH M9 on biopharmaceutics classification system based biowaivers - Scientific guideline
- ICH M10 on bioanalytical method validation - Scientific guideline
- ICH M11 guideline, clinical study protocol

template and technical specifications - Scientific guideline

- ICH M12 on drug interaction studies - Scientific guideline
- ICH Guideline M13A on bioequivalence for immediate-release solid oral dosage forms - Scientific guideline

2. CONCLUSION

Scientifically grounded ICH guidelines that eliminate superfluous research will lower development costs, enhance safety, and enable the release of drugs worldwide based on a single compliance. These guidelines are especially important for developing nations that lack the knowledge and resources to assess biosimilar submissions.

REFERENCES

1. Bhavya K, Manisha Vishnumurthy K, Rambabu D and Sumakanth M. ICH guidelines – "Q" series (quality guidelines) - A review. GSC Biological and Pharmaceutical Sciences, 2019;6(3): 89- 10.
2. Strohl WR In: Zhiqiang A (ed) Therapeutic monoclonal antibodies: from bench to clinic. Wiley, Hoboken; 2009.
3. Crommelin DJA, Storm G, Verrijk R, de Leede I, Jiskot W, Hennik WE Shifting paradigms; Biopharmaceuticals versus low molecular weight drugs. Int J Pharm. 2003;266:3–16.
4. ICH Secretariat International Conference on Harmonization (ICH) guideline ICH Q6B; 1999.
5. Specifications: Test procedures and acceptance criteria for biotechnological/biological products. ICH Secretariat, Geneva.
6. ICH Secretariat International Conference on Harmonization (ICH) guideline ICH Q2(R1); 2005.
7. Validation of analytical procedures: text and methodology. ICH Secretariat, Geneva Quinine Actinometry as a method for calibrating ultraviolet radiation intensity in lightstability testing of pharmaceuticals.
8. Yoshioka S. et al. Drug Development and Industrial Pharmacy. 1994;20(13):2049- 2062.
9. Pharmaceutical Stability Testing to Support Global Market: Pharm asp, Edited by: Huynh Ba K, Published by: Springer Science+ Business Media, LLC, 2333 Spring Street, NY 10013, USA; 2010.
10. Anand Raj, Dr. Gaurav Kumar Sharma and Dr. Kaushal Kishore Chandrul, A review on ich guidelines – "Q" series (quality guidelines). World Journal of Pharmacy and Pharmaceutical Sciences.2021;10(9).
11. Somvanshi Y and Satbhai P. ICH Guidelines and Main Focus on Stability Guidelines for New Formulation and Dosage Forms. World Journal of Pharmaceutical Research. 2015;4 (10):561-578. 5.
12. Sarfaraz K Niazi , Waleed Mohammed Al-Shaqha , Zafar Mirza, Proposal of International Council for Harmonization (ICH) Guideline for the Approval of Biosimilars, J Mark Access Health Policy, 2022 Nov 17;11(1):2147286.
13. Glossary of ICH terms and definitions. 2023;4.
14. Mark E. Arnold, Stephanie Cape, Fan Jin and Robert Nelson, ICH M10: History, Publication and Initial Perspectives on Global Implementation; 2022.
15. Andrew Fisher, ICH E6 (R3) Good Clinical Practice, Medicines and Healthcare products Regulatory Agency; 2023

Green Synthesis of Ag-Ni Hybrid Nanomaterials from *Andrographis Paniculata* leaf extract and Study of their Photocatalytic Activity

Dr. Ch. S. Anuradha

Assistant Professor, Department of Chemistry, Dr. V. S. Krishna Government Degree College (A), VISAKHAPATNAM -530013, INDIA.

ABSTRACT

An environmentally benign cost effective method is reported for green synthesis of Ag-Ni hybrid nanomaterials by using *Andrographis Paniculata* leaf extract. The phytomolecules present in the extract are acting as reducing agents, stabilizing and capping agents for the biosynthesized nanomaterials. The characterization studies are done by UV-Visible, FTIR, SEM, XRD, EDX and HRTEM analyses. These nanoparticles are further applied as photocatalysts for degradation of Malachite Green dye by irradiation under sunlight. The optimum conditions found in the degradation of malachite green dye are pH **8**, weight of catalyst **30 mg**, dye concentration of **10 ppm** and contact time of **120 minutes**. A maximum photodegradation of **82%** is obtained under these optimum conditions.

KEY WORDS

Hybrid nanomaterials (HNMs), *Andrographis Paniculata*, Malachite Green (MG), photodegradation.

INTRODUCTION

Nanotechnology involves the synthesis and application of materials having one of the dimensions in the range of 1 nm to 100 nm and acts as a channel between bulk materials and atomic or molecular structures. In recent times hybrid nanomaterials have gained considerable attention because of their importance for magnetic, optical and catalytic applications in multiple fields [1]. Various physical, chemical and biological methods have been employed for the synthesis of hybrid nanomaterials [2]. Several advantages of biological methods over physical and chemical methods are due to the fact that they are environmentally benign, less time consuming, cost effective with almost negligible industrial waste without use of toxic chemicals [3]. Biosynthesized hybrid nanomaterials are used in several contemporary fields viz. imaging, labeling, luminescence tagging, drug delivery and biomedical field because of their superior properties. Hybrid nanomaterials synthesized from plant extracts have been found to possess extraordinary catalytic activities [4].

Dyes are used widely in various fields such as cosmetics, leather, food and textile industries. The release of these industrial dye effluents into water shows adverse effect on quality of water [5]. One of such dye is malachite green (MG).

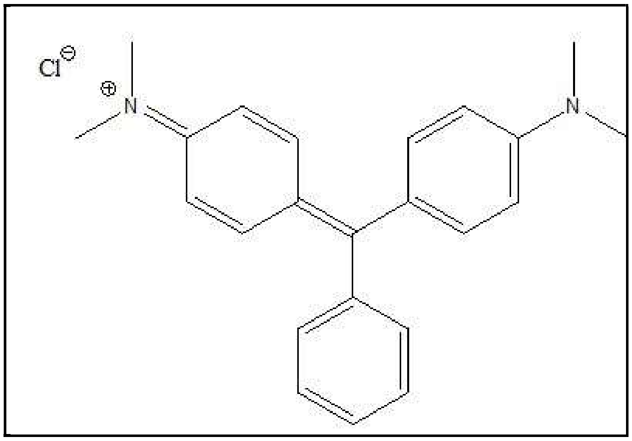

Figure 1 (a): Structure of Malachite Green dye

Malachite green dye is a cationic green crystalline water soluble dye and belongs to triphenyl methane category. (Figure1.a). MG dye is a potential environmental contaminant and a peril to public health as it is a multi-organ toxin proved as by both experimental clinical observations [6]. So it is necessary to exterminate the MG dye effluents from water. Many chemical, physical and biological treatment methods including adsorption, precipitation filtration, electrodialysis, coagulation, oxidation and membrane separation are used in the treatment of dye effluents [7]. Dye removal via degradation using photocatalysts is the most scathe less and desirable among all methods because of its sustainable and ecofriendly technology [8]. Recent times nanotechnology has been extended in the waste water treatment and nanoparticles are used as photocatalysts for degradation of dyes due to their extensive surface area [9].

Herein, an effortless and robust green method for synthesis of Ag-Ni hybrid nanomaterials (HNMs) is reported by using leaf extract of *Andrographis Paniculata* as a stabilizing, reducing and capping agent. These HNMs are employed as catalysts for photodegradation of MG dye under solar light irradiation. Various reaction conditions are observed and the optimum conditions are noted for the maximum photodegradation.

2. EXPERIMENTAL

2.1. Materials: Chemical reagents (silver nitrate and nickel nitrate) used in this study are of analytical grade. Deionised water is used to clean glassware, to prepare chemical solutions and for experimental procedure. Fresh leaves of *Andrographis Paniculata* are collected from botanical garden of Dr. V.S. Krishna Government Degree College (A), Visakhapatnam of Andhra Pradesh state in India.

2.2. Preparation of *Andrographis Paniculata* leaf extract: 100 g of fresh leaves are weighed and thoroughly washed with running tap water to remove detritus on surface of leaves followed by deionised water to get rid of other contaminants from leaves and dried up under shade for 10 days. These leaves are cut into tiny pieces and made homogenized powder by using home blender. The procured powder is placed in refrigerator at 4^o C which is kept in an air tight container. Now 200 mL deionized water is taken in 500 mL beaker to this 10 g stored powder is weighed and added. The contents in the beaker heated for 30 minutes at 50^o C with occasional stirring with glass rod and then cooled to acquire room temperature. The cooled concoction is filtered two times with Whatman No.1 filter paper and reserved in refrigerator at 4^o C. This is taken as leaf extract throughout the experiment (Figure: 1(b), 1(c)).

Figure 1(b): *Andrographis Paniculata* plant

Figure 1(c): *Andrographis Paniculata* leaf extract

2.3. Synthesis of Ag-Ni hybrid nanomaterials:

Equimolar (25 mM) concentrations of silver nitrate and nickel nitrate aqueous solutions are prepared separately in 100 mL volumetric flasks by dissolving 0.4246 g, 0.7267 g weight of $AgNO_3$ and $Ni(NO_3)_2$ in deionized water respectively. Synthesis of Ag-Ni HNM s is done by taking 100 mL of $AgNO_3$ solution in a 500 mL beaker, to this 90 mL of leaf extract, 100 mL of Ni $(NO_3)_2$ solutions are added by drop wise in simultaneous addition process. After this addition the beaker is placed on a magnetic stirrer for continuous agitation. This mixture is stirred at 70^{o}C for 50 minutes at pH 8 on magnetic stirrer. These synthesized HNMs are separated out by doing centrifugation at 4500 rpm for 45 minutes. The obtained HNM s are washed with deionised water two times to remove unwanted constituents and dried in oven at 80^{0} C for two hours. The resultant HNMs are collected (**Figure. 2**) and used for characterization.

Figure. 2: Ag-Ni HNMs

2.4. Characterization:

Formation of Ag-Ni HNM s is confirmed by UV-Visible absorption spectra using UV-2450 SHIMADZU double beam spectrophotometer, FTIR using Bruker, SEM, EDX studies are done by using Hitachi S-3700N machine and the morphology of HNM s is elucidated by HRTEM analysis with FEI Technai machine.

3. RESULTS AND DISCUSSION

3.1. UV-Visible spectral analysis:

UV-Visible absorption spectrum of Ag-Ni HNM s is presented in **Figure.3.** The characteristic surface plasmon resonance (SPR) band at around 437 nm is observed in Ag-Ni HNMs which confirms the nano size of the synthesized HNMs [10].

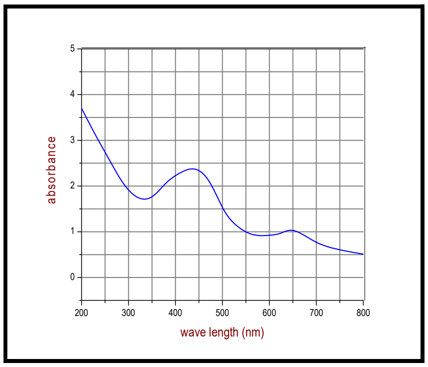

Figure. 3 : UV-Visible absorption spectrum of Ag-Ni HNM s

3.2. FTIR spectral analysis:

FTIR spectral data is used to identify different functional groups present in biomolecules of leaf extract and formed HNMs. These groups are responsible for the bioreduction of Ag^+, Ni^{+2} precursors and also for capping and stabilization of Ag-Ni HNMs. The FTIR spectrum of Ag-Ni HNM s exhibits major peak positions at 3210 cm^{-1}, 3414 cm^{-1} and 3384 cm^{-1} which indicate the N-H stretching vibrations of amines and O-H stretching of hydroxyl groups of alcohols and phenols. Intense peak at 1640 cm^{-1} is due to C=O stretching of amide group. Very small peak at 601 cm^{-1} indicates the presence of C-Cl group.

This spectral data clearly confirms that the surface of the nanoparticles is covered by plant secondary metabolites such as carbohydrates, glycosides, Saponin, phytosterols, phenolic compounds, tannins, flavonoids, proteins, aminoacids, diterpenes, carboxylic acids, amides, ketones and alkyl halides [11].

3.3. **SEM and EDX analysis:**

From energy dispersive X-ray analysis we can analyze all the elements present in the HNM s prepared by *Andrographis Paniculata* leaf extract. **Figure.4** shows EDX spectrum and elemental composition. This indicates the presences of Ag and Ni which confirms the formation of Ag-Ni hybrid nanomaterials. Scanning electron microscopic (SEM) images of Ag-Ni HNM s with various magnifications are given in **Figure 5**. From this it can be clearly noted that the prepared Ag-Ni HNMs are in the size range between 50 to 100 nm in diameter.

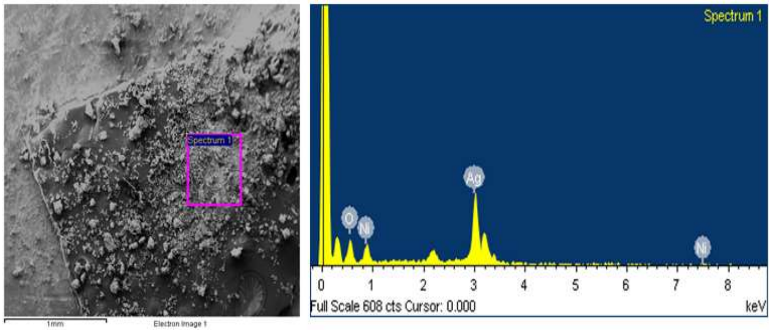

Figure. 4: EDX Analysis of Ag-Ni HNMs

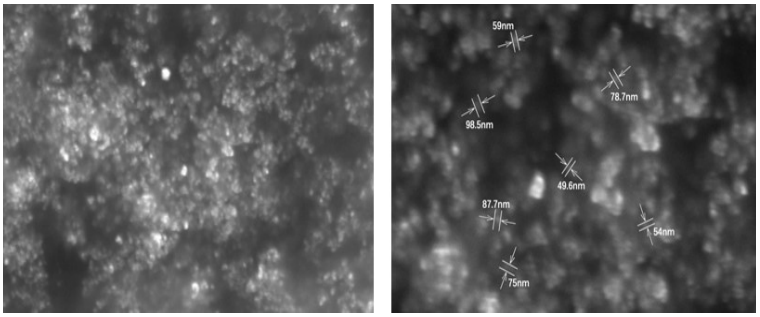

Figure. 5 : SEM images of Ag-Ni HNMs

3.4. HRTEM analysis: **Figure.6** shows the high resolution transmission electron microscopy (HRTEM) images for synthesized Ag-Ni HNMs. From these images, it is observed that Ag-Ni HNMs are formed with spherical morphology and crystalline structure below the size of 100 nm. It is also observed that, the two metal nanospheres emerge to be positioned adjacent to each other. It is also in strong accordance with the images from SEM analysis.

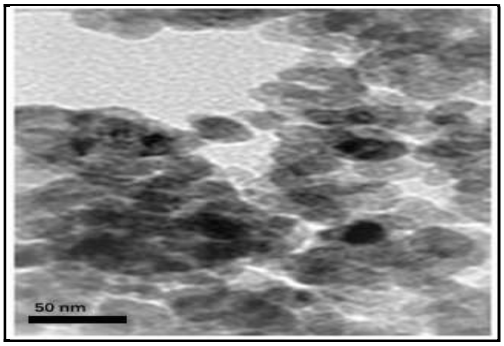

Figure .6: HRTEM image of Ag-Ni HNMs

3.5. Powder XRD analysis :

The XRD spectrum of green synthesized Ag-Ni HNM s from leaf extract is shown in **Figure: 7.** The peaks appeared at 2θ values of 38.30^0, 44.28^0, 64.38^0, $77.39\ ^0$ correspond to the Bragg's reflections of Ag(111), Ag(200), Ni(111), Ag(220), Ni(222) , Ag (311) planes respectively of face centered cubic crystal structure [12] as shown in the **Figure:7.** The numerically calculated value of the synthesized Ag-Ni HNMs materials corresponds to an average particle size of **23.35 nm**.

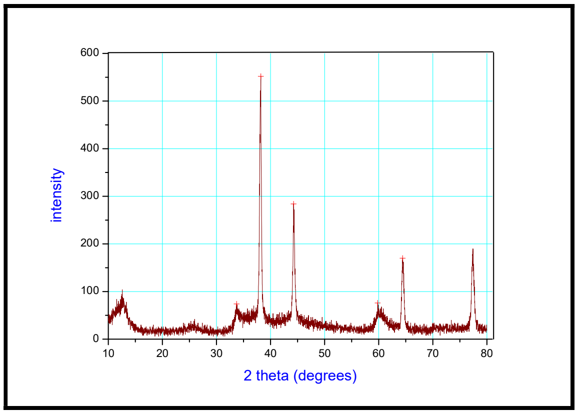

Figure:7 . XRD spectrum of Ag-Ni HNM s

4. Photodegradation studies on Malachite Green dye using Ag-Ni HNMs:

The photo degradation experiments are carried on Malachite Green dye using green synthesized Ag-Ni HNM s acting as a catalyst. Initially, 50 ppm of malachite green stock solution is prepared. Then reaction mixtures are prepared by adding certain amount of Ag-Ni HNM s (10 mg, 20 mg, 30 mg, 40 mg, 50 mg, 60 mg,70 mg, 80 mg) to 100 mL of malachite green for distinct concentrations(5 ppm, 10 ppm, 15 ppm, 20 ppm, 25 ppm, 30 ppm, 35 ppm). The pH of the reaction mixtures is maintained in the experiments at various values for both acidic and basic range

(i.e. pH 3,4,5,6,7,8,9,10,11) by adding 0.1 N H_2SO_4 or 0.1 N NaOH solutions when required. Now this mixture is agitated for 20 minutes in dark condition to attain adsorption-desorption equilibrium between malachite green and Ag-Ni HNM s. Sun light is used as irradiating source to reaction mixture for studying photodegradation during 11.00 am to 3.00 pm. At regular 30 minutes time intervals, aliquot part of the reaction mixture is taken, centrifuged to remove the photocatalyst particles and optical absorption properties are analyzed by using UV-Visible Spectrophotometer. The absorbance is observed by varying parameters like changing the time of contact between the catalyst and the dye, pH of the reaction mixture, concentration of the dye solution and dosage of the catalyst. Malachite green shows the highest absorption at 617 nm [13]. To determine the percentage degradation of MG dye solution following equation (2) is used.

$$\%\ \text{degradation} = \left(\frac{A_0 - A_t}{A_0}\right) \times 100 \quad \ldots \quad (2)$$

Where, A_0 is the initial absorbance of the MG solution at zero minutes and A_t is the absorbance of the degraded solution after time t minutes.

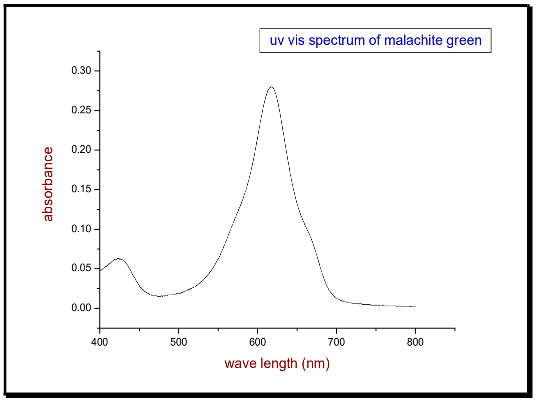

Figure 8(a): UV- Visible spectrum of Malachite Green

To study the photocatalytic activity of the Ag-Ni HNM s on malachite green visible region of the light source is selected on UV-visible spectrophotometer. Absorption spectrum of 10 ppm malachite green solution is shown in **Figure 8(a).** Highest absorption peak at 617 nm is observed and this maximum absorption peak is considered to monitor the photodegradation reaction of MG dye for all further studies in this paper.

4.1. Effect of time of contact:

Photodegradation capacity of the Ag-Ni HNMs on malachite green dye is studied in the presence of sunlight by batch mode experiments. The efficiency of HNMs photocatalyst on degradation of MG is expected to be increased by increasing contact time. The effect of contact time is carried out by taking 10 ppm of 100 mL MG dye solution and 10 mg of HNM s (pH at 7) as catalyst load which is shown in **Figure 8(b).** From the initial part of the graph i.e upto 120 min, % photodegradation is exhibiting rapid rise. However, above 120 minutes the slope is relatively less steeper although % photodegradation remains still considerably predominant thus shows higher values.

Thus, upto 120 min, the % photodegradation of the dye by using the HNMs photocatalyst is found to be rapid, and above 120 min it becomes relatively less rapid although active even upto 180 min. This is due to strong adsorption forces that predominate between the dye and the HNMs as the number of the reactive sites on the photocatalyst are largely vacant during initial periods of contact time. But after 120 minutes of contact period, equilibrium between the number of vacant sites of adsorption and the dye molecules appears to be established although at slower rate, hence exhibit slightly slower rise of % photodegradation [14].

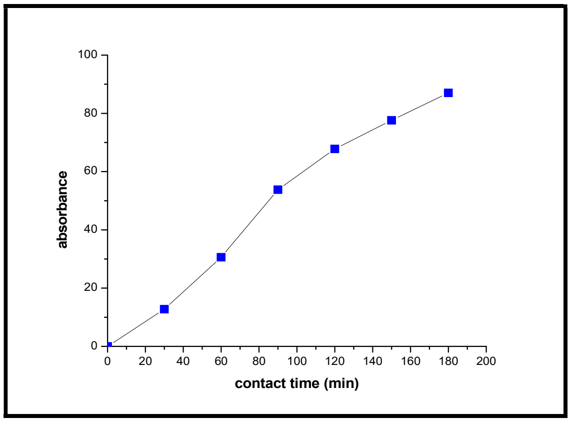

Figure 8(b): Effect of contact time on photo degradation

4.2. Effect of initial concentration of MG dye solution:

Initial concentration of MG dye solution is also expected to affect the rate of photo degradation. To investigate this fact, dosage of HNM s nanocatalyst is kept constant at 10 mg, maintaining the dye solution pH at 7 and the time of irradiation as 180 minutes. However one parameter (the initial concentration of the MG dye solutions) is varied at 5 ppm, 10 ppm, 15 ppm, 20 ppm, 25 ppm , 30 ppm and 35 ppm. The rate of photodegradation can be represented graphically in **Figure 8(c).**

It can be observed from the figure that, the maximum photodegradation is found at 5 ppm, and then it decreases with further rise in the concentration of MG dye solution. Thus as the initial concentration of the dye increases beyond 5 ppm, % photodegradation decreases [15]. This observation can be explained by the fact that at the low initial concentration of the dye solution, large number of dye molecules could be adsorbed on the surface of HNMs. Increasing the initial concentration of the dye can result competitive adsorption among the dye molecules while the area of active reaction sites on the catalyst is fixed. Consequently the % photodegradation of MG dye decreases.

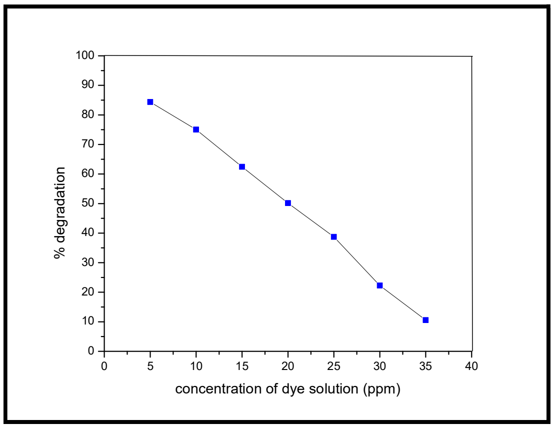

Figure.8(c): Effect of concentration of MG dye solution on photodegradation

4.3. Effect of pH:

pH of dye solution can influence the adsorption of dye on the photocatalyst. Keeping pH as variable, all other parameters are kept constant viz. the initial concentration of the malachite green solution is taken as 10 ppm, the concentrations of the photocatalyst as 10 mg and with time of irradiation 120 minutes. Different solutions of various pH values from 3 to 11 are prepared. Photodegradation efficiencies are compared which is shown in **Figure: 8(d).**

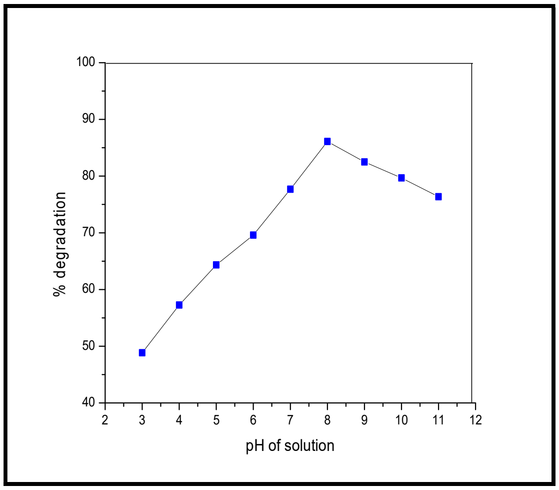

Figure:8(d): Effect of pH on photodegradation

It is observed that by increasing pH of the MG dye solution, the % photodegradation of MG dye on the photocatalyst enhances up to pH 8 and on further increase of pH, the rate of photodegradation is diminished. At pH less than four, lower values of % photodegradation are observed. Solution pH may influence both solution chemistry and surface active sites of the adsorbent. At acidic pH, H^+ ions of the water molecules, may race with dye ions for the adsorption sites of the catalyst surface, there by hindering the adsorption of the dye. As the pH value increases, the number of H^+ ions of the aqueous solution reduces, hence the cationic dye molecules could approach the catalyst surface at a faster rate, thus exhibit an fast increase in the rate of % photodegradation. At pH 8 the adsorption is maximum, hence the photo degradation is found to be maximum. At pH >8, the malachite green dye may not be maintained

in its cationic form due to high concentration of OH^- ions in the aqueous dye solution. Consequently, the electrostatic repulsion increases between the MG dye and negatively charged catalyst surface. As a result the photodegradation slowly decreases from pH 8 to 11.

4.4. Effect of dosage of photo catalyst:

In photodegradation process, one of the important parameters of decolourizing of dye solution is dosage of the photocatalyst. To avoid splurge of costly catalyst and attain the maximum absorption of photons optimization of the catalyst dosage is important. For this, dosage amount is varied from 10 mg to 80 mg taken in 100 ml of 10 ppm MG dye at pH 8 with contact time 120 minutes. The degradation of MG is shown in **figure 8(e).**

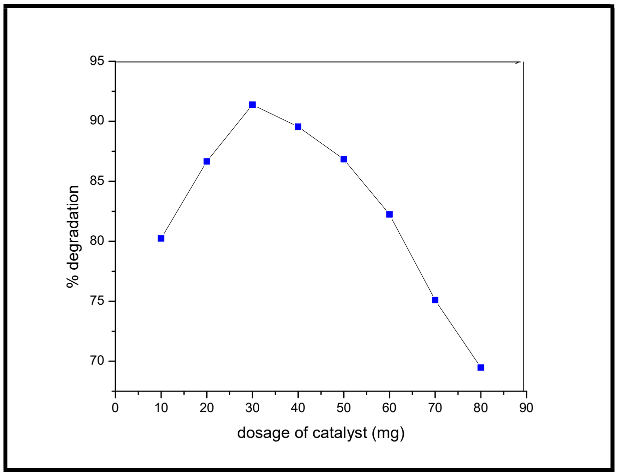

Figure 8(e): Effect of dosage of catalyst on photo degradation

From the graph it can be concluded that, by increasing dosage of catalyst from 10 mg to 80 mg in 100 ml dye solution, the % photodegradation of the MG dye shows an increasing trend up to 30 mg. This is because the increase in amount of catalyst up to 30 mg would increase the number of reactive sites that produce more reactive species [16]. On further increase of catalyst dosage, % photodegradation of MG dye decreases because the catalyst particles form more turbid suspensions at higher loadings, which increase the scattering of the solar light and reduce the penetration of light into the reaction mixture.

CONCLUSION

An ecologically safe method is projected in this report to synthesize Ag-Ni hybrid nanomaterials from *Andrographis Paniculata* leaf extract. From UV-VIS spectral analysis it is confirmed that the particles are in nanoscale as per the positions of the Surface Plasmon Resonance (SPR) bands. FTIR data confirms the presence of secondary metabolites of phyto molecules that act as the bio reducing and capping agents of the formed nanoparticles. Results of XRD, SEM and TEM analyses proved that Ag-Ni HNM s are in spherical morphology and cubic crystalline structure with size between 20-100 nm. The photocatalytic activity of these nanomaterials is examined under sunlight for degradation of MG dye which is an environmental pollutant. The % photodegradation of MG dye changes with parameters such as contact time, concentration of MG dye, pH and photocatalyst dosage. From this research study on bimetallic Ag-Ni HNM s synthesized from *Andrographis Paniculata* leaf extract, the optimum conditions found in the degradation of MG dye is pH **8**, weight of catalyst **30 mg**, dye concentration of **10 ppm** and contact time of **120 minutes**. A maximum photodegradation of **82%** is obtained under these optimum conditions.

REFERENCES

[1] Ijaz, I., Gilani, E., Nazir, A., & Bukhari, A. (2020). Detail review on chemical, physical and green synthesis, classification, characterizations and applications of nanoparticles. *Green Chemistry Letters and Reviews*, *13*(3), 223-245.

[2] Loza, K., Heggen, M., & Epple, M. (2020). Synthesis, structure, properties, and applications of bimetallic nanoparticles of noble metals. *Advanced functional materials*, *30*(21), 1909260.

[3] Scala, A., Neri, G., Micale, N., Cordaro, M., & Piperno, A. (2022). State of the art on green route synthesis of gold/silver bimetallic nanoparticles. *Molecules*, *27*(3), 1134.

[4] Tiri, R. N. E., Gulbagca, F., Aygun, A., Cherif, A., & Sen, F. (2022). Biosynthesis of Ag–Pt bimetallic nanoparticles using propolis extract: Antibacterial effects and catalytic activity on NaBH4 hydrolysis. *Environmental Research*, *206*, 112622.

[5] Al-Tohamy, R., Ali, S. S., Li, F., Okasha, K. M., Mahmoud, Y. A. G., Elsamahy, T., ... & Sun, J. (2022). A critical review on the treatment of dye-containing wastewater: Ecotoxicological and health concerns of textile dyes and possible remediation approaches for environmental safety. *Ecotoxicology and Environmental Safety*, *231*, 113160.

[6] Hussain Hakami, A. A., Ahmed, M. A., Khan, M. A., AlOthman, Z. A., Rafatullah, M., Islam, M. A., & Siddiqui, M. R. (2021). Quantitative analysis of malachite green in environmental samples using liquid chromatography-mass spectrometry. *Water*, *13*(20), 2864.

[7] Gadekar, M. R., & Ahammed, M. M. (2016). Coagulation/flocculation process for dye removal using water treatment residuals: modelling through artificial neural networks. *Desalination and Water Treatment*, *57*(55), 26392-26400.

[8] Ansari, A. A., Shamim, M. A., Khan, A. M., & Anwar, K. (2022). Nanomaterials as a cutting edge in the removal of toxic contaminants from water. *Materials Chemistry and Physics*, 127092.

[9] Joseph, A., & Vijayanandan, A. (2022). Review on Support Materials Used for Immobilization of Nano-Photocatalysts for Water Treatment Applications. *Inorganica Chimica Acta*, 121284.

[10] Kumar, A. G., Sankarganesh, P., Parthasarathy, V., Bhuvaneshwari, J., & Anbarasan, R. (2022). In-vitro and in-vivo biological potential of the prepared Feroniella lucida mediated silver nanoparticles. *Journal of Sol-Gel Science and Technology*, *101*(2), 411-419.

[11] Gebre, S. H. (2023). Bio-inspired synthesis of metal and metal oxide nanoparticles: the key role of phytochemicals. *Journal of Cluster Science*, *34*(2), 665-704.

[12] Renuka, R., Devi, K. R., Sivakami, M., Thilagavathi, T., Uthrakumar, R., & Kaviyarasu, K. (2020). Biosynthesis of silver nanoparticles using Phyllanthus emblica fruit extract for antimicrobial application. *Biocatalysis and Agricultural Biotechnology*, *24*, 101567.

[13] Meena, P. L., Poswal, K., & Surela, A. K. (2022). Facile synthesis of ZnO nanoparticles for the effective photodegradation of malachite green dye in aqueous solution. *Water and Environment Journal*, *36*(3), 513-524.

[14] Elkady, M. F., & Hassan, H. S. (2021). Photocatalytic degradation of malachite green dye from aqueous solution using environmentally compatible Ag/ZnO polymeric nanofibers. *Polymers*, *13*(13), 2033.

[15] El-Hout, S. I., El-Sheikh, S. M., Gaber, A., Shawky, A., & Ahmed, A. I. (2020). Highly efficient sunlight-driven photocatalytic degradation of malachite green dye over reduced graphene oxide-supported CuS nanoparticles. *Journal of Alloys and Compounds*, *849*, 156573.

[16] Bibi, S., Ahmad, A., Anjum, M. A. R., Haleem, A., Siddiq, M., Shah, S. S., & Al Kahtani, A. (2021). Photocatalytic degradation of malachite green and methylene blue over reduced graphene oxide (rGO) based metal oxides (rGO-Fe3O4/TiO2) nanocomposite under UV-visible light irradiation. *Journal of Environmental Chemical Engineering*, *9*(4), 105580.

International Journal of Applied Pharmaceutics

ISSN- 0975-7058 Vol 15, Issue 6, 2023

Original Article

AN ELECTROMETRIC METHOD FOR THE DETERMINATION OF IMPACT OF DMSO-WATER MIXTURES ON pKa VALUES OF SALICYLIC ACID DERIVATIVES

M. BALAKRISHNA[1], R. NEERAJA[2], J. SURESH KUMAR[3], M. RAMANAIAH[4]*

[1]Department of Chemistry, Lendi Institute of Engineering and Technology, Vizianagaram-535005, India. [2]Department of Chemistry, Dr. V. S. Krishna Govt. Degree and P. G. College, Visakhapatnam, A. P, India. [3,4]Department of Chemistry, Aditya Institute of Technology and Management, Tekkali-532201, India

***Corresponding author: M. Ramanaiah; *Email: ramanaiahmalla4@gmail.com**

Received: 28 Aug 2023, Revised and Accepted: 28 Sep 2023

ABSTRACT

Objective: The main objective of this present study is to conduct an experiment to analyze the variation of protonation-deprotonation equilibria with regards to the dielectric constants of an organic medium, influence of errors on protonation constants and effect of pH on the percentage of species.

Methods: The present investigation was carried out by using pH meter at a temperature of 303 K and ionic strength of 0.16 mol dm^{-3} in Dimethyl sulfoxide (DMSO)-water mixtures. The processing of data was done by using Gran plot titration. The advanced principles of mathematics and fuzzy logic have been employed to correlate chemical problems, known as chemometrics. To obtain best-fit chemical models, a modelling strategy such as SCPHD is used and a computer program MINIQUAD 75 is also employed for the refinement of results.

Results: In the present study, we found the influence of dielectric constants of a medium Dimethyl sulfoxide (DMSO)-water on protonation constants of 5-Sulfosalicylic acid and 5-Hydroxysalicylic acid has been studied. The species distribution diagrams were presented and understood the effect of pH on the percentage of species. The obtained skewness values are ranging from 0.11-0.36 and–0.56-0.38, for 5-Sulfosalicylic acid (5-SSA) and 5-Hydroxysalicylic acid (5-HSA), respectively, which describes the distribution curves are right skewed and left skewed. The kurtosis values are ranging from 2.12-3.56, which indicates the peak of the distribution curve exhibits both platykurtic and leptokurtic pattern. The changes in the concentrations of some influential parameters such as log F, acid, alkali, volume of titrands, ligand causes variation of stability constants and the order of the effect of influential parameters on stability constants are as alkali>acid>ligand>volume of titrand>log F.

Conclusion: It is observed that the significant influence of co-solvent Dimethyl sulfoxide (DMSO)-Water mixtures on the protonation constants of ligands also studied how some factors such as changes in concentrations of ligand, acid, base log F and volume of the solution have influence on the protonation constants.

Keywords: Acid-base equilibria, 5-Sulfosalicylic acid, 5-Hydroxysalicylic acid, Dimethyl sulfoxide, Protonation constant and dielectric constant

DOI: https://dx.doi.org/10.22159/ijap.2023v15i6.49253. Journal homepage: https://innovareacademics.in/journals/index.php/ijap

INTRODUCTION

The solubility and the bioavailability of a drug affect the therapeutic efficacy of the drug when released from its dosage form. Solubility is one of the major parameters to attain the desired plasma drug concentration. The poor solubility of the drug may result in limited absorption, further leading to the decrease in bioavailability [1]. Measurement of drug concentration in biological fluids, such as blood or urine, following drug administration, is considered a direct and efficient method for the determination of systemic drug bioavailability [2]. Drug disposition means the change in the position of drug molecules after administration into the system. As per the pharmacological view: Drug is a substance which can cause positive or negative effect to the system. But in actual, a drug is a chemical substance comprised with a definite chemical structure when a chemical substance goes into a system which itself is governed by the pH-partition hypothesis. The disposition of drug molecules involves administration, distribution, metabolism, excretion and toxicity (ADMET) [3]; every drug has its beneficial pharmacological activity as well as unavoidable side effects [4]. Drug discovery is a method and time-thorough process which is aimed at developing new drug candidates [5].

Salicylic acid derivatives like 5-SSA and 5-HSA have numerous applications in drug designing [6-9]. The dielectric constant is a macroscopic property which plays a significant role in the solution properties of the reaction medium. It is a useful technique in characterizing molecular ordering in solutions and the value of the dielectric constant is strongly related to the chemical structure of a molecule and to its intermolecular interactions. The dielectric constant is one of the characteristics of liquid. The proton-ligand and metal-ligand stability constants are strongly affected by the dielectric constant of the medium because of the fact that at least one of the constituents is charged and the other is either changed or has a dipole. Variations in the relative strengths of acids and bases with changing solvents should be a function of the charge, the radius of the ion and the dielectric constants of the medium. DMSO is most commonly used in biochemistry. It is a polar solvent can dissolve many compounds in it, which property makes DMSO to have a number of applications in drug designing and synthesis [10].

The speciation analysis of harmful and necessary metal ion complexes helps clarify the role of biologically active site cavities and drug residue interacting with the metal ion. Number of studies has been performed on chemical speciation in aqueous media under the same conditions as in natural systems. These are used as models for the systems that exist in natural water and biofluids. Nevertheless, Biosystems are linked to low dielectric mediums of varying magnitudes, and metabolic reactions are carried out in rigid compartments. The binary mixtures of dipolar aprotic and protic solvents have current interest in biological, chemical, pharmaceutical, technological and laboratory applications because mixed solvents manifest physicochemical properties as compared to those of pure constituents of the mixture amongst the physicochemical properties, dielectric constant of the mixed solvents, which is sensitive to molecular interactions specially H-bond formation, enhances or controls most of the applications, and hence precise the dielectric characterization is important. The study of chemical speciation plays a very important role to understand nutrition, human biology and toxicology, which will also helpful to understand the nature of an element in the sample [11]. One of the most important parameter in pharmaceutical is acid dissociation constants, ionization of functional groups with respective to pH; they are very useful in understanding the properties of new drug substances.

The present study deals with the dissociation and salvation processes in solutions of drugs and is important to elucidate the connection between chemical ability and biological activity; salicylates are used as food preservatives. In addition, salicylic acid and its derivatives have been widely used in medicine and analytical chemistry. This medium has been chosen to study the acid-base equilibria to mimic the physiological conditions where the concept of equivalent solution dielectric constant for active site cavities of protein or drug is applicable. In the present investigation, we have studied the protonation constants of both the ligands 5-SSA and 5-HSA in various mixtures of DMSO-water and to study the effect of dielectric constants on protonation constants through acid-base titrations. Speciation profoundly influences both the toxicity and bioavailability of an element. The data obtained would be useful to those who are working in biomedicine.

MATERIALS AND METHODS

The chemicals required to carry out this present investigation is 5-SSA (TCI, India) and 5-HSA (TCI, India). Both the ligand solutions were prepared for 0.05M; this is done by dissolving the substance in distilled water. The dissolution of the ligand substances can be increased by adding little amount of hydrochloric acid (Qualigens, India); here, the acid concentration maintains the ligand solution at 0.05M. The ionic strength of the system was maintained at 0.16 mol L^{-1} using pure sodium chloride (Qualigens, India). Carbonate-free sodium hydroxide (Qualigens, India) solution and hydrochloric acid solutions are prepared for acid-base titrations by maintaining their concentrations at 0.4 mol L^{-1} and 0.2 mol $L^{-1,}$ respectively.

Alkalimetric titrations

An Equiptronics-made EQ614 A model pH meter was used to carry out the titrations in the present study. Before using the instrument, it was calibrated by using two standard solutions i.e. Borax and Potassium hydrogen phthalate, all the titrations are carried out at 303.0 K. The electrode was calibrated by keeping it the percentage of DMSO-water mixtures in which the study has to be carried out, the process is call the equilibrium process of the electrode. The process of keeping electrode in the DMSO-water mixtures has to be continued to all the mixtures under which the study was done. For better results from the electrode, the equilibrium process has to be done by allowing the electrode at least a week days before the titration. The data were analyzed using a one-way classification in order to determine the errors [12, 13]. The method Gran plot is used to calculate the concentrations of base and acid [14, 15]. The acid-base titrations are carried out at various compositions of DMSO-water mixtures; in the present investigation, the DSMO-Water mixtures are having the composition of 0.0-60.0% v/v, The amounts of 5-SSA and 5-HSA in the titrands ranging from 0.25-0, 50 mmol. The total initial concentrations of ingredients are given in table 1.

Table 1: Total initial concentrations of ingredients (in mmol) in proton-ligand titrations

DMSO% (v/v)	TL0	
	5-SSA	5-HSA
0.0	0.2499	0.2449
	0.3748	0.3673
	0.4998	0.4898
10	0.2493	0.2493
	0.3740	0.3740
	0.4987	0.4987
20	0.2445	0.2488
	0.3667	0.3732
	0.4890	0.4977
30	0.2442	0.2510
	0.3663	0.3765
	0.4885	0.5021
40	0.2505	0.2483
	0.3757	0.3724
	0.5010	0.4966
50	0.2494	0.2437
	0.3667	0.3656
	0.4989	0.4875
60	0.2439	0.2499
	0.3659	0.3748
	0.4879	0.4998

Modeling strategy

One of the best computer programs like SCPHD is used in the present study to determine the stability constant values [16] and correction factor, and also another computer program MINIQUAD75 has been employed to refine the obtained data [17, 18]. In the present study, we studied the influence of various compositions of DMSO-water mixtures on the protonation constant values.

RESULTS AND DISCUSSION

In generally the biochemical processes will occurs at a pH 7.0, i.e. neutral medium. The physiological pH is 7.2 to 7.4. Normal biochemical processes occur in aqueous solutions at about neutral pH. Physiological pH is about 7.2 to 7.4. The relation between secondary formation function and equilibrium constants can be understood with the equation below.

$$\bar{n}_H = \frac{\beta_{011} * FH_i + 2 * \beta_{012} * FH_i^2}{1 + \beta_{011} * FH_i + 2 * \beta_{012} * FH_i^2}$$

Where $\beta_{011} = K_1^H$ and $\beta_{012} = K_1^H * K_2^H$ and FH_i is the free hydrogen ion concentration. It is very useful to study the dimeric species and equilibria using secondary formation functions. The formation functions/can be defined as one mole of ligand and it is bounded with the average number of protons, one mole of ligand, which consumes the average number of moles of alkali (a). The number of dissociable protons of the ligand, total concentration, total acid concentration and the concentration of hydroxide ions can be calculated using a computer program called SCPHD, which is used in our present study. The equation employed to calculate the above said can be given as $\bar{n}_{Hi} = (NDP_i + TLE_i + E_i + OH_i - ALK_i - FH_i)/TLE_i$ It is very clear that there should be an overlap in a curve drawn between $\bar{n}_H$ versus pH, which indicates that the absence of formation of dimeric species. The overlapping of curves are observed in the case of the 5-SSA and 5-HSA, it confirms that there are no dimeric species are formed (fig. 1). A computer program MINIQUAD75 has been employed to simulate all the titration curves.

The half-integral values for the two ligands are 0.5 and 1.0, which says that both ligands have two protonation-deprotonation equilibria in the pH range of the present investigation. The number of associable and dissociable protons of a ligand can be understood with help of fig. 2, which is plotted between and pH, where a number of associable protons. From the fig. 2, it is confirmed that the two ligands has 3 dissociable protons as the maximum value of a is+3 for both ligands.

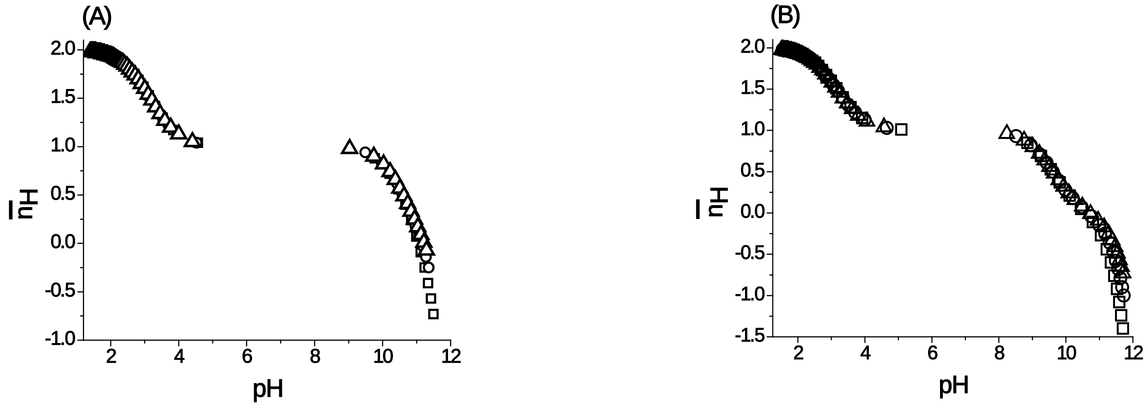

Fig. 1: Plots of n̄H /versus pH in 30% v/v DMSO-water mixture: (A) 5-SSA and (B) 5-HSA, (□) 0.25 (○) 0.38 (Δ) 0.50 mmol

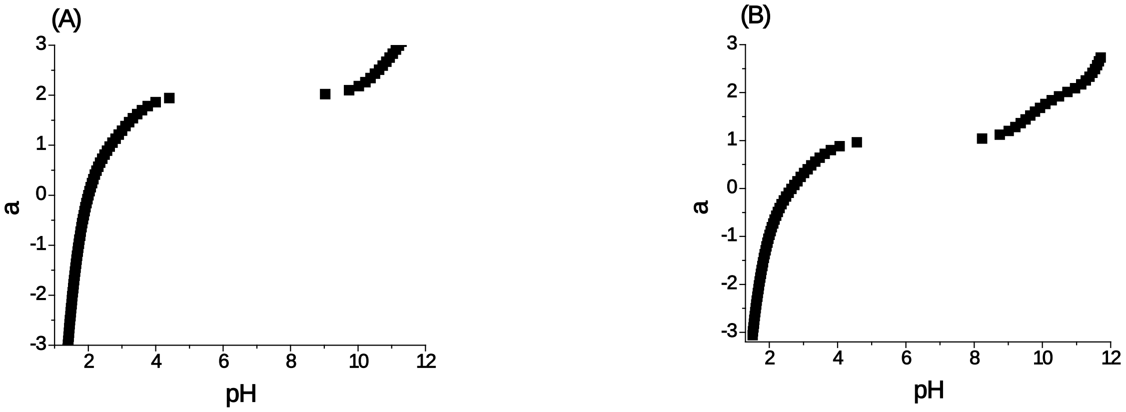

Fig. 2: Variation of a with pH in 40% v/v DMSO-water mixture: (A) 5-SSA (B) 5-HAS

The statistical parameters were calculated in the present study for the best-fit models; the calculated parameters, such as formation constants log β_i, Ucorr, skewness, kurtosis, R-Factor and Chi-square, were present in the table 2. The standard deviation values for log β are very low, which indicates the experimental data represents the model.

Residual analysis

The statistical data obtained in the present study are smaller than the tabular values. The $\chi2$ values are ranging from 1.21-6.88 and skewness values are ranging from-0.56-0.36 for 5-SSA and 5-HSA. The kurtosis values obtained in the present investigation for both 5-SSA and 5-HSA shows platykurtic. The obtained R-factor values also suggest that the present model is acceptable.

Effect of systematic errors in concentrations on best fit model

Effect of errors in the concentrations of acid, base, ligand is very useful as they show deviations in the protonation constant values but MINIQUAD75 does not have an in-built provision for the assessment of errors. To obtain a best fit chemical model, a critical evaluation has to be done by introducing pessimistic errors in the ingredients and checked for the variation in the protonation constant vales along with standard deviation. The changes in the protonation constants of both ligands are presented in the below table 3. It is observed that there are errors in their constants majorly due to change in the concentrations of acid and alkali; the rest of the ingredients shows very less influence.

Table 2: Best-fit chemical models of acido-basic equilibria of 5-SSA and 5-HSA in DMSO-water mixtures

% v/v DMSO	Log β_1(SD)	Log β_2(SD)	NP	Ucorr	Skewness	Kurtosis	χ^2	R-Factor
5-Sulfosalicylic acid (pH range 1.70-11.30)								
0.00	10.92(2)	13.23(1)	91	7.65	0.14	3.03	6.66	0.0166
10.0	10.86(1)	13.35(1)	82	21.52	0.11	2.68	8.91	0.0421
20.0	10.89(2)	13.70(3)	79	36.17	0.16	3.01	7.65	0.0256
30.0	10.72(3)	13.85(2)	69	42.24	0.18	2.97	5.45	0.0102
40.0	10.68(5)	13.91(4)	65	17.89	0.36	2.86	1.21	0.0213
50.0	10.54(2)	13.82(5)	58	57.14	0.16	2.64	2.35	0.0547
60.0	10.66(2)	14.02(78)	45	46.72	0.31	2.12	1.86	0.0279
5-Hydroxysalicylic acid (pH range 1.70-11.30)								
0.00	10.23(1)	13.05(1)	135	6.53	-0.56	2.90	6.88	0.0110
10.0	9.80(1)	12.89(2)	89	11.59	0.38	3.12	5.42	0.0679
20.0	9.69(4)	12.82(4)	75	29.12	-0.14	2.89	3.19	0.0456
30.0	9.70(3)	13.02(5)	67	38.61	-0.16	3.34	3.98	0.0278
40.0	9.57(1)	12.93(6)	58	66.14	0.24	2.78	2.81	0.0156
50.0	9.50(2)	12.98(6)	49	54.98	0.09	3.46	7.24	0.0118
60.0	9.52(1)	13.23(4)	38	47.09	0.26	2.57	2.76	0.0135

U_{corr}= U/(NP-m) X 10^8; NP = Number of points; SD = Standard deviation

Table 3: Effect of errors in influential parameters on the protonation constants in 10% v/v DMSO-water mixture

Ingredient	% Error	Log β_{mlh} (SD)			
		5-SSA		5-HSA	
	0	LH_2^-	LH^{2-}	LH_3	LH_2^-
		10.86(1)	13.35(1)	9.80(1)	12.89(2)
Alkali	+5	11.01(2)	14.01(1)	10.01(1)	13.12(2)
	+2	10.98(2)	13.78(1)	10.17(1)	13.29(2)
	-5	11.14(1)	13.96(1)	10.15(1)	13.35(2)
	-2	11.24(1)	13.01(1)	10.21(1)	13.10(2)
Acid	+5	11.75(1)	13.89(1)	10.20(1)	13.21(2)
	+2	11.56(2)	13.90(1)	10.35(1)	13.19(2)
	-5	11.23(1)	14.01(1)	10.15(1)	13.46(2)
	-2	10.37(1)	14.14(1)	10.68(1)	13.37(2)
Ligand	+5	10.75(1)	13.11(1)	9.89(1)	12.82(2)
	+2	10.69(1)	13.47(1)	9.70(1)	12.79(2)
	-5	10.79(1)	13.52(1)	9.85(1)	12.95(2)
	-2	10.59(1)	13.58(1)	9.78(1)	12.91(2)
Log F	+5	10.82(1)	13.41(1)	9.86(1)	12.86(2)
	+2	10.73(1)	13.56(1)	9.88(1)	12.81(2)
	-5	10.71(1)	13.25(1)	9.78(1)	12.92(2)
	-2	10.75(1)	13.38(1)	9.89(1)	12.94(2)
Volume	+5	10.79(2)	13.53(1)	9.89(1)	12.79(2)
	+2	10.74(1)	13.55(1)	9.87(1)	12.83(2)
	-5	10.89(1)	13.29(1)	9.76(1)	12.86(2)
	-2	10.81(2)	13.30(1)	9.81(1)	12.93(2)

Effect of the dielectric constant of the medium

The dielectric constant is an important property of any solvent; the polarity of the solvent affects the stability constants. The dielectric constant of a solvent and the electrostatic forces between ions and solution directly shows their impact on acid and base strength characteristics. According to previous [19, 20] studies and Born's [21, 22] equation, electrostatic contacts affect the dielectric constant of the system. The effect of dielectric constants on stability constants can be observed in fig. 3. The linear variation in the protonation constants of 5-SSA and 5-HSA shows the dominance of electrostatic interactions.

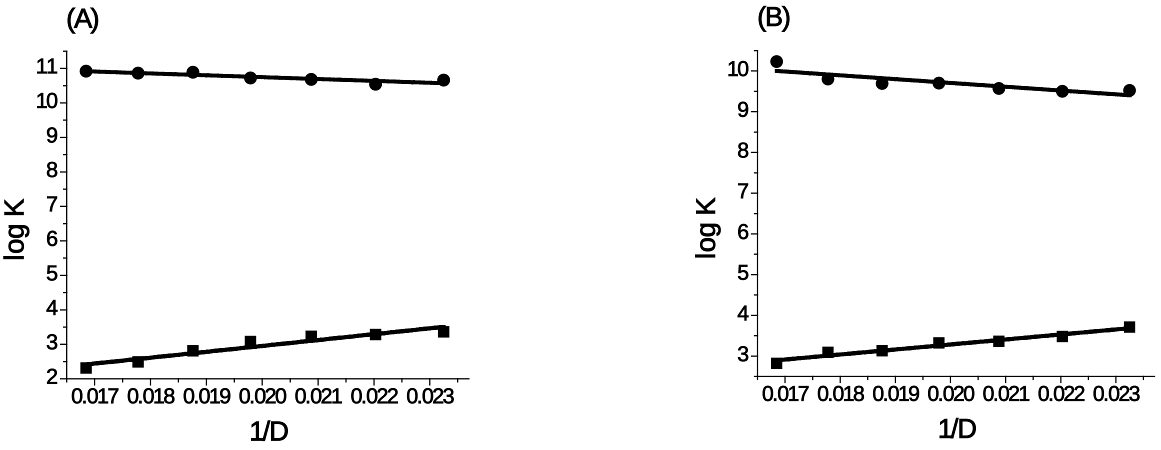

Fig. 3: Variation of stepwise protonation constants (log K) with reciprocal of dielectric constants in DMSO-water mixture, (A) 5-SSA, and (B) 5-HSA (■) log K$_1$ (● log K$_2$

Distribution diagrams

The typical distribution plots produced by DISPLOT [23-27], 5-Sulfosalicylic acid has three dissociable protons, one among three has low protonation constant value and will dissociate at a pH lower than 2.0 and unable to see due to the glass membrane electrode sensitivity, the existence of the ligand will be as LH_2^-,LH^{2-} , and L3$^-$. In the same way 5-Hydroxysalicylic acid has three dissociable protons, one among the three has high protonation constant and will dissociate at a pH 12.0, this range of pH makes the glass electrode unable to detect the protonation as the sensitivity is high at the pH. The existence of 5-HSA will be as LH_3 at low pH and LH_2^- and LH^{2-}.

From fig. 4(A), it is observed that the ligand 5-SSA in the form of as LH_2^-shows 98% of species up to the pH 2.0, as the pH is increasing the deprotonation of LH_2^-takes place and the percentage of species slowly falling down and possess very less percentage of species at the pH 8.0. Percentage of species of LH^{2-}starts increasing with pH and exhibits 98% of species at the pH 7.0. As the pH is increasing further, the percentage of species falling down and produce very less percentage at the pH 11.0. The other form of 5-SSA ligand i.e. L^{3-} increases with pH and possess high percentage of species at a pH 11.0.

Now, the LH_3 form of 5-HSA possess high percentage of species at a pH 2.0 and the percentage starts falling down with respective to increase in the pH. The LH_2^- form of 5-HSA possess maximum percentage of species at pH 7.0 and the percentage gradually decreasing with increase in the pH. Another form of the ligand i.e. LH^{2-}gradually increases with increases with increase in the pH and exhibits highest percentage of species at pH 11.0. This is observed in the fig. 4(B). The effect of pH on the percentage of species of both ligands was studied in between the pH range 1.7-11.5.

The protonation-deprotonationequilibria of both the ligands 5-SSA and 5-HSA were shown in the fig. 5.

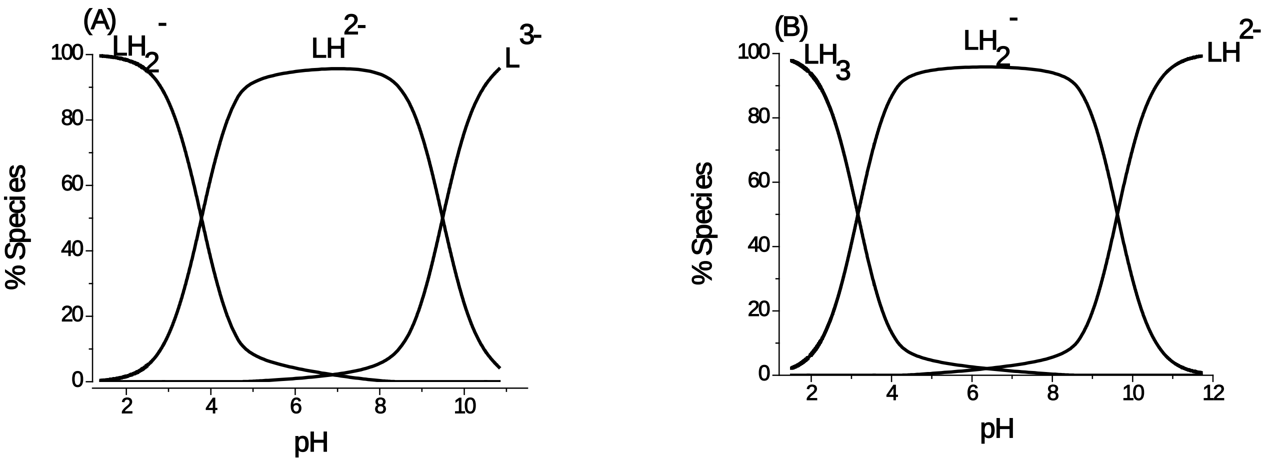

Fig. 4: Species distribution diagrams of (A) 5-SSA and (B) 5-HSA in 20% v/v DMSO-water mixture

(A). 5-Sulfosalicylic acid

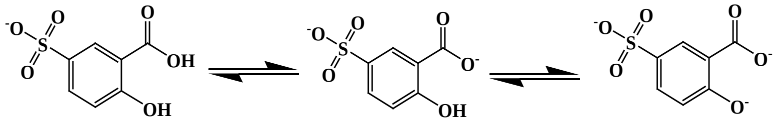

LH_2^- LH^{2-} L^{3-} pH: 1.5-7.0 pH: 1.5-11.0 pH: 7.0-11.0

(B). 5-Hydroxysalicylic acid

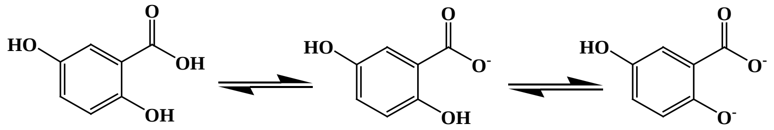

LH_3 LH_2^- LH^{2-} pH: 1.5-6.5 pH: 1.5-11.5 pH: 5.5-11.5

Fig. 5: Protonation-deprotonation equilibria of 5-SSA (A) and 5-HSA (B)

CONCLUSION

The half-integral values of both ligands confirm that they have three dissociable protons, 5-SSA has three dissociable protons and exists as LH_2^-, LH^{2-} and L^{3-} and 5-HSA has three dissociable protons and they exist as LH_3, LH_2^- and LH^2. The kurtosis values says that the system possess platykurtic. The skewness values of both the ligands ranging from 0.56-0.36 and the $\chi 2$ values are ranging from 1.21-6.88. The curve drawn between/versus pH indicates the absence of dimeric species. The changes in the concentration of alkali and acid shows major influence on protonation constants of both the ligands than the other ingredients such as ligand, log F and volume. The linear variation in the protonation constants of 5-SSA and 5-HSA due to the effect of dielectric constants of DMSO-water mixtures shows the dominance of electrostatic forces.

FUNDING

The authors declare that no funds, grants, or other support were received during the preparation of this manuscript.

AUTHORS CONTRIBUTIONS

All the authors have contributed equally.

CONFLICT OF INTERESTS

Declared none

REFERENCES

1. Krishna SR, Ramu A, Vidyadhara S, Rani AP. Bioavailability enhancement by floating micro balloons of dipyridamole and clopidogrel: *in vivo* pharmacokinetic study. Int J App Pharm. 2021 Jun 1;13(6):216-20. doi: 10.22159/ijap.2021v13i6.42316.
2. El-Mahdy MM, Rasheedy MM, Ibrahim EA, Fathallah D. Bioavailability study of ondansetron gel in rabbits and human volunteers applying UPLC as an analytical tool and evaluation of, the antiemetic effect of ondansetron gel in cisplatin-induced emesis in rats. Int J Pharm Pharm Sci. 2020 Mar 1;12(3):68-82.
3. Supriyo Saha DP. Computational approaches related to drug disposition. Int J Pharm Pharm Sci. 2021 Jul 1;13(7):19-27 3.
4. Masurkar PP. A need of a better pharmacovigilance system in India. Asian J Pharm Clin Res. 2017 Jan 1;10(1):22-4. doi: 10.22159/ajpcr.2017.v10i1.14797.
5. Chaitanya Sai G, Judy J, Desgn BM. Binding affinity studies and *in silico* admet predictions of novel isoxazoles as potential antibacterial. Int J Curr Pharm Res. 2022 Apr 1;14(4):74-7.
6. Balakrishna M, Srinivasarao G, Ramanaiah M, Nageswara Rao G, Ramaraju B. Influence of dielectric constants on protonation equilibria of 5-sulfosalicylic acid and 5-hydroxy salicylic acid in urea-water mixtures. J Ind Chem Soc. 2017 Jan 1;94(1):37-45.
7. Ramanaiah M, Goutham Sri S, Balakrishna M, Ramaraju B, Sailaja BBV. Effect of nonionic micelles of triton X-100 on protonation equilibria of salicylic acid derivatives. J Ind Chem Soc. 2017 Mar 1;94(3):253-9.
8. Balakrishna M, Srinivasa Rao G, Ramanaiah M, Ramaraju B, Nageswara Rao G. pH metric investigation on the chemical speciation of Co(II), Ni(II) and Cu(II) complexes with 5-hydroxysalicylic acid in urea-water mixtures. J Ind Chem Soc. 2017 Aug 1;94(8):905-12.
9. Balakrishna M, Srinivasa Rao G, Ramanaiah M, Ramaraju B, Nageswara Rao G. Effect of dielectric constants of co-solvent DMF on protonationequlibria of 5-sulfosalicylic acid and 5-hydroxysalicylic acid. Res J Pharm Biol Chem Sci. 2015 Sep 1;6(5):1430-8.
10. Rao CN, Kumari VG, Sailaja BBV. Solvent effect on protonation equilibria of L-asparagine and maleic acid in dimethyl sulfoxide. J Ind Chem Soc. 2014 Jun 1;91(6):1021-7.
11. Ramanaiah M, Goutham Sri S, Balakrishn M, Rama Raju B. Effect of cationic micelles of cetyltrimethylammoniumbromide on

protonation equilibria of salicylic acid derivatives. J Chil Chem Soc. 2017 Dec 1;62(4):3677-82.

12. Balakrishna M, Srinivasa Rao G. Study of ternary complex stability constants of Co(II),Ni(II), and Cu(II) with 5-sulfosalicylic acid and 5-hydroxysalicylic acid in DMF-water mixtures. Res J Chem Environ. 2017 Nov 1;21(11):20-8.
13. Raju BR, Devi KS, Rao GN. Speciation studies of some essential metal complexes of 1, 10-phenanthroline in dioxin–water mixtures. Proc Natl Acad Sci India. 2011 Oct 1;81:265-72.
14. Gran G. Determination of the equivalence point in potentiometric titrations. Part II Analyst. 1952 Jan 1;77(920):661-71. doi: 10.1039/an9527700661.
15. Gran G. Equivalence volumes in potentiometric titrations. Anal Chim Acta. 1988 Jan 1;206:111-23. doi: 10.1016/S0003-2670(00)80835-1.
16. Sudhakar C, Shaik A, Ramanaiah M, Nageswara Rao C. Effect of solvent on protonation equilibria of L-serine and L-tryptophan in ethylene glycol-water mixtures. Res J Chem Environ. 2021 Nov 1;25(7):124-9. doi: 10.25303/257rjce12421.
17. Gans P, Sabatini A, Vacca A. An improved computer program for the computation of formation constants from potentiometric data. Inorg Chim Acta. 1976 Jan 1;18:237-9. doi: 10.1016/S0020-1693(00)95610-X.
18. Balakrishna M, Rao GS, Ramanaiah M, Rao GN, Ramaraju B. Speciation studies of ternary complexes of Co(II), Ni(II), and Cu(II) with 5-sulfosalicylic acid and 5-hydroxy salicylic acid in urea-water mixtures. Res J Pharm Technol. 2017 Nov 1;10(11):3681-6. doi: 10.5958/0974-360X.2017.00667.9.
19. Bunton CA, Romsted LS, Sepulveda LA. A quantitative treatment of micellar effects upon deprotonation equilibriums. J Phys Chem. 1980 Oct 1;84(20):2611-8. doi: 10.1021/j100457a027.
20. Chaimovich H, Bonilha JBS, Politi MJ, Quina FH. Ion exchange in micellar solutions. 2. Binding of hydroxide ion to positive micelles. J Phys Chem. 1979 Jul 1;83(14):1851-4. doi: 10.1021/j100477a011.
21. Born M. Volumen und hydratationswarme der Ionen. Z Physik. 1920;1(1):45-8. doi: 10.1007/BF01881023.
22. Ramanaiah M, Balakrishna M, Neeraja R, Gouthamsri S, Seetharam P. The formation analysis of Ca (ii), Mg (ii), Zn (ii) and 5-hydroxy salicylic acid binary complexes in cetyltrimethylammonium bromide cationic micelles. Ind J Pharm Edu Res. 2023 Sep 1;57(3s):s734-41. doi: 10.5530/ijper.57.3s.83.
23. Neeraja R, Bindu GH, Ramanaiah M. A pH metric investigation on mixed-ligand complexes of transition metal ions with selective bio-ligands in surfactant–aqua mixture. Res J Chem Environ. 2021 Mar 1;25(3):21-30.
24. Ramanaiah M, Seetharam P, Balakrishna M, Raju BR. Potentiometric studies of complex equlibria of CaII, MgII and ZnII with 5-sulphosalicylic acid in cationic micelles of CTAB. Heliyon. 2019;5(8):e02157. doi: 10.1016/j.heliyon.2019.e02157, PMID 31417969.
25. Seetharam P, Balakrishna M, Mohan BS, Satyanarayana G, Sailaja BBV. Potentiometric studies on bioactive material species of ternary complexes. Russ J Gen Chem. 2020;90(12):2467-72. doi: 10.1134/S1070363220120397.
26. Balakrishna M, Srinivasa Rao G, Ramanaiah M, Nageswara Rao G, Rama Raju B. pH metric investigation on speciation studies of 5-sulfosalicylic acid complexes of Co(II), Ni(II) and Cu(II) in DMF-water mixtures. Der Pharma Chemica. 2016 Aug 1;8(8):150-7.
27. Balakrishna M, Srinivasa Rao G, Ramanaiah M, Nageswara Rao G, Rama Raju B. Influence of the dielectric constant of the medium on the chemical speciation of Co(II), Ni(II) and Cu(II) complexes with 5-hydroxy salicylic acid in DMF-water mixtures. Res J Pharm Biol Chem Sci. 2017 Mar 1;8(2):88-96.

Journal of Advanced Scientific Research

Available online through https://sciensage.info

ISSN
0976-9595
Research Article

STUDY OF ANTIBACTERIAL EFFICACY OF GREEN -SYNTHESIZED SILVER-NICKEL HYBRID NANOPARTICLES

Ch. S. Anuradha[1], S. Padmavathi[2]

[1]*Department of Chemistry, Dr. V.S. Krishna Government Degree (A) & P.G College, Visakhapatnam, Andhra Pradesh, India*
[2]*Department of Botany, Dr. V.S. Krishna Government Degree (A) & P.G College, Visakhapatnam, Andhra Pradesh, India*
**Corresponding author: anuradha.chs@gmail.com*

Received: 11-08-2022; Accepted: 18-09-2022; Published: 30-09-2022

https://doi.org/10.55218/JASR.202213807

ABSTRACT

An eco-friendly green strategy is presented for the synthesis of Ag-Ni hybrid nanoparticles taking a medicinal plant, *Aerva lanata* for phytoreduction of the precursor salt solutions. The synthesized nanoparticles are characterized by instrumental techniques such as UV-Visible, FTIR, EDX, FESEM and HRTEM. These particles are found to possess significant antibacterial efficacy against both Gram-positive and Gram-negative bacteria based on investigation by Well Diffusion method.

Keywords: Hybrid nanoparticles (HNPs), *Aerva lanata (*AL), Gram-positive bacteria, Gram-negative bacteria, minimum inhibitory concentration (MIC).

1. INTRODUCTION

Nanotechnology involves the manipulation of materials having one of the dimensions in the range of 0.1-100 nm [1]. It has its applicability in different fields like biology, chemistry, physics, engineering and medicine [2]. There are two types of methods generally adopted for fabricating nanomaterials; top-down methods and bottom-up methods. In top down method we transform material progressively from bulk substrate until the desired nanomaterial is obtained. Bottom-up strategies are employed starting from the atomic or molecular precursors and by gradually assembling it until the preferred structure is formed [3].

Remarkable expansion of nanotechnology has spread out its applications in biomedical sciences, nutrition, energy sciences, nanobiotechnology, cosmetics, mechanics, optics, chemical industries and drug-gene delivery [4]. Alloying of two different metals in nanosize may enhance the characteristics of their corresponding monometallic nanoparticles. These hybrid nanoparticles show greater stability and catalytic activity than monometallic nanoparticles [5]. Generally nanometals are synthesized by physical or chemical reduction methods which are hazardous and expensive.

In contrast, plant mediated green methods are eco-friendly, cheaper and benign for the synthesis of nanometals. Secondary metabolites present in plant extract will act as bio-reducing and capping agents for the resulted nanoparticles [6].

Antibacterial agents are very important in the textile industry, water disinfection, medicine, and food packaging. Organic compounds used for disinfection have notable disadvantages including toxicity to the human body and therefore the interest in inorganic nanoparticles has increased as they are benign to greater extent [7]. Nanoparticles are increasingly used to target bacteria as an alternative to antibiotics [8]. Traditional methods like herbal extracts used to the synthesize nanometal particles have shown extensive consent in medicine. These synthesized nanometal particles have great bactericidal activity than bulk metals because of its adsorption at bacterial surface. Metals like silver, copper, gold, nickel etc., in the nanodimensions are hypothesized to be able to participate in sub-cellular reactions as their size is comparable to biological molecules. Bimetallic nanoparticles composed of two different metals have drawn a greater interest than the monometallic nanopaticles due to the properties differ from pure elemental particles include unique size dependent, optical, electronic, thermal, catalytic and biological effects [9]. Plant mediated green synthesized HNPs have increased attention towards their antimicrobial properties as they contain bioactive phytochemicals as stabilizing and capping agents.

In this present study, an effortless and robust green method is reported for the synthesis of Ag-Ni hybrid nanoparticles (HNPs) by using leaf extract of *Aerva lanata* as a reducing and capping agent. The synthesized HNPs are studied for their antibacterial activity against Gram-positive, Gram- negative bacteria.

2. EXPERIMENTAL

2.1. Materials

Chemical reagents used (silver nitrate and nickel nitrate) in this study were of analytical grade. Deionized water was used to clean glassware, to prepare chemical solutions and for experimental procedure. Fresh leaves of *Aerva lanata* were collected from agricultural lands in Nellimarla village, Vizianagaram district, Andhra Pradesh state, India.

2.2. Preparation of *Aerva lanata* leaf extract

Hundred g of fresh leaves are weighed and thoroughly washed with running tap water to remove detritus on surface of leaves followed by deionized water to get rid of other contaminants from leaves and dried up under shade for 10 days. These leaves are cut into tiny pieces and made homogenized powder by using home blender. The procured powder is placed in refrigerator at 5°C which is kept in an air tight container. Now 200mL deionised water was taken in 500mL beaker and to this 10 g stored powder was added. The contents in the beaker were heated for 20 minutes at 60°C with occasional stirring with glass rod and then cooled to acquire room temperature. The cooled concoction was filtered twice with Whatman No.1 filter paper and reserved in refrigerator at 5°C. The extract was taken as leaf extract throughout the experiment.

2.3. Synthesis of Ag-Ni bimetallic nanoparticles

Equimolar (25 mM) concentrations of silver nitrate and nickel nitrate aqueous solutions were prepared separately in 100 mL volumetric flasks by dissolving 0.4246 g, 0.7267 g weight of $AgNO_3$ and $Ni(NO_3)_2$ in deionized water respectively. Synthesis of Ag-Ni HNPs was done by taking 100 mL of $AgNO_3$ solution in a 500 mL beaker, to this 90 mL of leaf extract, 100 mL of $Ni(NO_3)_2$ solution were added drop wise in simultaneous addition process. After this addition the beaker was placed on a magnetic stirrer for continuous agitation. This mixture was stirred at 70°C for 70 minutes at pH 8 on magnetic stirrer. Synthesized HNPs were separated out by doing centrifugation at 5000 rpm for 40 minutes. The obtained HNPs were washed with deionized water twice to remove unwanted constituents and dried in oven at 80°C for two hours. The resultant HNPs particles were collected and used for characterization.

2.4. Characterization

Synthesized HNPs were characterized by various instrumental techniques. UV-Visible analysis shows the formation of HNPs by SPR band at band at around 439 nm and FTIR spectrum of Ag-Ni HNPs exhibits major peak positions at 3212 cm^{-1}, 3416 cm^{-1} and 3382 cm^{-1}which indicate the N-H stretching vibrations of amines and O-H stretching of hydroxyl groups of alcohols and phenols. Intense peak at 1642 cm^{-1} is due to C=O stretching of amide group. Very small peak at 601 cm^{-1} indicates the presence of C-Cl group.

From energy dispersive X-ray analysis (EDX), we can analyze all the elements present in the HNPs which indicate the existence of Ag and Ni which confirms the formation of Ag-Ni bimetallic nanoparticles. This is also supported by the EDX study which gives quantitative data of silver and nickel compositions in HNPs**.** By Field Emission Scanning electron microscopic (FESEM) images of Ag-Ni HNPs (Fig. 1), it can be clearly noted that the prepared Ag-Ni bimetallic nanoparticles are in the size range between 50 and 100 nm in diameter.

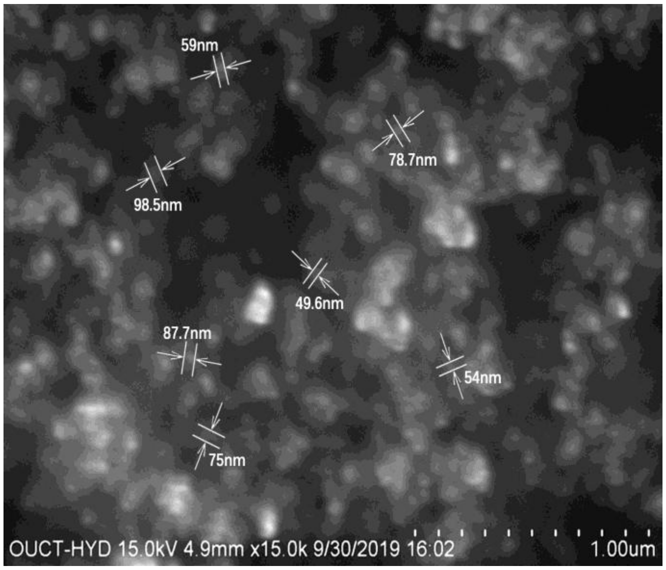

Fig. 1: FESEM Image of HNPs

HRTEM shows that Ag-Ni HNPs are figured with spherical morphology and crystalline structure below 100 nm in size. More specifically, the two metal nanospheres are shown and spotted adjacent to each other. It is also in strong agreement with the micrographs from FESEM analysis. Powder XRD analysis confirms that HNPs have FCC crystal structure (Fig. 2) with average particle diameter of 23.3 nm.

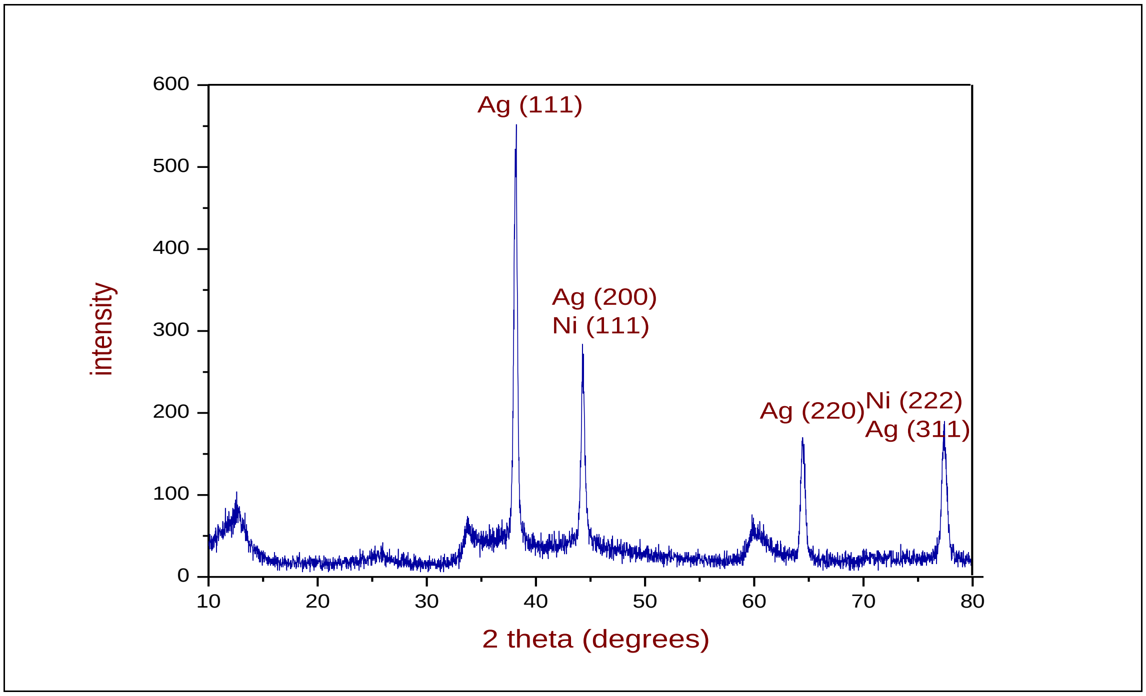

Fig. 2: XRD Image of HNPs

3. INVESTIGATION OF ANTIBACTERIAL ACTIVITY

3.1. Reagents and Materials

The antibacterial study was performed using four bacterial strains i.e. *Bacillus subtilis* (MTCC211), *Escherichia coli* (MTCC443), *Staphylococcus aureus* (MTCC6908), *Pseudomonas aeruginosa* (MTCC2581). The cultures were procured from IMTECH, Chandigarh, India.

3.2. Antimicrobial activity

Antimicrobial activities of the compounds investigated are evaluated by agar-well diffusion method [10]. The standardized cultures of test bacteria are first evenly spread onto the surface of Mueller Hinton Agar plates using sterile cotton swabs. Five wells (6 mm diameter) were made in each plate with sterile cork borer. Twenty microlitres of the nanocompound and positive control were added in wells. Streptomycin (10 µg) was used as reference antibiotic. Diffusion of compounds, antibiotic and DMSO were allowed at room temperature for 1 h. All of the plates were then covered with lids and incubated at 37°C for 24 h. After incubation, plates were observed for zone of bacterial growth inhibition. The size of inhibition zones is measured and antimicrobial activity of the compounds is expressed in terms of the average diameter of inhibition zone in millimeters. Those compounds that are unable to exhibit inhibition zone (inhibition zone diameter less than 6 mm) are considered non-active. The compound is tested in triplicate with two independent experiments and the mean values of inhibition zone diameters are taken.

4. RESULTS AND DISCUSSION

Ag-Ni HNPs are studied for their antimicrobial activity against two gram positive bacteria and two gram negative bacteria. In case of gram positive bacteria, the test organisms are *Staphylococcus aureus* and *Bacillus subtilis,* the nanocompound shows significant antibacterial activity in all the four concentrations under study (Fig. 3). Ag-Ni HNPs demonstrate significant activity against the two selected gram positive bacteria, 16 mm against *S. aureus* and 17 mm against *B. subtilis* at 1 mg concentration. In case of gram negative bacteria, the test organisms were *Pseudomonas aerugisona* and *Escherichia coli*. The compound shows antibacterial activity against these two bacteria in all the four concentrations studied (Fig. 4). Ag-Ni nanocompound demonstrates remarkable activity against the two selected gram positive bacteria, 15 mm against *P. aeruginosa* and 14 mm against *E. coli* at 1mg concentration.

Table 1: Antibacterial activities of nanocompound against gram positive bacteria

Compound Name	Zone of inhibition (mm)							
	Gram positive *(Staphylococcus aureus)*				Gram positive *(Bacillus subtilis)*			
	1mg	0.75mg	0.5mg	0.25mg	1mg	0.75mg	0.5mg	0.25mg
Ag Ni	16	13	11	9	17	14	12	10
Streptomycin	29				31			

Table 2: Antibacterial activities of nanocompound against gram negative bacteria

Compound Name	Zone of inhibition (mm)							
	Gram negative *(Pseudomonas aerugisona)*				Gram negative *(Escherichia coli)*			
	1mg	0.75mg	0.5mg	0.25mg	1mg	0.75mg	0.5mg	0.25mg
Ag Ni	15	10	8	8	14	13	12	10
Streptomycin	26				27			

Fig. 3: Antibacterial activities of HNPs against gram positive bacteria

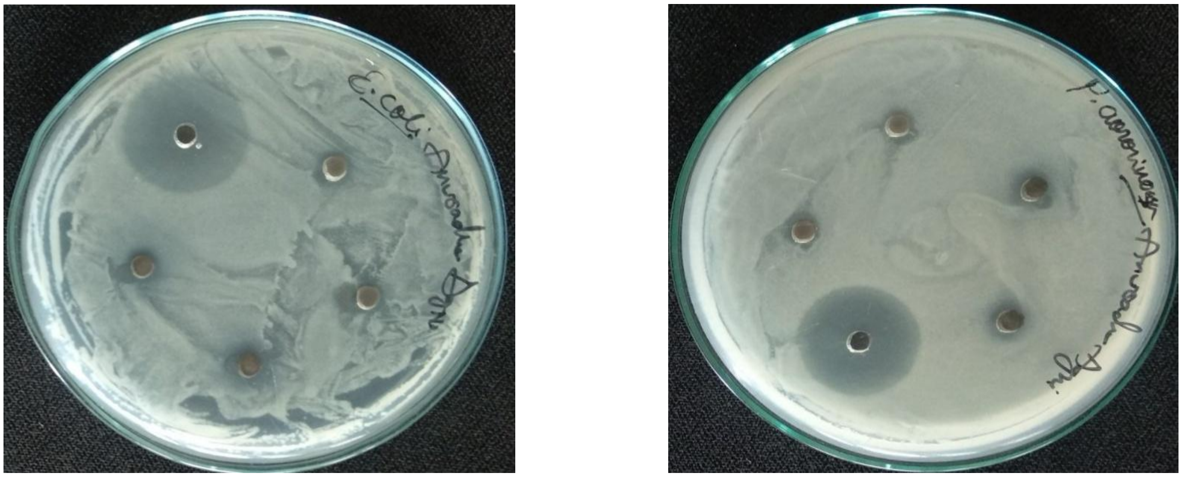

Fig. 4: Antibacterial activities of HNPs against gram negative bacteria

5. CONCLUSION

These findings demonstrate that green synthesized Ag-Ni hybrid nanoparticles are found to possess moderate anti bacterial activity against gram positive bacteria (*Bacillus subtilis* and *Staphylococcus aureus*) and gram negative bacteria (*Escherichia coli* and *Pseudomonas aeruginosa*) respectively. This antimicrobial activity of nanoparticles is attributed to the capped plant secondary metabolites that are present on their surface. With the future expansion of this present work in mind, considering the evolution of new drug resistant strains, the synthesized HNPs may be administered against those strains and they may be also examined and reported in the future. The future research may be directed for the genetic manipulation of plants to increase the metal tolerance and metal accumulation ability.

Conflict of interest

None declared

Source of funding

None declared

6. REFERENCES

1. Bennett JW. *Antibiotics: Current Innovations and Future Trends*, 2015; **07**:1–18.
2. Hajipour MJ, Fromm KM, Ashkarran AA, Aberasturi DJD, Larramendi IRD, Rojo T, Serpooshan V, Parak WJ, Mahmoudi M. *Trends in Biotechnology*, 2012; **30(10)**:499–511.
3. Wang L, Hu C, Shao L. *International Journal of Nanomedicine*, 2017; **12:**1227–1249.
4. Ouay BL, Stellacci F. *Nano Today*, 2015; **10(3)**:339–354.
5. Slavin YN, Asnis J, Hafeli UO, Bach H. *Journal of Nanobiotechnology*, 2017; **15(1)**:10-24.
6. Sharma G, Kumar A, Sharma S, Naushad M, Dwivedi RP, Alothman ZA, Mola GT. *Journal of King Saud University – Science,* 2017; **05**:12-20.
7. Jiao M, Zhang P, Meng J, Li Y, Liu C, Luo X, Gao, M. *Biomaterials science*, 2018; **6(4)**:726-745.
8. Singh A, Gautam PK, Verma A, Singh V, Shivapriya PM, Shivalkar S, Samanta SK. *Biotechnology Reports,* 2020; **25**:427-432.
9. Gad M M, Abualsaud R, Rahoma A, Al-Thobity A M, Al-Abidi K S, Akhtar S. *International journal of nanomedicine*, 2018; **13**:283-288.
10. Daeschel M A. Procedures to detect antimicrobial activities of microorganisms. in food biopreservatives of microbial origin: CRC Press; 2019. pp. 57-80.

J Mater Sci: Mater Electron (2023) 34:955

Optical response of Eu^{3+}-activated $MgAl_2O_4$ nanophosphors for Red emissive LED Applications

B. Nageswara Rao[1,2,3], P. Tirupathi Rao[1], Sk. Esub Basha[1], D. S. L. Prasanna[4,6], K. Samatha[2], and R. K. Ramachandra[1,5,*]

[1] Crystal Growth and Nano-Science Research Center, Department of Physics, Government College (A), Rajamahendravaram 533105, Andhra Pradesh, India
[2] Department of Physics, Andhra University, Visakhapatnam 530003, Andhra Pradesh, India
[3] Department of Physics, Dr V S Krishna Government Degree College (A), Visakhapatnam, India
[4] Department of Chemistry, Acharya Nagarjuna University, Guntur 522510, A.P, India
[5] Government Degree College, Chodavaram, Visakhapatnam 531036, Andhra Pradesh, India
[6] Department of Chemistry, Dr V S Krishna Government Degree College (A), Visakhapatnam, India

Received: 28 December 2022
Accepted: 25 March 2023

ABSTRACT

Eu^{3+}-activated magnesium aluminate phosphors were successfully synthesized by nitrate–citrate gel combustion method and thermally treated at 650, 750, 850, and 950°C. The powder X-ray diffraction pattern showed that all $MgAl_2O_4$:$x$$Eu^{3+}$ ($0 \leq x \leq 0.10$) samples exhibit crystallized cubic phase of spinel structure with space group Fd-3 m. The Debye–Scherrer equation is used to estimate average crystallite size values and are found to be 8.5–12.1 nm, that are also confirmed by high-resolution transmission electron microscopy (HRTEM) images. TGA–DTG results suggest that the maximum decomposition of the precursors were observed below 600°C. Accordingly, the decomposition temperature was taken 650°C and above. The functional groups of the powder samples were determined by FTIR. Energy levels were characterized, and the band gap energy (E_g) has been calculated using UV–Vis absorption spectroscopy and found to be in the range of 5.08–5.19 eV. The FESEM images shows that the nanoparticles are agglomerated and are in nonuniform spherical shape with reduced average particle size from 27 ± 4.1 to 24.1 ± 3.3 nm. Further, the elemental composition of the as-prepared samples was analyzed by using energy-dispersive X-ray spectra (EDAX). The photoluminescent property of $MgAl_2O_4$:$x$$Eu^{3+}$ samples was investigated using room-temperature emission spectroscopy. These phosphors show different emissions of Eu^{3+} corresponding to $^5D_0 \rightarrow {}^7F_{J=1,2,3,4}$ transitions which lie in the wavelength range from 590 to

---

Address correspondence to E-mail: drkrcr@gmail.com; ramc@gcrjy.ac.in

https://doi.org/10.1007/s10854-023-10341-w

703 nm. The red emission transition $^5D_0 \rightarrow ^7F_2$ ($\Delta J = 2$) centered at 612 nm has been known to be hypersensitive, strong, and more intense of all samples. The PL emission intensity increases up to 4 mol% Eu^{3+} concentration and then decreases due to the process of concentration quenching. The chromaticity color coordinates were obtained from the luminescence emission spectrum. The temperature-dependent luminescence property of $MgAl_2O_4$:4%Eu^{3+} phosphor has also been discussed. These results showed that $MgAl_2O_4$:$x$$Eu^{3+}$ could be a prominent material for the production of artificial red light in red LEDs.

1 Introduction

Spinel oxides with the formula AB_2O_4, where A and B are divalent and trivalent cations, respectively, were effectively used as electric, magnetic, catalysis, ceramic, chemical, electronic, and optical materials [1]. They have also been acted as a stable host for persistent luminescence when rare-earth (RE)/transition-metal ions are incorporated into the host lattice [2].

Magnesium Aluminate spinel (MAS) with chemical formula $MgAl_2O_4$, where Mg^{2+} divalent metal cation normally occupies a tetrahedral site and Al^{3+} trivalent metal cations occupy the octahedral sites of a cubic packed crystal [3] have the cubic space group Fd-3 m. $MgAl_2O_4$ spinel is a ternary oxide with face center cubic structure (fcc) is one of the most important optically transparent materials that exhibit excellent properties such as high melting point, low thermal expansion coefficient, high mechanical strength, low density, high chemical resistance to both acidic and basic slags, relatively low dielectric loss, high thermal shock resistance, wide optical band gap, moderate refractive index, good poisson's ratio, excellent hot strength, high resistance to changes in the environment, resistance to slag corrosion, and excellent catalytic properties [4–8]. MAS has been widely employed in many industrial applications including color display, humidity sensors [9], tuneable solid-state lasers, refractory materials [10], lamp industry, catalyst supports [11], and transparent ceramics [12].

$MgAl_2O_4$ spinel doped with RE ions have been employed in luminescent and picture tube applications and this incorporation enhances the emission efficiency of the phosphor materials. $MgAl_2O_4$ has also been used as host material for glow phosphors doped with Mn^{2+} [13], Ti^{4+} [14], Nd^{3+} [15], Dy^{3+} [16], Mn^{2+}, Cr^{3+} [17], Er^{3+}, Yb^{3+} [18], Ti^{4+}, Mn^{2+} [19], Gd^{3+} [20], Eu^{2+} [21], Tb^{3+} [22], Eu^{3+}, Dy^{3+} [23], and Sm^{3+} [24]. Several preparative methods have been used for the synthesis of spinel nanophosphors including solid-state reaction method [25], co-precipitation, spray-drying, microwave-assisted hydrothermal method, sol-gel synthesis, molten salt process, nebulized spray pyrolysis (NSP) [26], solvothermal method, polyol method, aqueous wet chemical method, and combustion methods [20]. In the present investigation, we have reported the synthesis of Eu^{3+}-doped magnesium aluminate spinel's ($MgAl_2O_4$:$x$$Eu^{3+}$, $0 \leq x \leq 0.10$) by citrate–nitrate gel combustion method [18]. This preparation technique has been chosen because, it can produce a homogenous product in a short amount of time, offers low temperature initiation, excellent particle size distribution, less cost effective, high purity, and good morphological control. We have been investigated the influence of Eu^{3+} doping concentration on structural from powder X-ray diffraction (XRD), optical from UV–Vis, spectroscopic from FTIR, microstructural from FESEM, elemental composition from EDAX, morphological from HRTEM, and luminescent properties from emission spectra. The valence mismatch between Mg^{2+} and Eu^{3+} and their difference in size can be manifested by broad emission bands [15].

In this paper, we also demonstrated the $MgAl_2O_4$ spinel as an active host material for the luminescence as well as for the energy transfer to doped Eu^{3+} ions in the application of high efficiency phosphors for red LEDs. Eu^{3+}-activated $MgAl_2O_4$ is reported to be synthesized using a simple citrate–nitrate gel combustion method, which is considered as an active phosphor material for the development of pure red LEDs in optoelectronic applications. I. Omkaram et al. have already been investigated the photoluminescence study on $MgAl_2O_4$:Eu^{3+} phosphor in the literature [25] and the incorporated Eu^{3+} ion is observed to emit red color in the emission spectrum. However, the study of the effect of high annealing temperature on the photoluminescence emission of $MgAl_2O_4$:4%Eu^{3+} has not been investigated in the literature to the best of our knowledge. The main objective of the present work is to study the optical properties of the as-synthesized pure and Eu^{3+}-doped $MgAl_2O_4$ samples as a function of Eu^{3+} doping concentration (2, 4, 6, 8, and 10 mol%) and their temperature-dependent photoluminescence investigations for optimal concentration (4 mol% Eu^{3+}) at progressively high annealing temperatures (650, 750, 850, and 950°C). The observed emission channels and CIE color coordinates of $MgAl_2O_4$:$x$$Eu^{3+}$ phosphor materials were also reported in detail.

2 Experimental section

2.1 Sample synthesis

Figure 1 shows the synthesis of Eu^{3+}-doped $MgAl_2O_4$ powders. All analytical grade reagent chemicals were purchased and used without further purification in this experimental study. The precursors used for the synthesis are listed in Table 1. Citrate–nitrate gel combustion process was employed to prepare the bare and Eu^{3+}-doped $MgAl_2O_4$ nanophosphors using magnesium nitrate hexahydrate [$Mg(NO_3)_2{\cdot}6H_2O$], aluminum nitrate nonahydrate [$Al(NO_3)_3{\cdot}9H_2O$], and Citric Acid [$C_6H_8O_7.H_2O$] as starting materials. Metal nitrates were added as oxidizers and citric acid was used as a chelating agent. Each material was weighed by using a high precision (0.0001 g) balance. The procedure used to prepare Eu^{3+}-doped $MgAl_2O_4$ nanophosphors as follows: Stoichiometric amounts of $Al(NO_3)_3{\cdot}9H_2O$ and $Mg(NO_3)_2{\cdot}6H_2O$ and Citric Acid ($C_6H_8O_7.H_2O$) were dissolved in deionized water (D. W.) and subsequent sonication as well as mixing at ambient temperature for 1 h to obtain transparent solution. In addition, Eu_2O_3 is dissolved in dilute HNO_3 to prepare homogeneous solution, which is slowly added to the above resultant solution. Subsequently, the final precursor solution was placed into glass containers and introduced onto a Magnetic stirrer at 120 °C until the formation of a brown resin as a burnt ash product. After that the above product was transferred into a silica crucible and calcined in a muffle furnace at 650, 750, 850, and 950°C for 12 h in air atmosphere to obtain Eu^{3+}-doped $MgAl_2O_4$ phosphors. The mole concentration of the activator Eu^{3+} ion varied as 0.02, 0.04, 0.06, 0.08, and 0.10 from an appropriate stoichiometric ratio.

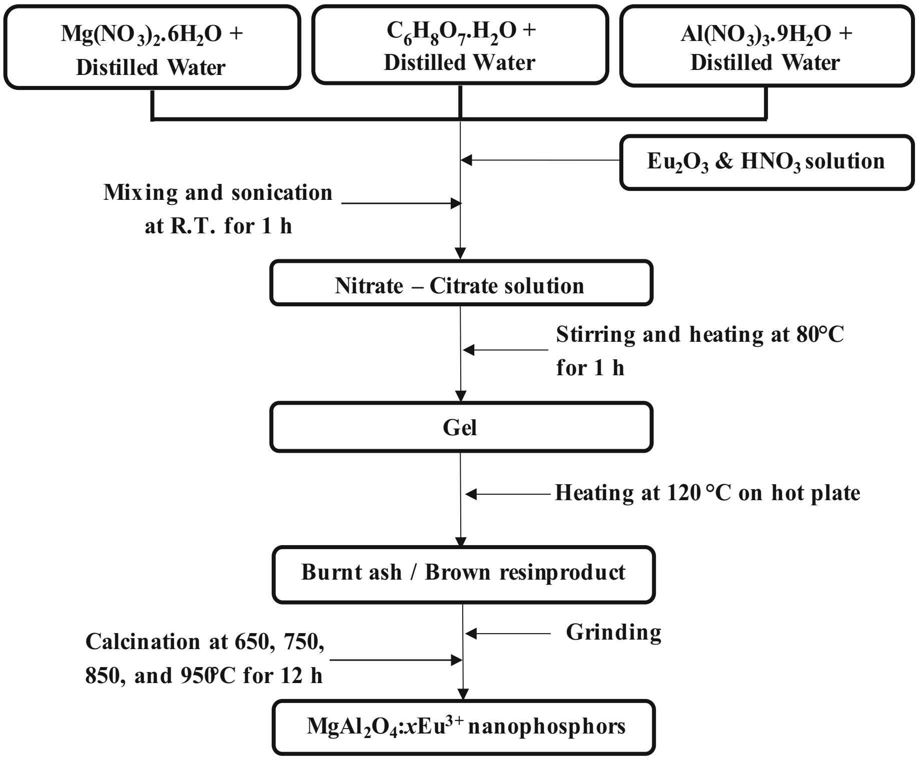

Fig. 1 Flowchart of the synthesis procedure of $MgAl_2O_4$:$x$$Eu^{3+}$ nanophosphors by nitrate–citrate gel combustion method

Table 1 Primary chemicals used for synthesis of Eu^{3+}-doped $MgAl_2O_4$ powders

Chemical name	Chemical formula	Molecular Weight (g/mol)	Purity	Manufacturer
Magnesium nitrate hexahydrate	$Mg(NO_3)_2{\cdot}6H_2O$	256.41	99.0%	Fisher Scientific
Aluminum nitrate nonahydrate	$Al(NO_3)_3{\cdot}9H_2O$	375.13	98.0%	Fisher Scientific
Citric Acid	$C_6H_8O_7$	192.12	99.5%	Fisher Scientific
Europium(III) oxide	Eu_2O_3	351.93	99.9%	Sigma-Aldrich

2.2 Sample characterization

The phase purity and crystallinity of Eu^{3+}-doped $MgAl_2O_4$ phosphors were examined by powder X-ray diffraction measurements using PANalytical X'pert Pro diffractometer, CuKα radiation (K = 1.5406 Å) with a nickel filter. For XRD analysis, data were collected at a scan rate of 1°/min with a 0.02° step size for 2θ from 10° to 80°. Thermal gravimetric analysis of the precursors was performed using TG–DTA analyzer (NETZSCH STA 409) in the range temperature 35–950°C with SiC as heating element. FTIR spectra were recorded using PerkinElmer Spectrometer, Frontier using KBr as a reference after calcinations in the wavenumber range 4000–400 cm^{-1}. UV–visible diffuse reflectance spectra (DRS) were performed in an Agilent Cary 5000 UV–Vis NIR spectrometer with an attached diffuse reflectance accessory in the wavelength range of 200–800 nm to estimate the energy band gap of the samples. Field emission scanning electron microscope (FESEM, Hitachi S-4800) was used to examine surface morphology of the prepared nanophosphors. High-resolution transmission electron microscopy (HRTEM) images were made using JEOL JEM 2100 to investigate the crystalline structure of the samples. The Photoluminescence (PL) studies have been carried out using a Horiba Flurolog-3 spectrofluorometer (450 W Xenon lamp). All the measurements were performed at room temperature. The chromaticity color coordinates of the samples were recorded according to the Commission Internationale de l'Eclairage (CIE) by using Spectra Lux Software v.2.0 Beta.

3 Results and discussion

3.1 Powder X-Ray diffraction (XRD) studies

The phase purity and crystal structure of the undoped and Eu^{3+}-doped $MgAl_2O_4$ nanophosphors prepared by nitrate–citrate gel combustion were analyzed using the powder X-ray diffraction data. The PXRD patterns of the $MgAl_2O_4{:}xEu^{3+}$ ($0 \leq x \leq 0.10$) powders are shown in Fig. 2a. All the observed diffraction peaks of the samples have been indexed to the pure cubic phase of $MgAl_2O_4$ of space group: $O^7{}_h$ (Fd-3 m) with the spinel-type structure which is well comparable with the standard pattern [JCPDS # 21-1152] [23]. No additional peaks were detected for the doped $MgAl_2O_4$ up to 10 mol% of Eu^{3+} doping level indicates that the Eu elements are homogeneously mixed and may be well doped into the $MgAl_2O_4$ lattice. The higher intensities of peaks of annealed samples with narrower width suggest a complete formation of highly crystallized the spinel structure. The average crystallite size of the Eu^{3+}-doped $MgAl_2O_4$ nanoparticles was calculated using the Scherrer formula:

$$D = \frac{K\lambda}{\beta(2\theta)\cos\theta}, \quad (1)$$

where λ is the wavelength of the incident X-rays (1.5406Å), θ is the diffraction angle, β(2θ) being the full width at half maximum (FWHM) of the observed diffraction peak in radians, K is 0.9, and D is the average diameter of the crystallite, respectively [22]. The prepared samples show several diffraction peaks have been indexed to (111), (220), (311), (400), (422), (511), (440), (531), (620), and (533) miller planes of high and moderate intensities as shown in Fig. 2a. The average crystalline size (D) of $MgAl_2O_4{:}xEu^{3+}$ was estimated from the X-ray line broadening and is reduced from 12.1 to 8.5 nm by the incorporation of

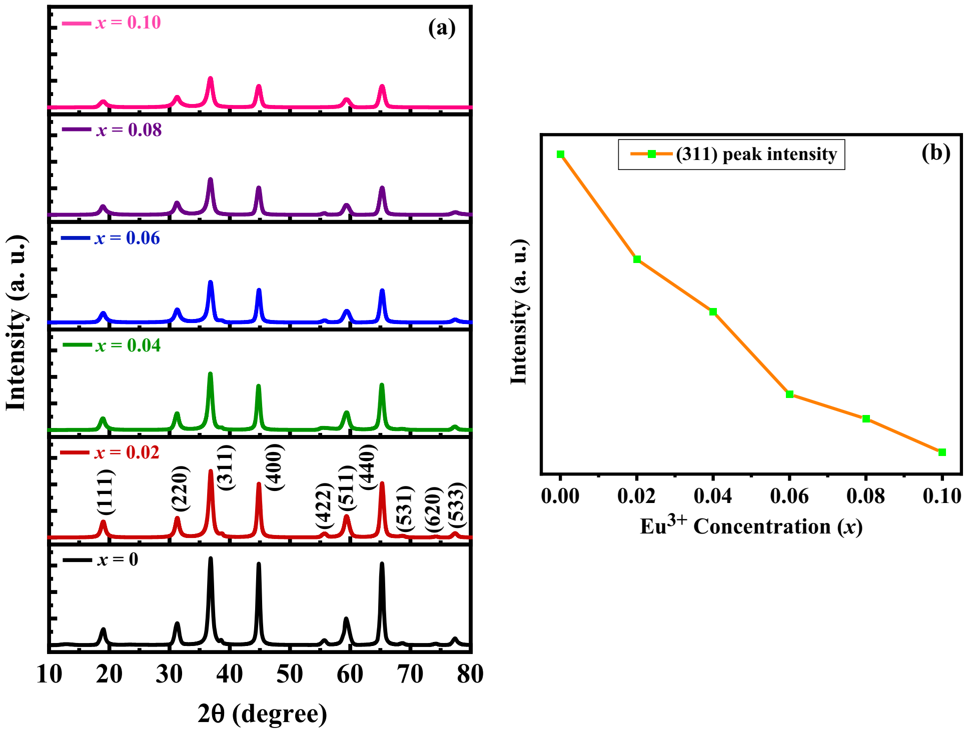

Fig. 2 **a** The powder XRD pattern of $MgAl_2O_4$:$x$$Eu^{3+}$ ($0 \le x \le 0.10$) series calcined at 950 °C for 12 h. **b** Variation of (311) peak intensity in the powder XRD pattern with Eu substitution

Eu^{3+} from 0.0 to 0.10 revealing the presence of nanosized particles in the grown phosphors. Figure 2b shows that the XRD peak intensities were slightly decreased with an increase of Eu^{3+} doping content, which indicates reduced crystallinity [27]. The reduced crystallinity is consistent with the decreased crystalline sizes of $MgAl_2O_4$:$x$$Eu^{3+}$ phosphors evaluated from the peak widths using Debye–Scherrer equation.

Figure 3 shows the variation of the microstructural parameters, the lattice constant (a), the crystallite size (D), dislocation density (δ), and microstrain (ε) with Eu^{3+} concentration. The overall increase in the dislocation density and microstrain with increasing Eu^{3+} content is attributed to either (i) due to the creation of some stresses and strains caused by the incorporation of Eu element into the $MgAl_2O_4$ crystal lattice or (ii) due to increased grain boundaries (Fig. 3b) [13]. Figure 3a shows the variation of the lattice parameter and the crystallite size (D) with the addition of Eu^{3+}. The lattice constant and crystallite size that relatively decreased with increasing Eu^{3+} doping concentration may be attributed to the lattice distortion caused by the difference in ionic radius between Eu^{3+} (1.07 Å) and Mg^{2+} (0.78Å) and it indicates that Eu^{3+} is successfully incorporated into host lattice and occupy Mg^{2+} tetrahedral sites. Figure 3d demonstrates the variation of unit cell volume of $MgAl_2O_4$:$x$$Eu^{3+}$ as a function of Eu^{3+} content.

The cation–anion bond lengths at octahedral and tetrahedral sites are denoted with d_{Al-O} and d_{Mg-O}, respectively. The bond distances of Mg–O and Al–O are defined as [28]

$$d_{Mg-o} = \sqrt{3}a(u - 1/4) \tag{2}$$

$$d_{Al-O} = a\sqrt{(u - 5/8)^2 + 2(u - 3/5)^2)}, \tag{3}$$

where a is the lattice parameter and u is the positional parameter of the oxygen atoms referred to the origin at -43 m in the space group of Fd-3 m. The bond lengths of Mg–O and Al–O decrease with increasing the Eu^{3+} doping concentration in an approximated linear fashion (Fig. 3c). The two bond lengths cross each other, with Al–O larger than Mg–O at concentrations lower than 6 mol% Eu^{3+} and vice versa [29, 30]. Close to this concentration, Al–O and Mg–O bond lengths become equal in the spinel structure.

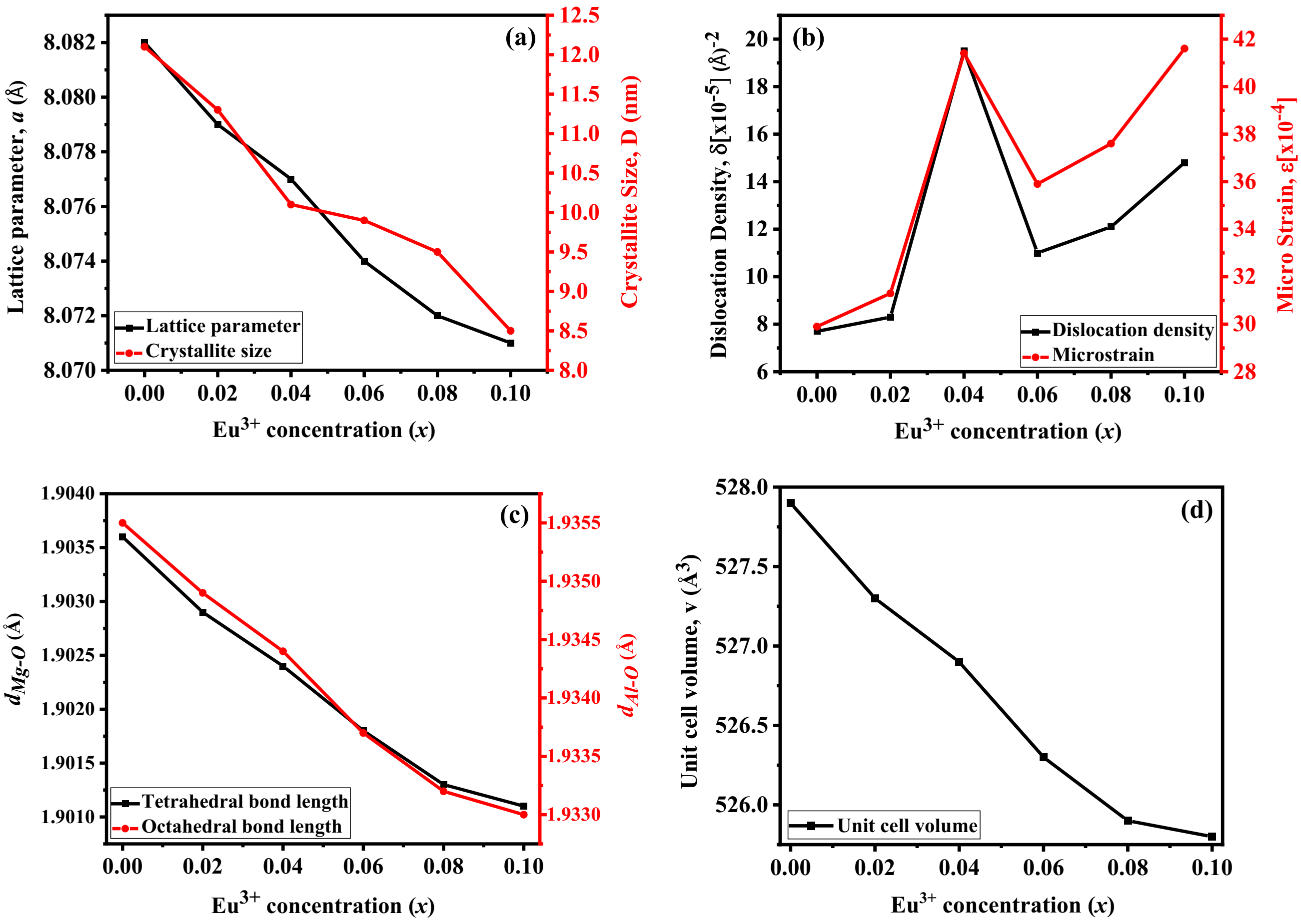

Fig. 3 Structural parameters variation of $MgAl_2O_4$:$x$$Eu^{3+}$ with Eu^{3+} doping concentration **a** Lattice parameter and Average crystallite size; **b** Dislocation density and Microstrain; **c** Bond lengths of Mg–O and Al–O; and **d** Avg. unit cell volume

3.2 Thermogravimetric analysis (TGA)

Decomposition of basic combustion-gel product was analyzed by plotting percentage weight against temperature (TGA curve), while the origins of exothermic/endothermic peaks were studied by DTA [31]. The stability/decomposition of $MgAl_2O_4$:10 mol% Eu^{3+} precursor compound have been done on Thermogravimetric analysis upto 950 °C in the presence of N_2 gas (Fig. 4). In the initial stage, the weight loss of 8.06 wt% below the temperature of 170 °C (peak at 102 °C) is due to the evaporation of physically adsorbed water. The second weight loss of 17.04 wt% occurs in the range of 180–325 °C with peak at 265 °C, due to the release of nitrogen and oxygen. Further, in the third stage, the weight loss of 20.45 wt% observed in the temperature range of 330-440°C (peak at 390 °C) can be attributed to the removal of CO_2 and residual organic moieties. A small peak at 480°C with a slight weight loss likely belongs to the incomplete crystallization [32]. From TGA–DTG results, no apparent weight loss occurs above 550–600°C. This indicates and confirms that the stable $MgAl_2O_4$ spinel phase is formed above 600 °C

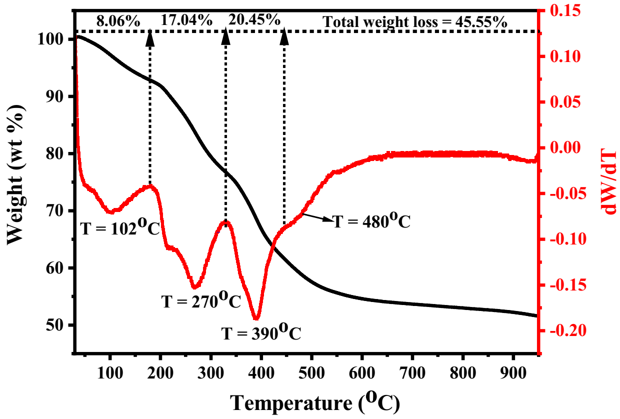

Fig. 4 TGA and DTG curves of dried citrate–nitrate gel product of $MgAl_2O_4$:$x$$Eu^{3+}$ (x = 0.10)

[33, 34]. Hence, the calcination temperature of the as-prepared sample was taken as 600°C or above.

3.3 Fourier transform infrared (FTIR) spectroscopic studies

Figure 5 shows the FTIR spectra recorded in the range 4000–500 cm^{-1} of $MgAl_2O_4$:xEu^{3+} powders. A strong broad band centered about 3465 cm^{-1} is associated with O–H stretching vibrations (symmetric & anti-symmetric) of molecular water adsorbed in the structure [24]. The characteristic band centered at 2345 cm^{-1} is corresponding to the atmospheric carbon dioxide (CO_2) absorption on metallic cations [35]. The peaks between 750 and 1200 cm^{-1} are due to O–H bending mode. Vibration bands present around 690 and 514 cm^{-1} are related to the inorganic network and their characteristic band peaks become much sharper with increasing doping concentration of Eu^{3+}. These peaks are attributed to the presence of AlO_6 groups and lattice vibration of Mg–O stretching. AlO_6 groups building up the $MgAl_2O_4$ phosphors, which is the only crystalline phase present as it was anticipated from the XRD studies of the calcined powders [16]. The vibration band at 1553 cm^{-1} can be assigned to H–O–H deformation bending mode. The absorption peak at 1382 cm^{-1} may be derived from the existence of nitrate [36]. The absorption peaks at 1170–980 cm^{-1} in the pure sample are assigned to the vibration of hydroxyl-metal (Mg or Al) bands [37, 38].

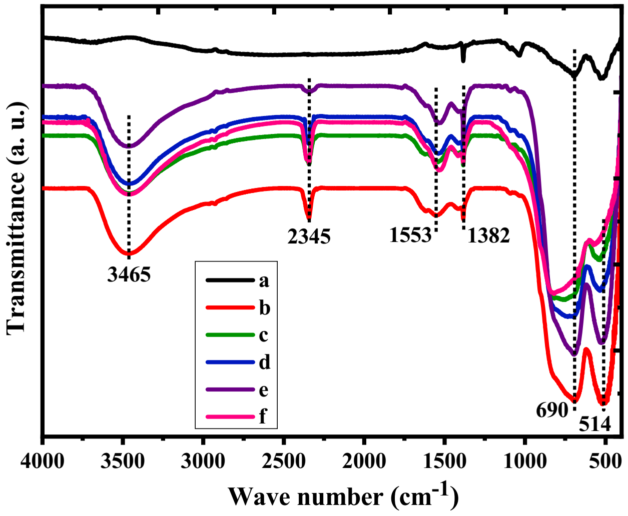

Fig. 5 Fourier transform infrared (FTIR) spectra of $MgAl_2O_4$:xEu^{3+} phosphors at 950°C for 12 h [**(a)** $x = 0.00$, **(b)** $x = 0.02$, **(c)** $x = 0.04$, **(d)** $x = 0.06$, **(e)** $x = 0.08$, and **(f)** $x = 0.10$]

The shape of the absorption bands does not change and their areas and intensities are reduced in Eu^{3+}-doped samples. FTIR spectra confirmed the formation of pure $MgAl_2O_4$ with no other secondary phase or additional impurities. The broad to weak band around 690 cm^{-1} is related to the vibration frequency of Al^{3+} in octahedral site of AlO_6^{3-} groups due to the microstructure changes by the substitution of Eu^{3+} into host lattice (Table 2).

3.4 UV–visible diffuse reflectance spectroscopy

The absorption characteristics of undoped and Eu^{3+}-doped $MgAl_2O_4$ phosphors have been studied using the UV–Vis absorption spectroscopy. Figure 6(a) represents the absorption spectra of $MgAl_2O_4$:xEu^{3+} ($0 \leq x \leq 0.10$) samples, which shows three absorption bands situated around 215, 250, and 370 nm. The absorption peak centered at 215 nm may be assigned to emerge from band-to-band absorption of the unsubstituted material [13]. The strong absorption bands located at 250 nm can be associated to originate from $O^{2-}(2p) \rightarrow Al^{3+}(3d)$ charge transfer due to the electron's excitations from the valence band to conduction band in the host crystal lattice. The absorption band around 370 nm in the doped samples is arising from the characteristic transition of Eu^{3+} ions [39, 40]. It can be clearly observed that the intensity of absorption peak at 250 nm is increased with increasing Eu^{3+} content. This is attributed to the fact that the Eu^{3+} changing the occupational site by replacing the Mg^{2+} instead of Al^{3+} in the host material [27]. Moreover, the peak centered at 250 nm is blue shifted in the absorption spectra with increasing Eu^{3+} doping concentration in Eu^{3+}-activated $MgAl_2O_4$ phosphors, which indicates the enhanced band gap (E_g) values of Eu^{3+}-doped $MgAl_2O_4$. The UV–Vis absorption studies indicate and suggest that the variation in Eu^{3+} doping content controls the Eu^{3+} occupational site (Mg^{2+} and Al^{3+}) in the host lattice and it also affects the absorption.

The band gap energies of pure and Eu^{3+}-doped $MgAl_2O_4$ nanoparticles were evaluated by well-known Tauc's relation:

$$\alpha h\nu = A\left(h\nu - E_g\right)^n, \tag{4}$$

where h is the Planck's constant, A is a constant, E_g is the band gap energy (in eV), α is the absorption

Table 2 FTIR peaks and their assignments of the Eu^{3+}-doped $MgAl_2O_4$.

Eu^{3+} Conc. (x)	Peak position of the assignment (cm^{-1})				
	AlO_6 group	Vibration mode of nitrate	H–O–H bending vibration	Absorption of atmospheric CO_2 on metallic cations	O–H stretching
0.00	513 693	1384	1524	–	3665
0.02	511 690	1385	1555	2343	3463
0.04	532 750	1385	1541	2345	3465
0.06	534 732	1385	1538	2347	3466
0.08	528 702	1384	1532	2346	3469
0.10	568 812	1384	1528	2351	3468

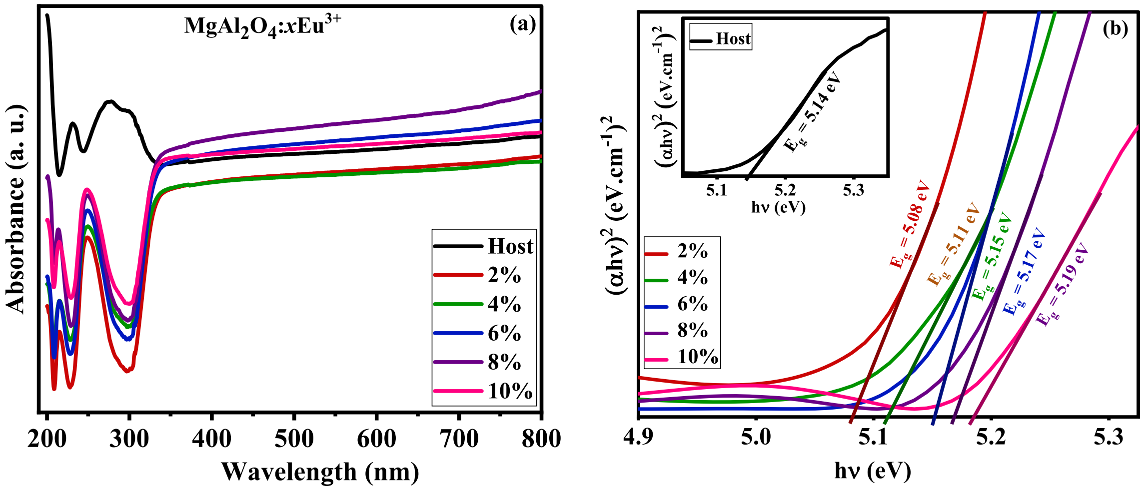

Fig. 6 **a** UV–Visible absorption spectra of $MgAl_2O_4{:}xEu^{3+}$ phosphors at 950°C for 12 h; and **b** Tauc's plots of $(\alpha h\nu)^2$ vs. hν of $MgAl_2O_4{:}xEu^{3+}$ phosphors with increase in Eu^{3+} concentrations (The inset shows Tauc's plot of Host material)

coefficient, ν is the incident photons frequency, and n equals to ½ for direct allowed transitions. The direct band gap E_g was estimated by extrapolating the linear fitted region to $[\alpha h\nu]^2 = 0$ in the tauc plot of $[\alpha h\nu]^2$ versus hν for absorption measurements, for $MgAl_2O_4$ as it is a direct band gap material. The band gap energy estimated from tauc's plot is 5.14 eV for pure $MgAl_2O_4$ and for Eu^{3+}-doped $MgAl_2O_4$, the E_g is increasing from 5.08 to 5.19 eV as shown in Fig. 6b [41, 42]. So, a quantum size effect is correlated for Eu^{3+}-doped $MgAl_2O_4$, where the band gap increases and crystallite size decreases with Eu^{3+} doping concentration. The absorption measurements suggest that varying the Eu^{3+} doping concentration regulates the band gap energy (Table 3).

Table 3 The band gap energy values of $MgAl_2O_4{:}xEu^{3+}$ nanophosphors calculated by Tauc's plot

S. No.	Concentration of Eu^{3+}	Direct band gap energy E_g (eV)	Average crystallite size (nm)
1	0.0	5.14	12.1
2	0.02	5.08	11.3
3	0.04	5.11	10.1
4	0.06	5.15	9.9
5	0.08	5.17	9.5
6	0.10	5.19	8.5

3.5 FESEM analysis

The structure and the particle morphology of the synthesized nanopowders have been analyzed by Field emission scanning electron microscopy (FESEM) images. The magnified FESEM micrographs of the pure, 2%, 6%, and 10% Eu^{3+}-substituted $MgAl_2O_4$ spinel phosphor nanoparticles are shown in Fig. 7(a–d). These images clearly show that most of the nanoparticles exhibited spherical shape with variable particle sizes. The average particle diameter of the as-prepared materials is expressed in mean size ± SD nm. The average sizes of pure, 2%, 6%, and 10% Eu^{3+}-doped $MgAl_2O_4$ NPs were estimated as 27 ± 4.1 nm, 25.9 ± 5.3 nm, 25 ± 3.8 nm, and 24.1 ± 3.3 nm, respectively (Fig. 8(a–d)). So, the estimated average particle size of the spherical like shaped particles decreases with increasing Eu^{3+} doping concentration [43]. It is also evidenced from the FESEM images that the incorporation of Eu^{3+} cations in $MgAl_2O_4$ lattice did not alter the particle morphology of the phosphor particles significantly. FESEM micrographs at higher magnification illustrate that the grains of the prepared samples are agglomerated with several nanoparticles, shown in Fig. 7(a–d). Further it has been observed that the as-synthesized samples demonstrate the porous nature, which is attributed to the evolution of various gases during the process of gel combustion at high temperatures [44, 45].

3.6 EDAX spectroscopy

The energy-dispersive X-ray spectroscopy (EDAX) and associated element ratios for pure and 10% Eu^{3+}-doped $MgAl_2O_4$ powders are presented in Fig. 9(a–b). Pure $MgAl_2O_4$ and $MgAl_2O_4$:10% Eu^{3+} phases are determined to have the weight ratio of Mg:Al:O = 4.73:17.63:77.65 and Eu:Mg:Al:O = 10.94:12.40:28.51:48.15, respectively. The EDAX data demonstrate that the atomic ratios of the elements are very close to their stoichiometric amounts [46]. The successful substitution of Eu^{3+} in $MgAl_2O_4$ crystals was also confirmed by EDAX analysis, as is shown in spectra (Fig. 9b). Figure 9(c) represents the histogram of $MgAl_2O_4$:xEu^{3+} samples in weight%. The possible peaks that are presented are associated to the above elements, while the extra peaks in the spectrum may be attributed to gold and carbon tape, which were added during coating for the EDAX spectroscopic analysis [43].

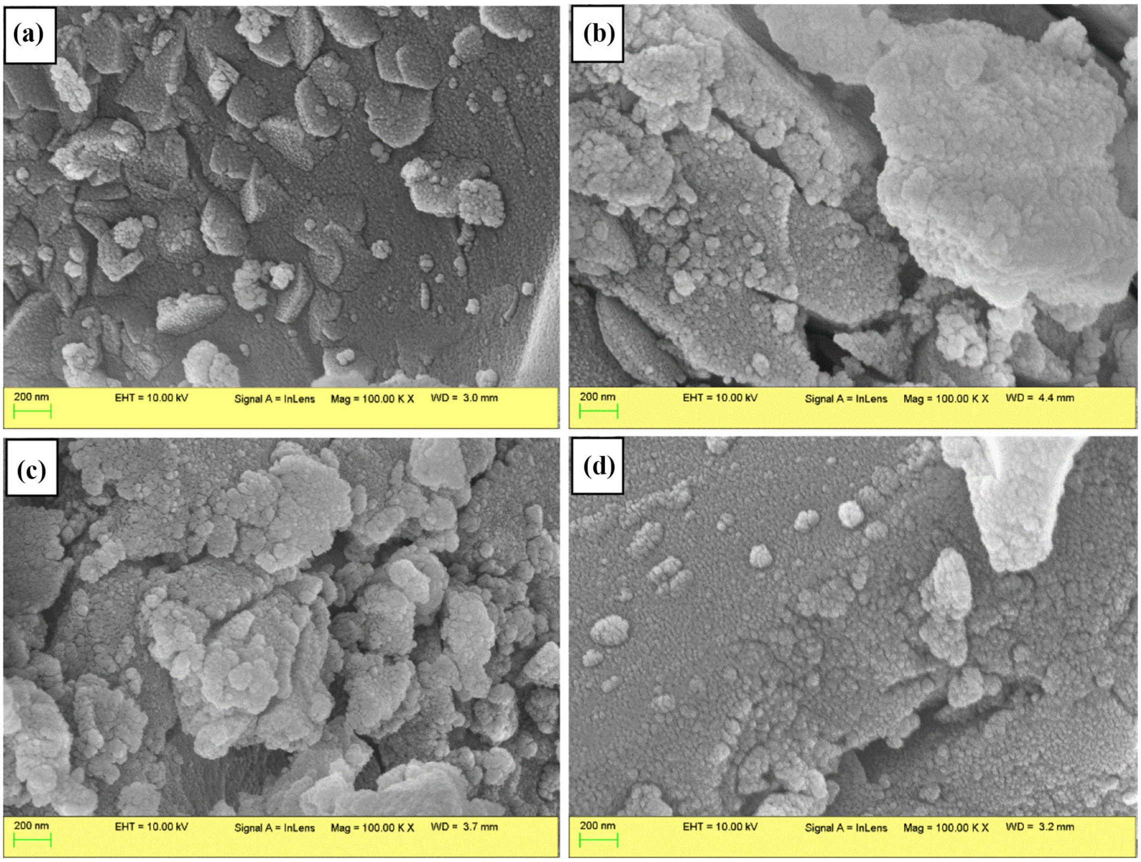

Fig. 7 FESEM images of prepared $MgAl_2O_4$:xEu^{3+} phosphors at different magnifications. **a** pure **b** $x = 0.02$ (c) $x = 0.06$ **d** $x = 0.10$

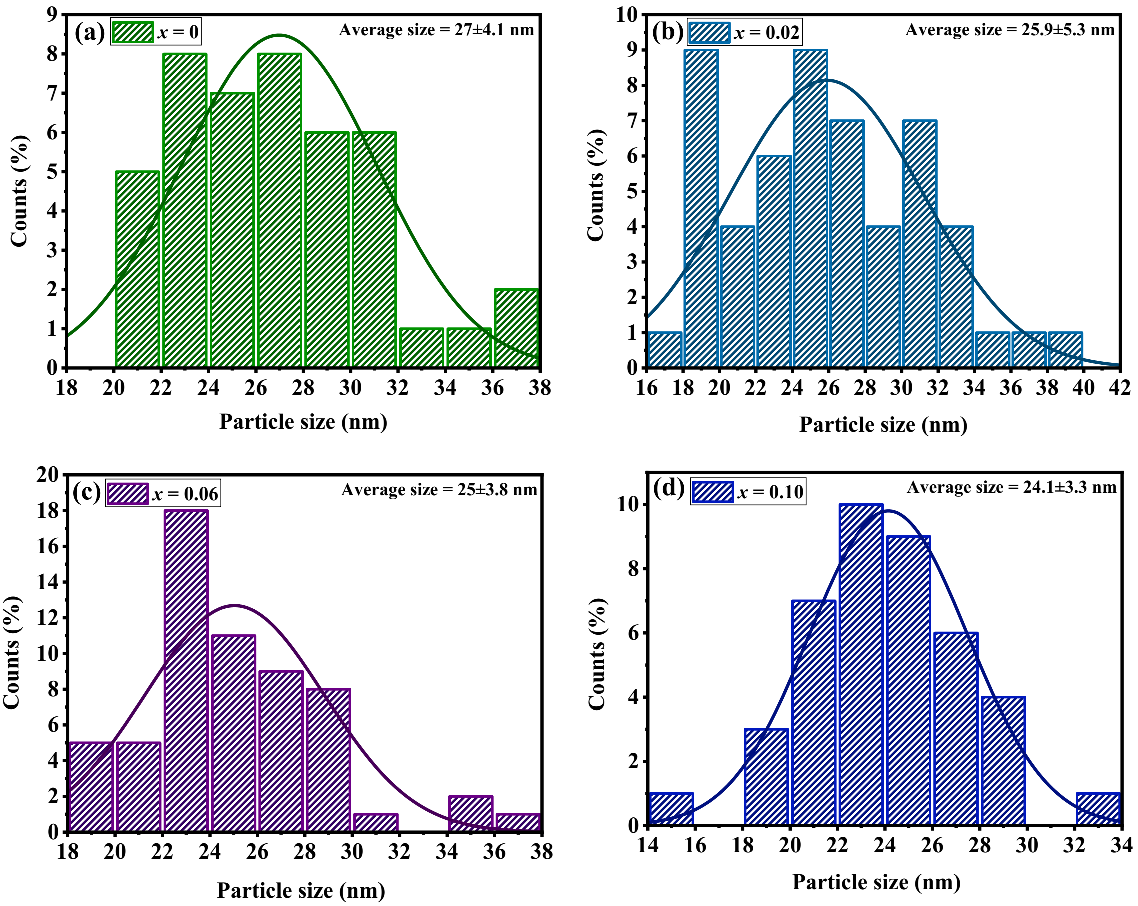

Fig. 8 Average particle size distribution histogram graph (FESEM) for pure and selected Eu^{3+}-doped $MgAl_2O_4$ samples

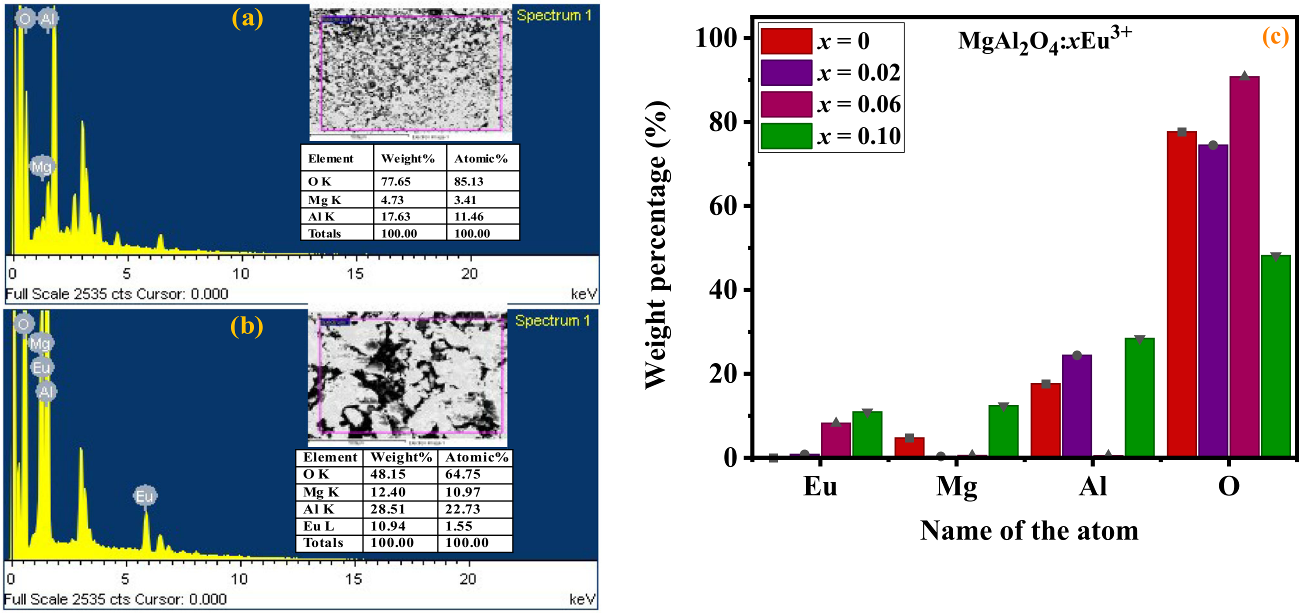

(a)

Element	Weight%	Atomic%
O K	77.65	85.13
Mg K	4.73	3.41
Al K	17.63	11.46
Totals	100.00	100.00

(b)

Element	Weight%	Atomic%
O K	48.15	64.75
Mg K	12.40	10.97
Al K	28.51	22.73
Eu L	10.94	1.55
Totals	100.00	100.00

Fig. 9 Elemental analysis of $MgAl_2O_4$:xEu^{3+} phosphors **a** pure; and **b** $x = 0.10$; respectively. **c** is the corresponding histogram representation in weight%

3.7 HRTEM with SAED analysis

The microstructure of the host and 10% Eu^{3+}-doped $MgAl_2O_4$ nanopowder samples were examined by HRTEM as shown in Fig. 10. HRTEM images in Fig. 10a, d demonstrate that the particles within the as-synthesized samples are composed of several nanosized crystallites of spherical shape and the average crystallite size is found to be 12.1 ± 2.4 nm, and 11.4 ± 2.8 nm for host and 10% Eu^{3+}-doped $MgAl_2O_4$ NPs, respectively (Fig. 11), in agreement to the XRD crystallite sizes presented in Fig. 3(a) [27]. The obtained rings in selected area electron diffraction (SAED) pattern of host and 10% Eu^{3+}-doped samples are illustrated in Fig. 10c, f, and have been indexed perfectly to highly crystalline pure cubic phase of the spinel structure, which agrees well with the XRD results [47]. The interplanar distance between the adjacent planes was estimated to be 4.63

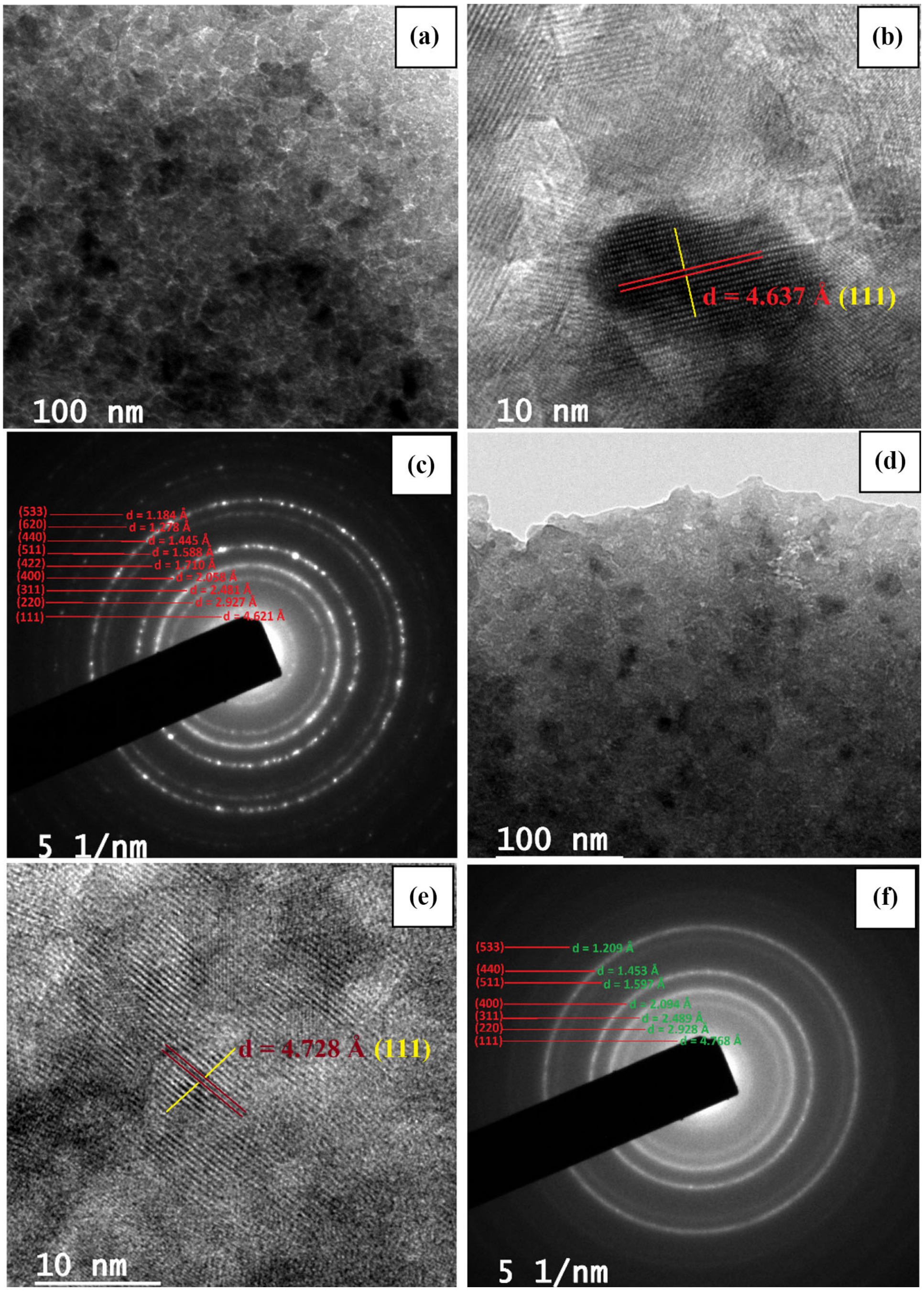

Fig. 10 TEM images of pure $MgAl_2O_4$ nanoparticles calcined at 950 °C for 12 h; **a** low-magnification TEM, **b** HRTEM, and **c** SAED spectrum and TEM images of $MgAl_2O_4$:10%Eu^{3+} nanoparticles calcined at 950 °C for 12 h; (**d**) low-magnification TEM, **e** HRTEM, and **f** SAED spectrum

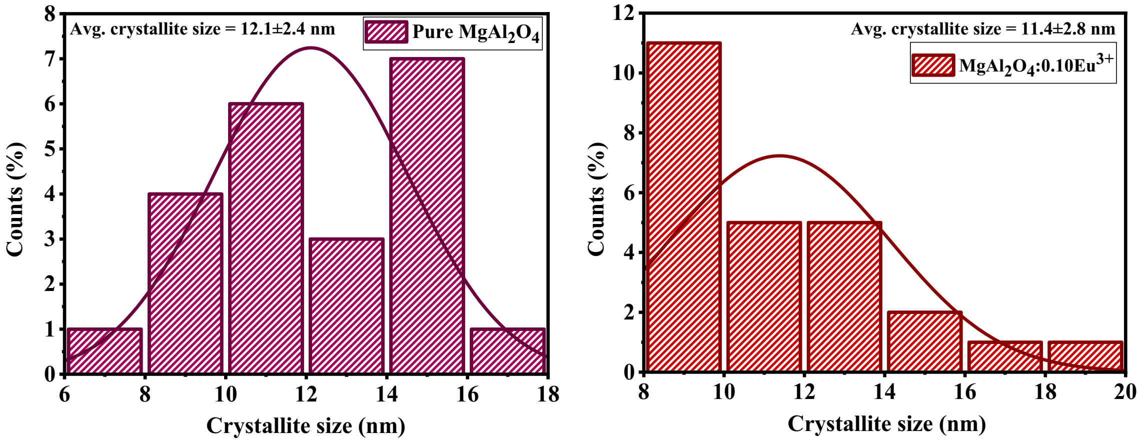

Fig. 11 Average crystallite size distribution histogram graph (HRTEM) for host and 10 mol% Eu^{3+}-doped $MgAl_2O_4$ samples

Å for undoped $MgAl_2O_4$ and 4.72 Å for $MgAl_2O_4$:10%Eu^{3+} from HRTEM images, which corresponds to (111) lattice plane (Fig. 10b, e).

3.8 Photoluminescence property studies

The photoluminescence emission spectrum of the $MgAl_2O_4$:$x$$Eu^{3+}$ nanophosphors annealed at 950 °C for 12 h, excited at 545 nm wavelength which exhibits four distinguishable peaks in the region of 580–740 nm is shown in Fig. 13a. These peaks are assigned to $^5D_0 \rightarrow {}^7F_J$ (J = 1, 2, 3, and 4) emission transitions, indicating the presence of Eu^{3+} ions in the $MgAl_2O_4$ host matrix and are named as $^5D_0 \rightarrow {}^7F_1$, $^5D_0 \rightarrow {}^7F_2$, $^5D_0 \rightarrow {}^7F_3$, and $^5D_0 \rightarrow {}^7F_4$ are observed around 590, 612, 654, and 703 nm, respectively [48]. From Fig. 13a, the hypersensitive $^5D_0 \rightarrow {}^7F_2$ ($\Delta J = 2$) transition peak centered around 612 nm is the most intense for all the samples of Eu^{3+} ion arising due to the shielding effect of 4f electrons by 5s and 5p electrons in the outermost shells of the europium ion [25]. It is obvious that the $^5D_0 \rightarrow {}^7F_1$ lines correspond to a magnetic dipole transition which will not change the crystal field strength around the Eu^{3+} ions and is independent of the symmetry. However, the $^5D_0 \rightarrow {}^7F_2$ lines that correspond to forced electric dipole transitions are hypersensitive and its emission intensity is highly dependent on site occupied by Eu^{3+} ions in the host lattice [49]. If the host matrix like $MgAl_2O_4$ is without inversion symmetry, the strong emission due to electrical dipole transition corresponding to 612 nm peak will appear and dominate in intensity when Eu^{3+} ions occupy noninversion symmetric Mg^{2+} sites of host lattice [50]. It is evident that the relative peak intensity of the emission spectra of Eu^{3+}-doped $MgAl_2O_4$ nanophosphor depends on the concentration of Eu^{3+} (Fig. 13a). The transition $^5D_0 \rightarrow {}^7F_2$ (612 nm) red emission intensity is much stronger than that of the $^5D_0 \rightarrow {}^7F_1$ (590 nm) orange emission. The energy level diagram of Eu^{3+} ion in $MgAl_2O_4$ is shown in Fig. 12.

In pure $MgAl_2O_4$, an energy band gap is created between the valence band (formed by O^{2-}) and the conduction band (formed by Mg^{2+} and Al^{3+}). The excitation process may take place in two ways, either by transferring the valence band electrons to the charge transfer band (CTB) or by jumping to the higher levels of Eu^{3+}. Under the excitation at 545 nm, the Eu^{3+} ions are excited from the ground state of $^7F_0$ to higher excited state [51]. After excitation, the excited Eu^{3+} ions (due to charge transfer) come to the $^5D_0$ state by nonradiative process. This process continues till $^5D_0$ energy level gets populated. Then the $^5D_0$ level is responsible for the fluorescence and it can make 4 transitions to the lower energy levels [27]. These four transitions correspond to four peaks in the PL emission spectra at 590 nm, 612 nm, 654 nm, and 703 nm. From Fig. 13(a), by increasing the Eu^{3+} content, the emission intensity of $^5D_0 \rightarrow {}^7F_2$ transition first reached to a maximum value at x = 0.04 from x = 0.02 and then decreased with an increase of Eu^{3+} concentration (x = 0.06, x = 0.08, and x = 0.10) due to a concentration quenching [25]. The phenomena of concentration quenching are ascribed due to energy transfer between (i) Eu^{3+} to Eu^{3+}, (ii) defect to Eu^{3+}, and (iii) Multiphonon-assisted electron–phonon

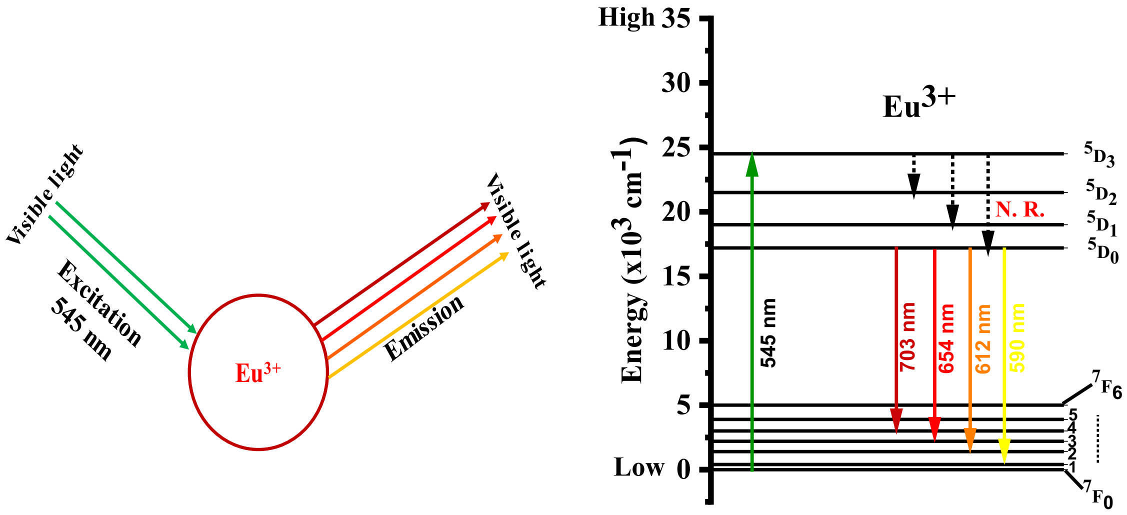

Fig. 12 Energy level diagram of Eu^{3+} ion in $MgAl_2O_4$:$x$$Eu^{3+}$ Phosphor

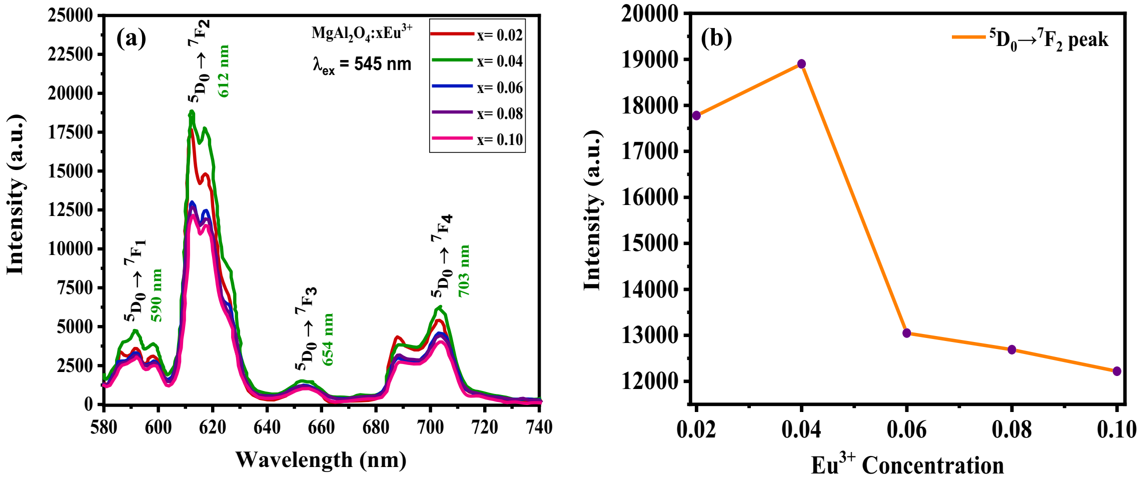

Fig. 13 **a** Room-temperature PL emission spectra of $MgAl_2O_4$:$x$$Eu^{3+}$ series; **b** PL emission intensity variation of $^5D_0 \rightarrow {}^7F_2$ in $MgAl_2O_4$:$x$$Eu^{3+}$ as a function of Eu^{3+} doping concentration

coupling. Hence, the dependence of luminescence intensity on the doping concentration of Eu^{3+} was studied and in $MgAl_2O_4$ the optimum content of Eu^{3+} was evaluated. This concentration dependence of emission intensity for the forced electric dipole transition of $^5D_0$–$^7F_2$ at 612 nm is shown in Fig. 13(b). The type of energy transfer between the neighboring Eu^{3+} ions and the nature of quenching process can be identified by evaluating the relative or critical distance. According to Blasse's formula, the critical distance (R_c) can be expressed as

$$R_c = 2\left[\frac{3V}{(4\pi C_o N)}\right]^{(1/3)}, \tag{5}$$

where N is the number of host cations in the unit cell of the host matrix, C_o is the concentration of the activator Eu^{3+} ions, and V is the volume of the unit cell. For optimum concentration of C_o = 0.04, the measured R_c value between Eu^{3+} and Eu^{3+} is 10.2 Å, which is greater than the standard value of 5 Å for the rare-earth ions indicating that the type of interaction mechanism involved in the energy transfer is via a multipole–multipole interaction process and is the major cause of concentration quenching. Moreover, the variation of relative or critical distance between the Eu^{3+} ions in $MgAl_2O_4$:$x$$Eu^{3+}$ phosphor with the Eu^{3+} doping concentration is shown in Fig. 14. It can be observed that the relative distance

(R_c) is decreased gradually with increasing Eu^{3+} doping concentration [52].

The similar results of microstructure, morphology, and photoluminescence of $MgAl_2O_4:Eu^{3+}$ red-emitting phosphors have been reported by C. Wenisch et al. [49]. Moreover, the PL emission results show that the Eu^{3+} ion was observed to be an isolated luminescence center and presented an intense red emission at 612 nm assigned to the $^5D_0 \rightarrow {}^7F_2$ transition with maximum intensity in $MgAl_2O_4:xEu^{3+}$ phosphors. The optimum Eu^{3+} doping concentration was obtained to be 4% for the best luminescence process, eventually $MgAl_2O_4$:4%Eu^{3+} was chosen for the temperature-dependent PL emission study. Several researchers reported the optimum Eu^{3+} concentration in the range of 1 to 2 mol%. Also, the annealing process plays an important role in the successful substitution of Eu^{3+} ions into the $MgAl_2O_4$ host matrix and consequently influences its luminescent properties. So, the temperature-dependent PL analysis for $MgAl_2O_4$ with optimum doping concentration of Eu^{3+} were studied. The PL emission spectrum of 4% Eu^{3+}-doped $MgAl_2O_4$ sample annealed progressively at 650, 750, 850, and 950°C for 12 h recorded in the wavelength range from 580 to 740 nm excited at 545 nm is shown in Fig. 15a. It exhibits four $^5D_0 \rightarrow {}^7F_1$, $^5D_0 \rightarrow {}^7F_2$, $^5D_0 \rightarrow {}^7F_3$, and $^5D_0 \rightarrow {}^7F_4$ transitions arising from the Eu^{3+} ion with the $^5D_0 \rightarrow {}^7F_2$ dominant transition. From Fig. 15a of PL spectra, it is evident that the relative intensities of all the transitions were increased with increasing temperature for $MgAl_2O_4$:4%Eu^{3+} sample. This is due to the fact that the Eu^{3+} ions can be transferred more rapidly and successfully into the $MgAl_2O_4$ host lattice during thermal diffusion process as homogeneous purity phase. If the phosphor is thermally heated, the divalent europium ion oxidizes to Eu^{3+} state as the temperature increased and thereby creating more luminescent centers on the surface. Moreover, the energy transfer to the Eu^{3+} emission centers from the host turns into more significant as the material is treated at higher temperatures. The presence $^5D_0 \rightarrow {}^7F_2$ transition as more intense peak assigned to 612 nm of Eu^{3+} ions indicates that there will be no center of symmetry around Eu^{3+} ion in $MgAl_2O_4$ sample heated at 950°C when recorded under excitation at 545 nm [53]. Temperature dependence of the photoluminescence intensity of the forced electric dipole transition $^5D_0 - {}^7F_2$ of $MgAl_2O_4:xEu^{3+}$ at optimum concentration (x = 4%Eu^{3+}) was analyzed and confirmed at excitation wavelength 545 nm (Fig. 15b).

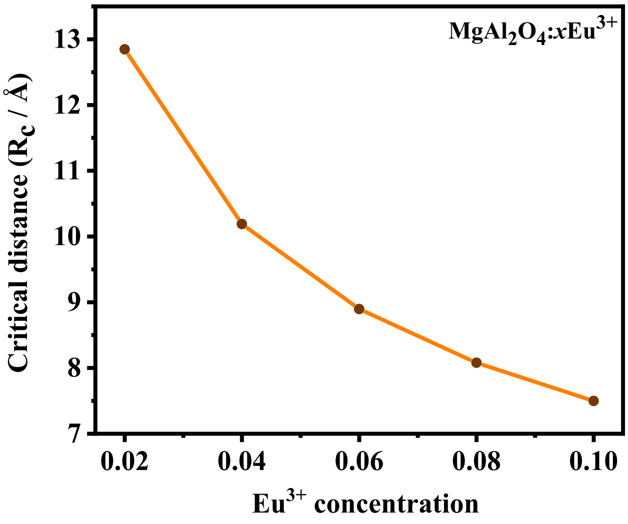

Fig. 14 The variation of critical distance with Eu^{3+} doping concentration of $MgAl_2O_4:xEu^{3+}$ nanophosphor

3.9 CIE diagram

Figure 16 shows the Commission International de I'Eclairage (CIE) 1931 chromaticity diagram of $MgAl_2O_4:xEu^{3+}$ nanophosphors calcined at 950 °C for 12 h. The perception of the color purity will be analyzed from the CIE chromaticity diagram with the help of emission color coordinates of the luminescent material. The CIE chromaticity color coordinates of the nanophosphors samples can be estimated by using three numbers (X, Y, Z) known as tristimulus colorimetry system from the emission spectra under the excitation at 545 nm wavelength [54]. The (x, y) color coordinates were evaluated based on emission spectra and found to lie in red region of CIE diagram (Fig. 16). Correlated color temperature (CCT) is another important parameter to assess the nanophosphor performance, which specifies the color appearance of light emitted was derived by CIE color coordinates [40, 55]. CCT is calculated by transforming the (x, y) coordinates of the light source to (u', v'). The CIE chromatic coordinates, CCT, (x, y) and color rendering index (CRI) of Eu^{3+}-doped $MgAl_2O_4$ samples are illustrated in Table 4.

On doping with Eu^{3+}, as there is no obvious change observed in the spectral profile of the CIE diagram, the color coordinates demonstrate that the

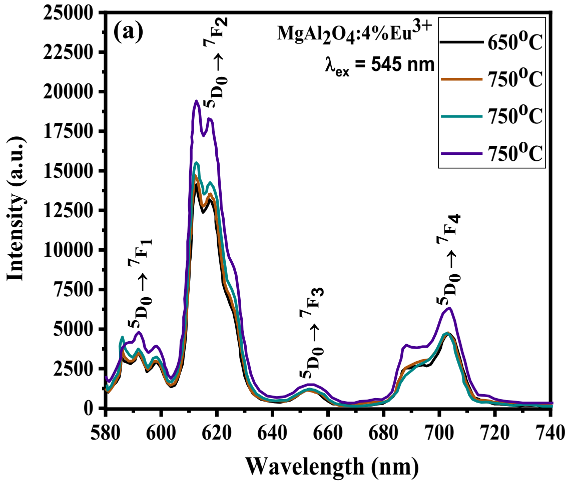

Fig. 15 **a** PL Emission spectra of $MgAl_2O_4$:4%Eu^{3+} phosphors; **b** PL emission intensity variation of $^5D_0 \rightarrow {}^7F_2$ in $MgAl_2O_4$:4%Eu^{3+} as a function of annealing temperature

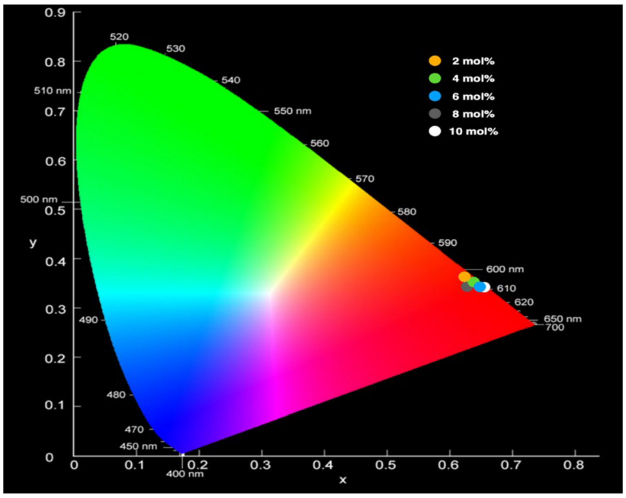

Fig. 16 CIE Chromaticity color coordinates diagram from emission spectra excited at 545 nm of $MgAl_2O_4$:xEu^{3+} nanophosphors calcined at 950 °C for 12 h

as-prepared $MgAl_2O_4$:xEu^{3+} nanophosphors emit intense bright red light (Fig. 16). The CIE diagram of 4% Eu^{3+}-doped $MgAl_2O_4$ at 950 °C presents CIE color coordinates of $x = 0.6582$ and $y = 0.3415$ showing the maximum intensity which are in good agreement with National Television System Committee (NTSC) red color coordinates (0.67, 0.33). This color tunability of the host lattice by changing the concentration of Eu^{3+} (2–10 mol%) is attributed to the possible energy transfer between the energy levels of activator (Eu^{3+}) ions. The calculated CCT values were found to be 2553.588–2618.01 K (< 5000 K), which is regarded as a cool red light. Thus, the observed high PL brightness along with excellent CCT value indicates that these phosphors can be highly useful in red LEDs for the production of artificial in red light and in solid-state display as well as other optical device applications [35, 56].

Table 4 CIE chromaticity color coordinates of Eu^{3+}-doped $MgAl_2O_4$ nanophosphors calcined at 950°C for 12 h

Sample	Concentration (mol %)	Color coordinates		u'	v'	CCT (K)	CRI
		x	y				
$MgAl_2O_4$:xEu^{3+}	2	0.6592	0.3405	0.4570	0.5313	2609.364	22
	4	0.6582	0.3415	0.4552	0.5316	2568.382	24
	6	0.6579	0.3419	0.4540	0.5316	2553.588	24
	8	0.6590	0.3401	0.4574	0.5311	2618.01	23
	10	0.6579	0.3411	0.4556	0.5314	2575.439	24

4 Conclusions

In summary, synthesis of undoped and Eu^{3+}-doped $MgAl_2O_4$ red-emitting nanophosphors with different Eu^{3+} doping concentrations have been achieved by the nitrate–citrate gel combustion route, which is a simple and cost-effective chemical process. The powder XRD pattern shows that Eu^{3+} is successfully doped in the host crystal lattice. The average crystallite size of nanophosphors decreased from 12.1 to 8.5 nm with increasing Eu^{3+} doping content. The TGA combined with DTG results showed that single-phase $MgAl_2O_4$:$x$$Eu^{3+}$ spinel begins to form at around 600 °C. Vibration bands of the as-prepared samples corresponding to the presence of AlO_6 groups in FTIR spectra are related to the inorganic network. The band gap energy of the host and Eu^{3+}-doped phosphors was estimated from the UV–Vis spectra using Tauc's plot and is found to vary between 5.08 and 5.19 eV due to ionic exchange, indicating that E_g depends on Eu^{3+} content. The charge transfer $O^{2-} \rightarrow Al^{3+}$ transition as a result of the excitation of electrons into the conduction band of $MgAl_2O_4$ largely influence the absorption band at 250 nm. The FESEM studies showed the relatively spherical morphology of the agglomerated nanoparticles with average particle size ~ 30 nm and successful substitution of Eu^{3+} in $MgAl_2O_4$ host lattice, which was also confirmed by EDAX analysis. The HRTEM images demonstrated that the obtained $MgAl_2O_4$:$x$$Eu^{3+}$ powders are in nanometer dimensions with average crystallite size 11.4 ± 2.8–12.1 ± 2.4 nm. The hypersensitive $^5D_0 \rightarrow {}^7F_2$ ($\Delta J = 2$) transition at 612 nm is attributed to the well-known red emission Eu^{3+} electric dipole transition (EDT) and is most intense. The process of quantum quenching is observed in $MgAl_2O_4$:$x$$Eu^{3+}$ and the optimum value of doping concentration is obtained to be 4 mol% Eu^{3+} from the emission spectra. Moreover, the improved photoluminescence intensity of $MgAl_2O_4$:4%Eu^{3+} sample at progressively high temperatures has also been characterized. The as-prepared $MgAl_2O_4$:$x$$Eu^{3+}$ phosphor material shows bright red emission along with good CCT values, which make it useful as an important phosphor for red emission LED applications.

Acknowledgements

The authors express their sincere thanks to the DST-FIST Central Instrumentation Laboratory, Government College Autonomous, Rajahmundry, Andhra Pradesh and SSCU, IISc, Bengaluru for providing lab and instrumentation facilities for the preparation of Luminescent Nanomaterials.

Authors contribution

RRK: Conceptualization, Methodology, and Supervision; BNR, EBS, and DSLP: Experimentation and Writing—Original draft preparation; PTR: Visualization and data Investigation; KS: Writing—Reviewing and Editing.

Data availability

The authors are ready to provide any research data, which have been mentioned in the manuscript on request.

Declarations

Conflict of interest There are no conflicts of interest.

References

1. R.C. Ropp, *Luminescence and the Solid State*, 2nd edn. (Elsevier, Amsterdam, 2004)
2. D. Levy, A. Pavese, M. Hanfland, Am. Mineral 88, 93 (2003)
3. B.P. Uberuaga, D. Bacorisen, R. Smith, J.A. Ball, R.W. Grimes, A.F. Voter, K.E. Sickafus, Phys. Rev. B 75, 104116 (2007)
4. S.K. Mohan, R. Sarkar, Mater. Design 110, 145 (2016)
5. F.Y. Cui, A. Kundu, A. Krause, M.P. Harmer, R.P. Vinci, Acta Mater 148, 320 (2018)
6. N. Habibi, Y. Wang, H. Arandiyan, M. Rezaei, Adv. Powder Technol. 28, 1249 (2017)
7. R. Nakhowong, S. Kiennork, P. Wongwanwattana, T. Seetawan, R. Chueachot, Mater. Lett. 220, 234 (2018)
8. S. Sinhamahapatra, M. Shamim, H.S. Tripathi, A. Ghosh, K. Dana, Ceram. Int. 42, 9204 (2016)
9. O. Shpotyuk, A. Ingram, H. Klym, M. Vakiv, I. Hadzaman, J. Filipecki, J. Eur. Ceram. Soc. 25, 2981 (2005)
10. J. Jeon, Y. Kang, J.H. Park, Y. Chung, Ceram. Int. 43, 15074 (2017)
11. F. Li, Y. Zhao, Y. Liu, Y. Hao, R. Liu, D. Zhao, Chem. Eng. J. 173, 750 (2011)
12. G. Gusmano, G. Montesperelli, E. Traversa, G. Mattogno, J Am. Ceramic Soc. 76, 743 (1993)

13. C. Dlamini, M.R. Mhlongo, L.F. Koao, T.E. Motaung, T.T. Hlatshwayo, S.V. Motloung, Appl. Phys. A 126, 75 (2020)
14. T. Sato, M. Shirai, K. Tanaka, Y. Kawabe, E. Hanamura, J. Lumin 114, 155 (2005)
15. P.J. Dereń, K. Maleszka-Bagińska, P. Głuchowski, M.A. Małecka, J. Alloys Compd. 525, 39 (2012)
16. I. Omkaram, S. Buddhudu, Opt. Mater. 32, 8 (2009)
17. Q. Sai, C. Xia, H. Rao, X. Xu, G. Zhou, P. Xu, J. Lumin. 131, 2359 (2011)
18. V. Singh, V. Kumar Rai, S. Watanabe, T.K. Gundu Rao, L. Badie, I. Ledoux-Rak, Y.-D. Jho, Appl. Phys. B 108, 437 (2012)
19. A. Jouini, H. Sato, A. Yoshikawa, T. Fukuda, G. Boulon, K. Kato, E. Hanamura, J. Cryst. Growth 287, 313 (2006)
20. V. Singh, G. Sivaramaiah, J.L. Rao, S.H. Kim, J. Lumin. 143, 162 (2013)
21. J. Qiao, Z. Xia, J. Appl. Phys. 129, 200903 (2021)
22. I. Omkaram, G. Seeta Rama, Raju, S. Buddhudu, J. Phys. Chem. Solids 69, 2066 (2008)
23. A.S. Maia, R. Stefani, C.A. Kodaira, M.C.F.C. Felinto, E.E.S. Teotonio, H.F. Brito, Opt. Mater. 31, 440 (2008)
24. W. Nantharak, W. Wattanathana, W. Klysubun, T. Rimpongpisarn, C. Veranitisagul, N. Koonsaeng, A. Laobuthee, J. Alloys Compd. 701, 1019 (2017)
25. I. Omkaram, B. Vengala Rao, S. Buddhudu, J. Alloys Compd. 474, 565 (2009)
26. R. Djenadic, M. Botros, H. Hahn, Solid State Ionics 287, 71 (2016)
27. V. Maphiri, B. Dejene, T. Motaung, T. Hlatshwayo, O. Ndwandwe, S. Motloung, Nanomater Nanotechnol 8, 184798041880064 (2018)
28. T. Yamanaka, Y. Takéuchi, Z. Für Kristallographie - Crystalline Mater. 165, 65 (1983)
29. U.D. Wdowik, K. Parliński, A. Siegel, J. Phys. Chem. Solids 67, 1477 (2006)
30. G.B. Andreozzi, F. Princivalle, H. Skogby, A. Della Giusta, Am. Min. 85, 1164 (2000)
31. S. Sanjabi, A. Obeydavi, J. Alloys Compd. 645, 535 (2015)
32. S.K. Behera, P. Barpanda, S.K. Pratihar, S. Bhattacharyya, Mater. Lett. 58, 1451 (2004)
33. S. Tripathy, D.S. Saini, D. Bhattacharya, J. Asian. Ceam. Soc. 4, 149 (2016)
34. M.F. Zawrah, H. Hamaad, S. Meky, Ceram. Int. 33, 969 (2007)
35. C. Pratapkumar, S.C. Prashantha, H. Nagabhushana, D.M. Jnaneshwara, J. Science: Adv. Mater. Devices 3, 464 (2018)
36. C. Luan, D. Yuan, X. Duan, H. Sun, G. Zhang, S. Guo, Z. Sun, D. Pan, X. Shi, Z. Li, J. Sol-Gel Sci. Technol. 38, 245 (2006)
37. A.K. Adak, S.K. Saha, P. Pramanik, J. Mater. Sci. Lett. 16, 234 (1997)
38. Y.-J. Lin, C.-J. Wu, Surf. Coat. Technol. 88, 239 (1997)
39. S.V. Motloung, B.F. Dejene, R.E. Kroon, O.M. Ntwaeaborwa, H.C. Swart, T.E. Motaung, Optik 131, 705 (2017)
40. P. Du, J.S. Yu, Sci. Rep. 7, 11953 (2017)
41. A. Ali, I.H. Gul, M.Z. Khan, F. Javaid, J. Korean Ceram. Soc. (2022)
42. M. Dongol, M.M. El-Nahass, A. El-Denglawey, A.F. Elhady, A.A. Abuelwafa, Curr. Appl. Phys. 12, 1178 (2012)
43. A. Mazhar, A.H. Khoja, A.K. Azad, F. Mushtaq, S.R. Naqvi, S. Shakir, M. Hassan, R. Liaquat, M. Anwar, Energies 14, 3347 (2021)
44. P. Pathak, R. Kurchania, Phys. B: Condens. Matter. 545, 119 (2018)
45. S. Gul, M.A. Yousuf, A. Anwar, M.F. Warsi, P.O. Agboola, I. Shakir, M. Shahid, Ceram. Int. 46, 14195 (2020)
46. B.V. Naveen Kumar, K. Venkata Rao, E. Basha Shaik, Y. Nirmal Rajeev, K. Ramachandra Rao, S. Cole, Luminescence 37, 1942 (2022)
47. M.G. Brik, J. Papan, D.J. Jovanović, M.D. Dramićanin, J. Lumin. 177, 145 (2016)
48. I.V. Beketov, A.I. Medvedev, O.M. Samatov, A.V. Spirina, K.I. Shabanova, J. Alloys Compd. 586, S472 (2014)
49. C. Wenisch, H.-D. Kurland, J. Grabow, F.A. Müller, J. Am. Ceram. Soc. 99, 2561 (2016)
50. S. Saha, S. Das, U.K. Ghorai, N. Mazumder, B.K. Gupta, K.K. Chattopadhyay, Dalton Trans. 42, 12965 (2013)
51. J. Wu, J. Wang, J. Lin, Y. Xiao, G. Yue, M. Huang, Z. Lan, Y. Huang, L. Fan, S. Yin, T. Sato, Sci. Rep. 3, 2058 (2013)
52. W. Ran, H.M. Noh, S.H. Park, B.K. Moon, J.H. Jeong, J.H. Kim, J. Shi, Sci. Rep. 8, 5936 (2018)
53. S.V. Motloung, B.F. Dejene, O.M. Ntwaeaborwa, H.C. Swart, R.E. Kroon, Chem. Phys. 487, 75 (2017)
54. T. Samuel, Ch.S. Kamal, K. Sujatha, V. Veeraiah, Y. Ramakrishana, K.R. Rao, Optik 127, 10575 (2016)
55. C. Pratapkumar, S.C. Prashantha, H. Nagabhushana, M.R. Anilkumar, C.R. Ravikumar, H.P. Nagaswarupa, D.M. Jnaneshwara, J. Alloys Compd. 728, 1124 (2017)
56. E.B. Shaik, B.V.N. Kumar, S.K. Chirauri, K.R. Rao, J. Mater. Sci: Mater. Electron. 33, 105 (2022)

Materials Chemistry and Physics 308 (2023) 128174

Contents lists available at ScienceDirect

Materials Chemistry and Physics

journal homepage: www.elsevier.com/locate/matchemphys

Exploring the optical and biological aspects of sodium- doped CuO nanoparticles

B. Nageswara Rao [a,b,c], P. Tirupathi Rao [a], Sk.Esub Basha [a], D.S.L. Prasanna [d,f], K. Samatha [b], R.K. Ramachandra [a,e,*]

[a] *Crystal Growth and Nano-Science Research Center, Department of Physics, Government College (A), Rajamahendravaram, 533105, Andhra Pradesh, India*
[b] *Department of Physics, Andhra University, Visakhapatnam, 530003, Andhra Pradesh, India*
[c] *Department of Physics, Dr V S Krishna Government Degree College (A), Visakhapatnam, India*
[d] *Department of Chemistry, Acharya Nagarjuna University, Guntur, 522510, Andhra Pradesh, India*
[e] *Government Degree College, Chodavaram, Visakhapatnam, 531036, Andhra Pradesh, India*
[f] *Department of Chemistry, Dr V S Krishna Government Degree College (A), Visakhapatnam, India*

HIGHLIGHTS

- Undoped and Na-doped CuO nano-powders were synthesized by coprecipitation method.
- XRD, FESEM and HRTEM were used to analyse the structural properties and surface morphology of the nano-powders.
- The influence of Na doping on the optical parameters of the nano-powders was investigated.
- The antibacterial activity of the nano-powders was tested against Gram-negative and Gram-positive bacteria.
- The highest antifungal activity was achieved against Candida albicans.

ARTICLE INFO

Keywords:
Copper oxide
Sodium-doping
Co-precipitation
Antibacterial activity
Antifungal activity

ABSTRACT

In this article, we present a novel coprecipitation technique for synthesizing pure and sodium-doped CuO ($Cu_{1-x}Na_xO$) nano powders with different sodium concentrations (x = 0, 0.01, 0.02, 0.04, 0.06, 0.08, and 0.10). The structural properties of the samples were analysed using powder X-ray diffraction (PXRD), which revealed an average crystallite size of 12.48–10.50 nm. The bonding nature of the $Cu_{1-x}Na_xO$ samples was described by Fourier transform infrared (FTIR) spectroscopy. The UV–Visible spectroscopic analysis showed a band gap energy of 1.240–1.456 eV and a refractive index that decreased with an increase in Na doping concentration. Field emission scanning electron microscopy images revealed the spherical, flower-shaped, and flake-like morphologies of the nanoparticles, which had sizes ranging from 42.45 ± 5.49–33.98 ± 4.32 nm. Energy-dispersive X-ray spectroscopy and elemental mapping were used to confirm the purity of the samples and the presence of Cu, O, and Na elements in the $Cu_{1-x}Na_xO$ samples. High-resolution transmission electron microscopy photomicrographs confirmed that the samples were polycrystalline and the nanoparticles exhibited nucleation with lattice spacing, as shown by selected-area electron diffraction patterns. Furthermore, the $Cu_{1-x}Na_xO$ nano powders exhibited efficient antibacterial and antifungal activities. The antibacterial activity was tested against major bacterial strains, and the highest inhibition zones were observed to be 13.67 ± 1.11 mm ($x = 0.06$), 10.67 ± 0.94 mm ($x = 0.10$), 15 ± 1.11 mm ($x = 0.10$), and 9.25 ± 0.25 mm ($x = 0.06$) for *P. aeruginosa*, *B. subtilis*, *S. aureus*, and *K. pneumonia*, respectively. In addition, the antifungal activity of the Na-doped CuO nano powders was found to be enhanced against polymorphic fungus *C. albicans* and filamentous fungus *A. niger* with dopant concentration. These results suggest that Na-doped CuO NPs have potential applications in formulating new antifungal drugs and treating various life-threatening bacterial infections.

---

* Corresponding author. Crystal Growth and Nano-Science Research Center, Department of Physics, Government College (A), Rajamahendravaram, Andhra Pradesh, 533105, India.

E-mail addresses: drkrcr@gmail.com, ramc@gcrjy.ac.in (R.K. Ramachandra).

https://doi.org/10.1016/j.matchemphys.2023.128174
Received 12 April 2023; Received in revised form 13 June 2023; Accepted 9 July 2023

1. Introduction

In the recent past the research on nanomaterials has drastically increased due to various features such as their unique chemical and physical properties [1]. Nanostructures are having dimensions in the nanoscale range and possess excellent efficiency towards bio-medicinal activity of various pathogens because of their high chemical steadiness, small particle size, and large surface to volume (S/V) ratio.

Particularly metal oxide nanoparticles (NPs) have gained sufficient interest due to their wide range of applications in solar cells, sunscreens, gas censors, cosmetics, oxygen pumps, diesel fuels, and bottle coatings to block ultraviolet radiation [2–4]. Copper oxide (CuO) nanoparticles are among one of the most extensively attracted transition metal oxides because of their biomedical, antimicrobial, anticancer, antioxidant, and biocide applications [5,6]. CuO is a p-type semiconductor with optical band gap of 1.2 eV having unique photocatalytic, photovoltaic, magnetic, and electrical properties [7]. These nanoparticles have been used for different applications such as lithium-ion batteries, near-infrared filters, super-capacitors, catalysis, spintronics, magnetic storage media, and nanofluids [8,9].

The fabricated CuO nanoparticles as reported in the literature have different morphologies, such as needle-like, cauliflower-like, shuttle-like, microspheres, rhombic crystal strips, ellipsoidal, sinter-like, rice-like, rod- like [10–14] etc.

Further, the substitution of metal ions into CuO may affect the electrical, magnetic, and optical properties due to the modification of its electronic structure. Several researchers have reported the fabrication of successful doping or co-doping with transition/rare earth metals including Co [15], Tb [16], Mg, Zn, Ce [17], Ag [18], Ni [19], Fe [20], Mn [21], Mn/Co [22], La/Ni [23], and Fe/Co [24]. S. Janet Priscilla et al. reported the synthesis and characterization of sodium doped CuO NPs [25] and in another study, Hafsa Siddiqui et al. has reported the structural, optical, and electrical properties of Na-doped CuO nanostructures [26], but still found limited research reported on Na-doped CuO nanoparticles. Interestingly, sodium, an alkali metal, plays an excellent role in the growth process of various metal oxide nanoparticles and observed the improved results in different application [27]. However, the detailed scientific investigation is still incomplete on optical, catalytic, structural, biological, and antimicrobial characterization of sodium-incorporated CuO NPs. Therefore, we reported in this work, the successful incorporate of sodium ions into CuO crystal lattice and rigorously studied the optical, structural, catalytic, morphological, antibacterial, and antifungal properties.

Pure and doped CuO nanostructures have been prepared by various chemical and physical methods available such as sol–gel route [28], Sonochemical technique [29,30], hydrothermal [31], electrodeposition process [32], precipitation-pyrolysis method [33], ball-milling [34], microwave irradiation method [35], colloidal thermal [36], solid-state reaction technique [37], chemical vapor deposition [38], co-precipitation process [39], and thermal decomposition method [40], etc. Facile co-precipitation route is most accessible and one of the simplest methods for preparing the metal oxide (MO) nanoparticles [39]. The co-precipitation method is advantageous over others as this process allows us to obtain desired nanomaterials with high degree of crystallinity, excellent homogeneity of nucleation, high purity, small size with definite morphology, and possibility to create homogenous precipitation and it requires minimal energy, lower reaction time and moderate temperature.

The sensitivity towards antimicrobial activity have become significant problem in healthcare and biomedical areas due to increasing various alarming pandemics attack these days. The treatment of these bacterial diseases and fungal infections have been studied using nanotechnology as a potential alternative to the present traditional antibiotics, which have certain restrictions associated to toxicity and exposure time [41,42]. The nanotechnology proposes appropriate solution to overcome such problems with the use of various nanomaterials that have a broad spectrum of size distributions, high surface to volume ratio, elemental compositions, surface charges, biocompatibility, greater surface to volume ratio, morphologies, and unique surface modification properties [43,44]. Specifically, doped metal oxide nanoparticles with tunable physicochemical properties and biological features such as superior antibacterial, and antifungal potentials, were attractive to be used as efficient antimicrobial tools to eradicate microbial infections [45–47]. However, still there is need to overcome a series of challenges with respect to better understanding of toxicity, process quality, biodistribution, and long-term effect of chemically synthesized nanomaterials to achieve accurate clinical translation.

In present study, an attempt has been made to prepare undoped and sodium doped CuO ($Cu_{1\text{-}x}Na_xO$) nano-powders by co-precipitation method. The synthesized nano-size powders were characterized by using PXRD, FTIR, UV–Visible, FESEM, EDS, HRTEM and SAED analyses. In addition, the obtained samples were screened for antibacterial activity studies by employing Gram(-ve) bacterial cultures *Pseudomonas aeruginosa*, *Klebsiella pneumoniae*, and Gram(+ve) bacteria *Bacillus subtilis*, *Staphylococcus aureus* using Disc diffusion method. Furthermore, the antifungal activities of $Cu_{1\text{-}x}Na_xO$ nano-powders were evaluated against two fungal species *Aspergillus niger* and *Candida albicans*.

2. Experimental section

2.1. Chemicals used

Copper(II) sulfate pentahydrate ($CuSO_4·5H_2O$) (≥98.00%), Deionized water (≥99.58%), Sodium Hydroxide Pellets (NaOH) (≥97.00%), and *Sodium acetate anhydrous LR* (CH_3COONa) (≥99.00%) were used. All the materials are used without further purification. The materials used for the synthesis were listed in Table 1.

2.2. Synthesis of $Cu_{1\text{-}x}Na_xO$ nano-powders

The pure copper oxide (CuO) nano-powders have been prepared by using the simplest facile co-precipitation approach. In the process, Copper(II) sulfate pentahydrate and *sodium acetate were used as* starting materials. For the synthesis of pure CuO, 24.96 g of $CuSO_4·5H_2O$ is dissolved in 100 ml of distilled water and continuously stirred it for 1 h. Similarly, 4 g of NaOH pellet is dissolved using 100 ml of distilled water in a separate glass beaker and constantly stirred for 1 h. Thereafter, the NaOH solution is slowly added dropwise to $CuSO_4·5H_2O$ solution at constant stirring rate for 3 h at 65 °C and as a result, precipitate solution was formed. This black precipitate solution is then centrifuged and washed many times repeatedly with ethanol and distilled water until the pH equals to 7. The solid precipitate precursor was dried at 90 °C in a hot air oven for 12 h and grinded using piston mortar. Subsequently, the dried samples are annealed at 450 °C in a muffle furnace at a heating rate of 2 °C/min for 3 h to obtain nano-sized pure CuO powders. The procedure involved in this approach is as follows:

Table 1
List of chemicals used with their purity and source used for synthesis of Na^+ doped CuO ($Cu_{1\text{-}x}Na_xO$) powders.

Precursor	Chemical formula	Molecular Weight (g/mol)	Purity (%)	Source
Copper(II) sulfate pentahydrate	$CuSO_4·5H_2O$	249.68	98.0–102.0	Merck Specialities Private Limited
Sodium acetate anhydrous LR	CH_3COONa	82.03	99.0	Molychem
Sodium Hydroxide Pellets	NaOH	40.00	97.0	Qualigens

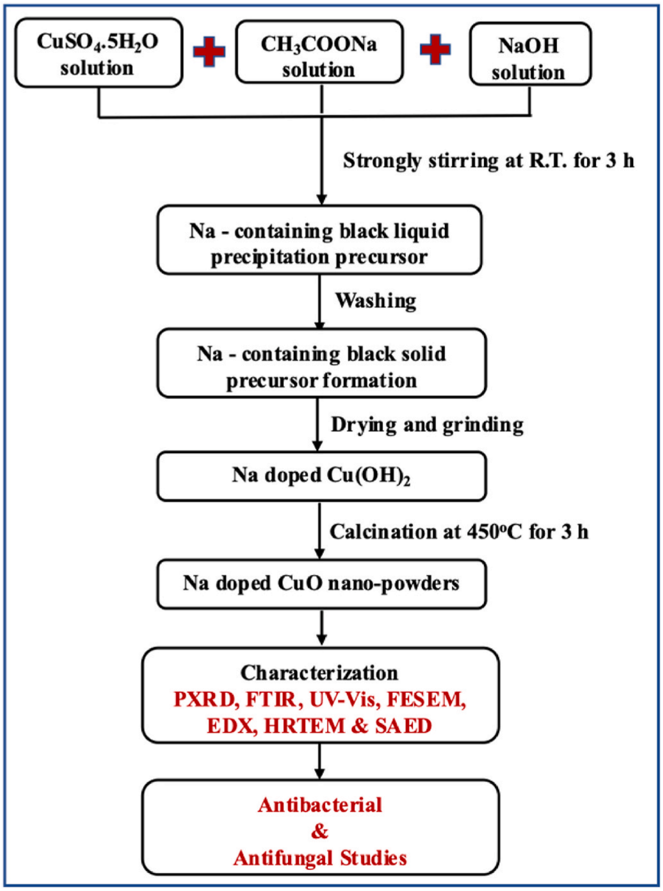

Fig. 1. The flow chart of sodium doped Copper oxide ($Cu_{1-x}Na_xO$) nano-powders synthesized by the Co-precipitation method.

$$CuSO_4 + 2NaOH \rightarrow Cu(OH)_2 + Na_2SO_4\ (aq) \tag{1}$$

$$Cu(OH)_2 \rightarrow \text{Sintering} \rightarrow \text{Pure } CuO + H_2O \tag{2}$$

For the synthesis of sodium doped copper(II) oxide nano-powders ($Cu_{1-x}Na_xO$), the stoichiometric aliquots of solutions of $CuSO_4 \cdot 5H_2O$, *Sodium acetate (CH3COONa)* and NaOH have been prepared in individual glass beakers and utilized as starting precursor solutions. For $Cu_{1-x}Na_xO$ ($x = 0$, 0.01, 0.02, 0.04, 0.06, 0.08 and 0.10), the same preparation procedure was followed as shown in Fig. 1. *CH3COONa* solution was adjoined completely into the $CuSO_4 \cdot 5H_2O$ solution by maintaining constant magnetic stirring at 65 °C for 3 h followed by the slow drop-wise addition of NaOH solution, resulted in the formation of homogeneous bluish mixture solution. The bluish coloured solution is then changed to a dark greenish coloured solution. This mixture solution has now undergone centrifuging and cleansing several times with ethanol and deionized water (1:1). Thereafter, the solid precursor was dehydrated at 90 °C in a vacuum oven for almost 12 h to eliminate moisture. Succeeding, the dehydrated sample was kept in a muffle furnace at 450 °C for 3 h to get a black coloured sodium doped CuO nano-powders and the obtained products kept for further characterizations.

2.3. Characterization

The powder X-ray Diffraction (PXRD) analysis was performed by PANalytical X'Pert PRO powder X-ray diffractometer using Cu Kα radiation in 20° to 80° range at normal temperature. The Fourier Transform Infra-Red (FT-IR) analysis was carried by using Thermo Nicolet 380 FTIR spectrophotometer in the wavenumber range of 4000 cm^{-1} – 500 cm^{-1}. The UV–Visible absorption analysis was executed in the wavelength range of 200–800 nm by UV-DRS-spectrophotometer, Thermofisher Evaluation 220. With the help of Field Emission Scanning Electron Microscope ΣIGMA™ FESEM (CARL ZEISS NTS Ltd), the field emission scanning electron microscopy (FESEM) analysis was studied. Energy Dispersive X-ray Spectrometer Quantax 200 with X Flash® 6130 performed the Energy Dispersive X-ray Spectroscopy and elemental mapping studies. The High-Resolution Transmission Electron Microscopy (HRTEM) study was performed by JEOL-2100+ High-Resolution Transmission Electron Microscope.

2.4. Antimicrobial activity test

Copper oxide nanoparticles (CuO-NPs) exhibit the strong antimicrobial activity against selective bacteria and fungi and they can be used as dynamic anti-bacterial agents as well as promising antifungal agents due to their high surface morphology [48]. The antimicrobial activity studies of the pure and Na doped CuO (1, 2, 4, 6, 8 & 10%) nano-powders were performed against four bacterial strains and two

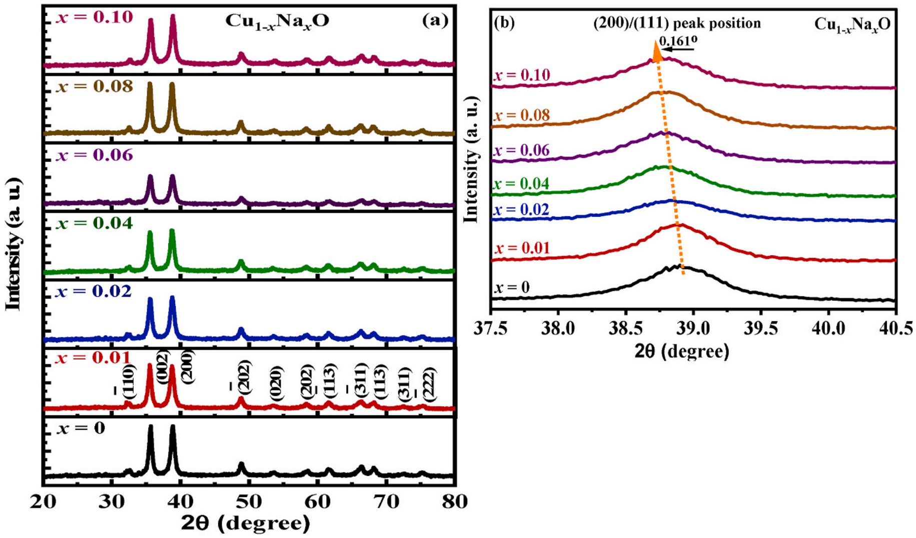

Fig. 2. (a) Comparison of powder x-ray diffraction (XRD) patterns of $Cu_{1-x}Na_xO$ samples calcined at 450 °C for 3 h; and **(b)** Shift of the (200)/(111) peak towards the low diffraction angle.

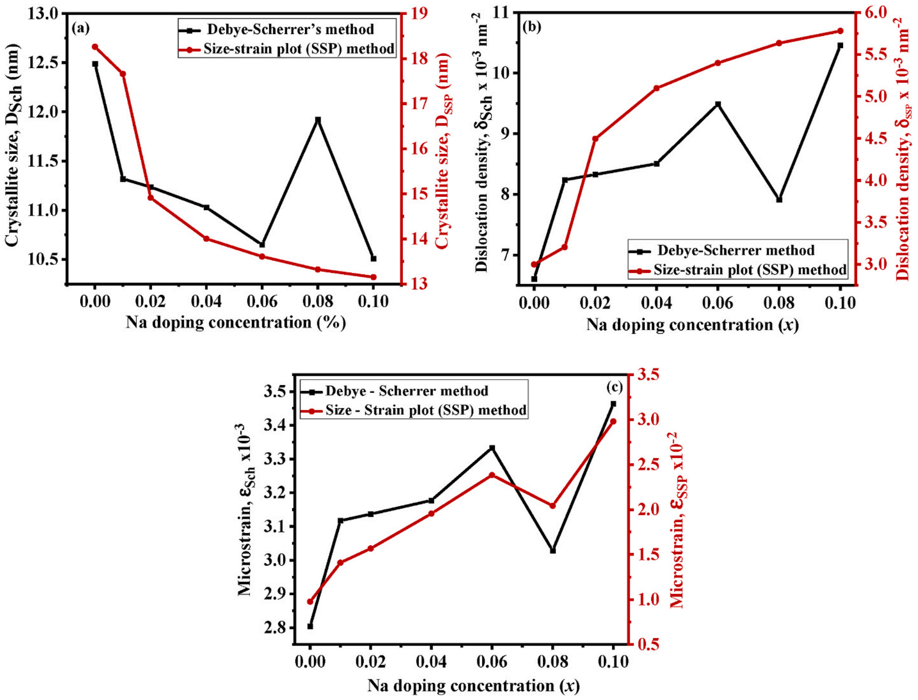

Fig. 3. Comparison **(a)** crystallite size between average Debye-Scherrer's (D_{Sch}) and Size-Strain plot (SSP) method (D_{SSP}), **(b)** dislocation density between average Debye-Scherrer's ($\delta_{avg.}$) and Size-Strain plot (SSP) method (δ_{SSP}), and **(c)** lattice strain among average Debye-Scherrer's (ε_{Sch}) and Size-Strain plot (SSP) method (ε_{SSP}) of $Cu_{1-x}Na_xO$ nano-powders.

Table 2

The average values of crystallite size (D), dislocation density (δ), lattice strain (ε), X-ray density ($\rho_{x\text{-}ray}$), unit cell volume (v), and crystallite volume (V) of $Cu_{1-x}Na_xO$ nano-powders, calculated according to Scherrer method.

Na^+ content (x)	D (nm)	$\delta x10^{-3}$ (nm^{-2})	ε x 10^{-3}	$\rho_{x\text{-}ray}$ (g/cm^3)	v (Å^3)	V (nm^3)
0	12.4874	6.6059	2.8040	6.5535	80.6210	1947.2390
0.01	11.3187	8.2367	3.1172	6.4915	80.9765	1450.0828
0.02	11.2367	8.3287	3.1371	6.4655	80.8848	1418.8004
0.04	11.0286	8.5061	3.1775	6.3819	81.1002	1341.3926
0.06	10.6491	9.4876	3.3332	6.3343	80.8591	1207.6443
0.08	11.9222	7.9139	3.0284	6.2283	81.3704	1694.6173
0.10	10.5095	10.4578	3.4639	6.2091	80.7544	1160.7713

Table 3

The calculated values of monoclinic unit cell parameters (a, b, c, and β) of $Cu_{1-x}Na_xO$ samples.

Na^+ content (x)	Lattice constants			Inter-axial angles		
	a (Å)	b (Å)	c (Å)	α (deg.)	γ (deg.)	β (deg.)
0	4.6922	3.4167	5.1025	90	90	99.432
0.01	4.7044	3.4207	5.1167	90	90	99.445
0.02	4.7048	3.4178	5.1121	90	90	99.562
0.04	4.7033	3.4204	5.1148	90	90	99.443
0.06	4.6969	3.4145	5.1072	90	90	99.419
0.08	4.7081	3.4265	5.1160	90	90	99.515
0.10	4.6925	3.4102	5.1004	90	90	99.512

fungal pathogens. The regular bacterial strains of *Pseudomonas aeruginosa* (Gram negative, MTCC ID - 424), *Staphylococcus aureus* (Gram positive, MTCC ID - 1430), *Klebsiella pneumoniae* (Gram negative, MTCC ID - 39), and *Bacillus subtilis* (Gram positive, MTCC ID - 441); while *Aspergillus niger* (MTCC ID - 281) and *Candida albicans* (MTCC ID - 183) fungi species were selected for this study. These bacterial and fungal strains were procured from the Microbial Type Culture Collection and Gene Bank (MTCC), Council of Scientific and Industrial Research (CSIR) - Institute of Microbial Technology (IMTECH), Sector – 39A, Chandigarh – 160036, India. The antimicrobial activities of $Cu_{1-x}Na_xO$ samples were employed by the well-established Kirby–Bauer disk diffusion technique on potato dextrose agar media (for fungal strains) and nutrient agar media (for bacterial strains) and disc plates [49].

The disk diffusion test by the Kirby–Bauer process [50] was screened to evaluate the observed antimicrobial activities of sodium-doped CuO nanopowders. The potato dextrose agar (PDA) media and nutrient agar media used for the antifungal and antibacterial activities were sterilized by the application of autoclave at 15 lbs pressure and 121 °C temperature for 15–20 min. To solidify the molten agar, the agar solution is poured into sterile circular glass Petri dishes. Then various fungi and bacteria were cultured separately 24 h in a broth and selected fungal and bacterial strains were uniformly introduced on a solidified dextrose agar media and nutrient agar in a glass Petri plates, respectively. Simultaneously, the Whatman filter paper disks of about 6 mm were individually coated with Na-doped CuO at the graded concentrations of 0 mg/ml, 10 mg/ml, 20 mg/ml, and 30 mg/ml and carefully introduced on the culture. Moreover, the 0 mg/ml concentration was considered to be the control in the experiment. The plates with bacterial cultures were kept for incubation at 37 °C for 24 h and the agar plates having fungal strains were kept for incubation at 24 °C for 48 h, respectively [51]. All the antimicrobial applications were performed in a sterile laminar flow cabinet. The obvious inhibition zones observed around the well were measured, which shows the antimicrobial activity.

When Na^+ ions are incorporated into the CuO host, with an increase in doping concentration of Na^+, the antimicrobial activity of Na-doped CuO NPs will be studied against selected pathogenic microorganisms including bacteria, and fungi in terms of zone of inhibition [8]. The zone of inhibition (ZoI) is the circular area observed around the antibiotic NPs on the disc where the microorganisms are unable to grow. The average value of zone of inhibition of as-prepared samples is measured using a ruler and is expressed as mean value ± SD in millimetres [10].

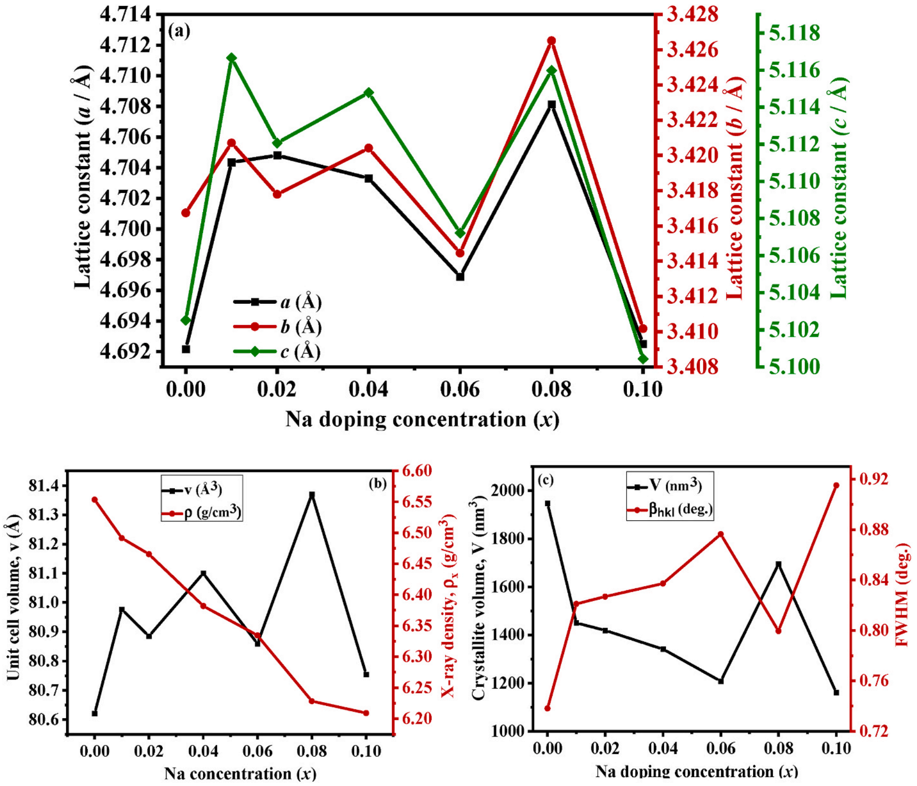

Fig. 4. The variation of **(a)** lattice parameters (*a*, *b*, and *c*); **(b)** unit cell volume and x-ray density; and **(c)** average FWHM and average crystallite volume of $Cu_{1-x}Na_xO$ nano-powders with Na doping concentration (*x*).

Table 4
The Bragg's angle (2θ), FWHM (β_{hkl}), Crystallite size (D) and inter-planar distance (d) of $Cu_{1-x}Na_xO$ (x = 0–0.10) for (200) diffraction peak.

Na^+ Content (*x*)	Bragg's angle (2θ) (deg.)	FWHM β_{hkl} (deg.)	D (nm)	Inter planar distance (d) (Å)
0	38.920	0.655	12.8643	2.3122
0.01	38.901	0.7052	11.9471	2.3133
0.02	38.876	0.7228	11.6548	2.3147
0.04	38.821	0.6982	12.0643	2.3178
0.06	38.811	0.7403	11.3769	2.3184
0.08	38.768	0.6877	12.2470	2.3209
0.10	38.759	0.7357	11.4464	2.3214

3. Results and discussion

3.1. Powder X-ray diffraction (XRD) analysis

The XRD pattern of the $Cu_{1-x}Na_xO$ (0, 1, 2, 4, 6, 8, 10 mol% Na) powders calcined in an air atmosphere at 450 °C for 3 h are shown in Fig. 2(a). All the reflection peaks in the XRD pattern matched well with JCPDS card number 45-0937 of bulk CuO, with lattice parameters of a = 4.6837 Å, b = 3.4226 Å, c = 5.1288 Å and β (angle) = 99.5400° and space group C 2/c. The diffraction peaks of $Cu_{0.99}Na_{0.01}O$ sample found at 32.41^O, 35.54^O, 38.77^O, 48.82^O, 53.53^O, 58.33^O, 61.59^O, 66.23^O, 68.10^O, 72.51^O, and 75.23^O obtained for the (−110), (002), (200), (−202), (020), (202), (−113), (−311), (113), (311) and (−222) planes correspond to a monoclinic symmetry structure. There are no extra peaks relating to secondary phase were obtained for $Cu_{1-x}Na_xO$ samples, indicating that the sodium ions are successfully substituted into the lattice site of Cu^{2+} without altering the CuO crystal structure. According to the XRD pattern, all the synthesized $Cu_{1-x}Na_xO$ samples were polycrystalline in nature. Also, the observed XRD intensity of the diffraction peaks decreases continuously up to $x = 0.06$, then strongly increased and is maximum at $x = 0.08$ for Na doped CuO with increasing Na doping concentration. This intensity variation may be attributed to the reduction in crystallinity of $Cu_{1-x}Na_xO$ [22]. The effect of sodium concentration on the mean crystallite size (D) of the ordered crystalline domains was estimated using the Debye-Scherrer formula [16]:

$$D = \frac{K\lambda}{\beta_{hkl}\cos\theta} \tag{3}$$

in which, K is shape factor constant (equal to 0.9), β_{hkl} is the peak width at FWHM (in radian), λ is the X-ray wavelength for Cu-target K_α radiation (1.5406 Å), and θ is the Bragg diffraction angle obtained from the 2θ value.

As shown in Fig. 3(a), the mean crystallite size was decreased with an increase in the doping concentration of Na into CuO matrix except at $x = 0.08$, where the sodium atoms have trapped in the nonequilibrium position from the equilibrium position. This reduction in crystallite size demonstrates the decreasing crystallinity of $Cu_{1-x}Na_xO$ samples and can be attributed to the lattice distortion of CuO due to the incorporation of Na.

In addition, micro-structural parameters, such as the dislocation density (δ) and lattice-strain (ε) can be evaluated using the Williamson–Smallman's relation and Stokes–Wilson's equation, respectively as:

$$\delta = \frac{1}{D^2} \tag{4}$$

$$\text{and } \varepsilon = \frac{\beta_{hkl}\cos\theta}{4} \tag{5}$$

It can be evidenced from Fig. 3(b and c), that the dislocation density and the micro-strain increased constantly on Na doping in the CuO as a result of decreased crystallite size and increased lattice defects except at $x = 0.08$. The calculated structural parameters were demonstrated in Table 2.

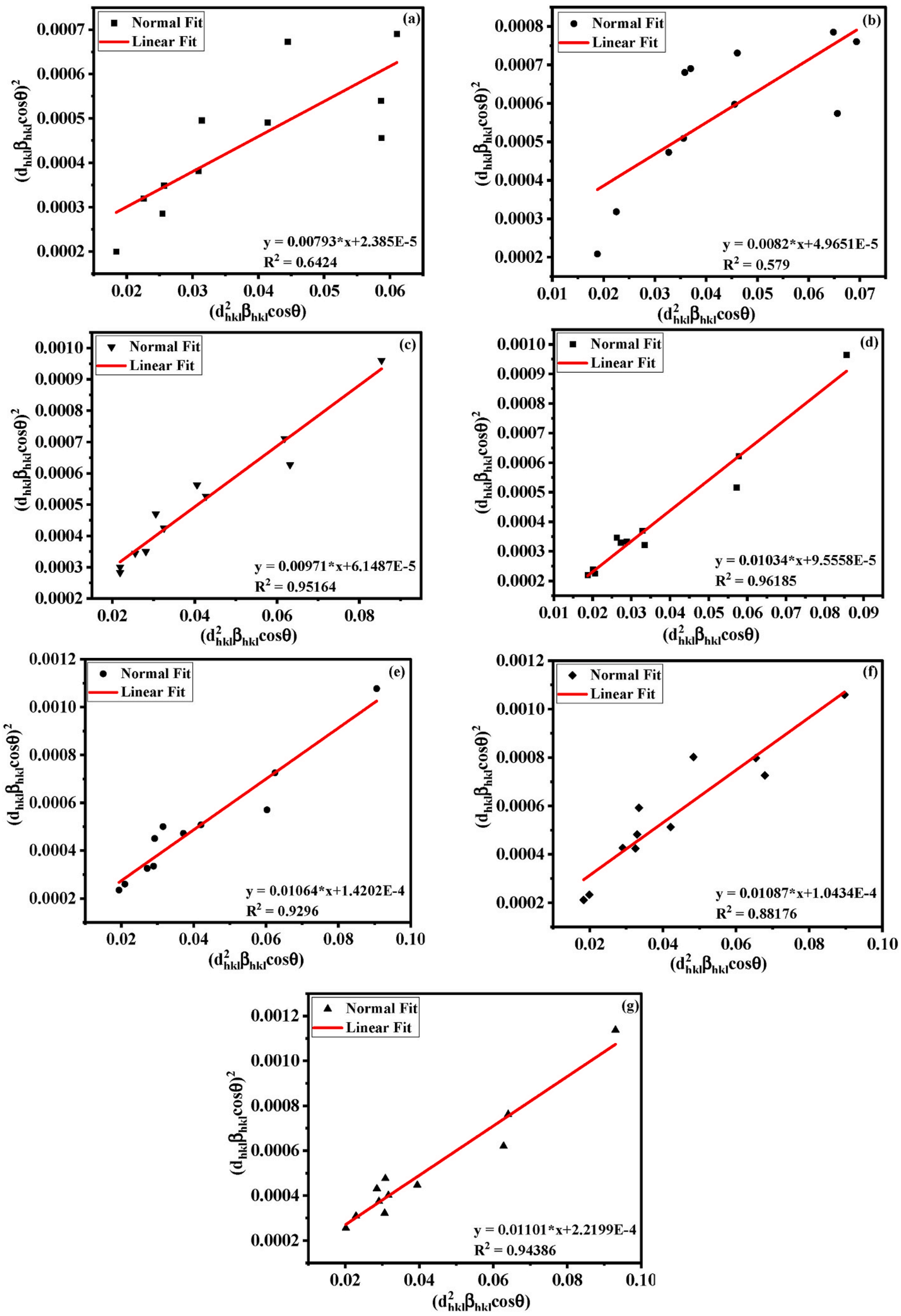

Fig. 5. Linear fit plots of Size-Strain plot (SSP) method for calculating crystallite size (D), dislocation density (δ), and lattice strain (ε) of **a** pure CuO NPs, **b**–**g** Na-doped CuO NPs.

Table 5

The average values of crystallite size (D), dislocation density (δ), and lattice strain (ε) of $Cu_{1\text{-}x}Na_xO$ nano-powders, calculated according to Size-strain plot (SSP) method.

Na^+ content (x)	D_{SSP} (nm)	δ_{SSP} x 10^{-3} (nm^{-2})	ε_{SSP} x 10^{-2}
0	18.262	2.999	0.976
0.01	17.660	3.206	1.409
0.02	14.914	4.496	1.568
0.04	14.005	5.098	1.955
0.06	13.610	5.398	2.383
0.08	13.323	5.634	2.043
0.10	13.153	5.78	2.979

The lattice parameters a, b, and c of $Cu_{1\text{-}x}Na_xO$ nano-powders were evaluated from the interplanar distances d_{200}, d_{020}, and d_{002} using the following relation for monoclinic crystal structure [52]:

$$\frac{1}{d^2}=\frac{1}{\sin^2\beta}\left(\frac{h^2}{a^2}+\frac{k^2\sin^2\beta}{b^2}+\frac{l^2}{c^2}-\frac{2hl\cos\beta}{ac}\right)\text{in Å} \tag{6}$$

where $\boldsymbol{a \neq b \neq c}$, $\alpha = \gamma = 90^O \neq \beta$ and d is the interplanar spacing between the atoms, α, β, and γ are the inter-axial angles, and h, k, l are the Miller indices of lattice planes.

The lattice parameters (a, b, and c) and the inter-axial angle (β) obtained are listed in Table 3. The variation of estimated values of the lattice constants a, b, and c as a function of Na doping concentration is shown in Fig. 4(a). It can be observed that all the lattice parameters are

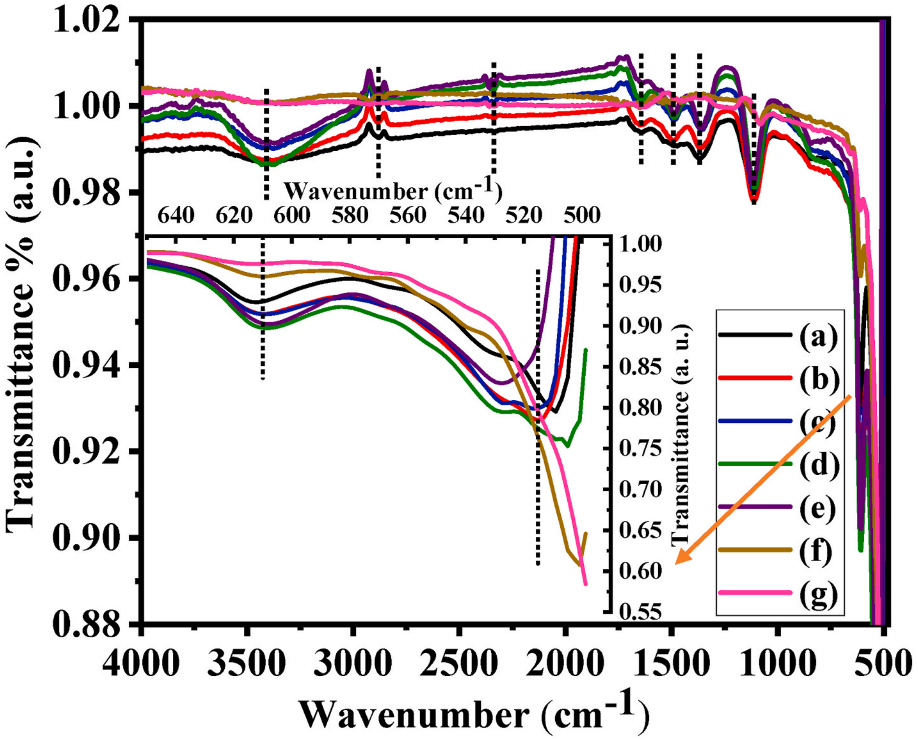

Fig. 6. FTIR spectra of $Cu_{1\text{-}x}Na_xO$ nano-powders for (a) pure, (b) 0.01, (c) 0.02, (d) 0.04, (e) 0.06, (f) 0.08, and (g) 0.10. Inset shows the magnified view of the stretching modes of Cu–O bond.

Table 6
FTIR peaks and their assignments of $Cu_{1\text{-}x}Na_xO$ nano-powders (x = 0–0.10).

Assignments	Wavenumber (cm^{-1})						
	$x = 0$	$x =$ 0.01	$x =$ 0.02	$x =$ 0.04	$x =$ 0.06	$x =$ 0.08	$x =$ 0.10
O–H stretching mode	3384	3397	3399	3340	3401	3410	3410
C–H stretching vibration	2880	2882	2882	2883.5	2883	2883	2885
Na–O signature	2336	2338	2337	2339	2339	2341	2341
ν(C = O)	1642	1645	1645	1645	1648	1650	1650
O–H stretching vibrations	1485	1492	1493	1493	1495	1500	1500
C–H stretching mode	1365	1365	1360	1359.5	1359.5	1367	1367
C–O stretching mode	1119	1112	1113.5	1109.5	1117.5	1088	1083
Cu–O stretching mode	612	610	610	608	607	611	614
Cu–O stretching vibration	509	514	515	505	527	530	530

first increases and then strongly reduced except at $x = 0.08$ as the sodium concentration increased. The lattice parameters *a*, *b*, and *c* were evaluated as 4.692, 3.416, and 5.102 Å for undoped CuO; and 4.692, 3.410, and 5.100 Å for $Cu_{0.90}Na_{0.10}O$ nano-powders, respectively. This characteristic behaviour is resulting from the tensile strain and stress developed by sodium dopants on the surface of CuO [20].

The crystallite volume (V), the unit cell volume (v), and the X-ray density ($\rho_{x\text{-}ray}$) were calculated using the following relations for monoclinic system as

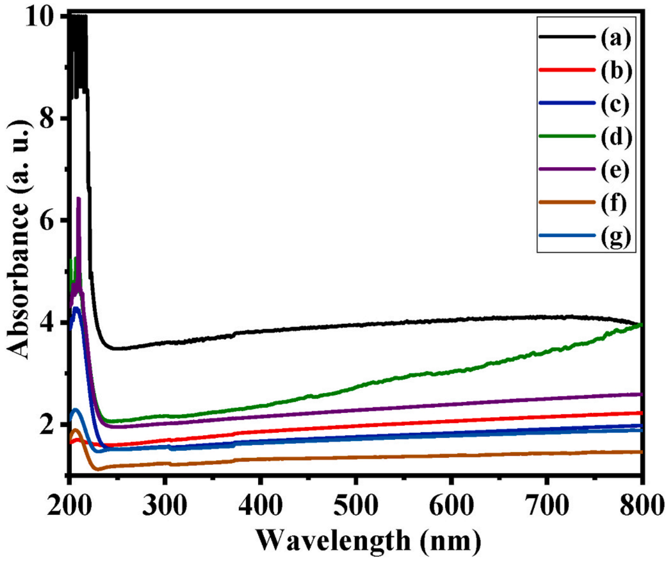

Fig. 7. UV–Vis optical absorption of $Cu_{1\text{-}x}Na_xO$ nano-powders for (a) pure, (b) 0.01, (c) 0.02, (d) 0.04, (e) 0.06, (f) 0.08, and (g) 0.10.

$$\mathbf{V} = \mathbf{D}^3 \text{ in } (\text{nm})^3, \tag{7}$$

$$\mathbf{v} = \boldsymbol{abc\ sin\ \beta} \text{ in } \left(\overset{\circ}{\text{A}}{}^3\right), \tag{8}$$

$$\text{and } \boldsymbol{\rho}_{x-ray} = \frac{ZM_w}{N_A \mathbf{v}} \text{ in } \left(\text{g} / \text{cm}^3\right), \tag{9}$$

where, Z is the number of atoms or molecules per unit cell, M_W is the molecular weight, v is the volume of the unit cell, and N_A is the

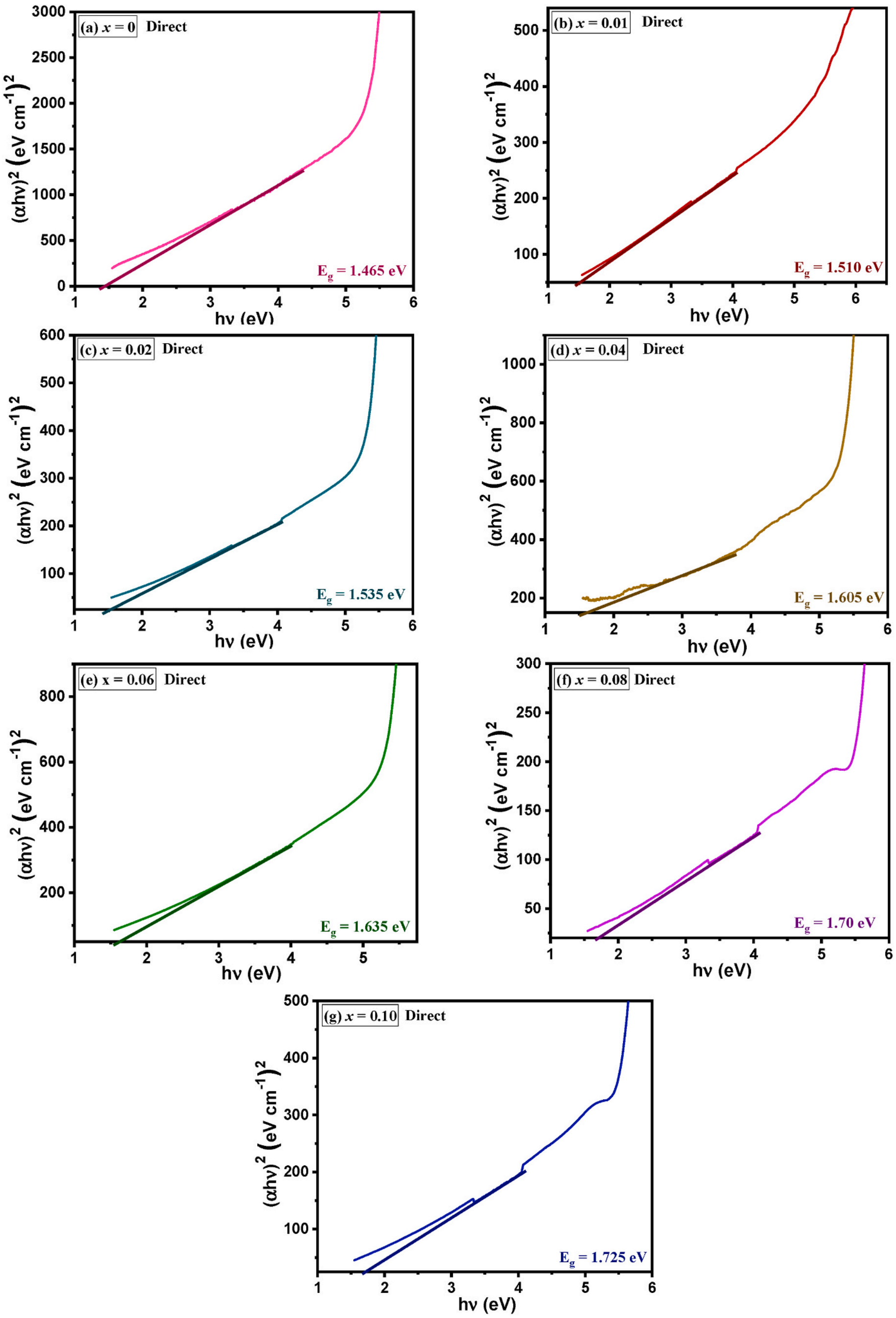

Fig. 8. Tauc's plot (direct band gap) of $Cu_{1-x}Na_xO$ nano-powders for (a) pure, (b) 0.01, (c) 0.02, (d) 0.04, (e) 0.06, (f) 0.08, and (g) 0.10.

Avogadro's number.

The observed reduction in x-ray volume density and the variation of unit cell volume with increasing Na doping concentration is shown in Fig. 4(b). This effect in x-ray density may be assigned to the reduced growth rate of CuO nanoparticles due to the decreasing adatom mobility in the host lattice over Na doping [53]. Fig. 4(c) shows the variation of average crystallite volume and average FWHM of $Cu_{1-x}Na_xO$ as a function of Na dopant concentration. Moreover, the unit cell volume of Na doped samples is enhanced compared to that of pure CuO with the addition of sodium as a consequence of the presence of the large number of surface atom dangling bonds [15].

The 2θ value, FWHM (β_{hkl}), crystallite size, and inter-planar distance of $Cu_{1-x}Na_xO$ for (200) diffraction plane was provided in Table 4. These results indicate that the (200) diffraction peak of Na-doped samples have shifted towards lower angles when compared with that of the undoped samples as seen in Fig. 2(b), which also confirms the successful incorporation of sodium into CuO matrix. This shift is due to the differences in the ionic radii of Cu^{2+} (0.73 nm) and Na^+ (1.02 Å) and is attributed to the distortion of lattice parameters [54].

The average crystallite size (D_{SSP}), and lattice strain (ε_{SSP}) were also analysed by the Size-Strain plot (SSP) method using the following relation [55]:

$$(\mathbf{d_{hkl}}.\boldsymbol{\beta_{hkl}}.\mathbf{cos}\ \boldsymbol{\theta})^2 = \frac{k\lambda}{D}\left(\mathbf{d^2_{hkl}}.\boldsymbol{\beta_{hkl}}.\mathbf{cos}\ \boldsymbol{\theta}\right) + \frac{\varepsilon^2}{4} \tag{10}$$

From the linear fit of experimental data as shown in the Fig. 5 (a - g), the micro-strain ($\boldsymbol{\varepsilon_{SSP}}$) was evaluated from the y-intercept, and the crystallite size ($\mathbf{D_{SSP}}$) was obtained from the slope. The values determined for D, δ, and ε using SSP method were provided in Table 5. These D, δ, and ε values were almost similar to those values measured by

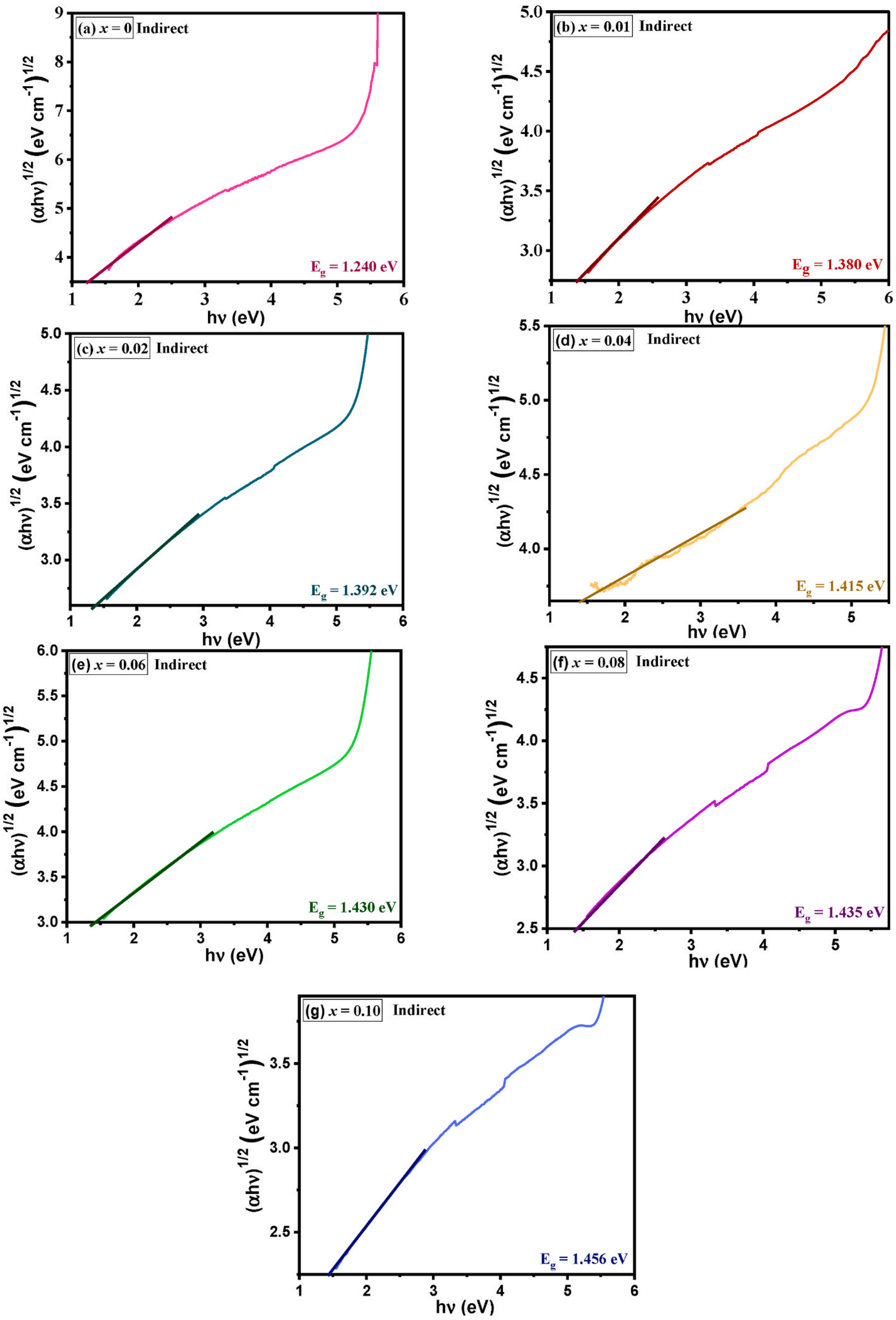

Fig. 9. Indirect band gap energies of $Cu_{1-x}Na_xO$ nano-powders for (a) pure, (b) 0.01, (c) 0.02, (d) 0.04, (e) 0.06, (f) 0.08, and (g) 0.10.

Debye – Scherrer method and their variation with Na doping concentration have shown in Fig. 3 (a – c). The values of crystallite size measured using SSP method was found to be reduced from 18.262 nm to 13.153 nm which an increasing amount of Na dopant concentration. However, the micro-strain evaluated from the Debye-Scherrer relation and the SSP method presents a large variation due to the averaging variance in the particle size distribution.

3.2. Fourier transform infrared spectrum (FTIR) analysis

The Fourier transform infrared (FTIR) spectroscopy is a technique used to identify various functional groups present in the samples by analysing different vibrational bands. Fig. 6(a–g) shows the FTIR pattern under the wavenumber range 4000–500 cm^{-1} of the pure and Na doped CuO nano-powders annealed at 450 °C for 3 h in the atmosphere of air. As shown in Fig. 6(b), the $Cu_{0.99}Na_{0.01}O$ sample exhibits a broad vibrational band between 3600 and 3100 cm^{-1} centred at 3400 cm^{-1} and a small absorption peak at 1492 cm^{-1}, which are attributed to the stretching vibrational modes of the hydroxyl group (-OH) [56]. The stretching modes of the vibration assigned to the C–H molecule was obtained at 2880 cm^{-1} and 1364 cm^{-1} [57]. The characteristic absorption peaks at 1645 cm^{-1} and 1112 cm^{-1} were corresponding to the stretching vibrations of C = O and C–O, respectively [58]. The presence these molecules is attributed to the improper thermal decomposition of the acetate group. The vibrational modes of metal – oxygen bonds were basically observed below the wavenumber of 1000 cm^{-1}. Accordingly, the frequency stretching modes associated to Cu–O bond of $Cu_{1-x}Na_xO$ samples have been obtained around 610 and 514 cm^{-1} [59]. The signature of sodium may be confirmed by the sharp absorption peak of Na–O bond at 2340 cm^{-1} in Na doped samples as compared to pure CuO

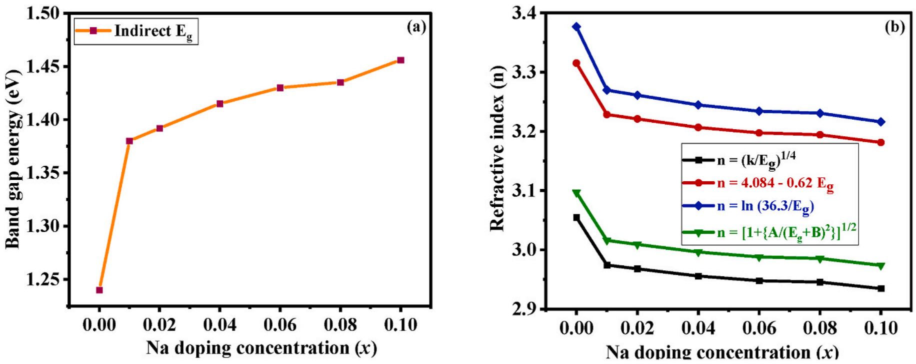

Fig. 10. Calculated variation of **(a)** Indirect band gap (E_g); and **(b)** Refractive index (n) as a function of Na doping concentration in $Cu_{1-x}Na_xO$ nano-powders.

Table 7
The estimated values of Optical bandgap energy (E_g) and the refractive index (n) of the polycrystalline $Cu_{1-x}Na_xO$ samples.

Na^+ content (x)	E_g (eV)		Refractive index (n)			
	Direct	Indirect	$(108/E_g)^{1/4}$	4.084 - 0.62 E_g	ln (36.3/E_g)	$[1+(\frac{A}{B+E_g})^2]^{1/2}$
0	1.465	1.240	3.055	3.315	3.377	3.097
0.01	1.510	1.380	2.974	3.228	3.27	3.016
0.02	1.535	1.392	2.968	3.221	3.261	3.009
0.04	1.605	1.415	2.956	3.207	3.245	2.996
0.06	1.635	1.430	2.948	3.197	3.234	2.988
0.08	1.700	1.435	2.945	3.194	3.231	2.985
0.10	1.725	1.456	2.935	3.181	3.216	2.974

sample, in which it is not present [60]. Furthermore, no additional IR active vibrational peaks were obtained in the wavenumber range of 605–660 cm^{-1} confirming the non-existence of secondary phase, i.e., Cu_2O phase [61]. It is also observed from the XRD results that the as-prepared nano-powders does not manifest the presence of cuprous oxide (Cu_2O). Hence, the FTIR analysis shows that the Na is successfully substituted into CuO monoclinic crystal lattice. To analyse the doping effect of sodium, all the FTIR patterns of $Cu_{1-x}Na_xO$ ($x = 0, 0.01, 0.02, 0, 04, 0.06, 0.08,$ and 0.10) nano-materials are plotted at the same scale for better comparison and the absorption peaks along with their assignments are tabulated in Table 6. The vibrational peaks of $Cu_{1-x}Na_xO$ become sharper with increasing sodium doping content upto $x = 0.04$, then gradually decreases and appeared to be dull. Moreover, the vibrational peaks shifting towards the higher wavenumber (blue shifted) with an increase in doping concentration of sodium is observed may be due to smaller crystalline size of Na-doped CuO nano-powders in comparison to that of pure CuO samples [62,63].

3.3. *UV–visible analysis*

The UV–Visible absorption spectroscopy was used to analyse the bandgap energy (E_g) as well as the mode of electronic transitions. The absorption spectra of $Cu_{1-x}Na_xO$ nano-powders in the region 200–800 nm were shown in Fig. 7. A strong fundamental peak about 208 nm and an absorption edge at 304 nm were observed may be due to direct transition of electrons and surface plasmon resonance of metal oxide, respectively [64,65]. The fundamental absorption peak of the coprecipitation synthesized $Cu_{1-x}Na_xO$ nano-powders was shifted from 208.5 nm to 205.5 nm with increasing sodium dopant concentration as shown

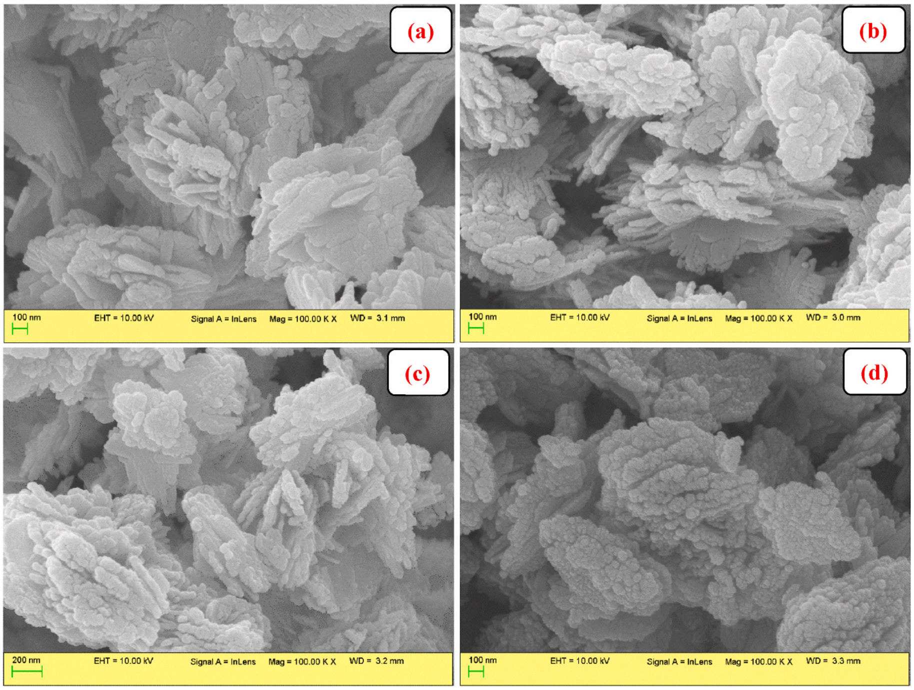

Fig. 11. FESEM images of $Cu_{1-x}Na_xO$ nano-powders; **(a)** $x = 0$, **(b)** $x = 0.02$, **(c)** $x = 0.06$, and **(d)** $x = 0.10$, respectively.

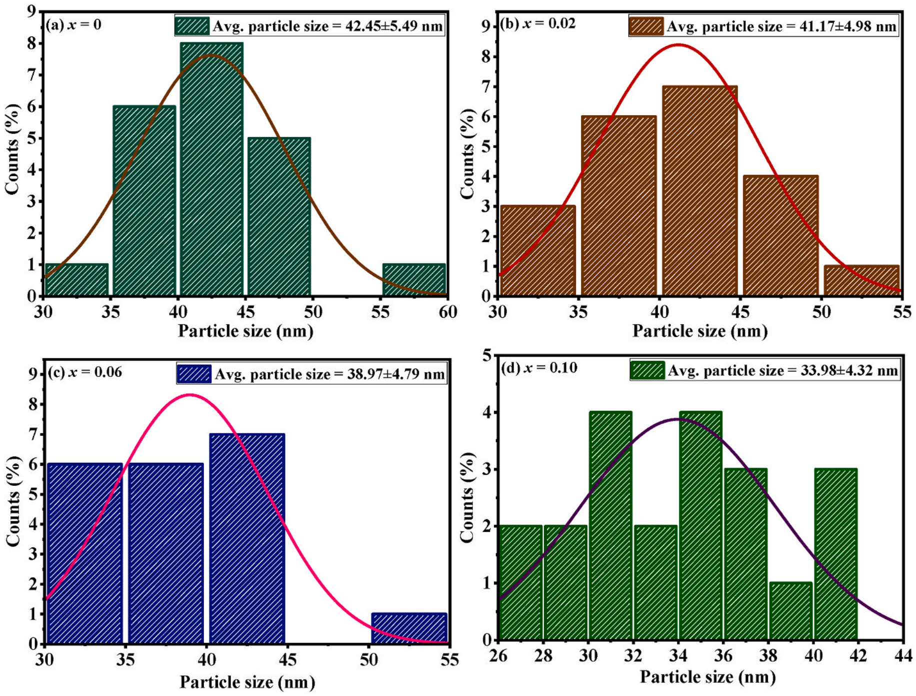

Fig. 12. Histogram representation (FESEM micrographs) of particle size distribution of $Cu_{1-x}Na_xO$ nano-powders; (a) $x = 0$; (b) $x = 0.02$; (c) $x = 0.06$; and (d) $x = 0.10$, respectively.

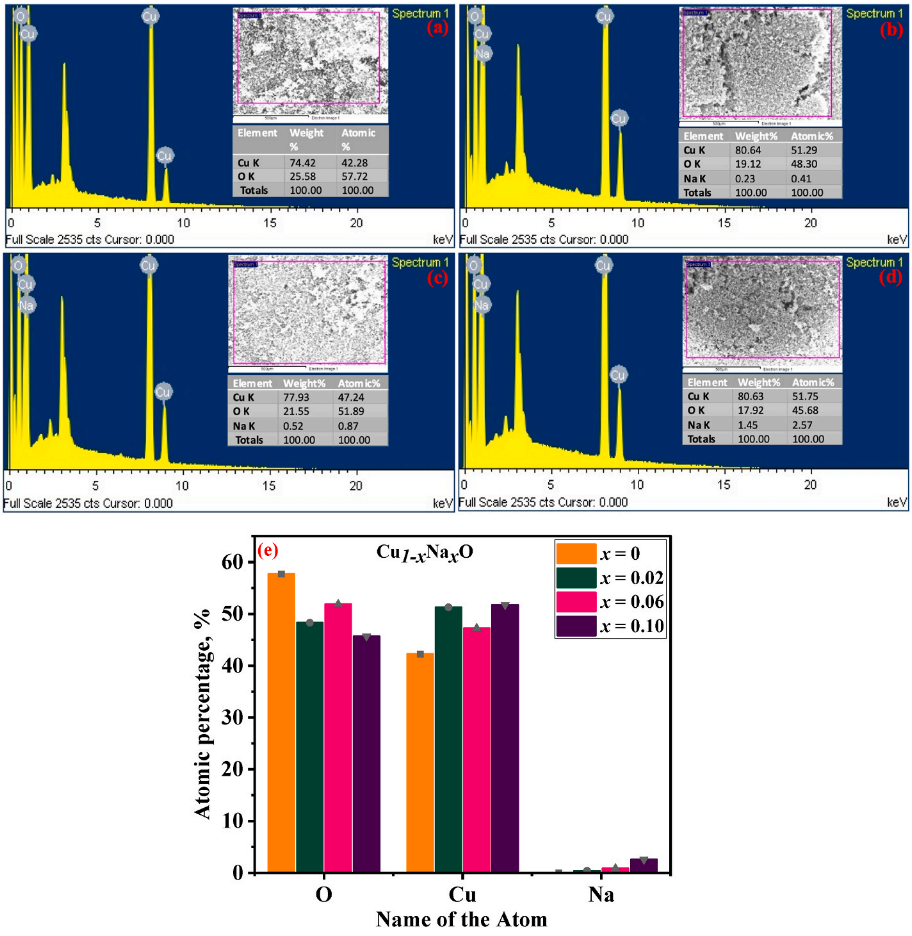

(a)

Element	Weight %	Atomic %
Cu K	74.42	42.28
O K	25.58	57.72
Totals	100.00	100.00

(b)

Element	Weight%	Atomic%
Cu K	80.64	51.29
O K	19.12	48.30
Na K	0.23	0.41
Totals	100.00	100.00

(c)

Element	Weight%	Atomic%
Cu K	77.93	47.24
O K	21.55	51.89
Na K	0.52	0.87
Totals	100.00	100.00

(d)

Element	Weight%	Atomic%
Cu K	80.63	51.75
O K	17.92	45.68
Na K	1.45	2.57
Totals	100.00	100.00

Fig. 13. The energy dispersive X-ray analysis (EDAX) spectra of $Cu_{1-x}Na_xO$ nano-powders; **(a)** $x = 0$; **(b)** $x = 0.02$; **(c)** $x = 0.06$; and **(d)** $x = 0.10$, respectively, inset tables shows the elemental composition. **(e)** is the corresponding histogram representation in atomic percentage.

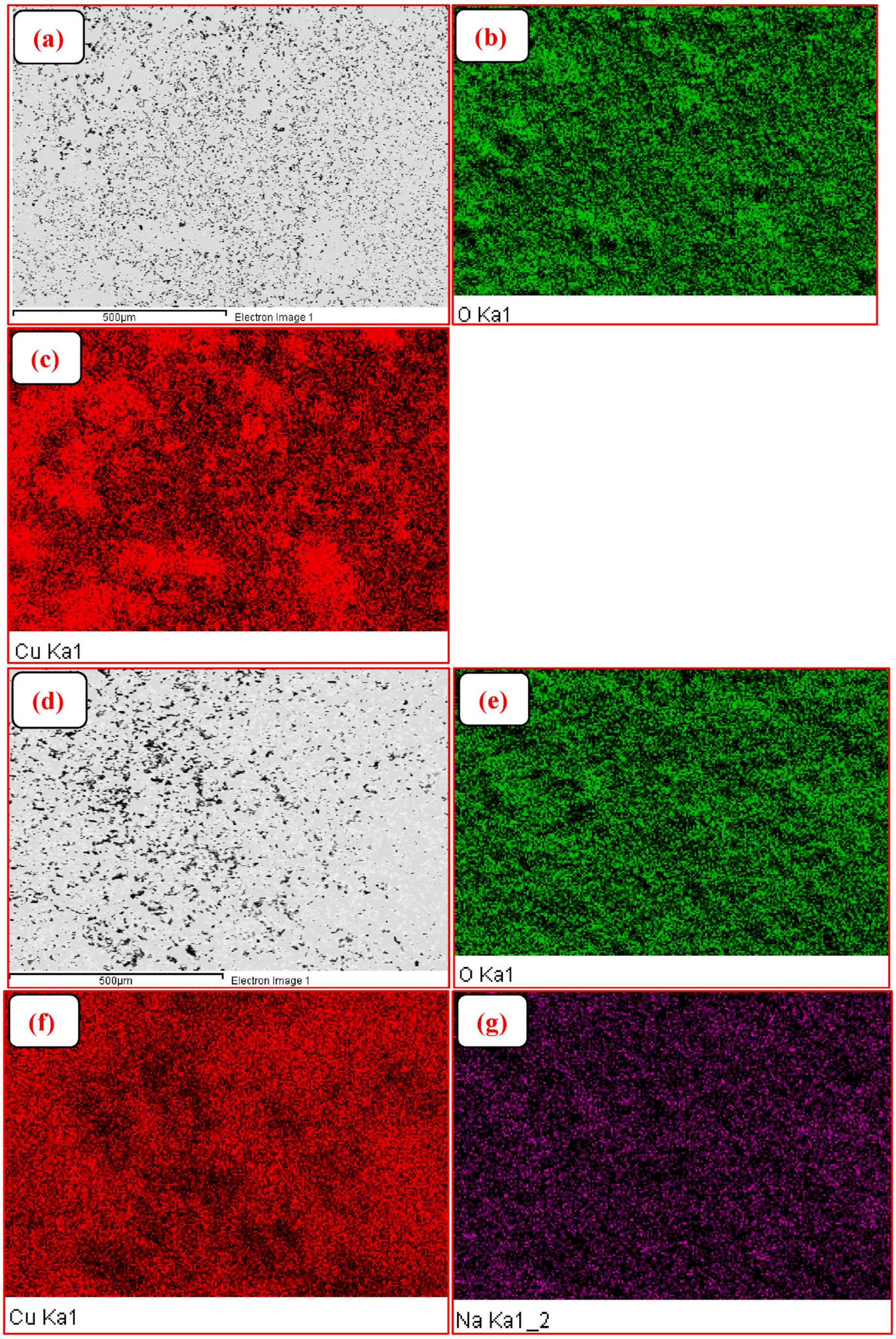

Fig. 14. (a) EDAX element layered image of pure CuO, and (b - c) elemental mapping for O, and Cu respectively; (d) EDAX element layered image of $Cu_{0.90}Na_{0.10}O$, (e - g) elemental mapping images for O, Cu and Na respectively.

in Fig. 7. Hence, it can be clear that the optical properties of pure and sodium doped CuO samples were largely depends on the particle crystallite size and doping concentration of Na [66]. The direct/indirect bandgap energy (E_g) value is estimated by the Tauc's equation [67] as

$$(\boldsymbol{\alpha h\nu})^{r} = \mathbf{A}\ (\mathbf{h\nu} - \mathbf{E_g}) \tag{11}$$

where, α is optical absorption coefficient (cm^{-1}), $h\nu$ is photon energy (eV), A is the energy independent constant related to the material, r is an exponent is equal to 2 for a direct electronic transition and ½ for an indirect electronic transition, and E_g is the bandgap energy (eV). The indirect and direct bandgap (E_g) can be calculated by extrapolating the linear portion of the curve to the photon energy axis. The plots of $(\alpha h\nu)^2$ versus $h\nu$ and $(\alpha h\nu)^{1/2}$ versus $h\nu$ of as-synthesized samples were given in Figs. 8 and 9, used to evaluate the direct and indirect E_g values, respectively. The indirect optical band gap (E_g) energy values of $Cu_{1-x}Na_xO$ nano-powders obtained are in the range of 1.240–1.456 eV, which were higher as compared to the band gap value of bulk CuO (1.2 eV in bulk) confirms the quantum confinement effect. Further, the measured band gap value increases with increasing sodium doping concentration as depicted in Fig. 10(a). This characteristic variation of $Cu_{1-x}Na_xO$ semiconducting materials is mainly due to the trapping of free charge carriers, and lattice deformation due to the strain caused by surface defects [53,68]. Therefore, the blue shift in the band gap energy makes the Na doped CuO samples ideal for the applications of semiconductor devices including photo-detectors, photovoltaic cells, and

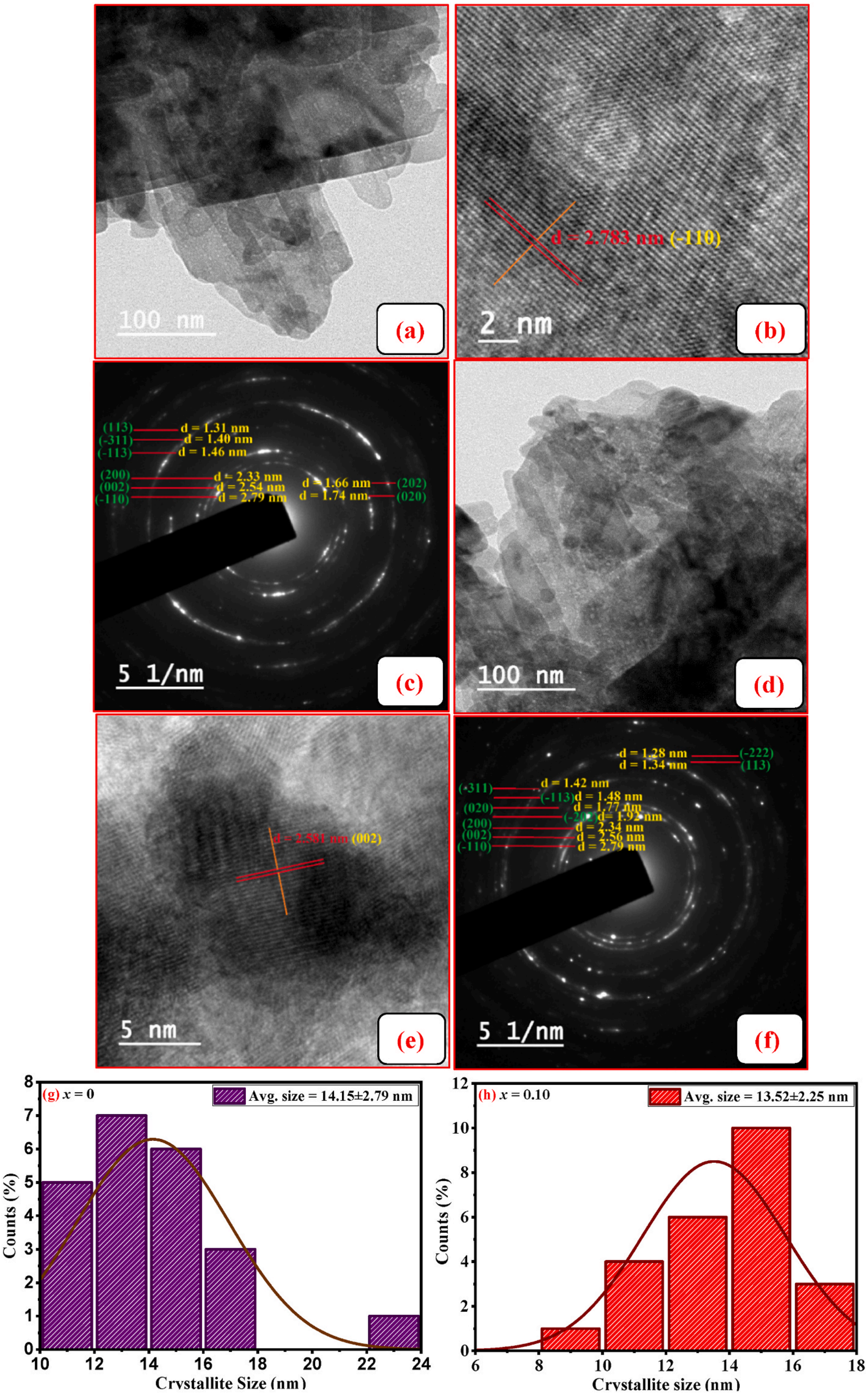

Fig. 15. TEM bright-field images of the as-synthesized (a) pure CuO and (d) $Cu_{0.90}Na_{0.10}O$ NPs; and (b, e) are the corresponding HRTEM micrographs, respectively; (c, f) are the typical corresponding selective area electron diffraction (SAED) patterns, respectively; (g, h) are the corresponding range of histograms with the Gauss fitting curve for evaluating the average crystallite size and its distribution, respectively.

photo-amplifiers [16]. The indirect/direct E_g values obtained were listed in Table 7. The values of direct energy band gap of $Cu_{1-x}Na_xO$ are found to be 1.465–1.725 eV, which are in close agreement with the reported values of 1.34–1.50 eV by Anu et al. [15] in the literature.

The optical refractive index (n) of semiconductor nanomaterials was estimated from the above calculated bandgap energy (E_g) values using four distinct atomic models, named as Ravindra et al. [69], Ravindra and Gupta [70,71], Reddy et al. [72], and Herve and Vandamme [52] by using the following relations:

$$n^4 . E_g = 108 \tag{12}$$

$$n = 4.084 - 0.62\ E_g \tag{13}$$

$$E_g\ .\ e^n = 36.3 \tag{14}$$

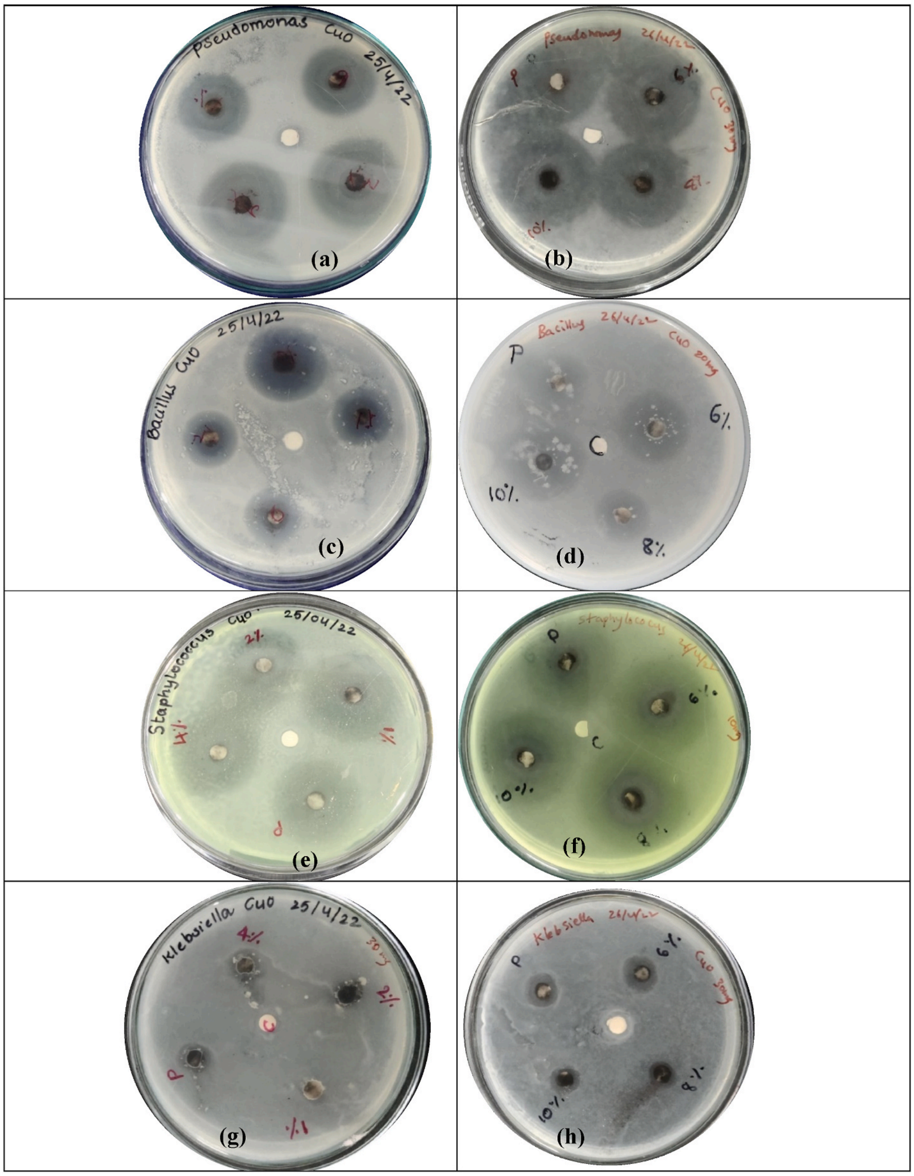

Fig. 16. Antibacterial activity of $Cu_{1\text{-}x}Na_xO$ with different sodium concentrations against the bacterial strains (a - b) *P. Aeruginosa*, (c - d) *B. subtilis*, (e - f) *S. aureus*, and (g- h) *K. pneumoniae*.

$$\mathbf{n} = \sqrt{\mathbf{1} + \left[\frac{\boldsymbol{A}}{\boldsymbol{E_g} + \boldsymbol{B}}\right]^2} \qquad (15)$$

where the values of numerical constants A and B are 13.6 and 3.4 eV, respectively.

Fig. 10 (b) shows that the estimated refractive index (n) is larger than 2 and it was found to decrease with increasing Na doping concentration. The refractive index (n) values obtained at band gap region are in the range of 3.055–2.935, 3.315–3.181, 3.377–3.216, and 3.097–2.974 according to the four models, Ravindra et al., Ravindra and Gupta, Reddy et al., and Herve and Vandamme respectively. Hence it was evident that, pure CuO and $Cu_{0.99}Na_{0.01}O$ have high refractive index, while lower value of refractive index corresponds to $Cu_{0.90}Na_{0.10}O$ (Table 7). All the four atomic models show a similar fashion. Generally, the refractive index is used to measure the transparency of a semiconductor optical material to the incident radiation. Therefore, these results depict the Na doped CuO samples have been used as integrated optoelectronic devices and photovoltaic cells.

3.4. Field emission scanning electron microscopy (FESEM) analysis

The size, shape and surface morphology of the as-prepared $Cu_{1\text{-}x}Na_xO$ nano-powders annealed at 450 °C for 3 h were examined using FESEM. The FESEM images of pure and selected Na doped CuO materials were presented in Fig. 11(a–d) shows irregular spherical morphology of the particles. The values of mean particle size were 42.45 ± 5.49, 41.17 ± 4.98, 38.97 ± 4.79, and 33.98 ± 4.32 nm for pure, 2, 6, and 10% Na-doped CuO, respectively estimated by using the particle distribution curves as shown in Fig. 12(a–d). Clearly, the average particle size observed by FESEM micrographs is slightly larger in comparison with XRD and HRTEM and is due to the self-aggregation of many nanoparticles [18]. Also, a slight variation in the particle size was observed in Na doped CuO NPs when compared with pure CuO NPs. Moreover, the small nuclear spherical particles are self-agglomerated into cauliflower-shaped structures and also align themselves in hierarchical growth to form closely oriented flake-like structures. The mean size of the composite nanocauliflowers and nanoflake-like structures depends on the Na doping concentration [24].

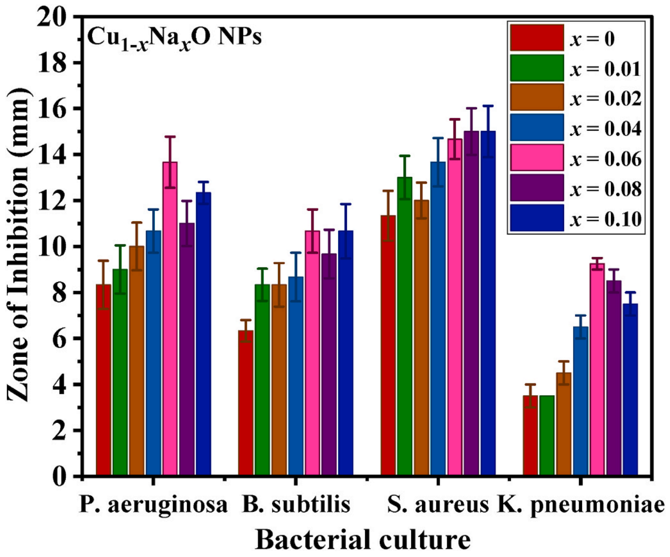

Fig. 17. Histogram representation of antibacterial activity of the compounds towards the *P. aeruginosa, B. subtilis, S. aureus* and *K. pneumoniae bacteria*. The values are Mean ± SD (n = 4**).** *P < 0.0001 Compared to control (Pure CuO).

3.5. Energy dispersive X-ray spectroscopy (EDAX) and mapping analysis

The EDAX compositional analysis was performed to observe the purity and formation of Cu$_{1-x}$Na$_x$O nano-powder samples. The EDAX spectra is confirmed the presence of elements Cu K and O K alone in pure CuO; and Cu K, O K, and Na K in Na doped CuO samples (Fig. 13 (a) – (d)), which also reveals the successful incorporation of Na $^+$ at Cu^{2+} lattice sites in CuO crystal lattice [20]. The atomic ratios of Cu:O in pure CuO and Cu:O:Na in Na doped CuO were determined by the EDAX analysis revealed as histogram in Fig. 13(e). From Fig. 13(e), it was evident that the emission of sodium gradually increases with increasing sodium doping concentration in the as-prepared samples [19]. Moreover, the elemental mapping of each constituent element in the grown samples was studied by EDAX mapping measurements as depicted in Fig. 14 and it was observed that the Cu, O, and Na elements in Cu$_{1-x}$Na$_x$O samples are uniformly distributed in composition [26,73]. Hence the Na-related prominent peak in all the EDAX spectra (Fig. 13 b–d) shows the occurrence of sodium atoms in the Cu$_{1-x}$Na$_x$O nanostructures.

3.6. High resolution transmission electron microscopy (HRTEM) analysis

Fig. 15 (a, b) shows the TEM and HR-TEM micrographs of pure CuO nano-powders synthesized using coprecipitation method. The interplanar spacing between the adjacent lattice planes of pure CuO was obtained 2.783 nm which corresponds to (−110) lattice plane. The SAED pattern of undoped CuO nanopowders was given in Fig. 15 (c), which shows bright and sharp spots as well as lattice planes showing poly-crystallite nature [54,65]. The observed SAED pattern clearly demonstrating the monoclinic crystal structure of pure CuO and the obtained HR-TEM results are in excellent agreement with PXRD pattern. The pure CuO nanopowders reveals agglomerated spherical and flakes like particles with mean particle size of ∼14.15 ± 2.79 nm (Fig. 15 (g)).

The TEM image of 10% Na-doped CuO (Cu$_{0.90}$Na$_{0.10}$O) sample (Fig. 15 (d)) depicts comparatively small particles of spherical and flakes-like structures. The TEM image also shows the formation of aggregated secondary particles from few primary nanoparticles, owing to their high surface areas and lower dimensions. The interplanar distance estimated from HRTEM image (Fig. 15 (e)) was 2.581 nm, which shows the presence of (002) plane in Cu$_{0.90}$Na$_{0.10}$O. The lattice plane reflections observed from the corresponding SAED pattern (Fig. 15 (f)) of Cu$_{0.90}$Na$_{0.10}$O sample also reveals the monoclinic crystal structure. Fig. 15 (h) shows the histogram representation with Gauss fitting curve of Cu$_{0.90}$Na$_{0.10}$O NPs and the average particle size is found to be 13.52 ± 2.25 nm, which is compared with the XRD result [74,75].

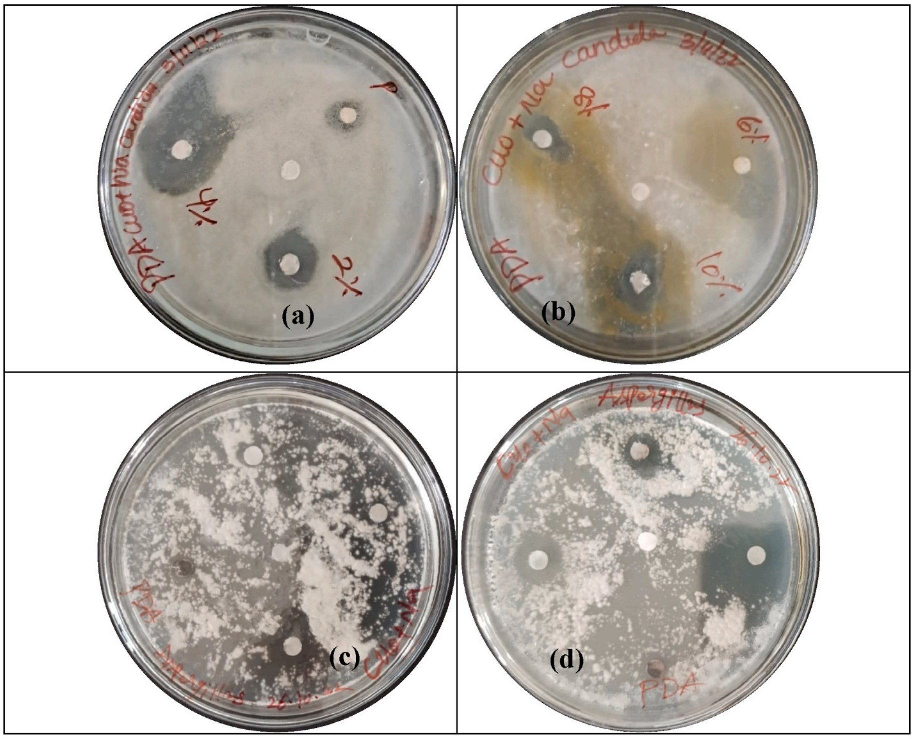

Fig. 18. Antifungal activity of Cu$_{1-x}$Na$_x$O NPs with different sodium concentrations against the fungal strains **(a - b)** *C. albicans*, and **(c - d)** *A. niger*.

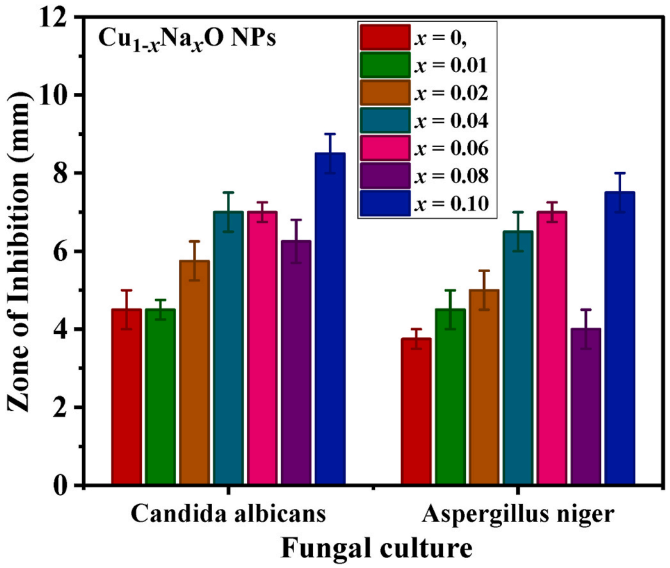

Fig. 19. Histogram representation of antifungal activity of the compounds towards the fungi *C. albicans* and *A. niger*. The values are Mean ± SD ($n = 4$). *$P < 0.0001$ Compared to control (Pure CuO).

3.7. Antimicrobial activity

The Antimicrobial activity of coprecipitation synthesized pure and Na substituted CuO NPs was tested by measuring the zone of inhibition (ZOI) with different Na doping concentrations (1, 2, 4, 6, 8, and 10%) against various bacterial and fungal strains. The antibacterial activity of $Cu_{1-x}Na_xO$ samples is studied for two Gram positive bacterial strains (*Bacillus subtilis, Staphylococcus aureus*) and two Gram negative bacterial organisms (*Pseudomonas aeruginosa, Klebsiella pneumoniae*) by the zone of inhibition method, where the inhibition zone around each Petri dish is estimated in mm by using the meter ruler [50].

The inhibition of $Cu_{1-x}Na_xO$ nanoparticles is demonstrated against various pathogenic bacteria as follows. The gram-negative bacteria cell has a thin wall of single layer peptidoglycan (PG) molecule, whereas the outer membrane of gram-positive bacteria cell is a thick wall having multi-layer peptidoglycans. As the peptidoglycan is negative charged, the presence of PG macromolecules produces an overall negative charge in both type of bacteria. However, due to a greater number of peptidoglycans, the gram-positive bacteria are more negatively charged than the gram-negative bacteria. Hence, there is an electrostatic attraction between CuO nanoparticles and bacteria cell walls because of positive charge of the CuO NPs [49]. This interaction of more positive Cu ions with negative peptidoglycan ions over the surface of bacteria will disrupt the outer membrane or cell wall.

Fig. 16 shows the observed zone of inhibition around each disc of pure and Na doped CuO NPs over gram-positive bacteria species (*Bacillus subtilis* and *Staphylococcus aureus);* and gram-negative bacteria (*Pseudomonas aeruginosa* and *Klebsiella pneumoniae*). The results showed that, for gram positive bacteria, the inhibition zone is increased with increasing Na doping concentration, which is attributed to reduced crystallite size [48]**.** The as-synthesized NPs with large particle size demonstrated bacteriostatic effect, while those with small size showed bactericidal activity [4]. The highest radial diameter of the inhibitory zone observed for $Cu_{0.90}Na_{0.10}O$ of *B. subtilis* and *S. aureus* was 10.67 ± 0.94 and 15 ± 1.11 mm, respectively (Fig. 17). $Cu_{1-x}Na_xO$ NPs exhibited higher antibacterial activity against *S. aureus* than *B. subtilis* [76]. Interestingly, in case of gram-negative bacteria, the effect of Na^+ doping content on the antibacterial activity of CuO NPs shows different results. Apparently, $Cu_{0.94}Na_{0.06}O$ NPs presented the best antibacterial effect with observed maximum zone of inhibition 13.67 ± 1.11 and 9.25 ± 0.25 mm for *P. aeruginosa* and *K. pneumonia*, respectively (Fig. 17). When the Na^+ doping concentration further enhanced beyond 6%, Na-doped CuO NPs exhibited decreased antibacterial activity [17]. It can be observed that, the zone of inhibition for all the as-grown NPs follows the sequence as *S. aureus* > *P. aeruginosa* > B. subtilis > *K. pneumoniae*. This significant variation of antibacterial activity towards Gram-negative and Gram-positive bacteria may be assigned to the differences in their metabolism, net negative charge, cell structure, level of interaction of bacteria species with $Cu_{1-x}Na_xO$ nanoparticles [15]. The superior antibacterial activity of Na doped CuO materials may also due to the synergetic interaction between sodium and ZnO nanoparticles as a result of the greater formation of reactive oxygen species (ROS) when compared to the individual materials. Thus, CuO NPs with addition of Na exhibited synergistic antibacterial activity against *S. aureus* and *P. aeruginosa* bacteria [59]**.**

3.8. Antifungal activity

The antifungal study of pure and Na-doped CuO nanoparticles were shown in Fig. 18. The as-prepared nanoparticles with different Na concentrations were subjected to their antifungal activity against polymorphic fungus *C. albicans* and filamentous fungus *A. niger.* The $Cu_{1-x}Na_xO$ NPs presented higher antifungal activity against *C. albicans* with the maximum zone of inhibition of 8.5 ± 0.5 mm, followed by *A. niger* whose highest zone of inhibition was measured to be 7.5 ± 0.5 mm, respectively. The pure and Na-doped CuO NPs shows increased tendency of the zone of inhibition against *A. niger* except for 8% Na doping content, where the crystallite size of the NPs is observed to be high (Fig. 19) [51]. Clearly, the antifungal activity of $Cu_{1-x}Na_xO$ nanoparticles increases with an increase in the Na doping concentration and it is size dependent. Similarly, the pure and Na-graded CuO NPs shows active antifungal effect against the fungus *C. albicans* and the zone of inhibition is found to be increasing at lower Na doping content, but no significant change was observed in the zone of inhibition for high dopant concentration [20]. However, the highest antifungal activity against *C. albicans* was obtained for $Cu_{0.90}Na_{0.10}O$ nanoparticles. At high doping concentration of Na, the metal ions liberated from $Cu_{1-x}Na_xO$ nanoparticles may increase the antifungal effect by damaging the cell wall or membrane and will diffuse into cells [77,78]. Hence, Na doped CuO NPs showed profound antifungal activity against fungi *C. albicans* and *A. niger* [79].

4. Conclusion

We have reported the synthesis of pure and sodium doped CuO cauliflower-shaped and flake-like nanostructures by a simple coprecipitation route after thermal treatment at 450 °C for 3 h. The $Cu_{1-x}Na_xO$ nano-powders with single phase was confirmed by XRD and SAED and present the monoclinic crystal structure. The band gap energy of $Cu_{1-x}Na_xO$ materials is found to be increased and the refractive index, which is estimated based on the measured band gap energy, is reduced with increasing Na doping concentration. The existence of Na^+ in CuO was evidenced from the Na–O absorption peak at 2340 cm^{-1} in FTIR and sodium related peak in EDAX spectra. The FESEM and HR-TEM studies predicted that the irregular spherical NPs are agglomerated into nano cauliflower-shaped and flake-like structures alignment and the mean particle size changed according to Na doping concentration. The antibacterial studies of pure and Na doped CuO NPs confirmed an increased antibacterial activity against Gram positive (*S. aureus* and *B. subtilis*) bacterial strains except for $x = 0.08$, while $Cu_{0.94}Na_{0.06}O$ NPs shows high antibacterial effect against Gram negative (*P. aeruginosa* and *K. pneumonia*) bacteria. The antifungal activity of $Cu_{1-x}Na_xO$ NPs shows an increased zone of inhibition against fungus *A. Niger*, while the highest inhibitory zone against *C. albicans* is achieved for $Cu_{0.90}Na_{0.10}O$ nanoparticles. It is concluded that the resulted coprecipitation synthesized $Cu_{1-x}Na_xO$ NPs showed significant antibacterial and high antifungal activities. Thus, the antimicrobial studies of pure and sodium doped CuO

NPs elicited their usage in future medical applications as promising antifungal drugs and the treatment of dangerous bacterial infections.

CRediT authorship contribution statement

B. Nageswara Rao: Experimentation, Writing – original draft. **P. Tirupathi Rao:** Visualization, Investigation. **Sk.Esub Basha:** Experimentation, Writing – original draft. **D.S.L. Prasanna:** Writing – review & editing. **K. Samatha:** Visualization, Investigation. **R.K. Ramachandra:** Conceptualization, Methodology, Supervision.

Declaration of competing interest

The authors declare that they have no known competing financial interests or personal relationships that could have appeared to influence the work reported in this paper.

Data availability

Data will be made available on request.

References

[1] M. Sahooli, S. Sabbaghi, R. Saboori, Synthesis and characterization of mono sized CuO nanoparticles, Mater. Lett. 81 (2012) 169–172, https://doi.org/10.1016/j.matlet.2012.04.148.

[2] Y.-Z. Tsai, N.-F. Wang, M.-R. Tseng, F.-H. Hsu, Transparent conducting Al and Y codoped ZnO thin film deposited by DC sputtering, Mater. Chem. Phys. 123 (2010) 300–303, https://doi.org/10.1016/j.matchemphys.2010.04.015.

[3] M.K. Gupta, N. Sinha, B.K. Singh, B. Kumar, Synthesis of K-doped p-type ZnO nanorods along (100) for ferroelectric and dielectric applications, Mater. Lett. 64 (2010) 1825–1828, https://doi.org/10.1016/j.matlet.2010.05.044.

[4] C. Ratnasamy, J.P. Wagner, Water gas shift catalysis, Catal. Rev. 51 (2009) 325–440, https://doi.org/10.1080/01614940903048661.

[5] S. Nations, M. Long, M. Wages, J.D. Maul, C.W. Theodorakis, G.P. Cobb, Subchronic and chronic developmental effects of copper oxide (CuO) nanoparticles on xenopus laevis, Chemosphere 135 (2015) 166–174, https://doi.org/10.1016/j.chemosphere.2015.03.078.

[6] F. Perreault, S.P. Melegari, C.H. da Costa, A.L. de Oliveira Franco Rossetto, R. Popovic, W.G. Matias, Genotoxic effects of copper oxide nanoparticles in Neuro 2A cell cultures, Sci. Total Environ. 441 (2012) 117–124, https://doi.org/10.1016/j.scitotenv.2012.09.065.

[7] M.K. Gupta, N. Sinha, B. Kumar, *p* -type K-doped ZnO nanorods for optoelectronic applications, J. Appl. Phys. 109 (2011), 083532, https://doi.org/10.1063/1.3574656.

[8] A.B. Devi, D.S. Moirangthem, N.C. Talukdar, M.D. Devi, N.R. Singh, M.N. Luwang, Novel synthesis and characterization of CuO nanomaterials: biological applications, Chin. Chem. Lett. 25 (2014) 1615–1619, https://doi.org/10.1016/j.cclet.2014.07.014.

[9] Q. Zhang, K. Zhang, D. Xu, G. Yang, H. Huang, F. Nie, C. Liu, S. Yang, CuO nanostructures: synthesis, characterization, growth mechanisms, fundamental properties, and applications, Prog. Mater. Sci. 60 (2014) 208–337, https://doi.org/10.1016/j.pmatsci.2013.09.003.

[10] A.P. Jeyakumari, M. Ramakrishnan, Y. Nithyanandhi, S. Renuka, Structural and antibacterial activity of copper oxide nano particles, IOSR J. Appl. Phys. 1 (2017) 57–63, https://doi.org/10.9790/4861-17002015763.

[11] D. Li, Y.H. Leung, A.B. Djurišić, Z.T. Liu, M.H. Xie, J. Gao, W.K. Chan, CuO nanostructures prepared by a chemical method, J. Cryst. Growth 282 (2005) 105–111, https://doi.org/10.1016/j.jcrysgro.2005.04.090.

[12] H. Zhu, C. Zhang, Y. Yin, Rapid synthesis of copper nanoparticles by sodium hypophosphite reduction in ethylene glycol under microwave irradiation, J. Cryst. Growth 270 (2004) 722–728, https://doi.org/10.1016/j.jcrysgro.2004.07.008.

[13] H.T. Zhu, C.Y. Zhang, Y.M. Tang, J.X. Wang, Novel synthesis and thermal conductivity of CuO nanofluid, J. Phys. Chem. C 111 (2007) 1646–1650, https://doi.org/10.1021/jp065926t.

[14] B.R. Bade, S.R. Rondiya, Y.V. Hase, M.P. Nasane, S.B. Jathar, S.V. Barma, K. B. Kore, D.S. Nilegave, S.R. Jadkar, A.M. Funde, Hydrothermally synthesized CuO nanostructures and their application in humidity sensing, Pune, India, https://doi.org/10.1063/5.0043341, 2021.

[15] Anu, N. Thakur, K. Kumar, K.K. Sharma, Application of Co-doped copper oxide nanoparticles against different multidrug resistance bacteria, Inorg. Nano-Metal Chem. 50 (2020) 933–943, https://doi.org/10.1080/24701556.2020.1728554.

[16] L. Vimala Devi, S. Sellaiyan, T. Selvalakshmi, H.J. Zhang, A. Uedono, K. Sivaji, S. Sankar, Synthesis, defect characterization and photocatalytic degradation efficiency of Tb doped CuO nanoparticles, Adv. Powder Technol. 28 (2017) 3026–3038, https://doi.org/10.1016/j.apt.2017.09.013.

[17] Y. Lv, L. Li, P. Yin, T. Lei, Synthesis and evaluation of the structural and antibacterial properties of doped copper oxide, Dalton Trans. 49 (2020) 4699–4709, https://doi.org/10.1039/D0DT00201A.

[18] S. Iqbal, M. Javed, A. Bahadur, M.A. Qamar, M. Ahmad, M. Shoaib, M. Raheel, N. Ahmad, M.B. Akbar, H. Li, Controlled synthesis of Ag-doped CuO nanoparticles as a core with poly(acrylic acid) microgel shell for efficient removal of methylene blue under visible light, J. Mater. Sci. Mater. Electron. 31 (2020) 8423–8435, https://doi.org/10.1007/s10854-020-03377-9.

[19] L.M. Dwivedi, N. Shukla, K. Baranwal, S. Gupta, S. Siddique, V. Singh, Gum Acacia modified Ni doped CuO nanoparticles: an excellent antibacterial material, J. Cluster Sci. 32 (2021) 209–219, https://doi.org/10.1007/s10876-020-01779-7.

[20] A. Pugazhendhi, S.S. Kumar, M. Manikandan, M. Saravanan, Photocatalytic properties and antimicrobial efficacy of Fe doped CuO nanoparticles against the pathogenic bacteria and fungi, Microb. Pathog. 122 (2018) 84–89, https://doi.org/10.1016/j.micpath.2018.06.016.

[21] H. Zhu, F. Zhao, L. Pan, Y. Zhang, C. Fan, Y. Zhang, J.Q. Xiao, Structural and magnetic properties of Mn-doped CuO thin films, J. Appl. Phys. 101 (2007), 09H111, https://doi.org/10.1063/1.2711711.

[22] S.M. Yakout, A.M. El-Sayed, Structural, morphological and ferromagnetic properties of pure and (Mn, Co) codoped CuO nanostructures, J. Supercond. Nov. Magnetism 29 (2016) 2961–2968, https://doi.org/10.1007/s10948-016-3641-9.

[23] H. Khmissi, A.M. El Sayed, M. Shaban, Structural, morphological, optical properties and wettability of spin-coated copper oxide; influences of film thickness, Ni, and (La, Ni) co-doping, J. Mater. Sci. 51 (2016) 5924–5938, https://doi.org/10.1007/s10853-016-9894-7.

[24] A.M. El Sayed, M. Shaban, Structural, optical and photocatalytic properties of Fe and (Co, Fe) co-doped copper oxide spin coated films, Spectrochim. Acta Mol. Biomol. Spectrosc. 149 (2015) 638–646, https://doi.org/10.1016/j.saa.2015.05.010.

[25] S.J. Priscilla, K. Sivaji, L. Vimaladevi, in: Synthesis and Characterization of Na Doped Cupric Oxide (CuO) Nanoparticles, 2017, 050128, https://doi.org/10.1063/1.4980361. Bhubaneswar, Odisha, India.

[26] H. Siddiqui, M.R. Parra, M.S. Qureshi, M.M. Malik, F.Z. Haque, Studies of structural, optical, and electrical properties associated with defects in sodium-doped copper oxide (CuO/Na) nanostructures, J. Mater. Sci. 53 (2018) 8826–8843, https://doi.org/10.1007/s10853-018-2179-6.

[27] A. Tabib, W. Bouslama, B. Sieber, A. Addad, H. Elhouichet, M. Ferid, R. Boukherroub, Structural and optical properties of Na doped ZnO nanocrystals: application to solar photocatalysis, Appl. Surf. Sci. 396 (2017) 1528–1538, https://doi.org/10.1016/j.apsusc.2016.11.204.

[28] N. Budiredla, A. Kumar, S. Thota, J. Kumar, Synthesis and optical characterization of Mg 1- x Ni x O nanostructures, Int. Sch. Res. Notices Nanomater. 2012 (2012) 1–8, https://doi.org/10.5402/2012/865373.

[29] N. Wongpisutpaisan, P. Charoonsuk, N. Vittayakorn, W. Pecharapa, Sonochemical synthesis and characterization of copper oxide nanoparticles, Energy Proc. 9 (2011) 404–409, https://doi.org/10.1016/j.egypro.2011.09.044.

[30] S. Anandan, G.-J. Lee, J.J. Wu, Sonochemical synthesis of CuO nanostructures with different morphology, Ultrason. Sonochem. 19 (2012) 682–686, https://doi.org/10.1016/j.ultsonch.2011.08.009.

[31] J. Gounder Thangamani, S.K. Khadheer Pasha, Hydrothermal synthesis of copper (II) oxide-nanoparticles with highly enhanced BTEX gas sensing performance using chemiresistive sensor, Chemosphere 277 (2021), 130237, https://doi.org/10.1016/j.chemosphere.2021.130237.

[32] A.J. Yin, J. Li, W. Jian, A.J. Bennett, J.M. Xu, Fabrication of highly ordered metallic nanowire arrays by electrodeposition, Appl. Phys. Lett. 79 (2001) 1039–1041, https://doi.org/10.1063/1.1389765.

[33] H. Fan, L. Yang, W. Hua, X. Wu, Z. Wu, S. Xie, B. Zou, Controlled synthesis of monodispersed CuO nanocrystals, Nanotechnology 15 (2004) 37–42, https://doi.org/10.1088/0957-4484/15/1/007.

[34] E. Ayoman, S.G. Hosseini, Synthesis of CuO nanopowders by high-energy ball-milling method and investigation of their catalytic activity on thermal decomposition of ammonium perchlorate particles, J. Therm. Anal. Calorim. 123 (2016) 1213–1224, https://doi.org/10.1007/s10973-015-5059-1.

[35] H. Wang, J.-Z. Xu, J.-J. Zhu, H.-Y. Chen, Preparation of CuO nanoparticles by microwave irradiation, J. Cryst. Growth 244 (2002) 88–94, https://doi.org/10.1016/S0022-0248(02)01571-3.

[36] D.I. Son, C.H. You, T.W. Kim, Structural, optical, and electronic properties of colloidal CuO nanoparticles formed by using a colloid-thermal synthesis process, Appl. Surf. Sci. 255 (2009) 8794–8797, https://doi.org/10.1016/j.apsusc.2009.06.056.

[37] J.F. Xu, W. Ji, Z.X. Shen, S.H. Tang, X.R. Ye, D.Z. Jia, X.Q. Xin, Preparation and characterization of CuO nanocrystals, J. Solid State Chem. 147 (1999) 516–519, https://doi.org/10.1006/jssc.1999.8409.

[38] D. Chua, S.B. Kim, K. Li, R. Gordon, Low temperature chemical vapor deposition of cuprous oxide thin films using a copper(I) amidinate precursor, ACS Appl. Energy Mater. 2 (2019) 7750–7756, https://doi.org/10.1021/acsaem.9b01683.

[39] B. Nageswara Rao, P. Tirupathi Rao, K. Vasudha, Sk. Esub Basha, D.S.L. Prasanna, T. Bhushana Rao, K. Samatha, R.K. Ramachandra, Physiochemical characterization of sodium doped zinc oxide nano powder for antimicrobial applications, Spectrochim. Acta Mol. Biomol. Spectrosc. 291 (2023), 122297, https://doi.org/10.1016/j.saa.2022.122297.

[40] C. Xu, Y. Liu, G. Xu, G. Wang, Preparation and characterization of CuO nanorods by thermal decomposition of CuC_2O_4 precursor, Mater. Res. Bull. 37 (2002) 2365–2372, https://doi.org/10.1016/S0025-5408(02)00848-6.

[41] L.B. Truong, D. Medina-Cruz, J.J. Martinez-Sanmiguel, A. Soto-Mendoza, I. G. Esquivel-Lopez, Y. Perez, M. Saravanan, H. Barabadi, J.L. Cholula-Diaz, E. Mostafavi, Biogenic metal nanomaterials to combat antimicrobial resistance, in: Emerging Nanomaterials and Nano-Based Drug Delivery Approaches to Combat

Antimicrobial Resistance, Elsevier, 2022, pp. 261–304, https://doi.org/10.1016/B978-0-323-90792-7.00011-7.

[42] A. Benko, K. Reczynska-Kolman, D. Medina-Cruz, J.L. Cholula-Diaz, C. O'Connell, L.B. Truong, L. Mart'nez, P. Kazimierczak, A. Przekora, S. Wilk, H. Barabadi, Y. Huttel, J.M. García-Martín, E. Pamula, T.J. Webster, Nanomaterials to aid wound healing and infection control, in: Antimicrobial Activity of Nanoparticles, Elsevier, 2023, pp. 19–67, https://doi.org/10.1016/B978-0-12-821637-8.00002-X.

[43] E. Mostafavi, A. Zarepour, H. Barabadi, A. Zarrabi, L.B. Truong, D. Medina-Cruz, Antineoplastic activity of biogenic silver and gold nanoparticles to combat leukemia: beginning a new era in cancer theragnostic, Biotechnol. Rep. 34 (2022), e00714, https://doi.org/10.1016/j.btre.2022.e00714.

[44] I. Virmani, C. Sasi, E. Priyadarshini, R. Kumar, S.K. Sharma, G.P. Singh, R. B. Pachwarya, R. Paulraj, H. Barabadi, M. Saravanan, R. Meena, Comparative anticancer potential of biologically and chemically synthesized gold nanoparticles, J. Cluster Sci. 31 (2020) 867–876, https://doi.org/10.1007/s10876-019-01695-5.

[45] S. Wilk, A. Przekora, P. Kazimierczak, D. Medina-Cruz, L. Martinez, C. O'Connell, L.B. Truong, K. Reczynska-Kolman, H. Barabadi, J.L. Cholula-Diaz, E. Pamula, Y. Huttel, J.M. García-Martín, T.J. Webster, A. Benko, Nanocomposite scaffolds and coatings for wound healing and infection control, in: Antimicrobial Activity of Nanoparticles, Elsevier, 2023, pp. 69–99, https://doi.org/10.1016/B978-0-12-821637-8.00007-9.

[46] H. Barabadi, K. Jounaki, E. Pishgahzadeh, H. Morad, N. Bozorgchami, H. Vahidi, Bioengineered metal-based antimicrobial nanomaterials for surface coatings, in: Antiviral and Antimicrobial Smart Coatings, Elsevier, 2023, pp. 489–539, https://doi.org/10.1016/B978-0-323-99291-6.00012-8.

[47] A. Vernet-Crua, D.M. Cruz, E. Mostafavi, L.B. Truong, H. Barabadi, J.L. Cholula-Diaz, G. Guisbiers, T.J. Webster, Green-synthesized metallic nanoparticles for antimicrobial applications, in: Nanomedicine, Elsevier, 2023, pp. 297–338, https://doi.org/10.1016/B978-0-12-818627-5.00014-2.

[48] J. Pasquet, Y. Chevalier, J. Pelletier, E. Couval, D. Bouvier, M.-A. Bolzinger, The contribution of zinc ions to the antimicrobial activity of zinc oxide, Colloids Surf. A Physicochem. Eng. Asp. 457 (2014) 263–274, https://doi.org/10.1016/j.colsurfa.2014.05.057.

[49] M.S. Usman, M.E. El Zowalaty, K. Shameli, N. Zainuddin, M. Salama, N.A. Ibrahim, Synthesis, characterization, and antimicrobial properties of copper nanoparticles, Int. J. Nanomed. 8 (2013) 4467–4479, https://doi.org/10.2147/IJN.S50837.

[50] A.W. Bauer, W.M. Kirby, J.C. Sherris, M. Turck, Antibiotic susceptibility testing by a standardized single disk method, Am. J. Clin. Pathol. 45 (1966) 493–496.

[51] J. Ramyadevi, K. Jeyasubramanian, A. Marikani, G. Rajakumar, A.A. Rahuman, Synthesis and antimicrobial activity of copper nanoparticles, Mater. Lett. 71 (2012) 114–116, https://doi.org/10.1016/j.matlet.2011.12.055.

[52] M.H. Babu, J. Podder, Bond length controlling opto-structural properties of Mn doped CuO thin films: an experimental and theoretical study, Mater. Sci. Semicond. Process. 129 (2021), 105798, https://doi.org/10.1016/j.mssp.2021.105798.

[53] D.E. Navarro-Lopez, R. Garcia-Varela, O. Ceballos-Sanchez, A. Sanchez-Martinez, G. Sanchez-Ante, K. Corona-Romero, D.A. Buentello-Montoya, A. Elias-Zuniga, E. R. Lopez-Mena, Effective antimicrobial activity of ZnO and Yb-doped ZnO nanoparticles against Staphylococcus aureus and Escherichia coli, Mater. Sci. Eng. C 123 (2021), 112004, https://doi.org/10.1016/j.msec.2021.112004.

[54] R. H R, S. M S, P. S, C.R. Ravikumara, N. H P, D. N, Costus Pictus leaf extract mediated biosynthesis of Fe and Mg doped CuO nanoparticles: structural, electrochemical and antibacterial analysis, Mater. Res. Express 6 (2019) 1150e5, https://doi.org/10.1088/2053-1591/ab4f20.

[55] A. Khorsand Zak, W.H. Abd. Majid, M.E. Abrishami, R. Yousefi, X-ray analysis of ZnO nanoparticles by williamson–hall and size–strain plot methods, Solid State Sci. 13 (2011) 251–256, https://doi.org/10.1016/j.solidstatesciences.2010.11.024.

[56] H. Mersian, M. Alizadeh, N. Hadi, Synthesis of zirconium doped copper oxide (CuO) nanoparticles by the pechini route and investigation of their structural and antibacterial properties, Ceram. Int. 44 (2018) 20399–20408, https://doi.org/10.1016/j.ceramint.2018.08.033.

[57] P. Mantecca, E. Moschini, P. Bonfanti, U. Fascio, I. Perelshtein, A. Lipovsky, G. Chirico, R. Bacchetta, L. Del Giacco, A. Colombo, A. Gedanken, Toxicity evaluation of a new Zn-doped CuO nanocomposite with highly effective antibacterial properties, Toxicol. Sci. 146 (2015) 16–30, https://doi.org/10.1093/toxsci/kfv067.

[58] D. Saravanakkumar, S. Sivaranjani, K. Kaviyarasu, A. Ayeshamariam, B. Ravikumar, S. Pandiarajan, C. Veeralakshmi, M. Jayachandran, M. Maaza, Synthesis and characterization of ZnO–CuO nanocomposites powder by modified perfume spray pyrolysis method and its antimicrobial investigation, J. Semiconduct. 39 (2018), 033001, https://doi.org/10.1088/1674-4926/39/3/033001.

[59] A. Azam, Size-dependent antimicrobial properties of CuO nanoparticles against Gram-positive and -negative bacterial strains, Int. J. Nanomed. (2012) 3527, https://doi.org/10.2147/IJN.S29020.

[60] M. Mayakannan, S. Gopinath, S. Vetrivel, Synthesis and characterization of antibacterial activities nickel doped cobalt oxide nano particles, Mater. Chem. Phys. 242 (2020), 122282, https://doi.org/10.1016/j.matchemphys.2019.122282.

[61] A.S. Ethiraj, D.J. Kang, Synthesis and characterization of CuO nanowires by a simple wet chemical method, Nanoscale Res. Lett. 7 (2012) 70, https://doi.org/10.1186/1556-276X-7-70.

[62] A. Ananth, S. Dharaneedharan, M.-S. Heo, Y.S. Mok, Copper oxide nanomaterials: synthesis, characterization and structure-specific antibacterial performance, Chem. Eng. J. 262 (2015) 179–188, https://doi.org/10.1016/j.cej.2014.09.083.

[63] M.M. Ba-Abbad, A.A.H. Kadhum, A. Bakar Mohamad, M.S. Takriff, K. Sopian, The effect of process parameters on the size of ZnO nanoparticles synthesized via the sol–gel technique, J. Alloys Compd. 550 (2013) 63–70, https://doi.org/10.1016/j.jallcom.2012.09.076.

[64] N.R. Dhineshbabu, V. Rajendran, N. Nithyavathy, R. Vetumperumal, Study of structural and optical properties of cupric oxide nanoparticles, Appl. Nanosci. 6 (2016) 933–939, https://doi.org/10.1007/s13204-015-0499-2.

[65] A. Muthuvel, M. Jothibas, C. Manoharan, Synthesis of copper oxide nanoparticles by chemical and biogenic methods: photocatalytic degradation and in vitro antioxidant activity, Nanotechnol. Environ. Eng. 5 (2020) 14, https://doi.org/10.1007/s41204-020-00078-w.

[66] E. Gharibshahi, E. Saion, Influence of dose on particle size and optical properties of colloidal platinum nanoparticles, Int. J. Mol. Sci. 13 (2012) 14723–14741, https://doi.org/10.3390/ijms131114723.

[67] A. Muthuvel, M. Jothibas, C. Manoharan, Effect of chemically synthesis compared to biosynthesized ZnO-NPs using Solanum nigrum leaf extract and their photocatalytic, antibacterial and in-vitro antioxidant activity, J. Environ. Chem. Eng. 8 (2020), 103705, https://doi.org/10.1016/j.jece.2020.103705.

[68] A.S.A. Alsubaie, Characterization and optical studies of hydroxyethyl cellulose-copper oxide nanocomposites, J. Spectrosc. 2022 (2022) 1–9, https://doi.org/10.1155/2022/8422803.

[69] T.S. Moss, A relationship between the refractive index and the infra-red threshold of sensitivity for photoconductors, Proc. Phys. Soc. B 63 (1950) 167–176, https://doi.org/10.1088/0370-1301/63/3/302.

[70] V.P. Gupta, N.M. Ravindra, Comments on the moss formula, Phys. Status Solidi 100 (1980) 715–719, https://doi.org/10.1002/pssb.2221000240.

[71] P. Hervé, L.K.J. Vandamme, General relation between refractive index and energy gap in semiconductors, Infrared Phys. Technol. 35 (1994) 609–615, https://doi.org/10.1016/1350-4495(94)90026-4.

[72] R.R. Reddy, S. Anjaneyulu, Analysis of the moss and ravindra relations, Phys. Status Solidi 174 (1992) K91–K93, https://doi.org/10.1002/pssb.2221740238.

[73] G. Durai, P. Kuppusami, K. Viswanathan, Investigation on microstructure and improved supercapacitive performance of Mn doped CuO thin films prepared by reactive radio frequency magnetron sputtering, J. Mater. Sci. Mater. Electron. 29 (2018) 2051–2058, https://doi.org/10.1007/s10854-017-8118-5.

[74] B. Jia, M. Qin, Z. Zhang, Z. Cao, H. Wu, P. Chen, L. Zhang, X. Lu, X. Qu, The formation of CuO porous mesocrystal ellipsoids via tuning the oriented attachment mechanism, CrystEngComm 18 (2016) 1376–1383, https://doi.org/10.1039/C5CE02249E.

[75] A. Bhattacharjee, M. Ahmaruzzaman, CuO nanostructures: facile synthesis and applications for enhanced photodegradation of organic compounds and reduction of p-nitrophenol from aqueous phase, RSC Adv. 6 (2016) 41348–41363, https://doi.org/10.1039/C6RA03624D.

[76] A. Azam, Oves Ahmed, Habib Khan, A. Memic, Antimicrobial activity of metal oxide nanoparticles against Gram-positive and Gram-negative bacteria: a comparative study, Int. J. Nanomed. (2012) 6003, https://doi.org/10.2147/IJN.S35347.

[77] Y. Liu, L. He, A. Mustapha, H. Li, Z.Q. Hu, M. Lin, Antibacterial activities of zinc oxide nanoparticles against Escherichia coli O157:H7: antibacterial ZnO nanoparticles, J. Appl. Microbiol. 107 (2009) 1193–1201, https://doi.org/10.1111/j.1365-2672.2009.04303.x.

[78] R. Katwal, H. Kaur, G. Sharma, Mu. Naushad, D. Pathania, Electrochemical synthesized copper oxide nanoparticles for enhanced photocatalytic and antimicrobial activity, J. Ind. Eng. Chem. 31 (2015) 173–184, https://doi.org/10.1016/j.jiec.2015.06.021.

[79] S.M. Dizaj, F. Lotfipour, M. Barzegar-Jalali, M.H. Zarrintan, K. Adibkia, Antimicrobial activity of the metals and metal oxide nanoparticles, Mater. Sci. Eng. C 44 (2014) 278–284, https://doi.org/10.1016/j.msec.2014.08.031.

RJC

RASĀYAN *J. Chem.*
Vol. 17 | No. 2 |552-561| April - June | 2024
ISSN: 0974-1496 | e-ISSN: 0976-0083 | CODEN: RJCABP
http://www.rasayanjournal.com
http://www.rasayanjournal.co.in

METHOD (RP-HPLC) DEVELOPMENT FOR BELUMOSUDIL QUANTIFICATION AND LC-MS CHARACTERISATION OF BELUMOSUDIL DEGRADANTS GENERATED IN DEGRADATIONS RESEARCH

Mamidi Gopi[1,✉], Thota Siva Prasad[2], Dharmasoth Ramadevi[3]
and Keloth Basavaiah[4]
[1]Department of Chemistry, Dr. V. S. Krishna Govt. Degree and PG College (A), Visakhapatnam,
Andhra Pradesh-5300013, India
[2]Reasearch Scholar, Andhra University Trans-Disciplinary Research Hub (A.U TDR-HUB),
Andhra University, Visakhapatnam, Andhra Pradesh-531019, India
[3]Department of Pharmaceutical Sciences, Dr. Samuel George Institute of Pharmaceutical
Sciences, Markapur, Andhra Pradesh-523316, India
[4]Department of Analytical Chemistry, Andhra University, Visakhapatnam,
Andhra Pradesh-530003, India
✉Corresponding Author: drgopichem@gmail.com

ABSTRACT

This article discusses the development and authentication of an isocratic mode stability-indicating RP-HPLC method for belumosudil (BLSL) measurement in bulk, Rezurock tablets, and degraded Rezurock samples. The BLSL and its degradants were separated well at room temperature using a Phenyl C18 column. The isocratic mode mobile phase comprised of a combination of 0.1% triethylamine and pure acetonitrile (40:60 v/v) delivered by 1.0 mL/min flow, and 254 nm was used for monitoring the effluents. Studies on BLSL's stress-triggered degradation revealed no impact on the suggested method's accuracy as well as specificity. During degradation investigations, four BLSL degradants were generated. They were DPA-1 (Rt – 0.734 min), DPA-2 (Rt – 0.785 min); DPO-3 (Rt - 1.749 min); DPW-4 (Rt- 1.082 min). The study also employed the LC-MS approach to characterize the generated four BLSL degradants. The DPA-1 spectra scans had *m/z* 99.042, 194.110, 372.123 and 489.173 fragment ions, DPA-2 spectra scans had *m/z* 91.042, 166.115, 238.090 and 309.163 fragment ions, DPO-3 spectra scans had *m/z* 95.042, 194.110, 254.085 and 353.153 fragment ions and DPW-4 spectra scans had *m/z* 95.042, 194.110, 263.109, 337.158 and 454.204 fragment ions. Based on scans, the molecular weight, probable structure, and likely path for their formation were proposed.

Keywords: Belumosudil, Stability, Degradation, HPLC, Degradants, Characterization, LC-MS.
RASĀYAN *J. Chem.*, Vol. 17, No. 2, 2024

INTRODUCTION

A systemic illness referred to as "graft-versus-host disease" develops when the recipient's bodily cells become targeted by the graft's immune cells, which recognize the host as nonself-cells.[1] The major factor attributing to morbidity along with death following transplantation of hematopoietic stem cells is thought to be "graft-versus-host disease". This consequence will kill over 10% of subjects.[2,3] Kadmon Pharmaceuticals has developed belumosudil (BLSL) to treat systemic sclerosis as well as chronic "graft-versus-host disease". BLSL was very first approved in the United States in July 2021 for the therapy of chronic "graft-versus-host disease" illness in adults and also pediatric patients who were 12 years or older.[4] The production and sale of many health-related products depend heavily on quality assurance and control. These two procedures ensure that the quality standards for health-related products have been met.[5] It is advised to carry out the quantitation of BLSL for quality control along with product development. Furthermore, assessing stability is a crucial step in developing of novel pharmacological medicines.

http://doi.org/10.31788/RJC.2024.1728793

Verifying how a drug molecule's or drug product's quality varies over time under the influence of numerous conditions, including light, humidity, acid, reducing agent, oxidizing agent, alkaline, and temperature, is the aim of stability testing.[6,7] This makes it possible to decide on appropriate storage settings, times for retests, and shelf life. So far, just a single RP-HPLC has been established by Padmavathi and Sowmya to determine the BLSL amount in their formulations and bulk forms.[8] Padmavathi and Sowmya utilized BDS C18 analytical column fixed at 30°C, phosphoric acid: acetonitrile (ratio 45:55 *v/v*) solvent mix with a stream rate of 1.0 mL/min as mobile phase, and 225.0 nm as detection and quantifying wavelength. BLSL retention time in the Padmavathi and Sowmya techniques was reported at 2.439 min. Padmavathi and Sowmya's technique did not report peak purities for BLSL in degradation conditions, characterization of BLSL degradants, and BLSL degradation pathway. In alignment with ICH requirements, this paper details the development and authentication of an isocratic mode stability-indicating RP-HPLC technique for the measurement of BLSL in the presence of all its components of degradation. With the use of LC-MS analysis, the degradation products of BLSL were assessed, and a suggested degradation route was also included.

EXPERIMENTAL

Chemicals

Sd Chemicals Ltd., (India) provided chromatography-mark acetonitrile and triethylamine. The same firm also provided high-quality analytical chemicals including peroxide, sodium hydroxide, and hydrochloric acid. The chromatography-marked water utilized in this investigation came from Milli Q (India).

BLSL API and BLSL Formulation

The supplier of BLSL API was BLD Pharma Tech Ltd (India). Rezurock tablet manufactured by Kadmon Pharmaceuticals (US) with a 200 mg per tablet label was employed in this research study.

Mobile Phase

The isocratic mode mobile phase comprised of a combination of 0.1% triethylamine and pure acetonitrile (40:60 *v/v*). The mobile phase was subjected to degassing over 10 min employing an ultrasonic sonicator ahead of being employed in the investigation. The membrane filter used for filtration of the mobile phase was of size 0.45 µm. As a diluent, the same mixture of mobile phase solvents was deployed.

BLSL Solutions

To make the stock BLSL solution, 5 mg of BLSL API was put into a 10 mL volumetric flask along with a few volumes of diluent. The flask was well-shook before further diluent was added to arrive at a 500 µg/mL concentration. All BLSL assay procedure validation parameters were tested using the working BLSL solution at the necessary concentrations (50 µg/mL) which was prepared after stock BLSL solution (500 µg/mL) had been diluted appropriately and well mixed.

Tablet BLSL Solutions

The mean weight of twenty BLSL tablets (Rezurock) was determined by weighing them. To make a finely ground powder, the tablets were blended in a dry, clean mortar. A precise amount of BLSL (5 mg) in the form of a finely powdered tablet was taken, dissolved in a minimal volume mobile phase, completely mixed, and agitated for 5 mins in a 10 mL volumetric flask. Up to 10 mL, of diluent solvent was added to produce a volume with 500 µg/mL concentrated tablet BLSL solution. Working tablet BLSL solution at the necessary concentration (50 µg/mL) for analysis was prepared after stock tablet BLSL solution (500 µg/mL) had been diluted appropriately and well mixed.

General Procedure

The "Waters Alliance" HPLC system, which has a quaternary pump and PDA detector, was used to develop and authenticate an isocratic mode stability-indicating RP-HPLC method for BLSL measurement. The BLSL and its degradants were separated well at room temperature using a Phenyl C18 column of length 150 mm, identification of 4.6 mm and 3.5 µm particle-sized dimensions. A 10 µl BLSL sample quantity for injection was applied for each study. An isocratic 1.0 mL/min input rate of the mobile phase was pumped through the phenyl column for the elution of BLSL and its degradants. Using the peak area response of BLSL measured at 254 nm wavelength, the BLSL assay was done.

BLSL Calibration Curve

To create the BLSL calibration curve, several series of BLSL solutions were made appropriately by diluting stock BLSL solution (500 µg/mL) with diluent. Six concentrations (12.5; 25.0; 37.5; 50.0; 62.5; and 75.0 µg/mL) were selected with a concentration spanning 12.50–75.00 µg/mL. Every BLSL concentration solution was evaluated following the general procedure given. Peak area, as well as peak height of BLSL, were submitted for least squares regression calculations to assess BLSL linearity. The result was a calibration equation that included the Y-intercept, slope, plus correlation coefficient.

Analysis of BLSL in Rezurock Tablets

Working tablet Rezurock solution (50 µg/mL concentration) was evaluated following the general procedure given. Peak area, as well as peak height of BLSL, were obtained. These data allow for the evaluation of the BLSL content in the tablet.

Mass Spectral Studies on BLSL

The "Triple Quad TM 5600" LC-MS/MS System controlled using "Analyst" software was used for this. To determine the BLSL fragmentation patterning, mass spectrum measurements were performed in the positive electrospray ionization manner in the mass span of 0–800 Da. Using a syringe pump, BLSL was directly fed into the mass spectrometer at a quantity of 50 µg/mL in the diluent. The mass parameters for BLSL analysis were tweaked correctly to generate an exclusive molecular ion peak for BLSL. Nebulizer and auxiliary gas were both high-purity nitrogen.

Degradation Studies

The compelled degradation investigation of BLSL employed conditions including 30% H_2O_2 (oxidizing reagent), 1.0 N HCl (acid reagent), 30% sodium bisulfate (reducing reagent), 1.0 N NaOH (alkaline reagent), Milli Q water (hydrolytic reagent), UV light (photo condition), and temperature (thermal condition).[9,10] 1.0 mL volume of 30% H_2O_2, 1.0 N HCl, 30% sodium bisulfate, 1.0 N NaOH, and Milli Q water were applied to degrade tablet Rezurock powder (500 µg/mL BLSL). For 30 min the solutions (Rezurock powder + 7 mL diluent + 1.0 mL of degradation reagent) were refluxed at a fixed temperature of 60 °C. The solutions went through filtering and then the right volume of dilution (up to 10 mL) was made. With diluent, subsequently dilute 5 mL of the deteriorated solutions to produce 50 mL for the BLSL degradation analysis. Thermal degradation tests involved placing 50 mg of solid dry tablet Rezurock powder at 105 ºC for a whole day (24 hr). A 24-hour photolytic degradation investigation with solid dry tablet BLSL powder (50 mg) was conducted beneath UV light inside a photochamber. The thermal degradation BLSL solution and photodegradation BLSL solution for BLSL degradation analysis was made following protocol as told in the section "Tablet BLSL solutions". Each of the stressed tablet Rezurock solutions was evaluated following the general procedure given. The BLSL assay of stressed samples was contrasted with the usual untreated BLSL.

LC-MS Studies on Degradants

The samples containing the degradants were submitted to LC-MS analysis with mass spectrum measurements performed in the positive electrospray ionization manner to better comprehend the structure of the degradants generated in the degradation scenarios that were carried out and also possible paths for degradant formation. Using LC-MS fragmentation investigation, each degradant's structural verification possible paths verification was ascertained.

RESULTS AND DISCUSSION

Optimization of BLSL Assay Conditions

For column selection, two columns like Phenyl C18 column and the Aligent C18 column were investigated. Both columns have a length of 150 mm, identification of 4.6 mm, and 3.5 µm particle-sized dimensions. Several solvent combinations, such as 0.1% formic acid/acetonitrile and 0.1% trimethylamine/acetonitrile with differing ratios, have been explored regarding mobile phase optimization. With 0.1% formic acid and pure acetonitrile (20:80 *v/v*) and Aligent C18 column, a very low plate count (353) was obtained. Just 353 plate counts and higher peak tailing (2.16) were obtained using the Aligent C18 column with 0.1% formic acid and pure acetonitrile (30:70 v/v). A peak with an RT of about 1.0 min was generated using pure acetonitrile (30% vol) and 0.1% formic acid (70% vol) in an Aligent C18 column. A disturbing baseline, a low plate count (245), and higher tailing (2.40) resulted in 0.1% formic acid, pure acetonitrile (50:50 v/v), and a Phenyl C18 column. We got the same results when 0.1% formic acid: pure acetonitrile (20:80 *v/v*), and a Phenyl C18 column was used. The same solvent blend in 30:70 (*v/v*) and the Phenyl C18 column also produced a lower plate count (1187). When 0.1% triethylamine: pure acetonitrile (40:60 *v/v*) and Phenyl C18 column were used, we got a good peak shape (tailing value of 0.98) with satisfactory plate count (6500) and more peak area (3710254) for BLSL (Fig.-1). The flow rate of solvents in column and column temperature was kept at 1.0 mL/min and room temperature, respectively, throughout all trail tests.

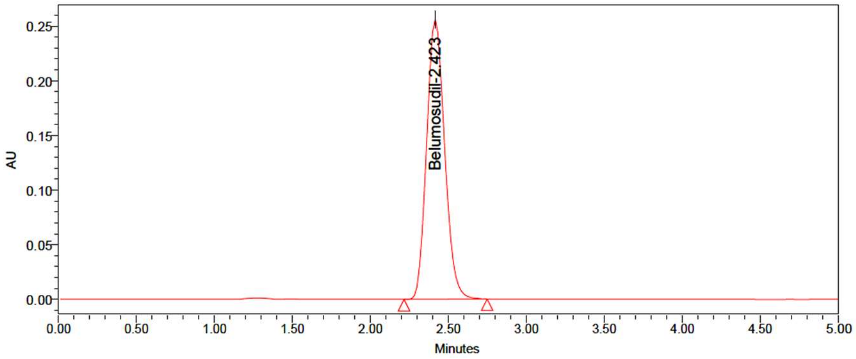

Fig.-1: BLSL Chromatogram using Phenyl C18 as the Preferred Column and 0.1% triethylamine: Pure Acetonitrile (40:60 V/V) as the Ideal Mobile Phase

The spectrum for BLSL dissolved in diluent was made. There were two determined λmax values for BLSL. One at 223.7 nm and the other at 292.4 nm. At 223.7 nm, BLSL had a greater response. Thus, 224 nm was chosen as the quantification wavelength.

Method Validation

Validated the newly established RP-HPLC BLSL assay procedure by adhering to ICH requirements.[11]

System Suitability

Six samples, each containing 50 µg/mL of BLSL, were evaluated following the aforementioned described "general procedure". In this study, the BLSL peak displayed good symmetry (mean - 0.930; %RSD – 0.130), with a satisfactory theoretical plate count (mean- 6575; %RSD – 0.545). BLSL retention time averaged 2.425 min, with a %RSD of 0.077. All parameters had RSDs substantially below 1%, signifying acceptable system suitability for BLSL analysis.

Selectivity

The "general procedure" given was followed for the assessment of the diluent blank, working BLSL solution (50 µg/mL), placebo, and tablet Rezurock solution (50 µg/mL). The chromatograms were assessed (Fig.-2). Without the intervention of the mobile phase and also excipients, the established "general procedure" demonstrated selectivity for BLSL analysis.

Linearity

Using the previously stated "general procedure," six concentrations (12.50, 25.00, 37.50, 50.00, 62.50, and 75.00 µg/mL) of BLSL were analyzed to examine the linearity. Having a correlation coefficient value of 0.9998, the linear equation for BLSL was $Y = 74279.74\ X + 16090.61$. In this equation, 'Y' is the BLSL peak response, and 'X' is the specified working BLSL concentration in µg/mL. The strong correlation coefficient findings (>0.999) established the good linearity exhibited by the BLSL calibration graph.

Sensitivity

The following formulas were implemented to figure out both the LOD and LOQ for BLSL based on the slope and standard deviation measurements from the linearity:

LOD = SD of BLSL area response/Slope of BLSL from linearity curve × 3.3
LOQ = SD of BLSL area response /Slope of BLSL from linearity curve × 10

For BLSL, the LOD was 0.15 µg/mL and the LOQ was 0.50 µg/mL, demonstrating adequate sensitivity for BLSL analysis by the specified "general procedure".

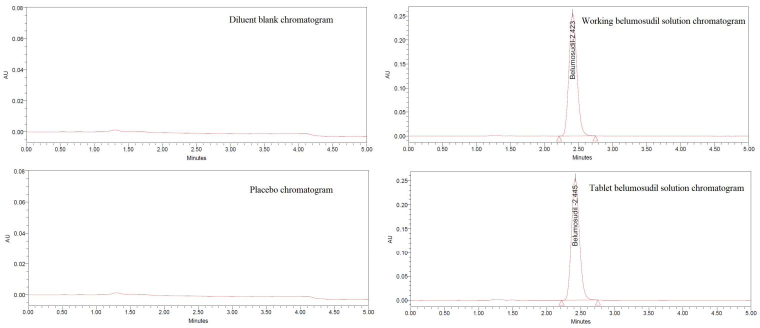

Fig.-2: Chromatograms Demonstrating Selectivity

Precision

System and method precisions for established "general procedure" were ensured by analyzing working BLSL solution (50 µg/mL) and BLSL spiked (50 µg/mL) Rezurock solution, respectively on the same day. By analyzing BLSL spiked (50 µg/mL) Rezurock solution (50 µg/mL) on a separate day employing an alternate operator and instrument, intermediate precision was verified. RSD (Table-1) is used for expressing the results. The findings demonstrated the great precision of the established "general procedure", with a deviation of fewer than 2%. This substantial level of precision is apt for QC evaluations of BLSL in the final pharmaceutical tablet Rezurock formulation.

Table-1: Precision Evaluation for BLSL Analysis

Precision →	System	Method	Intermediate
Sample ↓	BLSL Area	BLSL assay (%)	BLSL assay (%)
Mean	3738668	100.1	100.5
SD/RSD	21458.443/0.57	0.814/0.81	0.662/0.66

Accuracy

The implementation of accuracy involved producing three distinct tablet Rezurock samples that were spiked at 25 µg/mL, 50 µg/mL, and 75 µg/mL of BLSL. Three duplicates of each concentration solution were then injected followed by analysis using an established "general procedure". As indicated by Table-2, the accuracy findings (% BLSL assay) for the tested range (25 µg/mL, 50 µg/mL, and 75 µg/mL) were determined to fall between the 98–102 percent acceptance standards.

Table-2: Accuracy evaluation for BLSL analysis

Tested level ↓	Quantity Added (µg/mL)	Area Counts	Quantity Found (µg/mL)	% Quantity recovered
50 %	25	1835458	24.5	98.0
	25	1856471	24.8	99.2
	25	1869720	25.0	100.0
100 %	50	3752146	50.2	100.4
	50	3762148	50.3	100.6
	50	3726589	49.8	99.6
150 %	75	5563214	74.4	99.2
	75	5601529	74.9	99.9
	75	5598745	74.9	99.9
			Mean	99.6
			SD/RSD	0.551/0.55

Robustness

Robustness was investigated using planned little modifications, such as modest alterations to the mobile phase's composition and flow rate. The planned minor adjustments were carried out with a varied organic solvent proportion (acetonitrile) at 60% volume ± 5.0% volume and a flow speed of 1 mL/min ± 0.1 mL/min. The RDS% values for the BLSL assay (%) were used to evaluate the outcomes of deliberate modest alterations. As stated in Table 3, the RSD% was measured to have a value of < 2% in every instance. The findings demonstrated the great robustness of the established "general procedure".

Table-3: Robustness Evaluation for BLSL Analysis

Flow plus (mL/min)	Quantity for study (µg/mL)	Area obtained	% Assay evaluated	Flow minus (mL/min)	Quantity for study (µg/mL)	Area obtained	% Assay evaluated
1.1	50	3462279	100.3	0.9	50	3960105	99.6
	50	3454826	100.1		50	3974649	100.0
	50	3453007	100.0		50	3997997	100.6
		Mean	100.1			Mean	100.1
		SD/RSD	0.153/0.15			SD/RSD	0.500/0.50
Acetonitrile proportion plus	Quantity for study (µg/mL)	Area obtained	% Assay evaluated	Acetonitrile proportion minus	Quantity for study (µg/mL)	Area obtained	% Assay evaluated
65% volume	50	3520129	99.7	55% volume	50	3939870	98.7
	50	3511307	99.5		50	3940360	98.8
	50	3531989	100.1		50	3943200	98.8
		Mean	99.8			Mean	98.8
		SD/RSD	0.306/0.31			SD/RSD	0.058/0.06

Degradation Studies

The compelled degradation investigation on tablet Rezurock solution was carried out to ascertain the stability-indicating characteristics of the established "general procedure". Additionally, to make it easier to confirm and separate the active ingredient under investigation, "BLSL", from a variety of produced catalytic degradants. Additionally, this study offers details on BLSL's stability under various degradation scenarios executed (Table-4). The order of BLSL was: thermal condition > photo condition > 30% sodium bisulphate > Milli Q water > 1.0 N NaOH > 1.0 N HCl > 30% H_2O_2. This indicates a considerable degree of oxidation labile behavior for BLSL. This information is intended to help makers of drug generic products and bulk drug molecules optimize key quality features to minimize considerable peroxide exposure throughout the BLSL production process. About the BLSL principal peak, which has peak threshold estimates higher than purity angle estimates (Table-4), the present approach gave us extremely detailed information on the resolution including the separation performance of the neighboring co-eluted peaks under all degradation scenarios executed (Fig.-3).

Table-4: Robustness Evaluation for BLSL

Stress applied ↓	Quantity for study (µg/mL)	Area obtained	Stability (%) observed	Degradation (%) observed	Angle of purity	Threshold of purity
Control	50 µg/mL	3742814	99.9	0.1	0.129	5.234
Hydrolytic stress		3358216	89.7	10.3	1.359	5.152
Alkali stress		3274723	87.4	12.6	0.149	5.217
Thermal stress		3687540	98.5	1.5	1.371	5.168
Peroxide stress		3169254	84.6	15.4	0.171	5.229
Acid stress		3236528	86.4	13.6	0.164	5.261
Reduction stress		3627451	96.9	3.1	0.182	5.253
Photo stress		3655713	97.6	2.4	1.359	5.152

MS Spectra of BLSL

Five fragments in all were created from the BLSL, as Fig.-4 illustrates. The formula found for BLSL from mass studies was $C_{26}H_{24}N_6O_2$ and the experimental mass was 453.20.

Characterization of Degradants Produced

Upon treating BLSL with 1.0 N HCl (acid reagent), a single impurity (DPA-1) with a retention time scale of 0.734 min was generated. Through LC-MS spectral characterization (Fig.-5), the mass of DPA-1 was determined to be $(M+H)^+$ 489.1732, with a predicted molecular makeup of $C_{26}H_{25}N_6O_2^+$ and chemical name *N*-(1*H*-indazol-5-yl)-2-(3-(2-(isopropylamino)-2-oxoethoxy)phenyl)quinazolin-4-aminium.

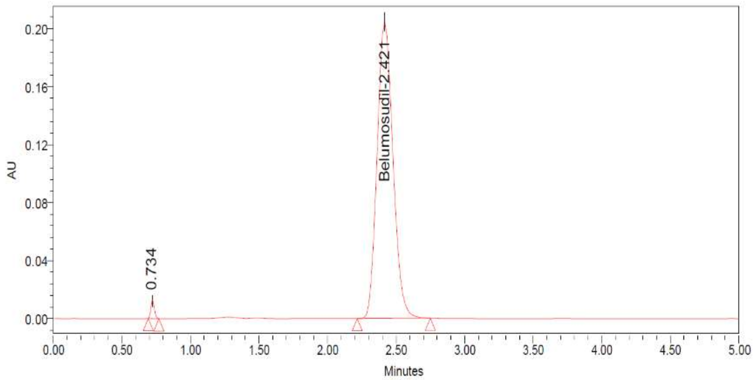

1.0 N HCl (acid reagent) induced BLSL degradation chromatogram

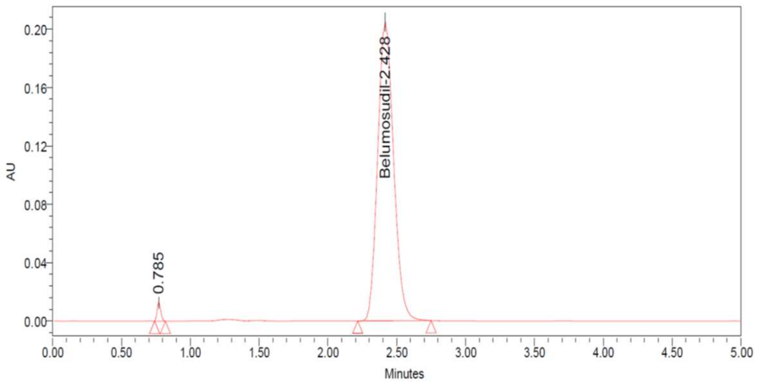

1.0 N NaOH (alkaline reagent) induced BLSL degradation chromatogram

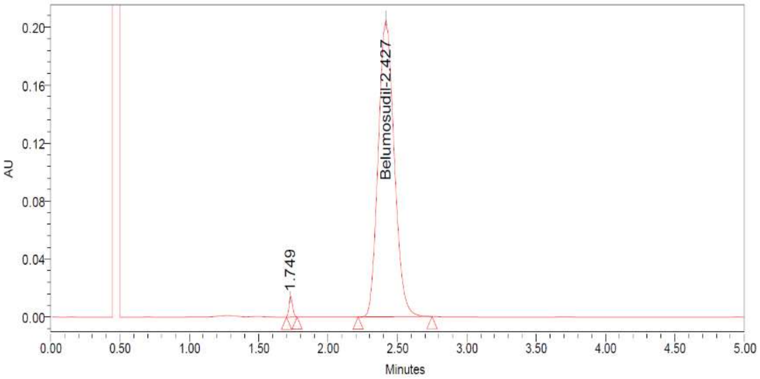

30% H_2O_2 (oxidizing reagent) induced BLSL degradation chromatogram

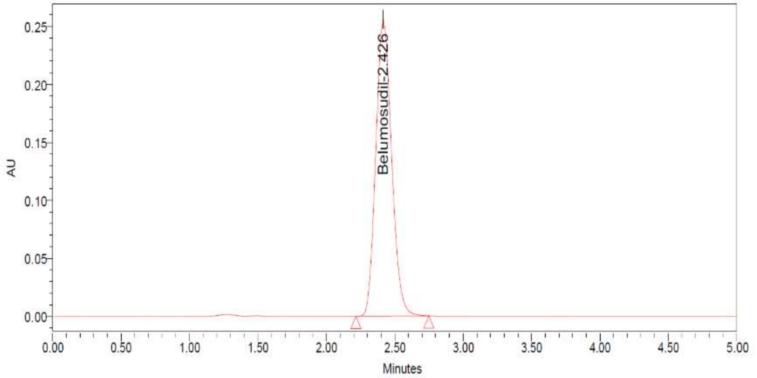

30% sodium bisulphate (reducing reagent) induced BLSL degradation chromatogram

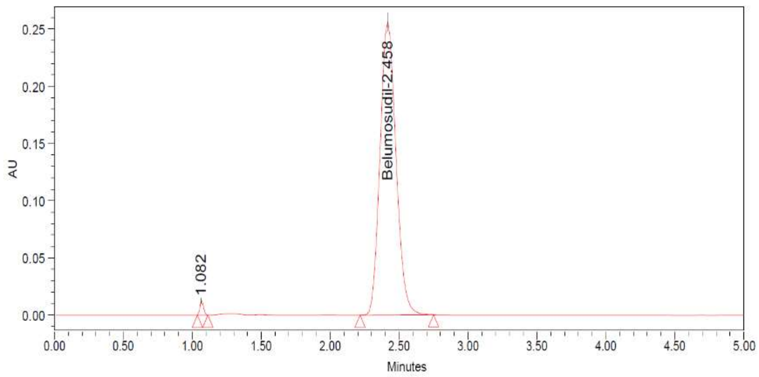

Milli Q water (hydrolytic reagent) induced BLSL degradation chromatogram

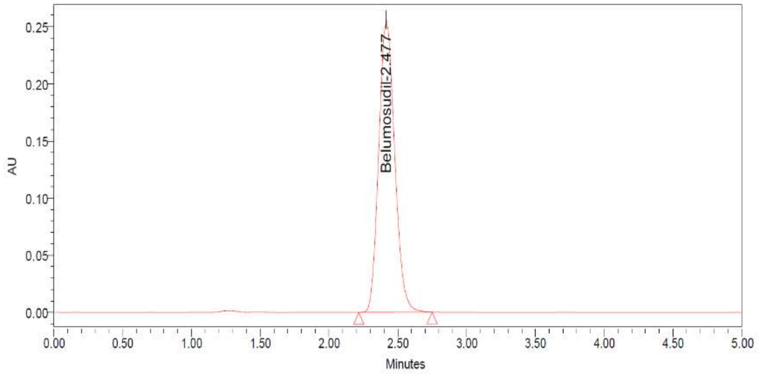

UV light (photo condition) induced BLSL degradation chromatogram

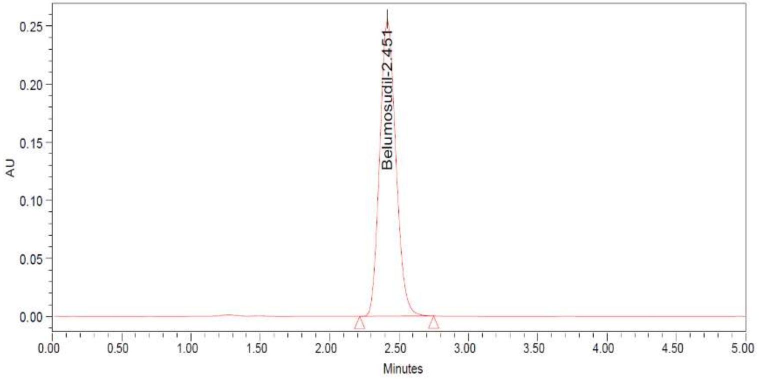

Temperature (thermal condition) induced BLSL degradation chromatogram
Fig.-3: Chromatograms of BLSL under all Degradation Scenarios Executed

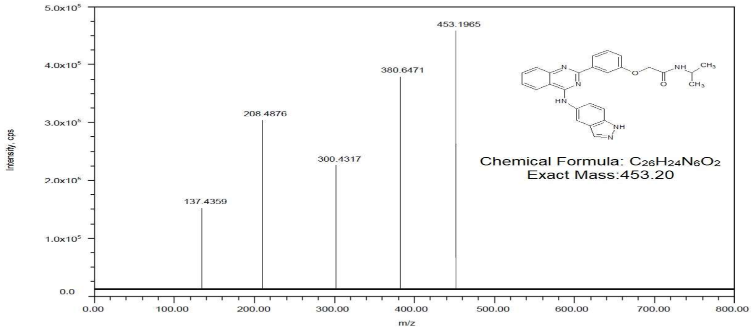

Fig.-4: BLSL Line Spectrum Obtained Through an MS Investigate

Figure-6 shows a probable route for the generation of DPA-1 from BLSL in an environment that is acidic. Upon degradation treatment with 1.0 N NaOH (an alkaline reagent), BLSL yielded one impurity (DPA-2) with a retention duration of 0.785 min. Through LC-MS spectral characterization (Fig.-5), the mass of

DPA-2 was determined to be $(M+H)^+$ 166.115, with a predicted molecular makeup of $C_{10}H_{15}NO$ and chemical name N-(phenoxymethyl)propan-2-amine. Figure-6 illustrates a likely pathway for BLSL to produce DPA-2 in an alkaline environment. After BLSL was oxidized with peroxide, one impurity (DPO-3) with a retention timescale of 1.749 min resulted. The mass of DPO-3 was ascertained to be $(M+H)^+$ 254.085 by LC-MS spectral analysis (Fig.-5), with an anticipated molecular composition of $C_{14}H_{11}N_3O_2$ and chemical name 3-(4-(hydroxyamino)quinazolin-2-yl)phenol. Figure-6 illustrates a likely pathway for BLSL to produce DPO-3 in a peroxide environment. Using Milli Q water treatment for hydrolysis, BLSL yielded an impurity (DPW-4) with a retention time scale of 1.082 min. The mass of DPW-4 was ascertained to be $(M+H)^+$ 337.158 by LC-MS spectral analysis (Fig.-5), with an anticipated molecular composition of $C_{19}H_{20}N_4O_2$ and chemical name 2-(3-(4-aminoquinazolin-2-yl)phenoxy)-N-isopropylacetamide. A plausible route for BLSL to generate DPW-4 in a neutral environment is depicted in Fig.-6.

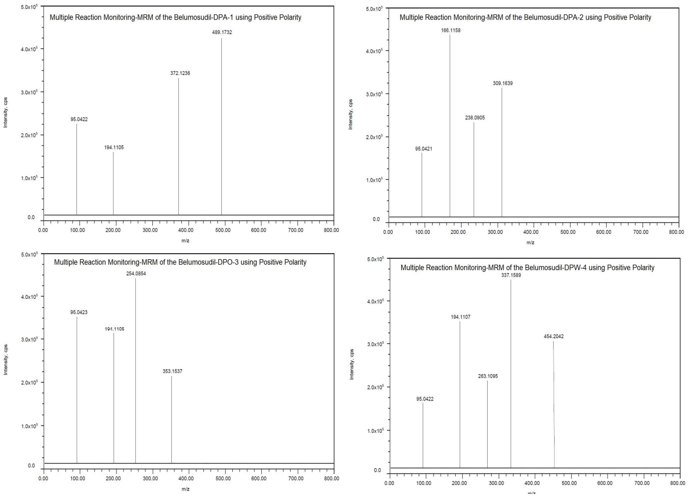

Fig.-5: Mass Spectral DPA-1, DPA–2, DPO-3 and DPW-4 Scans

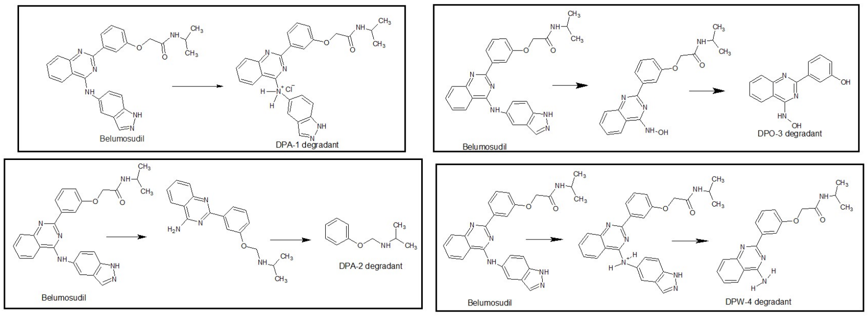

Fig.-6: Formation Path for DPA-1, DPA–2, DPO-3 and DPW-4

Method Applicability

To verify the method's applicability, the suggested "general procedure" was used with Rezurock tablets. The manufacturer claimed that each Rezurock pill included 200 mg of pure BLSL. The computed content of the 197.60 mg pure BLSL/Rezurock tablet was 98.80% of the BLSL amount as stated by the manufacturer. With recoveries ranging from 98.26% to 99.34%, the suggested "general procedure" proved to be accurate regarding BLSL determination and was deemed acceptable.

CONCLUSION

The development and authentication of an isocratic mode stability-indicating RP-HPLC technique for the measurement of BLSL was described herein for the first time. By meeting acceptance requirements, the validation guidelines supported the proposed quantitative method's validity for BLSL quantitation and detection at lower content levels in bulk and Rezurock tablets. All stressed Rezurock samples were analyzed, and the results show that the recommended “general procedure” is capable of identifying every degradant that has been produced, indicating the method's capacity for stability. The way BLSL degraded was investigated. The drug did not exhibit any impurity development, making it stable under reduction, thermal, and photolytic conditions. However, four BLSL degradants were formed, one each in acid (DPA-1), base (DPA-2), oxidation (DPO-3), and neutral (DPW-4) stress conditions. Employed the LC-MS approach successfully to characterize the generated four BLSL degradants.

CONFLICT OF INTERESTS

The authors declare that there is no conflict of interest.

AUTHOR CONTRIBUTIONS

All the authors contributed significantly to this manuscript, participated in reviewing/editing and approved the final draft for publication. The research profile of the authors can be verified from their ORCID ids, given below:

Mamidi Gopi http://orchid.org/0009-0008-8003-840X
Thota Siva Prasad http://orchid.org/0009-0004-9285-2311
Dharmasoth Ramadevi http://orchid.org/0000-0001-9379-9795
Keloth Basavaiah http://orchid.org/0000-0002-6227-4424

REFERENCES

1. G. Socié and J. Ritz, *Blood*, **124**, 374(2014), https://doi.org/10.1182/blood-2014-01-514752
2. T. Teshima and G.R. Hill, *Frontiers in Immunology*, **12,** 715424(2021), https://doi.org/10.3389/fimmu.2021.715424
3. M.O. Jamil and S. Mineishi, *International Journal of Hematology*, **101**, 452(2015), https://doi.org/10.1007/s12185-015-1785-1
4. H.A. Blair, *Drugs*, **81**, 1677(2021), https://doi.org/10.1007/s40265-021-01593-z
5. S. Ozawa, H.H. Chen, Y.A. Lee, C.R. Higgins, and T.T. Yemeke, *American Journal* of *Tropical Medicine* and *Hygiene*, **106**, 1778 (2022), https://doi.org/10.4269/ajtmh.21-1123
6. O. González-González, I.O. Ramirez, B.I. Ramirez, P. O'Connell, M.P. Ballesteros, J.J. Torrado and D.R. Serrano, *Pharmaceutics*, **14**, 2324(2022), https://doi.org/10.3390/pharmaceutics14112324
7. C. Ammann, *AAPS PharmSciTech*, **12**, 1264 (2011), https://doi.org/10.1208/s12249-011-9684-0
8. S.T. Padmavathi and P.S. Sowmya, *International Journal of Pharmacy and Pharmaceutical Research*, **25**, 119(2022).
9. ICH guidelines, ICH Harmonised Tripartite Guideline Stability, Q1A(R2): Stability testing of new drug substances and products, Geneva, Switzerland (2003).
10. WHO. Annex 10. Stability Testing of Active Pharmaceutical Ingredients and Finished Pharmaceutical Products. WHO; Geneva, Switzerland (2018).
11. ICH Guidelines, Validation of analytical procedures technical requirements for registration of pharmaceuticals for human use: Text and Methodology Q 2 (R1), Geneva, Switzerland (2005).

[RJC- 8793/2024]

Spectrochimica Acta Part A: Molecular and Biomolecular Spectroscopy 291 (2023) 122297

Contents lists available at ScienceDirect

Spectrochimica Acta Part A:
Molecular and Biomolecular Spectroscopy

journal homepage: www.journals.elsevier.com/spectrochimica-acta-part-a-molecular-and-biomolecular-spectroscopy

Physiochemical characterization of sodium doped zinc oxide nano powder for antimicrobial applications

B. Nageswara Rao [a,b,f], P. Tirupathi Rao [a], K. Vasudha [c], Sk. Esub Basha [a], D.S.L. Prasanna [d,g], T. Bhushana Rao [e], K. Samatha [b], R.K. Ramachandra [a,e,*]

[a] Crystal Growth and Nano-Science Research Center, Department of Physics, Government College (A), Rajamahendravaram, Andhra Pradesh 533105, India
[b] Department of Physics, Andhra University, Visakhapatnam, Andhra Pradesh 530003, India
[c] Department of Biotechnology, Government College (A), Rajamahendravaram, Andhra Pradesh 533105, India
[d] Department of Chemistry, Acharya Nagarjuna University, Guntur 522510, A.P., India
[e] Government Degree College, Chodavaram, Visakhapatnam, Andhra Pradesh 531036, India
[f] Department of Physics, Dr VS Krishna Government Degree College (A), Visakhapatnam, A.P, India
[g] Department of Chemistry, Dr VS Krishna Government Degree College (A), Visakhapatnam, A.P, India

HIGHLIGHTS

- This article reported the synthesis of pure and Na doped zinc oxide nano powders ($Zn_{1-x}Na_xO$) through co-precipitation process.
- Hexagonal wurtzite $Zn_{1-x}Na_xO$ nano powders with high crystallinity and stability were confirmed by XRD.
- The factors such as particle size and surface morphology were controlled with varying Na concentrations.
- The absorption peaks of as-synthesized $Zn_{0.99}Na_{0.01}O$ samples are recorded at 196, 284 and 365 nm, respectively.
- The as-prepared $Zn_{1-x}Na_xO$ nano powders were proved to be excellent antibacterial and antifungal agents.

GRAPHICAL ABSTRACT

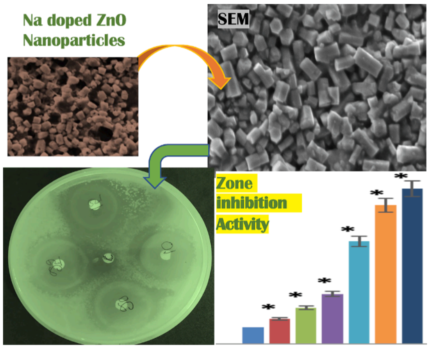

ARTICLE INFO

Keywords:
ZnO NPs
Semiconductors
Optical properties
Antibacterial activity
Antifungal activity

ABSTRACT

Zinc oxide (ZnO) is one of the semiconductor materials with unique antimicrobial properties towards various microorganisms. In this article, pure and Na doped ZnO nanopowders were synthesized by easiest and cost-effective co-precipitation process. X-ray diffraction (XRD), Fourier transform infrared spectroscopy (FT-IR), ultraviolet – visible (UV – Vis) spectroscopy, scanning electron microscopy (SEM), and Energy dispersive X-ray analysis (EDAX) techniques were used to characterize the particle size, surface morphology and chemical composition of prepared materials. The XRD analysis revealed that the samples exhibiting hexagonal wurtzite crystal structure with high crystallinity and the average crystallite size values increased from 23.51 to 28.118 nm. The UV – Vis spectroscopy results exposed that the bandgap energy (E_g) of the samples with the values in the range of 3.068–3.301 eV. The SEM micrographs showed that the morphology of the of synthesized particles are hexagonal and spherical in nanometric size. The EDX spectra confirmed the elemental composition of Na, Zn and O in the crystal lattice and FTIR spectroscopic data proved the formation of functional groups and the presence of

---

* Corresponding author.
E-mail address: ramc@gcrjy.ac.in (R.K. Ramachandra).

https://doi.org/10.1016/j.saa.2022.122297
Received 9 November 2022; Received in revised form 23 December 2022; Accepted 28 December 2022

chemical bonding at the ZnO interface. Antibacterial activity of pure and Na doped Zinc oxide nanoparticles against Gram-negative pathogens such as Escherichia coli, Pseudomonas aeruginosa & Klebsiella pneumoniae and Gram-positive pathogens such as *Staphylococcus aureus* reveal that the zone of inhibition increases with increasing Na concentration. The antifungal activity against *Aspergillus* and *Candida* was investigated. These results demonstrated that the pure and Na doped ZnO samples exhibit enhanced antibacterial and antifungal activity with increasing particle size in presence of visible light and they could be used as good antibacterial as well as antifungal agents.

1. Introduction

Semiconductor nanomaterials with large band gap have drawn much interest to the researchers in the field of electronics, optics, optoelectronics and photovoltaic cells. Amongst the various semiconductor nanoparticles discussed so far, Zinc Oxide is a II-VI group compound direct band gap semiconductor with E_g of 3.37 eV and has an exciton binding energy of 60 meV both at room temperature and crystallizes into hexagonal wurtzite structure. It has the ability to grow single crystals as well as high piezoelectricity and exhibit excellent photonic and electrochemical properties [1–3]. Due to these aspects of ZnO, it has been considered to be an important material for various applications ranging from optical sensors, UV laser diodes and nanotechnology-based devices such as plasma displays. Also, nano-powdered ZnO semiconductors have received broad attention because of its applications in the field of electrostatic dissipative coatings, transparent ulta-violet protection films, sensors, spintronic machinery, luminescence, optoelectronics, photocatalysis, varistors, laser technology, imaging, energy conversion, and communications to biotechnology etc. It is a unique material and has a diverse form of growth morphologies, such as nano-rods, nano-bars, nano-rings, nano-springs, stone shaped like nano-structures, nano-belts, nano-wires and nano-cages [4,5].

In recent times, much attention has been given on the synthesis process to produce pure and doped ZnO nanomaterials. ZnO is visible light transparent material and can be improved its conductivity by doping as the dopants have strong influence on the properties of ZnO such as the electrical, optical and optoelectronic properties. In addition, the average crystalline size (D), band gap (E_g) and optical properties of ZnO are improved by introducing dopants into Zinc Oxide matrix. The ZnO doped with various metals (Al, Co, Cd, Eu, Cu, Ni, Ag, Co) show improved properties, since these metals have ionic radius almost matches well with Zn^{2+} (0.74 Å) [6]. Over the last few years, many researchers reported the incorporation of second element into ZnO matrix leads to modify physical and chemical properties. Few of them reported are ZnO:Na [4], ZnO:Ga [5], ZnO:Al [6,7], ZnO:Cd [8], ZnO:Co [9], ZnO:Cr [10], ZnO:Cu [11], ZnO:Eu [12], ZnO:Fe [13], ZnO:In [14], ZnO:Li [15], ZnO:Mn, Fe [16], ZnO:Ni, Al [17], etc. Here, to obtain stable p-type ZnO semiconductor nanopowders, Column-IA (Li, Na, K) and Column-V (P, As, Sb) elements are needed to dope, since these elements acts as deep acceptors or interstitial donors that contribute p-type conductivity [3,18]. In the last few decades, a group of methods have been successfully used for the synthesis of pure and doped Zinc Oxide NPs, such as sol - gel, co-precipitation, solid state reaction method, thermal diffusion method and mild and simple solution method.

During the past few years, many researchers have published their findings on antimicrobial activities of pure and doped zinc oxide nanomaterials and showing that these nanostructures are acted as powerful antibacterial and antifungal agents. According to our literature, the antimicrobial activities of the Na doped ZnO ($Zn_{1-x}Na_xO$) towards various filamentous bacteria and fungi have been rarely reported. Four bacterial strains, Escherichia coli, Pseudomonas aeruginosa, Klebsiella pneumoniae and *Staphylococcus aureus* as well as two fungal pathogens, *Aspergillus* and *Candida* were used against pure and Na doped ZnO samples. However, to best of our knowledge, there is no study reported in the literature particularly for these selected bacterial and fungal strains. In the present paper, the research study demonstrates about synthesis of pure and Na doped ZnO nanoparticles by the simple, low cost and energy consumption effective co-precipitation method. We also studied the structural, morphological, optical, antibacterial, and antifungal properties of pure and Na doped ZnO samples [19,20].

2. Experimental

2.1. Chemicals used

Zinc acetate dihydrate [$Zn(CH_3COO)_2\cdot 2H_2O$, SRL chem. 99.5%] was used as the starting material for ZnO. Sodium nitrate [$NaNO_3$, Merck Ltd., 99.0%] was used as the source compound for doping with sodium. Sodium hydroxide pellets GR [NaOH, Loba Chemie, 98.0%] was used as an agent. All precursors are used without any further purification as they received.

2.2. Synthesis of the samples

ZnO nanostructures were successfully synthesized in an aqueous medium by taking zinc acetate dihydrate [$Zn(CH_3COO)_2\cdot 2H_2O$] and sodium hydroxide [NaOH] in a stoichiometric ratio according to the following chemical reactions (1), (2) and the formed sodium salt CH_3COONa has been removed by deionized water [21]:

$$Zn(CH_3COO)_2.2H_2O + NaOH \rightarrow Zn(CH_3COO)(OH) + CH_3COONa(\downarrow) \quad (1)$$

$$Zn(CH_3COO)\ (OH) + NaOH \rightarrow ZnO + CH_3COONa(\downarrow)\ + H_2O \quad (2)$$

The washing process was repeated until the pH of the solution was 7. For the synthesis of pure and sodium doped ZnO nano powders, Zinc acetate dihydrate [$Zn(CH_3COO)_2\cdot 2H_2O$], sodium nitrate [$NaNO_3$] and sodium hydroxide [NaOH] were used as precursors. During the synthesis of pure and sodium doped ZnO nanoparticles the main parameters such as, particle size, morphology, chemical composition and crystalline structure must be controlled [22]. Sodium doped zinc oxide nanostructures have been prepared by co-precipitation process and the synthesis procedure was shown in the Fig. 1. In this synthesis process, 21.95 g of $Zn(CH_3COO)_2\cdot 2H_2O$ was dissolved in 100 ml of distilled water in a glass beaker and stirred for 30 min using magnetic stirrer. After stirring at room temperature, an appropriate amount of sodium nitrate ($NaNO_3$) solution was prepared and added it to $Zn(CH_3COO)_2\cdot 2H_2O$ solution. Subsequently, 8 g of NaOH solution was prepared by using 100 ml of deionized water in a separate glass beaker and stirred it for 10 min. Now, this NaOH solution was slowly added drop by drop to the $Zn(CH_3COO)_2\cdot 2H_2O$ and $NaNO_3$ mixture solution under stirring condition. The suspension formed with the dropping of NaOH alkaline aqueous solution to the $Zn(CH_3COO)_2\cdot 2H_2O$ and $NaNO_3$ mixture solution and it was magnetic stirred for two hours at the room temperature. Now, the liquid white gel was formed under normal air condition, and it was vacuum filtered using membrane filtration assembly. The solid white gel was formed after vacuum filtration; it was heated in oven at 95 °C for 5 h to get Na-doped ZnO as white nano powders. Different masses of Sodium nitrate were mixed with the mixture of Zinc acetate and NaOH to vary the doping percentage (Na/Na + Zn).

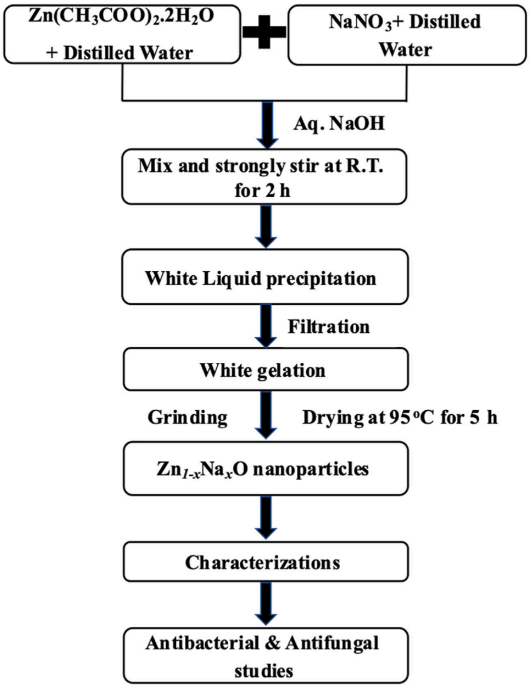

Fig. 1. Flow chart of the co-precipitation synthesis process of sodium doped zinc oxide nanopowders.

2.3. Instrumentation

$Zn_{1\text{-}x}Na_xO$ nanopowder samples were characterized by the powder XRD patterns recorded using a Bruker-D8 advance powder x-ray diffractometer with CuK_α radiation and a graphite monochromator in the angle (2θ) range of 30–80°. UV–Visible optical absorption studies for the optical transmission and absorption measurements were carried out for pure and Na doped ZnO nanopowders by Shimadzu UV-1601 spectrometer in the wavelength range of 200–800 cm. Fourier transform infrared spectroscopy was performed to identify the functional groups, which in turn determines the molecular structure of the synthesized nanopowders recorded using Varian-660 FTIR spectrometer in the wave number range of 400–4000 cm^{-1}. Scanning Electron Microscope with High-resolution provides detailed surface data of powder samples, which includes morphological structures, topographical structures and compositional information. For the purpose of these measurements, the powers were ultrasonically dispersed in alcohol and the suspension was deposited on the sample holder. Energy dispersive X-ray spectroscopy for elemental composition of the as-prepared samples was investigated by using EDX analysis.

2.4. Antimicrobial activity test

ZnO nanoparticles were reported as a superior antimicrobial agents and the performance was size and shape-dependent for many nanoparticles, the smaller the size the higher the activity due to their higher specific surface area [23]. However, the ZnO NPs shows strong inhibited fungal and bacterial growth at higher doping concentrations of Na. In the current paper, we reported four types of bacterial cultures and two standard fungal pathogens for $Zn_{1\text{-}x}Na_xO$ nanopowders with increased sodium dopant concentrations ($x = 0$, 0.01, 0.02, 0.04, 0.06, 0.08, and 0.10) for their antibacterial activity and antifungal effect, respectively. The bactericidal assay on one strain of Gram-positive Staphylococcus aureus and, three strain of Gram-negative bacteria Pseudomonas aeruginosa, Escherichia coli and Klebsiella pneumoniae was performed. In addition, the antifungal activities of as-synthesized samples towards the economically important fungi, Aspergillus and Candida have been studied.

The Kirby–Bauer disk diffusion method [24] was employed for evaluating antimicrobial activity. For screening antibacterial, antifungal activity nutrient agar medium and potato dextrose agar medium were prepared and sterilized by using autoclave at 121 °C and 15 lbs pressure for 15 to 20 min. The molten agar was poured into sterile Petri plates and allowed to solidify [25]. The 24 hrs old actively growing selected bacterial and fungal cultures were spread on solid nutrient agar plates and on PDA plates. Concurrently, sterilized Whatman filter paper disks of around 6–8 mm size were coated with the graded concentrations of Na-doped ZnO nanoparticle solution and carefully placed on the culture. The plates containing bacterial culture were incubated at 37 °C for 24 hrs and fungal cultures were incubated at 24 °C for 48 hrs.

The antimicrobial activity of the as-synthesized $Zn_{1\text{-}x}Na_xO$ nanopowders against all pathogenic microorganisms was studied in terms of zone of inhibition [26]. The zone of inhibition is the area appeared around pure and Na-doped ZnO samples coated in the disk at each respective concentrations where the growth of the microorganisms was arrested by the pure and Na-doped ZnO nanopowders. The measurement of the zone of inhibition was expressed in mm [27].

3. Results and discussion

3.1. XRD analysis

Fig. 2 shows the XRD patterns of as-synthesized pure and Na doped ZnO nanopowders. The XRD spectra of grown $Zn_{1\text{-}x}Na_xO$ samples show the various diffraction peaks corresponding to (100), (002), (101), (102), (110), (103), (200), (112), (201), (004) and (202) planes [28]. It is clear from XRD spectra line broadening; the co-precipitation synthesized powders are in nano-scale [6]. All the diffraction patterns of $Zn_{1\text{-}x}Na_xO$ confirmed the formation of hexagonal wurtzite structure of Zinc Oxide (JCPDS # 36-1451) [29]. No signal of extra diffraction peaks could be detected in this range of XRD corresponding to the sodium and its compounds due to its doping, leading to the formation of high purity single phase nanopowder samples. It is observed that Na ions are well doped into the hexagonal wurtzite ZnO matrix [30].

The average crystallite size (D) of Na doped ZnO nanostructures were calculated by using Debye-Scherrer's formula

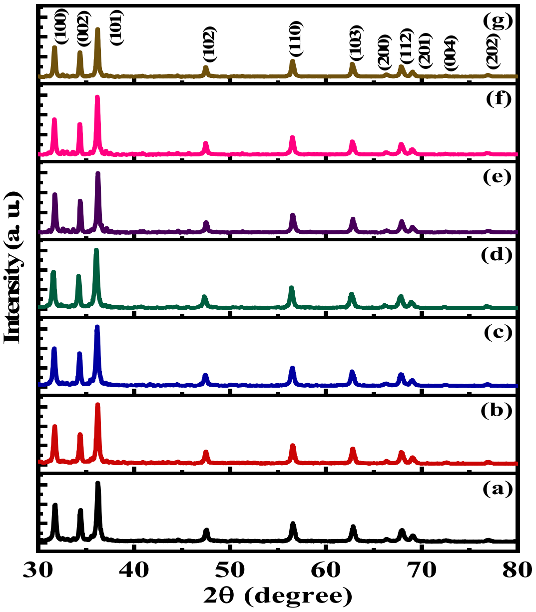

Fig. 2. X-ray diffraction pattern of $Zn_{1\text{-}x}Na_xO$ nanopowders, for × is equals to (a) 0, (b) 0.01, (c) 0.02, (d) 0.04, (e) 0.06, (f) 0.08 and (g) 0.10.

$$D(nm) = \frac{K\lambda}{\beta\cos\theta} \tag{3}$$

where K is the constant with value 0.94, λ represents wavelength of the X-ray of CuKα radiation (0.154 nm), β is the full width at half maximum (FWHM) of the diffraction peak and θ is the Bragg's angle and **D** is the crystallite size in nm. From the line broadening of XRD (Fig. 3a), it clearly indicates that the mean crystallite size is increases from 23.51 to 28.11 nm with increasing Na doping concentration.

The dislocation density (δ) is defined as a measure of the amount of defects and vacancies in the crystal, which can be calculated from the average crystallite size (D) using the formula,

$$\delta = \frac{1}{D^2} \tag{4}$$

and the micro strain (ε) of the samples induced was determined by

$$\varepsilon = \frac{\beta\cos\theta}{4} \tag{5}$$

respectively [31].

The calculated dislocation density and lattice strain both decreases with an increase in Na^+ ions doping concentration (Fig. 3b) due to the local distortion of lattice. The lattice cell volume (v) and bond length in Zn – O of $Zn_{1-x}Na_xO$ is increased up to × = 0.04, then slightly decreases and is minimum for × = 0.06 (Fig. 3a & c). The atom at × = 0.04 could be trapped and shifted from the non-equilibrium to the more equilibrium position thereby releasing the lattice strain. Also, there was a slight shift in the diffraction peak positions of the $Zn_{1-x}Na_xO$ samples. These diffraction peak shifts change the lattice parameters a and c.

Table 1 shows how both the lattice parameters a and c change as a function of Na doping concentration. The lattice constants a and c were found to be 3.250 and 5.207 Å for pure ZnO; and 3.255 and 5.214 Å for $Zn_{0.90}Na_{0.10}O$ samples, respectively (Fig. 3d). This variation of the lattice constants (a and c) and the lattice cell volume (v) is due to the following two aspects: (i) the size variation of the ionic radii of Zn^{2+} (0.74 Å) and Na^+(1.02 Å) and (ii) Increase in free carriers causes deformation of the conduction band potential [32,33].

The comparison of structural parameters such as Bragg's angle (2θ), FWHM (β), crystallite size (D) and inter-planar distance (d) of $Zn_{1-x}Na_xO$ (x = 0.00–0.10) for (1 0 1) diffraction peak were provided in Table 2 and it is observed that the inter planar spacing (d) was slightly varying with increasing Na concentration.

The bond length L (Å) of Zn – O is given by [34]:

$$L = \left[\left(\frac{a^2}{3}\right) + \left(\frac{1}{2} - u\right)^2 c^2\right]^{1/2} \tag{6}$$

Where a and b are lattice parameters and u denote the positional parameter, which measures the amount of displacement of each atom w.r.t. next atom along the c – axis in the wurtzite hexagonal structure and is given by:

$$u = \frac{a^2}{3c^2} + 0.25 \tag{7}$$

The reported bond length L (Å) value of Zn – O in the undoped ZnO unit cell viewed in a direction parallel to Zn^{2+} and O^{2-} atoms was given 1.9767 Å [35]. It can be observed that the calculated L(Å) values of as-prepared nanopowders matches well with the reported value and its variation with Na doping concentration is shown in Fig. 3a.

The Williamson and Hall graphs (W – H graphs) are plotted between 4 sinθ on X – axis and β_{hkl} cosθ on Y – axis for preferred peaks of diffraction of $Zn_{1-x}Na_xO$ nanoparticles are shown in Fig. 4**.** In W-H methodology, the average crystallite size (D_{avg}) and the micro strain (ε) of the pure and Na-doped ZnO samples are calculated from the y-intercept and slope of linear plot [36]. The structural parameters D_{avg} and ε values evaluated from W – H method are 40.78 nm and 0.00139 for pure ZnO; and 34.75 nm and 0.000825 for $Zn_{0.96}Na_{0.04}O$ samples,

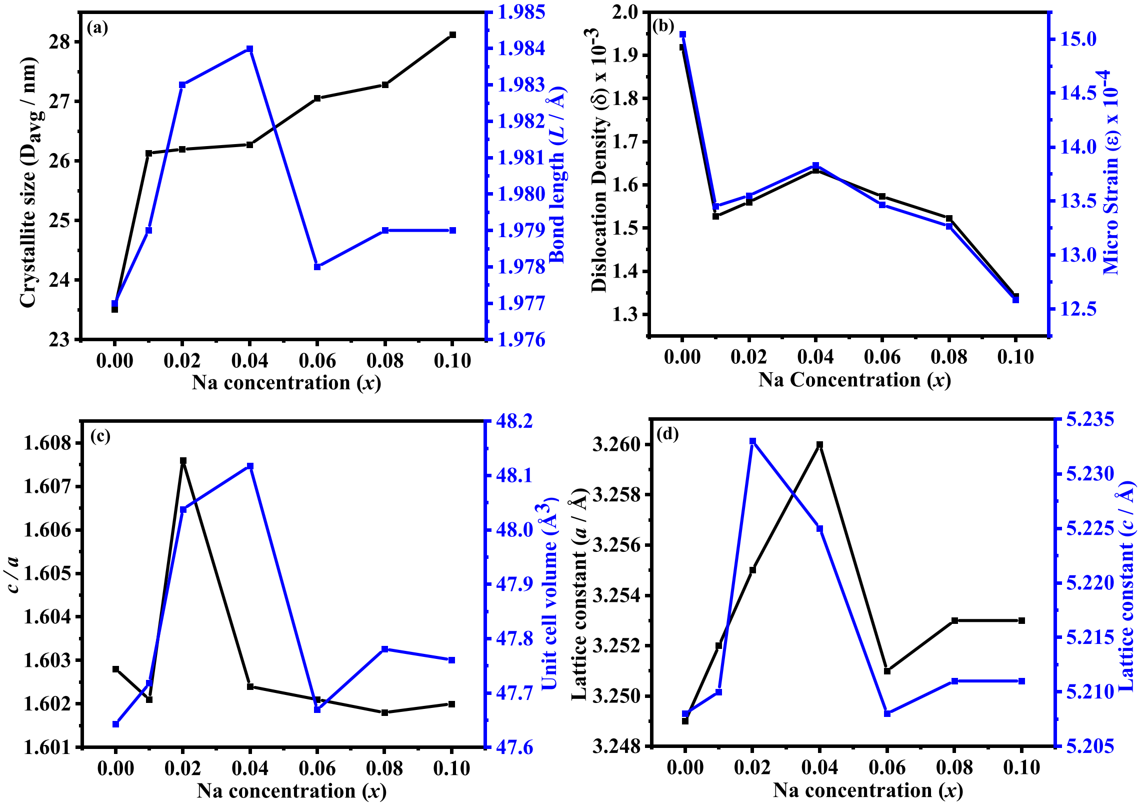

Fig. 3. The calculated structural parameters variations of $Zn_{1-x}Na_xO$ nanopowders with Na doping concentration **(a)** Average crystallite size and Bond length; **(b)** Dislocation density and Micro strain; **(c)** c/a ratio and Unit cell volume; and (d) Lattice constants (a and c).

Table 1
The average crystallite size, lattice constants (*a* and *c*) and unit cell volume of the $Zn_{1-x}Na_xO$ (x = 0–0.10) nano powders.

Na doping concentration (*x*)	Average crystallite size D_{avg} (nm)	Lattice Parameters		*c* / *a* ratio	Average Unit cell volume (Å^3)	Dislocation density (δ)	Micro strain (ε)	Bond Length L (Å) of Zn-O
		a = *b* (Å)	*c* (Å)					
x = 0	23.510	3.249	5.208	1.6028	47.643	1.919E-03	15.046E-04	1.977
x = 0.01	26.131	3.252	5.210	1.6021	47.718	1.527E-03	13.452E-04	1.979
x = 0.02	26.196	3.255	5.233	1.6076	48.038	1.560E-03	13.549E-04	1.983
x = 0.04	26.275	3.260	5.225	1.6024	48.118	1.634E-03	13.833E-04	1.984
x = 0.06	27.051	3.251	5.208	1.6021	47.669	1.573E-03	13.463E-04	1.978
x = 0.08	27.280	3.253	5.211	1.6018	47.781	1.523E-03	13.267E-04	1.979
x = 0.10	28.119	3.253	5.211	1.6020	47.761	1.342E-03	12.583E-04	1.979

Table 2
The Bragg's angle (2θ), FWHM (β), crystallite size (D) and inter-planar distance (d) of $Zn_{1-x}Na_xO$ (x = 0–0.10) for (1 0 1) diffraction peak.

Na doping Concentration (*x*)	Bragg's angle (2θ) (Deg)	FWHM β (Deg)	D (nm)	Inter planar distance (d) (Å)
x = 0	36.251	0.323	25.807	2.476
x = 0.01	36.218	0.301	27.694	2.478
x = 0.02	36.163	0.303	27.535	2.481
x = 0.04	36.075	0.275	30.348	2.487
x = 0.06	36.242	0.247	33.732	2.476
x = 0.08	36.192	0.251	33.271	2.479
x = 0.10	36.203	0.260	32.133	2.479

respectively.

3.2. *The UV–Vis optical absorption spectra*

UV–Visible absorption spectra are formed by suspending the as-prepared samples in deionized water for a long period of time at room temperature. Various optical absorption peaks were observed due to large exciton binding energy (60 mV) [6]. The UV–Vis optical absorption pattern of $Zn_{1-x}Na_xO$ nanopowders in the wavelength the range of 200 – 800 nm are showed in Fig. 5. The absorption peaks of $Zn_{0.99}Na_{0.01}O$ samples were recorded at 196, 284 and 365 nm, respectively and it is evident that all Na-doped ZnO samples shows excellent optical absorbance below the wavelength of 390 nm while a very small absorbance was found in the visible region. From the spectra it is obvious that Na doped ZnO strongly absorb around 370 nm compared to pure ZnO due to presence of sodium content [8]. These absorption peaks are due to the electronic transitions from deep level of valence band to conduction band. Due to the difference in the particle size and shape of $Zn_{1-x}Na_xO$ samples, the UV–Vis absorption peak pattern was slightly varying with an increase in Na^+ doping content [28].

The optical direct band gap of $Zn_{1-x}Na_xO$ samples is determined by Tauc's formula,

$$(\alpha h\upsilon)^n = B\left(h\upsilon - -E_g\right) \tag{7}$$

where, **B** is a constant of the material, **h*ν*** is the incident photon energy in eV, **h** is Planck's constant, $\mathbf{E_g}$ is the optical energy bandgap in eV, **n** is an exponent and n = 2/3, 1/3, 2 and 1/2 for direct forbidden, indirect forbidden, direct allowed and indirect allowed transitions respectively, and **α** is the absorption coefficient (in cm^{-1}) [31].

Plots of $(\alpha h\nu)^2$ vs photon energy (hν) of pure and Na doped ZnO samples are illustrated in Fig. 6. The direct allowed band gap energy (E_g) for which n = 2 is measured by the extrapolation of the linear portions of the curves on the X-axis as shown in the Fig. 6. Bulk form of ZnO has a direct gap of 3.15 eV. It can be noticed that the band gap measured in nano sized form is higher than the value of bulk ZnO as in the nano scale,

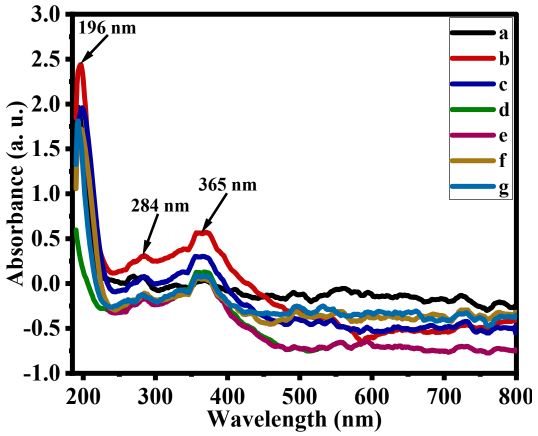

Fig. 5. Optical absorption spectra of $Zn_{1-x}Na_xO$ samples; (a) × = 0, (b) × = 0.01, (c) × = 0.02, (d) × = 0.04, (e) × = 0.06, (f) × = 0.08 and (g) × = 0.10.

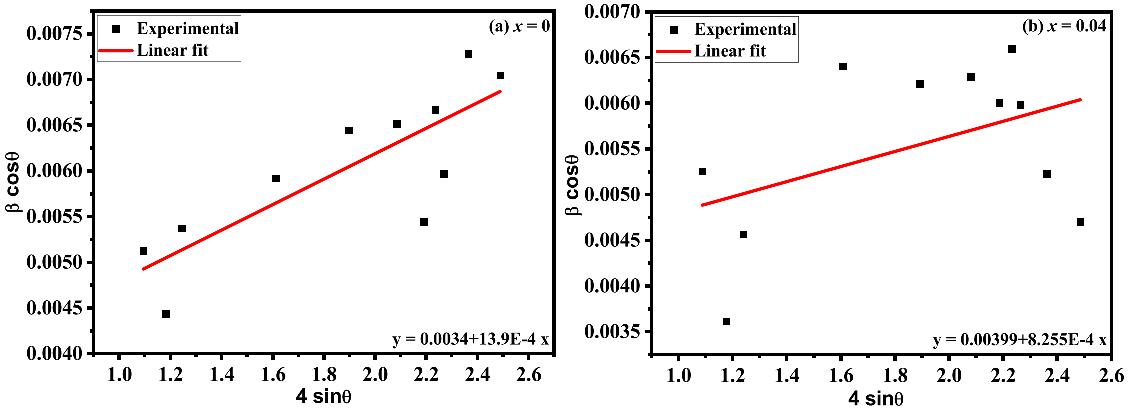

Fig. 4. W-H plots of $Zn_{1-x}Na_xO$ nanopowders; (a) × = 0 and (b) × = 0.04.

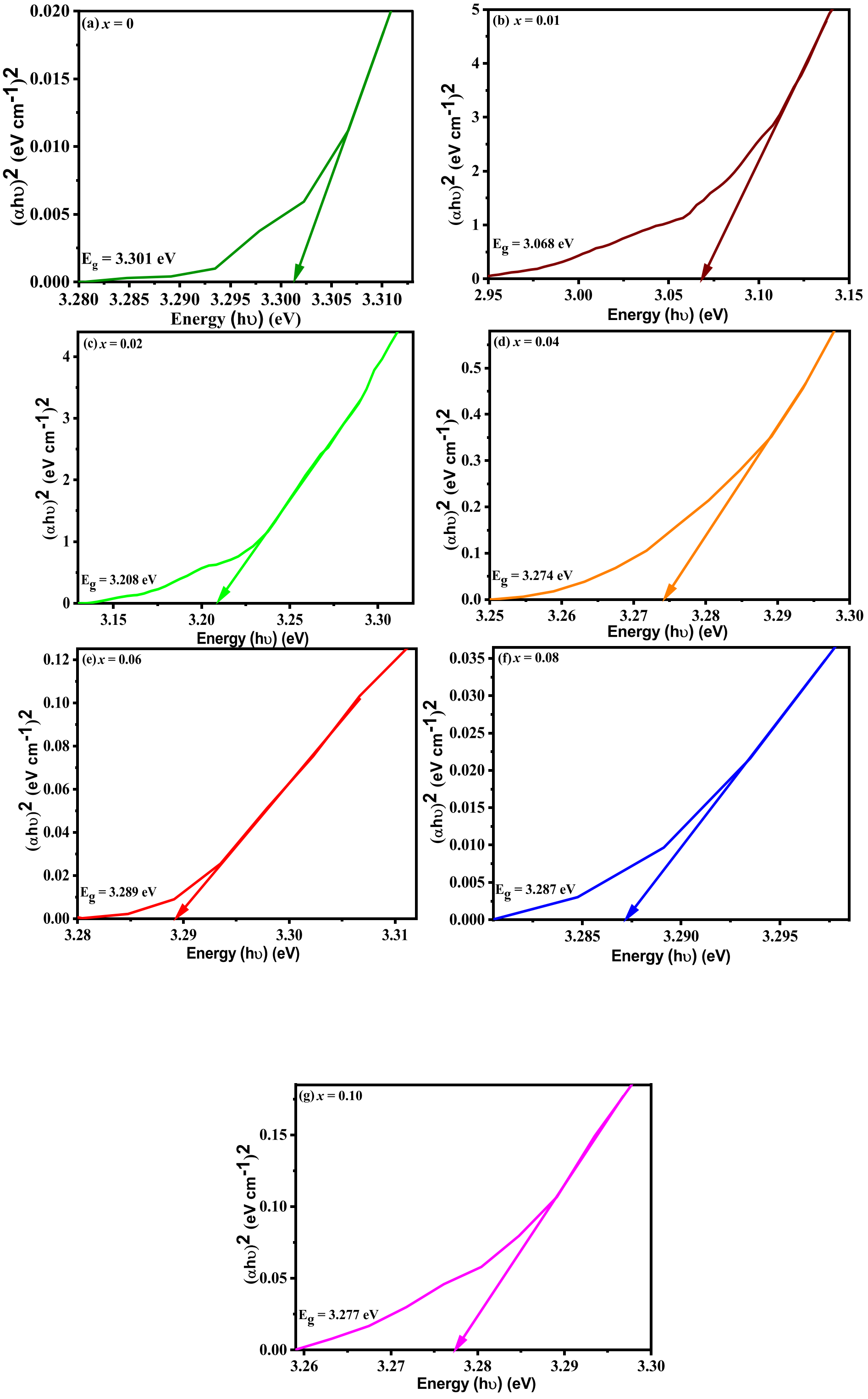

Fig. 6. Tauc plot of $[\alpha h\nu]^2$ versus photon energy ($h\nu$) to determine the band gap E_g of the as-prepared $Zn_{1-x}Na_xO$ nanopowders; (a) × = 0, (b) × = 0.01, (c) × = 0.02, (d) × = 0.04, (e) × = 0.06, (f) × = 0.08 and (g) × = 0.10.

the electronic levels become completely discrete in atoms and molecules of a semiconductor [37 –40].

Furthermore, the band gap energy (E_g) of the Na doped ZnO nanopowders increases up to × = 0.06 and reached maximum (3.289 eV), then slowdown and decreases as Na doping concentration increases as depicted in Fig. 7. This significant behaviour of E_g is due to the modification of electronic structural of ZnO over Na sustitution. So, it is clear that the synthesized $Zn_{1-x}Na_xO$ samples show the quantum-confinement effect.

3.3. FTIR studies

Fig. 8 represents the FTIR spectroscopic pattern of $Zn_{1-x}Na_xO$ nanopowders, which showed various peaks at 3412, 2996, 2360, 1550, 1391,

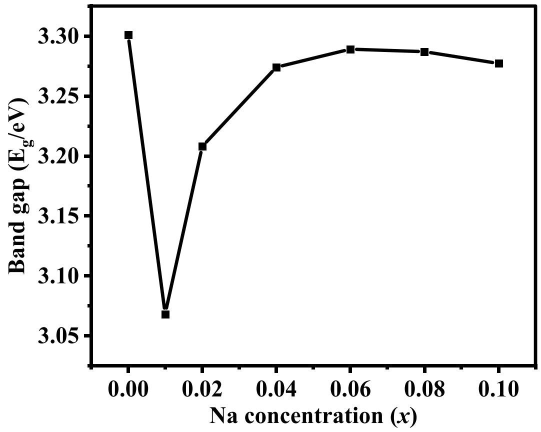

Fig. 7. The calculated variation of energy band gap (E_g) of wurtzite $Zn_{1-x}Na_xO$ nanopowders as a function of the Na doping concentration (x).

1018, 796, 633 and 425 cm^{-1} for $Zn_{0.90}Na_{0.10}O$ sample. The important functional groups such as ZnO, carboxylate (COO–) and hydroxyl (O–H) impurities can be seen. From the figure, the absorption band at 425 cm^{-1} is attributed to the Zn–O stretching vibration mode of phonons of the samples. The peaks around 633 cm^{-1} attributed to the existence of Na in Zinc Oxide lattice [10]. The O–H stretching mode of vibration found around 3412 cm^{-1}, which is a confirmation of presence of hydroxyl groups and water molecule on the surface of ZnO nanoparticles. The small absorption peaks about 2360 and 2996 cm^{-1} corresponds to C–H stretching vibration of alkane groups. C–O stretching modes of vibration corresponds to 1018 cm^{-1} and the symmetric and asymmetric stretching mode of vibration bands due to C=O and carboxylate found at 1550 and 1391 cm^{-1}, which is attributed to the Zinc Oxide nanopowders during co-precipitation synthesis [41]. This functional group appeared due to the non-uniform decomposition of the acetate group with mixed precursor solution. The FTIR analysis indicates the successful formation of hexagonal wurtzite ZnO nanoparticles. Table 3 provided information about the peak positions, nature of the peak, and vibrational modes from FTIR spectroscopic data of molecules of $Zn_{0.90}Na_{0.10}O$. From the Fig. 8, the FT-IR data of synthesized Na doped ZnO samples are similar to that of the pure ZnO. The modes of vibrations are slightly changes due to mismatch between ionic radius of Na^+ and Zn^{2+} which attributes the activation of defects and oxygen vacancies in the intrinsic host lattice of ZnO. So the red shift in the vibrational modes was caused by these activated impurities [42].

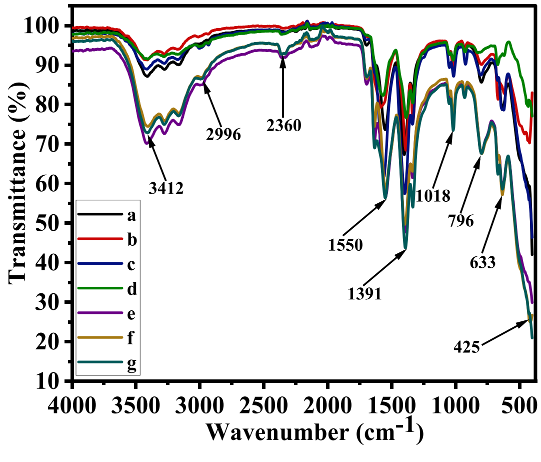

Fig. 8. FTIR spectra of $Zn_{1-x}Na_xO$ nanopowders; (a) × = 0, (b) × = 0.01, (c) × = 0.02, (d) × = 0.04, (e) × = 0.06, (f) × = 0.08 and (g) × = 0.10.

Table 3
FTIR spectroscopic data including absorption peaks and the corresponding functional groups of $Zn_{0.90}Na_{0.10}O$ sample.

S. No.	Absorption peak position (cm^{-1})	Nature	Bond/ Functional groups
1	3412	Very strong	–OH stretching mode
2	2996	Weak	C–H stretching mode of alkane groups
3	2360	Weak	C–H stretching vibration mode
4	1550	Very strong	ν_s (C–O) + δ (OC = O)
5			
6	1391	Very Strong	ν_s (C–O) + δ (OC = O)
7	1018	Strong	ν_s (C–O)
8	796	Weak	C–C stretching
9	633	Weak	Existence of Na in ZnO lattice
10	425	Strong	ZnO stretching vibration

3.4. Scanning Electron microscopy (SEM) analysis

Scanning Electron Microscopy (SEM) technique was used to examine the size, shape of the nanoparticles and surface morphology which includes topographical, morphological structures and growth mechanism of the particles. Fig. 9**(a–d)** shows the SEM micrographs of undoped and Na doped ZnO samples. These images clearly indicate the formation of nanoparticles with average size in the order of nanometer scale exhibiting hexagonal structure, which is also confirmed by XRD analysis. The morphology of $Zn_{1-x}Na_xO$ nanopowders contain mixer of uniformly distributed rod-like and bar-like particles in its morphology [43]. The particle size increases with increasing Na doping concentration. As sodium content increases, the shape of the particle's is changing from rod-like to non-uniform shaped stone-like structures which showed the structural morphology largely depends on the doping concentration. In all cases, an agglomeration of nanoparticles was observed due to densification of dispersed particles. Particularly, $Zn_{1-x}Na_xO$ samples consist of small number of stone-like and large number of rod / bar-like structures with the average diameters of around 375 nm and 273.5 nm, respectively. The crystallite sizes evaluated from the powder XRD calculations do not match well with the particle grain sizes obtained from SEM micrographs as the grains formed in the SEM images are the domains consists of aggregation of the nano-size crystallites (in the XRD) [11]. It can be seen that the powder XRD technique is more stringent method which leads to smaller sizes [44]. So, the substitution of Na influences changes in the shape, the crystallization and growth of ZnO nanoparticles and also causes an increase in the size of nanoparticles for higher concentration [45].

3.5. EDX spectroscopy

The Energy Dispersive X-ray (EDX) data gives the information about the elemental composition in atomic and weight percentage terms of the pure and Na doped ZnO nanopowders. The EDX analysis of $Zn_{1-x}Na_xO$ samples were shown in Fig. 10**(a-b)**. From the EDX images, it clearly indicates that the intensity and amount of Na element in the as-synthesized samples increases with increasing Na doping concentration. The peaks present in the EDX pattern may be related to Zn, Na and O only [30,41]. It can be evident that no other dispersive peaks were observed related to foreign elements and impurities, which provides the confirmation about the formation of single-phase sodium doped ZnO nanopowders [46]. Also, there are no independent peaks resulting from sodium and its compounds in the $Zn_{1-x}Na_xO$samples indicating the complete dissolution of sodium into ZnO crystal lattice.

EDX elemental analysis histogram depicts the number of different elements of $Zn_{1-x}Na_xO$ nanopowders in weight percentage, as shown in

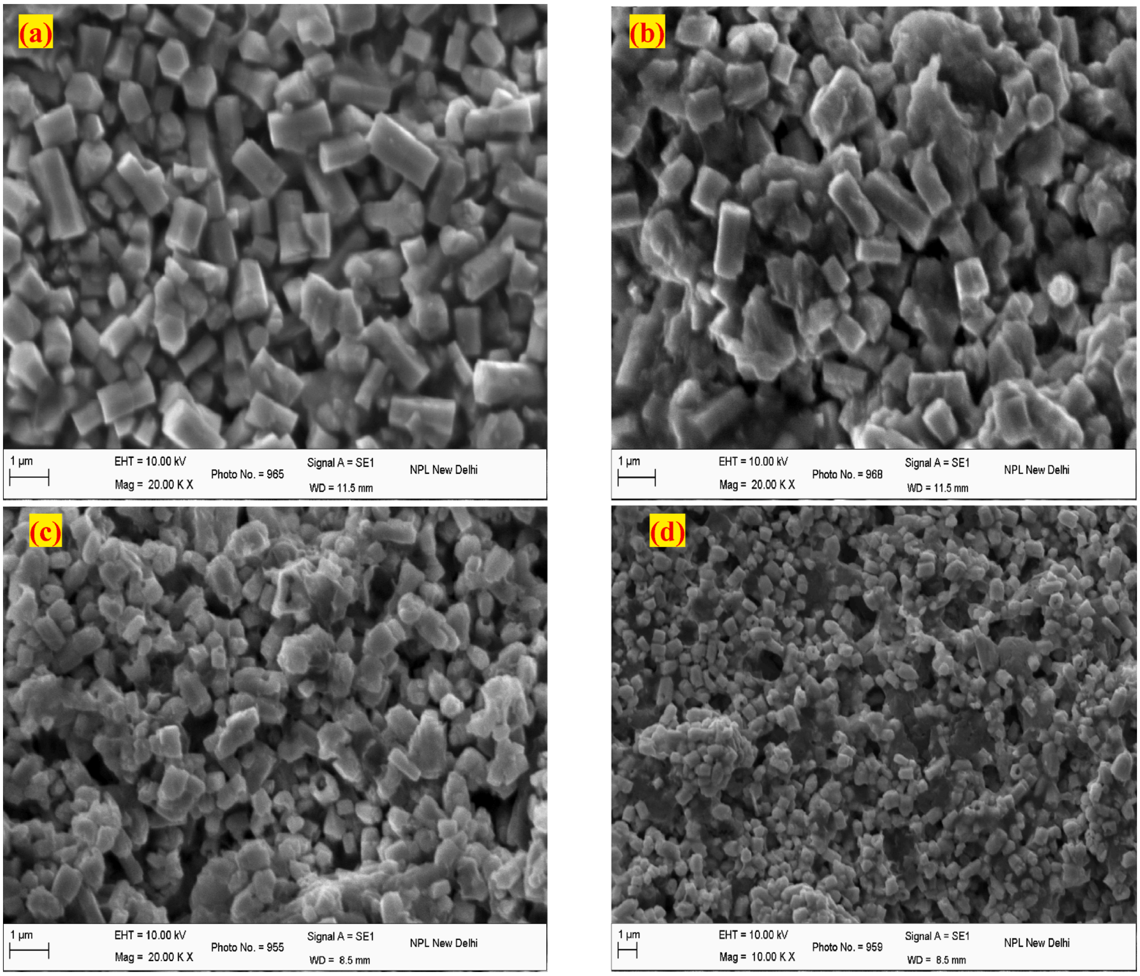

Fig. 9. **(a - d)** SEM micrographs of $Zn_{1-x}Na_xO$ nanopowders; (a) × = 0, (b) × = 0.02, (b) × = 0.06, and (d) × = 0.10.

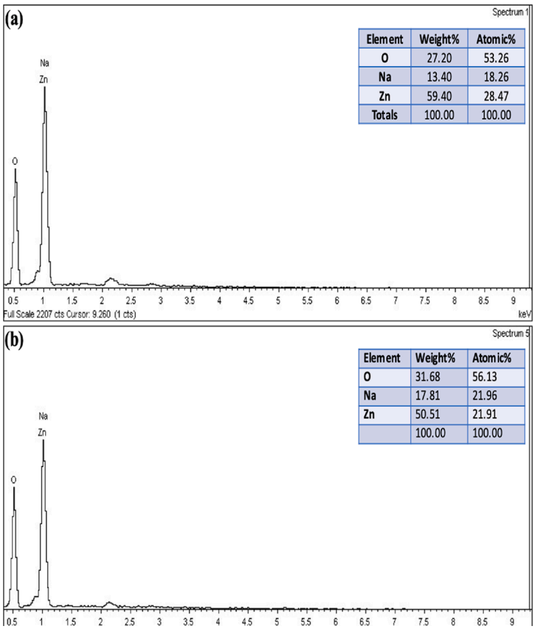

Element	Weight%	Atomic%
O	27.20	53.26
Na	13.40	18.26
Zn	59.40	28.47
Totals	100.00	100.00

Element	Weight%	Atomic%
O	31.68	56.13
Na	17.81	21.96
Zn	50.51	21.91
	100.00	100.00

Fig. 10. EDX analysis of (a) $Zn_{0.99}Na_{0.01}O$ and (b) $Zn_{0.90}Na_{0.10}O$ samples.

the Fig. 11. Clearly, the measured amounts of Zn and O elements are higher than that of the Na element in the as-synthesized samples.

3.6. Antibacterial and antifungal activity

The antibacterial activity of pure and graded concentrations of Na doped ZnO samples was tested using disk diffusion method against selected four different bacterial cultures namely *Escherichia coli,*

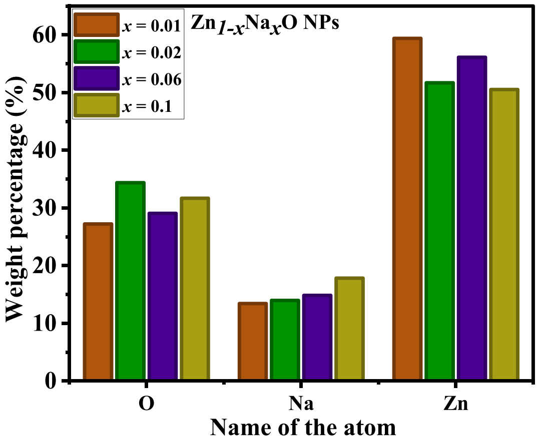

Fig. 11. Elemental analysis histogram representation in weight percentage of selected $Zn_{1-x}Na_xO$ samples.

Pseudomonas aeruginosa*, Klebsiella neumoniae* and *Staphylococcus aureus.* The Inhibition zone around the graded sample in the disc was depicted in the Fig. 12 and the estimated values of Zone of Inhibition in mm are plotted as histogram (Fig. 13) [46]. The results showed that the pure and Na doped ZnO nanopowders exhibit excellent bacterial growth in the disc for all bacteria; *E. coli, P.* aeruginosa*, K. neumoniae* and *S. aureus.* It is noted that the dose dependent highest growth inhibitory zone was observed with the increased dopant concentrations of Na than pure ZnO and the superior zone of Inhibition was obtained for $Zn_{0.90}Na_{0.10}O$ samples for all the bacterial strains.

The Antifungal activity of pure and Na doped ZnO nanopowders was also studied with different Na concentrations against two fungi *Candida* and *Aspergillus,* respectively. In the case of Candida as shown in Fig. 14(a - b)*,* the Inhibition zone is found to increase proportionally with increasing Na doping concentration and the highest Inhibition was observed at higher concentrations. No Inhibitory zone is obtained for control which is prepared using the stack without zinc oxide and tested in the disc. However, in the case of *Aspergillus* as depicted Fig. 14(c - d), the Zone of Inhibition is observed same at lower Na doping concentrations and obtained enhanced zone at higher concentrations. It can also be noted that, the increased Na dopant have shown more growth inhibitory effect against the fungal pathogens *Candida* and *Aspergillus* when compared to pure ZnO nanoparticles, which was evident in Fig. 15 [47]. The present study reported a significant high growth inhibitory zone against pure ZnO [48,49]. The results were noticed as extremely significant and the values are Mean ± SD (n = 4). *P < 0.0001 Compared to control (Pure ZnO).

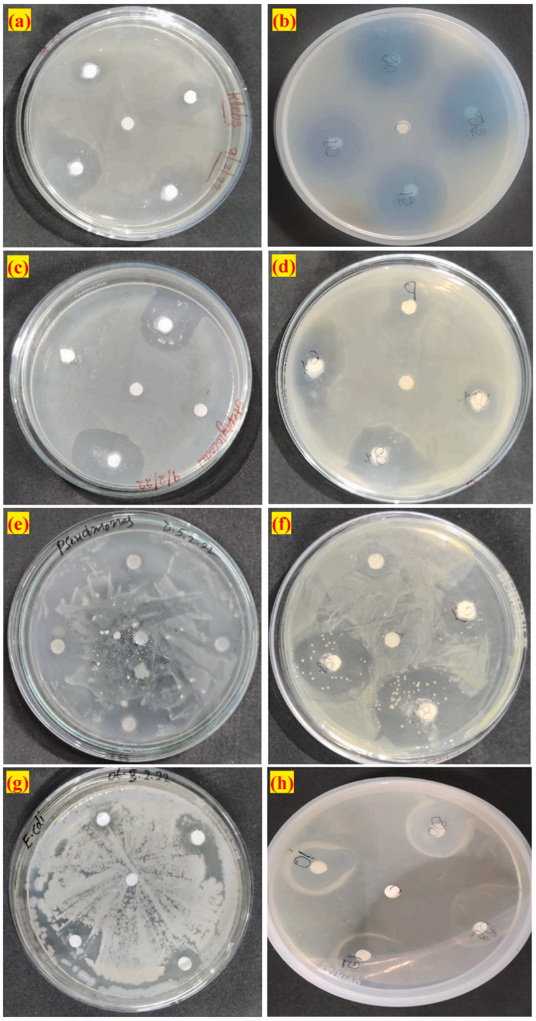

Fig. 12. Antibacterial activity of pure and Na doped ZnO nanoparticles against standard human pathogenic bacteria (**a-b:** *Klebsiella pneumoniae;* **c-d:** *Staphylococcus aureus;* **e-f:** *Pseudomonas aeruginosa*; and **g-h:** *Escherichia coli).*

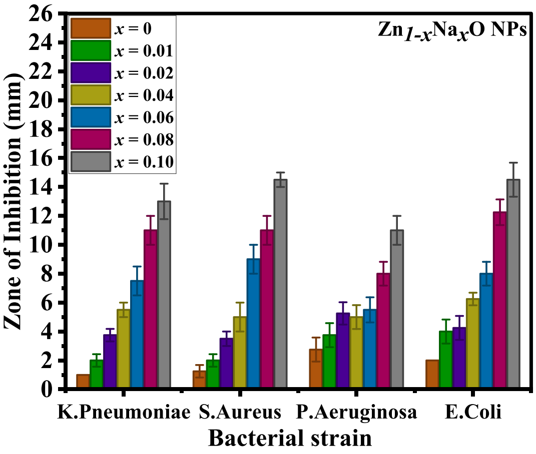

Fig. 13. The Zone of inhibition of pure and Na doped ZnO nanoparticles against Bacterial cultures. The values are Mean ± SD (n = 4). *P < 0.0001 Compared to control (Pure ZnO).

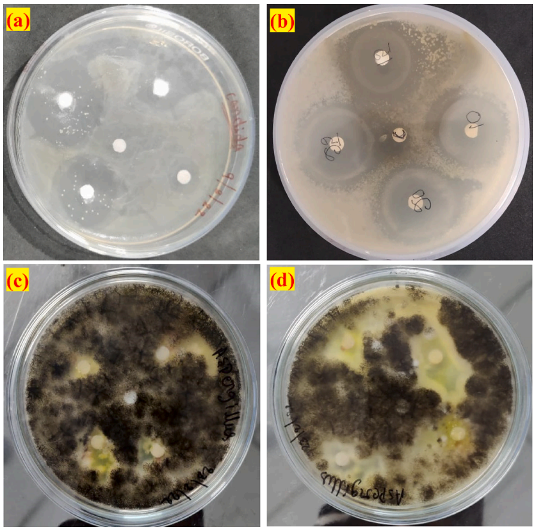

Fig. 14. Potent antifungal activity of pure and Na doped ZnO nanoparticles against pathogenic fungi (**a-b:** *Candida;* and **c-d:** *Aspergillus).*

4. Conclusions

In the present work, $Zn_{1-x}Na_xO$ nanopowders have been successfully synthesized by a simple co-precipitation method. It was evident from XRD studies that the as-synthesized $Zn_{1-x}Na_xO$ nanopowders exhibits hexagonal wurtzite structure and the average crystallite size determined by using the Scherrer formula increases and the calculated bond length L (Å) values were slightly varies with increase in Na-doping concentration. The average diameter estimated by the SEM micrographs of the prepared samples also increases, which confirms the surface area reduction with Na content. The FTIR analysis shows the presence of precursors and the formation of functional ZnO and Na doped ZnO nanopowders. The results obtained from UV – Vis spectroscopic data shows the suffered band gap between 3.068 and 3.301 eV and affected optical absorption band with the presence of Na concentration. The energy dispersive X-ray study confirms the successful incorporation of Na in the ZnO lattice. Antibacterial study against the microorganisms E. coli, P. aeruginosa, K. pneumoniae and *S. aureus* reveals that the zone of

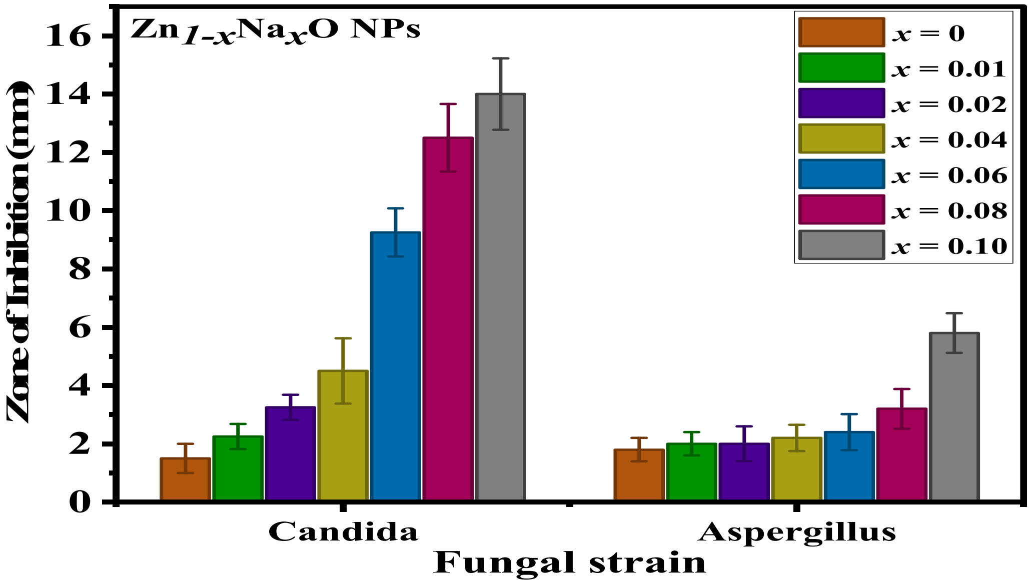

Fig. 15. The Zone of inhibition of pure and Na doped ZnO nanoparticles against fungal cultures. The values are Mean ± SD (n = 4**).** *P < 0.0001 Compared to control (Pure ZnO).

inhibition increases with increase in Na doping content. The antifungal study against the fungal pathogens *Aspergillus* and *Candida* shows that in case of *Candida* the inhibition zone increases with increase in Na concentration but in case of *Aspergillus* the inhibition zone is remained same for all Na concentrations except at very high concentrations. This study concluded that the as-synthesized nano powders may be used as antibacterial agents and antifungal medication in pharmaceutical applications.

CRediT authorship contribution statement

B. Nageswara Rao: Writing – original draft. **P. Tirupathi Rao:** Visualization, Investigation. **K. Vasudha:** Visualization, Investigation. **Sk. Esub Basha:** Writing – original draft. **D.S.L. Prasanna:** Writing – original draft. **T. Bhushana Rao:** Writing – original draft. **K. Samatha:** Writing – review & editing. **R.K. Ramachandra:** Conceptualization, Methodology, Supervision.

Declaration of Competing Interest

The authors declare that they have no known competing financial interests or personal relationships that could have appeared to influence the work reported in this paper.

Data availability

Data will be made available on request.

Acknowledgements

The authors are thankful to DST-FIST – Central Instrumentation Laboratory & Department of Physics, Government College (Autonomous), Rajahmundry, Andhra Pradesh and National Physical Laboratory (CSIR-NPL), New Delhi

References

[1] A. Naveed Ul Haq, A. Nadhman, I. Ullah, G. Mustafa, M. Yasinzai, I. Khan, Synthesis Approaches of Zinc Oxide Nanoparticles: The Dilemma of Ecotoxicity, Journal of Nanomaterials. 2017 (2017) 1–14.

[2] S. Sabir, M. Arshad, S.K. Chaudhari, Zinc Oxide Nanoparticles for Revolutionizing Agriculture: Synthesis and Applications, The Scientific World Journal. 2014 (2014) 1–8, https://doi.org/10.1155/2014/925494.

[3] A. Janotti, C.G. Van de Walle, Fundamentals of zinc oxide as a semiconductor, Rep. Prog. Phys. 72 (12) (2009) 126501.

[4] V. Parihar, M. Raja, R. Paulose, A Brief Review of Structural, Electrical and Electrochemical Properties of Zinc Oxide Nanoparticles, REVIEWS ON ADVANCED MATERIALS SCIENCE. 53 (2018) 119–130, https://doi.org/10.1515/rams-2018-0009.

[5] M. Snure, A. Tiwari, Band-gap engineering of $Zn_{1-x}Ga_xO$ nanopowders: Synthesis, structural and optical characterizations, J. Appl. Phys. 104 (2008), 073707, https://doi.org/10.1063/1.2988131.

[6] A. Vanaja, G.V. Ramaraju, S. Rao, Structural and Optical Investigation of Al Doped ZnO Nanoparticles Synthesized by Sol-gel Process, Indian Journal of Science and Technology. 9 (2016). https://doi.org/10.17485/ijst/2016/v9i12/87013.

[7] M. Chitra, K. Uthayarani, N. Rajasekaran, E.K. Girija, Preparation and Characterisation of Al doped ZnO Nanopowders, Physics Procedia. 49 (2013) 177–182, https://doi.org/10.1016/j.phpro.2013.10.024.

[8] S. Al-Ariki, N.A.A. Yahya, S.A. Al-A'nsi, M.H.H. Jumali, A.N. Jannah, R. Abd-Shukor, Synthesis and comparative study on the structural and optical properties of ZnO doped with Ni and Ag nanopowders fabricated by sol gel technique, Sci Rep. 11 (1) (2021), https://doi.org/10.1038/s41598-021-91439-1.

[9] J. El Ghoul, M. Kraini, L. El Mir, Synthesis of Co-doped ZnO nanoparticles by sol–gel method and its characterization, J Mater Sci: Mater Electron. 26 (2015) 2555–2562, https://doi.org/10.1007/s10854-015-2722-z.

[10] B. Babu, V.P. Manjari, T. Aswani, G.T. Rao, R.J. Stella, R.V.S.S.N. Ravikumar, Structural, optical and magnetic properties of Cr^{3+} doped ZnO nanopowder, Indian, J Phys. 88 (2014) 683–690, https://doi.org/10.1007/s12648-014-0473-y.

[11] U.S. Udayachandran Thampy, C.h. Rama Krishna, C.h. Venkata Reddy, B. Babu, Y. P. Reddy, P.S. Rao, R.V.S.S.N. Ravikumar, Spectral Investigations on Cu^{2+}-Doped ZnO Nanopowders, Appl Magn Reson. 41 (2011) 69–78, https://doi.org/10.1007/s00723-011-0234-4.

[12] L. Armelao, G. Bottaro, M. Pascolini, M. Sessolo, E. Tondello, M. Bettinelli, A. Speghini, Structure−Luminescence Correlations in Europium-Doped Sol−Gel ZnO Nanopowders, J. Phys. Chem. C. 112 (2008) 4049–4054, https://doi.org/10.1021/jp710207r.

[13] M.A. Ciciliati, M.F. Silva, D.M. Fernandes, M.A.C. de Melo, A.A.W. Hechenleitner, E.A.G. Pineda, Fe-doped ZnO nanoparticles: Synthesis by a modified sol–gel method and characterization, Materials Letters. 159 (2015) 84–86, https://doi.org/10.1016/j.matlet.2015.06.023.

[14] H. Shokry Hassan, A.B. Kashyout, I. Morsi, A.A.A. Nasser, I. Ali, Synthesis, characterization and fabrication of gas sensor devices using ZnO and ZnO: In nanomaterials, Beni-Suef University Journal of Basic and Applied Sciences. 3 (2014) 216–221, https://doi.org/10.1016/j.bjbas.2014.10.007.

[15] L. Fadillah, B. Soegijono, S. Budiawanti, I. Mudzakir, Fabrication and characterization of ZnO and Li doped ZnO by a sol-gel method, in: Depok, Jawa Barat, Indonesia, 2017: p. 030053. https://doi.org/10.1063/1.4991157.

[16] P.D. Candra Seta, P.E. Yunita, M.A. Baqiya, Darminto, Structural and Magnetic Characterization of Mn and Fe–doped ZnO Nanopowders, IOP Conf. Ser.: Mater. Sci. Eng. 196 (2017), 012018, https://doi.org/10.1088/1757-899X/196/1/012018.

[17] A. Sayari, L.E. Mir, Structural and Optical Characterization of Ni and Al Co-Doped ZnO Nanopowders Synthesized via the Sol-Gel Process, KONA. 32 (2015) 154–162. https://doi.org/10.14356/kona.2015003.

[18] N.S. Parmar, K.G. Lynn, Sodium doping in ZnO crystals, Appl. Phys. Lett. 106 (2) (2015) 022101.

[19] S. Fabbiyola, L.J. Kennedy, U. Aruldoss, M. Bououdina, A.A. Dakhel, J. JudithVijaya, Synthesis of Co-doped ZnO nanoparticles via co-precipitation: Structural, optical and magnetic properties, Powder Technology. 286 (2015) 757–765, https://doi.org/10.1016/j.powtec.2015.08.054.

[20] P.G. Devi, A.S. Velu, Synthesis, structural and optical properties of pure ZnO and Co doped ZnO nanoparticles prepared by the co-precipitation method, J Theor Appl Phys. 10 (2016) 233–240, https://doi.org/10.1007/s40094-016-0221-0.

[21] T.T. Ha, T.D. Canh, N.V. Tuyen, A Quick Process for Synthesis of ZnO Nanoparticles with the Aid of Microwave Irradiation, ISRN Nanotechnology. 2013 (2013) 1–7, https://doi.org/10.1155/2013/497873.

[22] L. Chandra, P.K. Sahu, R. Dwivedi, V.N. Mishra, Synthesis of Na doped ZnO nanoparticles for detection of reducing gases, in: in: 2016 IEEE Uttar Pradesh Section International Conference on Electrical, Computer and Electronics Engineering (UPCON), IEEE, Varanasi, India, 2016, pp. 102–105, https://doi.org/10.1109/UPCON.2016.7894633.

[23] S.V. Gudkov, D.E. Burmistrov, D.A. Serov, M.B. Rebezov, A.A. Semenova, A. B. Lisitsyn, A Mini Review of Antibacterial Properties of ZnO Nanoparticles, Front. Phys. 9 (2021), 641481, https://doi.org/10.3389/fphy.2021.641481.

[24] A.W. Bauer, W.M. Kirby, J.C. Sherris, M. Turck, Antibiotic susceptibility testing by a standardized single disk method, Am J Clin Pathol. 45 (1966) 493–496.

[25] A.T. Ravichandran, R. Karthick, K. Ravichandran, D. Ravinder, R. Chandramohan, Revealing the influence of the Bi dopant on the structural, photoluminescence and antibacterial properties of ZnO nanoparticles, J Mater Sci: Mater Electron. 29 (2018) 2784–2790, https://doi.org/10.1007/s10854-017-8206-6.

[26] N. Mahmoudi Khatir, Z. Abdul-Malek, A.K. Zak, A. Akbari, F. Sabbagh, Sol–gel grown Fe-doped ZnO nanoparticles: antibacterial and structural behaviors, J Sol-Gel Sci Technol. 78 (2016) 91–98, https://doi.org/10.1007/s10971-015-3922-y.

[27] B.-L. Guo, P. Han, L.-C. Guo, Y.-Q. Cao, A.-D. Li, J.-Z. Kong, H.-F. Zhai, D. Wu, The Antibacterial Activity of Ta-doped ZnO Nanoparticles, Nanoscale Res Lett. 10 (2015) 336, https://doi.org/10.1186/s11671-015-1047-4.

[28] G. S, A. Belay, C. Reddy AR, B. Z, Synthesis and Characterizations of Zinc Oxide Nanoparticles for Antibacterial Applications, J Nanomed Nanotechnol. s8 (2017), https://doi.org/10.4172/2157-7439.S8-004.

[29] A. George, S.K. Sharma, S. Chawla, M.M. Malik, M.S. Qureshi, Detailed of X-ray diffraction and photoluminescence studies of Ce doped ZnO nanocrystals, Journal of Alloys and Compounds. 509 (2011) 5942–5946, https://doi.org/10.1016/j.jallcom.2011.03.017.

[30] K. Pradeev raj, K. Sadaiyandi, A. Kennedy, S. Sagadevan, Z.Z. Chowdhury, M.R. B. Johan, F.A. Aziz, R.F. Rafique, R. Thamiz Selvi, R. Rathina bala, Influence of Mg Doping on ZnO Nanoparticles for Enhanced Photocatalytic Evaluation and Antibacterial Analysis, Nanoscale Res Lett. 13 (1) (2018), https://doi.org/10.1186/s11671-018-2643-x.

[31] D. Saravanakkumar, S. Sivaranjani, K. Kaviyarasu, A. Ayeshamariam, B. Ravikumar, S. Pandiarajan, C. Veeralakshmi, M. Jayachandran, M. Maaza, Synthesis and characterization of ZnO–CuO nanocomposites powder by modified perfume spray pyrolysis method and its antimicrobial investigation, J. Semicond. 39 (3) (2018) 033001.

[32] M. Leszczynski, J. Bak-Misiuk, J. Domagala, J. Muszalski, M. Kaniewska, J. Marczewski, Lattice dilation by free electrons in heavily doped GaAs:Si, Appl. Phys. Lett. 67 (1995) 539–541, https://doi.org/10.1063/1.115181.

[33] M. Leszczynski, H. Teisseyre, T. Suski, I. Grzegory, M. Bockowski, J. Jun, S. Porowski, K. Pakula, J.M. Baranowski, C.T. Foxon, T.S. Cheng, Lattice parameters of gallium nitride, Appl. Phys. Lett. 69 (1996) 73–75, https://doi.org/10.1063/1.118123.

[34] R.K. Yadav, P. Chauhan, Estimation of lattice strain in Mn-doped ZnO nanoparticles and its effect on structural and optical properties, Indian J. Pure Appl. Phy. 57 (2019) 881–890.

[35] U. Seetawan, S. Jugsujinda, T. Seetawan, A. Ratchasin, C. Euvananont, C. Junin, C. Thanachayanont, P. Chainaronk, Effect of Calcinations Temperature on Crystallography and Nanoparticles in ZnO Disk, MSA. 02 (2011) 1302–1306, https://doi.org/10.4236/msa.2011.29176.

[36] P.M. Kibasomba, S. Dhlamini, M. Maaza, C.-P. Liu, M.M. Rashad, D.A. Rayan, B. W. Mwakikunga, Strain and grain size of TiO_2 nanoparticles from TEM, Raman spectroscopy and XRD: The revisiting of the Williamson-Hall plot method, Results in Physics. 9 (2018) 628–635, https://doi.org/10.1016/j.rinp.2018.03.008.

[37] S.C. Das, R.J. Green, J. Podder, T.Z. Regier, G.S. Chang, A. Moewes, Band Gap Tuning in ZnO Through Ni Doping via Spray Pyrolysis, J. Phys. Chem. C. 117 (2013) 12745–12753, https://doi.org/10.1021/jp3126329.

[38] R. Priya, P. Sahay, N. Saxena, P. Rajput, V. Chawla, R. Sharma, O.P. Sinha, R. Krishna, Systematic study of Ni, Cu co-doped ZnO nanoparticles for UV photodetector application, J Mater Sci: Mater Electron. 32 (2021) 2011–2025, https://doi.org/10.1007/s10854-020-04968-2.

[39] A.A. Ansari, A.K. Parchur, M. Alam, A. Azzeer, Effect of surface coating on optical properties of Eu^{3+}-doped $CaMoO_4$ nanoparticles, Spectrochimica Acta Part A: Molecular and Biomolecular Spectroscopy. 131 (2014) 30–36, https://doi.org/10.1016/j.saa.2014.04.036.

[40] B.P. Singh, A.K. Parchur, R.S. Ningthoujam, A.A. Ansari, P. Singh, S.B. Rai, Enhanced photoluminescence in CaMoO4:Eu^{3+} by Gd^{3+} co-doping, Dalton Trans. 43 (2014) 4779, https://doi.org/10.1039/c3dt53408a.

[41] K. Raja, P.S. Ramesh, D. Geetha, Synthesis, structural and optical properties of ZnO and Ni-doped ZnO hexagonal nanorods by Co-precipitation method, Spectrochimica Acta Part A: Molecular and Biomolecular Spectroscopy. 120 (2014) 19–24, https://doi.org/10.1016/j.saa.2013.09.103.

[42] R. Saravanan, K. Santhi, N. Sivakumar, V. Narayanan, A. Stephen, Synthesis and characterization of ZnO and Ni doped ZnO nanorods by thermal decomposition method for spintronics application, Materials Characterization. 67 (2012) 10–16, https://doi.org/10.1016/j.matchar.2012.02.015.

[43] S. Suwanboon, P. Amornpitoksuk, A. Sukolrat, N. Muensit, Optical and photocatalytic properties of La-doped ZnO nanoparticles prepared via precipitation and mechanical milling method, Ceramics International. 39 (2013) 2811–2819, https://doi.org/10.1016/j.ceramint.2012.09.050.

[44] S. Bandyopadhyay, G.K. Paul, R. Roy, S.K. Sen, S. Sen, Study of structural and electrical properties of grain-boundary modified ZnO films prepared by sol–gel technique, Materials Chemistry and Physics. 74 (2002) 83–91, https://doi.org/10.1016/S0254-0584(01)00402-3.

[45] A. Bayat, A.R. Mahjoub, M.M. Amini, Synthesis of high crystalline hierarchical self-assembled $MMoO_4$ (M=Ca, Sr and Ba) super structures: Having hydrophilic surfaces and obvious red-shifted photoluminescence behavior, Materials Chemistry and Physics. 223 (2019) 583–590, https://doi.org/10.1016/j.matchemphys.2018.11.031.

[46] A.A. Bazrafshan, M. Ghaedi, S. Hajati, R. Naghiha, A. Asfaram, Synthesis of ZnO-nanorod-based materials for antibacterial, antifungal activities, DNA cleavage and efficient ultrasound-assisted dyes adsorption, Ecotoxicology and Environmental Safety. 142 (2017) 330–337, https://doi.org/10.1016/j.ecoenv.2017.04.011.

[47] A.S. Haja Hameed, C. Karthikeyan, V. Senthil Kumar, S. Kumaresan, S. Sasikumar, Effect of Mg^{2+}, Ca^{2+}, Sr^{2+} and Ba^{2+} metal ions on the antifungal activity of ZnO nanoparticles tested against Candida albicans, Materials Science and Engineering: C. 52 (2015) 171–177, https://doi.org/10.1016/j.msec.2015.03.030.

[48] S.A. Khan, S. Shahid, W. Bashir, S. Kanwal, A. Iqbal, Synthesis, characterization and evaluation of biological activities of manganese-doped zinc oxide nanoparticles, Trop. J. Pharm Res. 16 (2017) 2331–2339, https://doi.org/10.4314/tjpr.v16i10.4.

[49] H.S. Bhargav, S.D. Shastri, S.P. Poornav, K.M. Darshan, M.M. Nayak, in: Measurement of the Zone of Inhibition of an Antibiotic, IEEE, Bhimavaram, India, 2016, pp. 409–414, https://doi.org/10.1109/IACC.2016.82.

Asian Journal of Chemistry; Vol. 36, No. 1 (2024), 59-68

ASIAN JOURNAL OF CHEMISTRY

https://doi.org/10.14233/ajchem.2024.30625

Stability Indicating Methodology Development to Quantify Odevixibat Content: Application of LC-MS Methodology to Characterize Five Degradants of Odevixibat

THOTA SIVA PRASAD[1,*], MAMIDI GOPI[2] and KELOTH BASAVAIAH[3]

[1]Analytical Development Laboratory, Ajinomoto Bio Pharma Services India, Anakapalli District-531019, India
[2]Department of Chemistry, Dr. V.S. Krishna Govt. Degree and PG College (A), Visakhapatnam-530013, India
[3]Department of Analytical Chemistry, Andhra University, Visakhapatnam-530003, India

*Corresponding author: E-mail: dreambeleiveandbuild@gmail.com

Received: 23 September 2023; *Accepted*: 24 October 2023; *Published online*: 31 December 2023; AJC-21485

This investigation is concerned with development of HPLC technique that made use of a PDA sensor technology for the speedy assessment of odevixibat (OVBT) for the quality control of both their commercially marketed formulations as well as bulk form. The ODS inertsil column (4.6 mm, 5 µm, 250 mm), mobile phase set up by mixing 0.1% formic acid and acetonitrile in a 60:40 volumes, rate of flow of 1.0 mL/min and with detection using PDA at 223.7 nm was adopted for present procedure. Applying ICH specifications, the HPLC-based OVBT assay strategy was validated successfully for linearity (5.00 to 30.00 µg/mL), sensitivity (LOD-0.60 µg/mL; LOQ-2.00 µg/mL), precision (0.207-0.600% RSD), accuracy (98.9-100.8% assay) and robustness (0.53-1.16% RSD). Numerous stress degradations [acid, alkaline, reduction, oxidation, thermal, hydrolysis and photolytic] have been applied to odevixibat. The odevixibat is reported to be prone to instability in oxidative stress and more persistent during photo stress. The HPLC-based odevixibat assay approach could be implemented in quality assurance labs for the quantitative measurement of odevixibat in routine and stability sample analysis of odevixibat bulk and odevixibat capsule doses. Five degradants [OVBT-DP1 (acid stress), OVBT-DP2 (alkali stress), OVBT-DP3 (oxidative stress), OVBT-DP4 (reduction stress) and OVBT-DP5 (heat stress)] were formed. By evaluating mass spectral data of five degradants obtained through LC-MS approach, chemical structures of OVBT-DP1, OVBT-DP2, OVBT-DP3, OVBT-DP4 and OVBT-DP5 were elucidated. The degradation possible mechanisms for all the five degradants formation are also suggested.

Keywords: Odevixibat, Quality control, HPLC, Stress degradation, LC-MS, Degradants, Characterization.

INTRODUCTION

Odevixibat (OVBT) is a reversible suppressor of sodium/bile acid co-transporter [1] and used is an oral medical therapy which redirects bile acids from the liver. In July 2021, the European Union approved odevixibat for the medical management of progressive familial intrahepatic cholestasis in children who were 6-months aged and in August 2021, the USA approved odevixibat for the therapy of pruritus in progressive familial intrahepatic cholestasis children who were 3-months aged [2,3]. Odevixibat successfully decreased pruritus and also serum bile acids in kids with progressive familial intrahepatic cholestasis and odevixibat seemed generally tolerated satisfactorily in them [4].

Pharmaceutical preparations and bulk pharmaceuticals both benefit greatly from pharmaceutical analysis, which makes it necessary for assurance of quality and quality management [5,6]. Pharmaceutical analysis encompasses separating, identifying and estimating the relative quantities of the sample's components. Human health underwent a revolution as a consequence of the discovery and development of several novel drugs. These medications are only going to fulfill their purpose if they were provided in the right quantity and were free of contaminants [6]. Different chemical together with instrumental techniques that are used in drug assessment have all been developed over time in order to make medications function as intended [7,8]. These medications need to be identified and quantitated since impurities can form in them at different points during production, transit and storage, making treatment dangerous [9,10]. Analytical tools and methodologies are crucial in this regard. In order to more efficiently understand how different molecules function within intricate combinations of molecules found in chemical and biological systems, HPLC is utilized [11,12]. To ensure that every one of the components are determined in liquid chromatography, choosing the right kind of detection method is crucial. When a PDA is employed, a wavelength range may be programmed, allowing for the identification of every substance that absorb around this range in a single assessment [13,14].

Ahmed *et al.* [15] devised an HPLC method that utilized a UV sensor for determining odevixibat in pharmaceutical formulations and pure form. The approach developed by Ahmed *et al.* [15], however, fails to include reporting on peak purity while stability investigations and on the characterization of degradants.

The development of an HPLC technique that made use of a PDA sensor technology for the speedy assessment of odevixibat for the quality control of both their commercially marketed formulations as well as bulk form was one of the key focuses of the research. Numerous stress circumstances (acid, alkaline, reduction, oxidation, thermal, hydrolysis and photolytic) have been applied to investigate the forced degradation of HPLC-based odevixibat assay. Utilizing LC-MS, the degradation products generated pursuant to stress circumstances were characterized and a possible mechanism for their development was also put forward.

EXPERIMENTAL

Reference sample drugs and formulations: Odevixibat was supplied by Cadila Healthcare Ltd. (Ahmedabad, India). In this study, Bylvay capsules with 400 µg per capsule label from Alberto AB (Sweden) were utilized. The solvent, acetonitrile (chromatography grade), while the other analytical grade chemcials *viz*. disodium hydrogen phosphate, hydrochloric acid, sodium hydroxide, hydrogen peroxide were procured from Sd chemicals Ltd., India). The distilled water (chromatography, Milli Q, India) was used in this study analysis.

Configuration of chromatography for odevixibat assay: The HPLC type e-2695 series (Water Alliance) with PDA based detector (Water Alliance) was used to accomplish the odevixibat assay determination. The ODS inertsil column (4.6 mm, 5 µm, 250 mm,) was adopted to implement the current procedure. The mobile phase was set up by mixing 0.1% formic acid and acetonitrile in a 60:40 volumes ratio exactly with a average rate of flow of 1.0 mL/min, with detection using PDA at 223.7 nm at room condition temperature and injecting volume equal to 10 µL. After being degassed, the mobile phase prepared underwent filtering making use of 0.45 µ membrane filter paper.

Configuration of mass spectrometer: Xevo TQ-XS (Waters Alliance) triple quadrupole mass spectrometer was used to accomplish the degradants characterization. The positive ion ionization electrospray interfacing approach was put to use to regulate the mass spectrometer. The investigation of odevixibat degradation has been accomplished adopting the multiple reactions monitoring technique. Following are the operational parameters: 14 V and 5500 V of collision voltage energy and ion spray voltage, respectively; 550 and 120-250 ºC of source and drying gas temperatures, respectively; nitrogen as collision gas with 5 mL/min flow stream; 40 V, 10 V and 7 V of potential at decluster, entrance and exit, respectively; and dwell period of 1.0 s.

Odevixibat solutions: An amount of odevixibat standard equal to 20 mg/100 mL of acetonitrile was dissolved to obtain stock odevixibat solution. The stock odevixibat solution was serially gradient diluted using acetonitrile to produce the standard odevixibat solution, which contained the subsequent concentrations: 5.00, 10.00, 15.00, 20.00, 25.00 and 30.00 µg/mL, in order to make up the calibration odevixibat curve.

Calibration odevixibat curve: By evaluating standard odevixibat solutions with six different odevixibat concentrations, calibration graphs for odevixibat were established. Peak area of odevixibat was sketched on the Y-axis while odevixibat theoretical concentration was plotted over the X-axis to get a calibration odevixibat curve. The slope, intercept, correlation and regression model equation for odevixibat was derived.

Analysis of odevixibat in Bylvay capsules: Ten Bylvay (200 µg) capsules were emptied for odevixibat analysis. The capsule material, equivalent to 10 mg of odevixibat, was dissolved in 50 mL volumetric flask containing acetonitrile. After placing them in the sonicator for 15 min, the contents went through filtering *via* 0.45 µ membrane filter paper into dry flasks and filled up with acetonitrile to an exact amount of 50 mL. Aliquots of the above-mentioned Bylvay capsule solution were diluted with acetonitrile for generating Test Bylvay capsule solutions, resulting in odevixibat concentrations of 20 µg/mL and subsequently 10 µL test Bylvay capsule solution injected and analyzed HPLC-based odevixibat assay.

Stability studies: Numerous stress degradations (acid, alkaline, reduction, oxidation, thermal, hydrolysis and photolytic) have been applied to investigate the stability of odevixibat [16].

Acid degradation: Bylvay capsule content was precisely weighed at 67 mg (equal to 200 µg of odevixibat) into a 10 mL volumetric glass flask, to which 5 mL of acetonitrile was added and the mixture was subsequently sonicated for 20 min. The 1 mL of 1 N HCl was added and then left for 15 min. After 15 min, neutralized the solution through 1 mL of 1 N NaOH addition before diluting the solution to volume (10 mL) with acetonitrile and then mixed. In order to analyze the quantities of odevixibat in this solution while its acid degradation products were present, the solution was assessed through the HPLC-based odevixibat assay.

Alkaline degradation: In this assay, Bylvay capsule content (67 mg, equivalent to 200 µg of odevixibat) with 5 mL of acetonitrile and sonicated for 20 min in a 10 mL volumetric glass flask. The 1 mL of 1 N NaOH was added and then left for 15 min. After 15 min, the solution was neutralized using 1 mL of 1 N HCl addition before diluting the solution with acetonitrile. The components in volumetric glass flask were thoroughly shaked before being evaluated for odevixibat remove.

Peroxide degradation: For this analysis, the Bylvay capsule content (67 mg, equivalent to 200 µg of odevixibat) was freshly dissolved employing 5 mL of acetonitrile and sonicated for 20 min. This solution was oxidized with 1 mL of 10% H_2O_2 before being set aside for 15 min and then the mixture was adequately diluted with acetonitrile.

Reduction degradation: Bylvay capsule content was accurately weighed at 67 mg (200 μg of odevixibat) into a 10 mL volumetric glass flask, to which 5 mL of acetonitrile was added and then the mixture was sonicated for 20 min. Now, 1 mL of 10% sodium bisulphite was added and left aside for 15 min and then diluted the solution with acetonitrile and shaked the solution well.

Hydrolytic degradation: By mixing Bylvay capsule content (67 mg, equivalent to 200 μg of odevixibat) with 5 mL of acetonitrile, the solution was sonicated for 20 min and then 1 mL of HPLC water was added and waited for 15 min. After 15 min, the solution was diluted with acetonitrile.

Thermal degradation-procedure: The Bylvay capsule's contents (67 mg) were exposed for a duration of 6 h in oven at 105 ºC and then mixed with 5 mL of acetonitrile and finally sonicated for 20 min. After that make up with acetonitrile to the mark (10 mL).

Photolytic degradation: The Bylvay capsule's contents (67 mg or 200 g of odevixibat) were exposed for a duration of 6 h in sun light and then mixed with acetonitrile and sonicated for 20 min. After that make up with acetonitrile to the mark (10 mL).

RESULTS AND DISCUSSION

HPLC-based odevixibat assay optimization: The 200-400 nm range of wavelength was investigated to establish the odevixibat UV spectral characteristics. Two peaks (one at 223.7 nm and another at 292.4 nm) were observed after a quick scan at this spectrum (Fig. 1). The sensitivity and peak area of odevixibat were optimal at 223.7 nm, as a result, the same method was chosen for the odevixibat analysis.

The trail experimentations to optimize mobile phase for HPLC-based odevixibat assay were conducted using the ODS inertsil column (4.6 mm, 5 μm, 250 mm) with an average rate of flow of 1.0 mL/min, with detection using PDA at 223.7 nm at room condition temperature and injecting volume equal to 10 μL. When mobile phase was set up by mixing 0.1% phosphoric acid and acetonitrile in a 20:80 volumes ratio, good peak for odevixibat was obtained, but column efficiency was least (159 plate counts). Same combination (0.1% phosphoric acid + acetonitrile) in 40:60 volumes ratio produced unacceptable odevixibat peak shape. Same combination (0.1% phosphoric acid + acetonitrile) in equal volumes ratio also produced unacceptable odevixibat peak shape with broadening effect. Now, 0.1% formic acid was implemented as buffer instead of 0.1% phosphoric acid. The base line disturbance became apparent when the mobile phase was made up by combining 0.1% formic acid and acetonitrile in 50:50 volume ratios and 70:30 volume ratios, respectively. The 0.1% formic acid and acetonitrile in a 60:40 volume ratio combination were obtained in a well-mannered peak shape (tailing factor – 1.01), better sensitivity (peak area – 2518100), acceptable column efficiency (plate count – 6671) and with reasonable elution time (3.580 min) was obtained (Fig. 2).

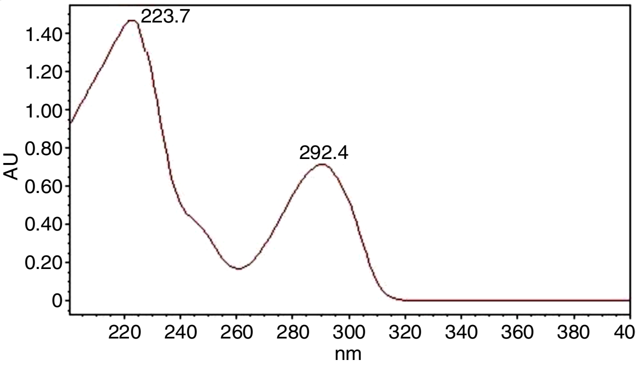

Fig. 1. UV spectrum of odevixibat

Validation: Applying ICH specifications, the HPLC based odevixibat assay strategy was validated [17].

System suitability: Six evaluations of the working odevixibat solution (20 μg/mL) were performed utilizing the HPLC-based odevixibat assay strategy. To demonstrate that the system as a whole worked well, the peak symmetry, the plate counts and the elution times were determined as system suitability

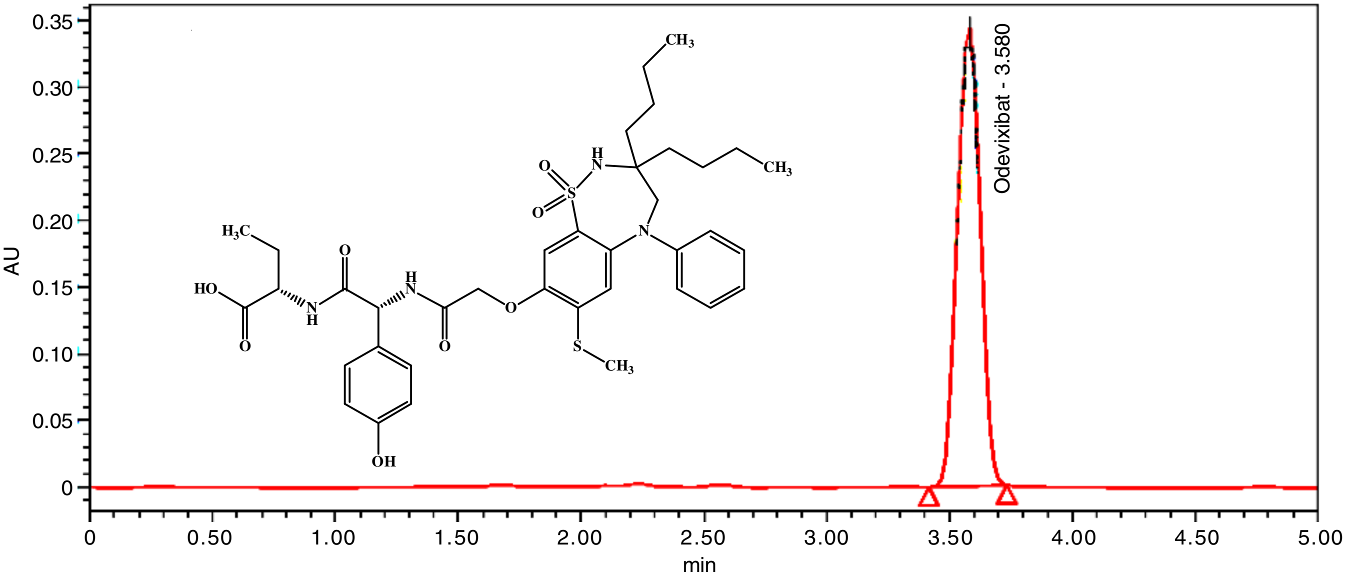

Fig. 2. HPLC chromatogram of odevixibat

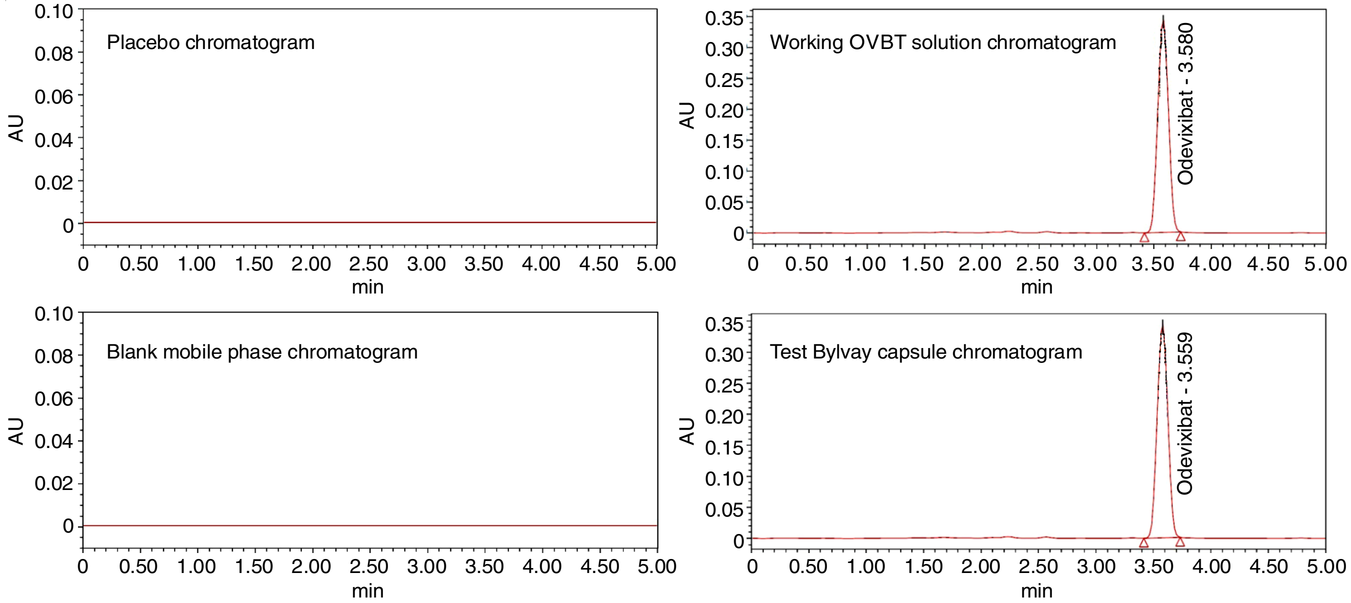

Fig. 3. Chromatograms for HPLC-based odevixibat assay for selectivity

metrics. According to Table-1, the collected data remained within the allowed constraints.

TABLE-1
SYSTEM SUITABILITY FOR EVALUATION OF ODEVIXIBAT

Sample	Plate count	Tailing factor	Elution time
OVBT 1	6675.0	1.01	3.580
OVBT 2	6684.0	1.02	3.584
OVBT 3	6657.0	1.04	3.582
OVBT 4	6672.0	1.02	3.588
OVBT 5	6663.0	1.05	3.587
OVBT 6	6624.0	1.04	3.581
Mean	6662.5	1.03	3.584
SD/RSD	21.0784/0.3164	0.0155/1.5041	0.0033/0.0911

Selectivity: By analyzing the working odevixibat solution (20 μg/mL), the placebo, the test Bylvay capsule solution (20 μg/mL) and the blank mobile phase and selectivity of the HPLC-based odevixibat assay was attained. The positive results (Fig. 3) obtained from employing the HPLC assay approach on the analyzed solutions indicate that the presence of additives in capsules and components in the mobile phase does not have any impact on the odevixibat evaluation.

Linearity: The linearity of the HPLC assay was assessed by measuring the peak area of different concentrations (5.00, 10.00, 15.00, 20.00, 25.00 and 30.00 μg/mL) of odevixibat under optimal conditions. Calibration curves were then developed to establish the relationship between the peak area and the corresponding quantities of odevixibat. The calibration curve (Fig. 4) demonstrated an acceptable connection over the concentration range of 5.00 to 30.00 μg/mL for odevixibat.

Sensitivity: The detection limit and quantification limit for odevixibat were calculated by applying ICH specifications (SD of odevixibat response/slope of odevixibat linearity curve × 3.3 formula for detection limit and SD of odevixibat response/slope of odevixibat × 10 formula for quantification limit). The detection limit and quantification limit were 0.60 μg/mL and 2.00 μg/mL, respectively for odevixibat, which illustrated the satisfactory sensitivity for HPLC assay.

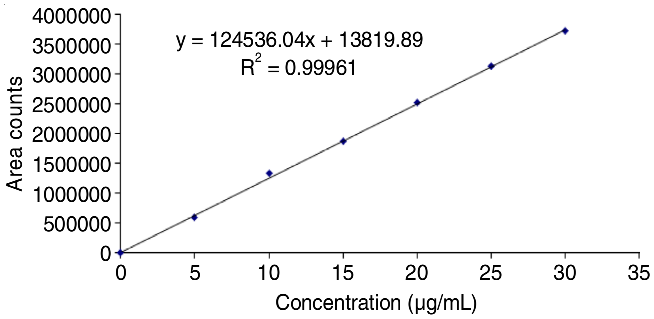

Fig. 4. Linearity curve of odevixibat

Precision: Six assay assessments were executed on working odevixibat solution (20 μg/mL, for system precision) and odevixibat spiked Bylvay capsule solution (20 μg/mL, for method precision) on the exact same day with one operator and also on an alternate day (for intermediate precision) by another operator on distinct apparatus employing the HPLC assay. Table-2 displays the outcomes for precision that have been generated. The RSD values of precision for the system, method and intermediate were 0.207%, 0.600% and 0.440%, respectively. The relative standard deviation (RSD) values for all precisions were found to be below the pre-determined limit (> 2%), which demonstrates the exceptional precision of the HPLC analysis.

Accuracy: The standard odevixibat was added to a Bylvay capsule solution in triplicate at concentration spiking extents of 50%, 100% as well as 150%. An evaluation of the average recovery of three levels is presented in Table-3. The average recovery for odevixibat was 99.8%, which falls within the generally acceptable accuracy limit.

Robustness: Three samples of Bylvay capsule solutions containing odevixibat (20 μg/mL) were injected while the flow rate and acetonitrile proportion were changed. The odevixibat percent assay was observed for evaluating the robustness of the HPLC-based OVBT assay in terms of % RSD. According to Table-4, the observed findings varied within the intended limits (RSD < 2%), demonstrating that purposefully changing the acetonitrile portion and flow rate parameters had no effect on the odevixibat HPLC assay.

Application: The proposed HPLC method was utilized to determine the odevixibat quantitatively and qualitatively in Bylvay capsules. The precision, as evaluated by the relative standard deviation (RSD%), was found to be 0.685%, whereas the accuracy, determined by the recovery rate, was 100.6%. The results indicated that the HPLC assay may be utilized to correctly and precisely evaluate the odevixibat concentration in Bylvay capsules.

Stability studies: The stability and degradation behavior of odevixibat were investigated under various conditions including acid, alkaline, reduction, oxidation, thermal, hydrolysis, and photolytic stress. These stress conditions were used to assess the stability-indicating and specificity traits of the approach. The extent of odevixibat degradation in all stress degradation experiments was determined based on the amount of odevixibat remaining in the directed stress degradations (Table-5). According to Table-5, odevixibat demonstrated stability in the specified order when subjected to various stress degradations. The order of stress levels, from highest to lowest, is as follows: photo stress > hydrolytic stress > heat stress > reduction stress > acid stress > alkali stress > oxidation stress. Odevixibat is susceptible to instability when exposed to oxidative stress and has enhanced persistence when exposed to photo stress.

TABLE-2
PRECISION STUDIES FOR EVALUATION OF ODEVIXIBAT

Precision →	System	Method	Intermediate
Sample ↓	Odevixibat area	Odevixibat assay (%)	Odevixibat assay (%)
OVBT 1	2518100	99.5	100.8
OVBT 2	2512025	100.2	99.5
OVBT 3	2512025	99.9	100.2
OVBT 4	2516525	99.6	100.1
OVBT 5	2518100	100.2	100.4
OVBT 6	2526125	98.6	99.9
Mean	2517150	99.7	100.2
SD/RSD	5201.49/0.207	0.599/0.600	0.442/0.440

TABLE-3
ACCURACY STUDIES FOR EVALUATION OF ODEVIXIBAT

Accuracy level	Odevixibat added (mg)	Odevixibat area counts	Odevixibat quantity (mg)	Odevixibat recovered (%)
50% accuracy	0.10	1257441	0.0999	99.9
	0.10	1263234	0.1004	100.4
	0.10	1249126	0.0992	99.2
100% accuracy	0.20	2535921	0.2015	100.8
	0.20	2526023	0.2007	100.4
	0.20	2507308	0.1992	99.6
150% accuracy	0.30	3772308	0.2997	99.9
	0.30	3761124	0.2988	99.6
	0.30	3733564	0.2967	98.9
			Mean	99.8
			SD/RSD	0.351/0.35

TABLE-4
ROBUSTNESS STUDIES FOR EVALUATION OF ODEVIXIBAT

Flow plus (mL/min)	Odevixibat quantity (µg/mL)	Odevixibat area	Odevixibat assay (%)	Flow minus (mL/min)	Odevixibat quantity (µg/mL)	Odevixibat area	Odevixibat assay (%)
1.1	20	2632709	99.4	0.9	20	2441736	100.6
1.1	20	2608951	98.5	0.9	20	2438961	100.5
1.1	20	2670654	100.8	0.9	20	2410764	99.3
		Mean	99.6			Mean	100.1
		SD/RSD	1.159/1.16			SD/RSD	0.723/0.72
Acetonitrile proportion plus	Odevixibat quantity (µg/mL)	Odevixibat area	Odevixibat assay (%)	Acetonitrile proportion minus	Odevixibat quantity (µg/mL)	Odevixibat area	Odevixibat assay (%)
45	20	2771340	99.8	35	20	2222811	99.1
45	20	2766851	99.6	35	20	2248629	100.3
45	20	2795160	100.6	35	20	2239482	99.9
		Mean	100.00			Mean	99.8
		SD/RSD	0.529/0.53			SD/RSD	0.611/0.61

TABLE-5
STABILITY STUDIES FOR ODEVIXIBAT

Stress applied	Odevixibat quantity (µg/mL)	Odevixibat peak area	Odevixibat stability (%)	Odevixibat degradation (%)	Angle of purity for odevixibat peak	Threshold of purity for odevixibat peak
Control	20	2515530	100.00	0.0	0.293	4.061
Acid stress	20	2224763	88.4	11.6	0.407	4.035
Alkali stress	20	2202274	87.6	12.4	0.401	4.055
Peroxide stress	20	2170715	86.3	13.7	0.473	4.054
Reduction stress	20	2245289	89.3	10.7	0.422	4.065
Thermal stress	20	2292177	91.1	8.9	0.485	4.062
Photo stress	20	2451436	97.5	2.5	0.454	4.071
Hydrolytic stress	20	2406401	95.7	4.3	0.425	4.057

Stability indicating trait and method's specificity trait: The designed HPLC method can separate odevixibat from every single degradation products, as illustrated in Fig. 5. To determine the purity of odevixibat peak, a diode-array analyzer and Empower edition two software were utilized. The Empower edition two software reported the peak purity for each spectrum to be within an automatically determined thres-hold limit as shown in Table-5. The results showed that the peak signal of odevixibat at 3.57 min remained consistent under various stress conditions (Fig. 6). The HPLC method yielded specific results and can be utilized as a stability indicating approach to evaluate odevixibat content in various materials, including stability samples.

MS characterization: Odevixibat's positive ESI-MS reveals a significant $[M+H]^+$ ion with *m/z* 188.997 (Fig. 7).

MS characterization of OVBT-DP1: Under acidic conditions, the degradation product OVBT-DP1 has *m/z* at 296.958 $[M+H]^+$ (Fig. 7); molecular formula of $C_9H_9ClO_5S_2$ was eluted at 0.864 min. The OVBT-DP1 can be elucidated as 2-(5-hydrosulfonyl-2-(methylthio)phenoxy)acetic hypochl-orous anhydride derived from the odevixibat structure. The potential degradation of odevixibat to OVBT-DP1 was suggested based on the observed MS data (Fig. 8).

MS characterization of OVBT-DP2: Under alkaline conditions, the degradation product OVBT-DP2 has *m/z* at 188.997 $[M+H]^+$ (Fig. 7) having molecular formula of $C_7H_8O_2S_2$ and was eluted at 1.219 min. The OVBT-DP2 structure was assigned as 4-hydrosulfonyl phenyl(methyl)sulfane derived from the odevixibat structure. The structure of OVBT-DP2 as shown in (Fig. 9) is suggested on the basis of degradation mass data of odevixibat.

MS characterization of OVBT-DP3: Under oxidative stress conditions, the degradation product OVBT-DP3 has *m/z* at 77.016 $[M+H]^+$ (Fig. 7) having molecular formula of $C_4H_4O_3$ and was eluted at 1.911 min. The OVBT-DP3 is assigned as 2-hydroxy acetic hypochlorous anhydride which was derived

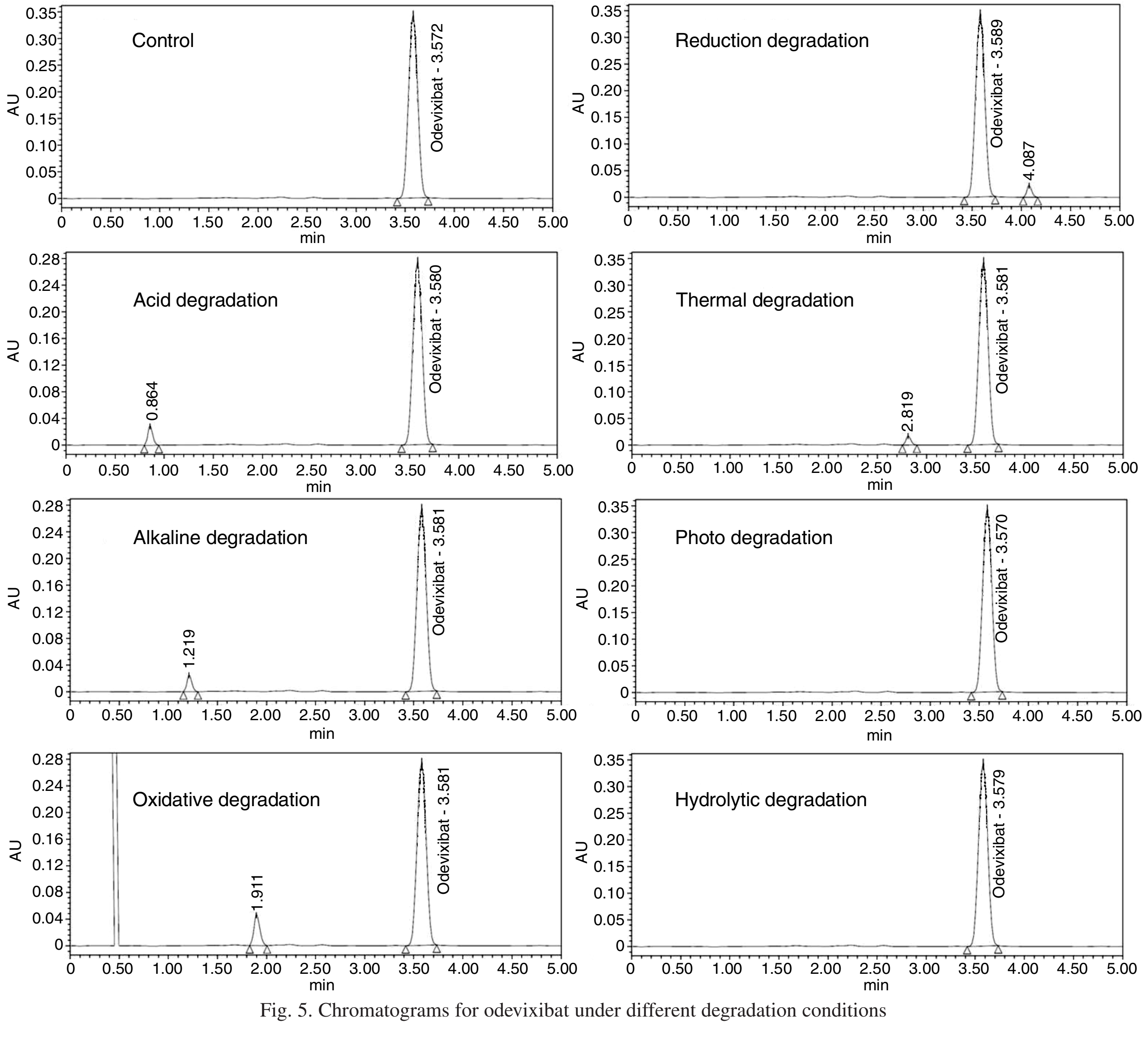

Fig. 5. Chromatograms for odevixibat under different degradation conditions

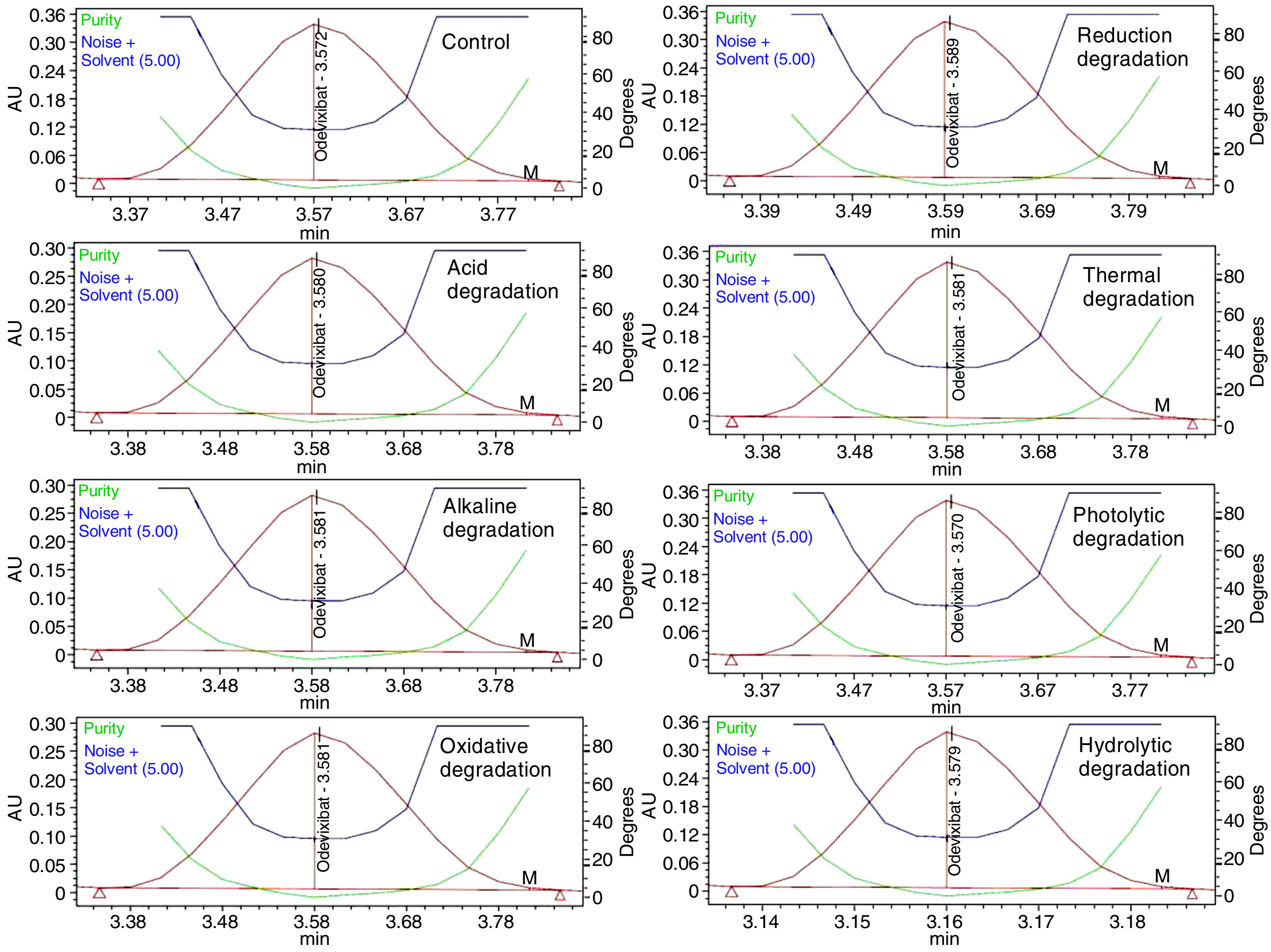

Fig. 6. Plots for peak purity of odevixibat in stress degradations

from the mass degradation spectral data of odevixibat (Fig. 10).

MS characterization of OVBT-DP4: The degraded product OVBT-DP4 *m/z* at 571.1535 $[M+H]^+$ (Fig. 7) having molecular formula of $C_{25}H_{34}N_2O_7S_3$ was eluted at 4.067 min. The structure of OVBT-DP4 is assigned as 2-((3,3-dibutyl-7-(methylthio)-1,1-dioxido-5-phenyl-2,3,4,5-tetrahydrobenzo[*f*][1,2,5]thiadiazepin-8-yl)oxyl)-1-oxoethane-1-sulfonic acid] derived from the odevixibat structure (Fig. 11).

MS characterization of OVBT-DP5: Upon thermal degradation, the degraded product OVBT-DP5 exhibit *m/z* at 303.145 $[M+H]^+$ (Fig. 7) having molecular formula of $C_{17}H_{22}N_2OS$ was eluted at 2.819 min. Based on the mass spectral data, the structure of OVBT-DP5 is assigned as sodium 2-(5-hydro-sulfonyl-4-(methyl(phenyl)amino)-2-(methylthio)phenoxy)acetate (Fig. 12) derived from the odevixibat structure.

Conclusion

An efficient and rapid high-performance liquid chromatography (HPLC) method was developed to quantify odevixibat in capsule formulations. The proposed HPLC assay was validiated in terms of selectivity, linearity, quantification limit, precision, accuracy, robustness, specificity and detection limit. The selectivity and stability of the HPLC method were proved by its capacity to resolve the various degradation components, including acid, alkaline, reduction, oxidation, thermal, hydrolysis and photolytic components. The validated HPLC method has successfully been analyzed odevixibat in capsule dosages. The degradation products resulting from the acid stress (OVBT-DP1), alkali stress (OVBT-DP2), oxidative stress (OVBT-DP3), reduction stress (OVBT-DP4) and thermal stress (OVBT-DP5) has been identified and their chemical composition and possible formation pathways were determined using LC-MS evaluations.

CONFLICT OF INTEREST

The authors declare that there is no conflict of interests regarding the publication of this article.

REFERENCES

1. S.M. Bedoyan, O.T. Lovell, S.P. Horslen and J.E. Squires, *Expert Opin. Pharmacother.*, **23**, 1771 (2022); https://doi.org/10.1080/14656566.2022.2140040
2. E.D. Deeks, *Drugs*, **81**, 1781 (2021); https://doi.org/10.1007/s40265-021-01594-y

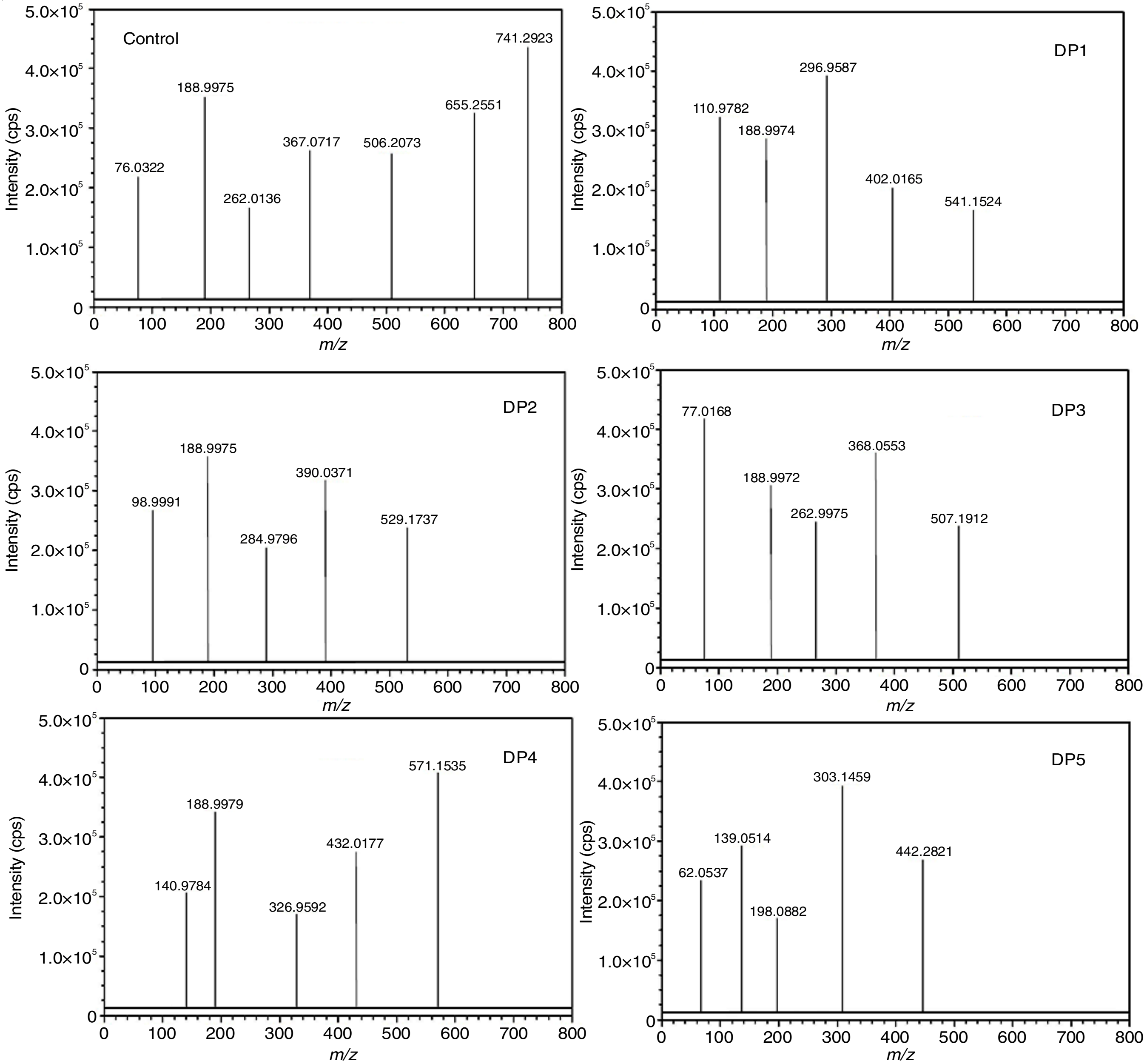

Fig. 7. MS spectrum of odevixibat, OVBT-DP1, OVBT-DP2, OVBT-DP3, OVBT-DP4 and OVBT-DP5

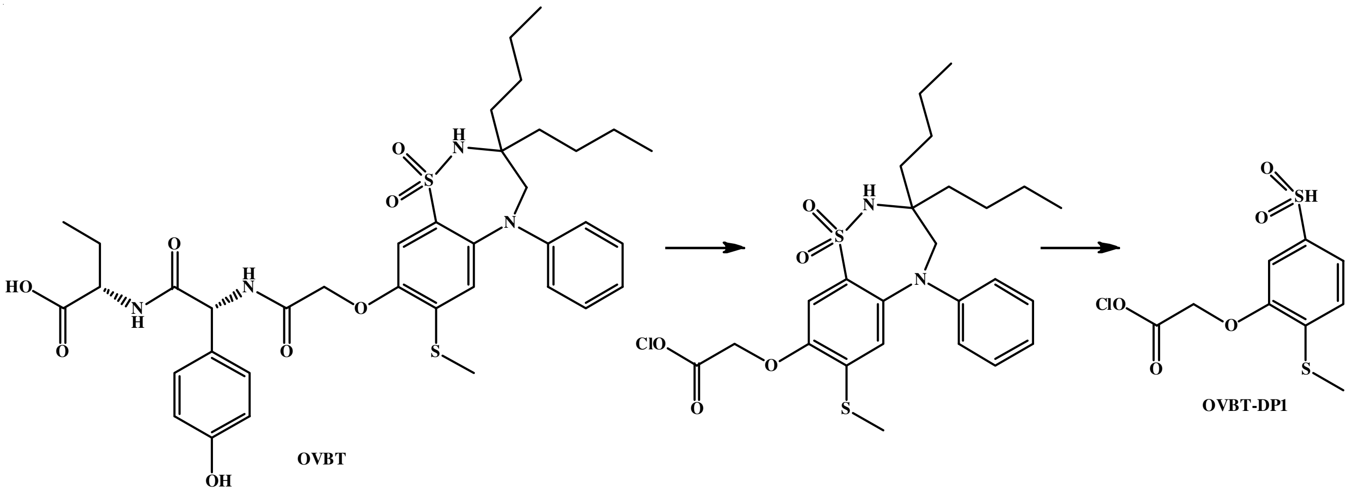

Fig. 8. Degradation of odevixibat to OVBT-DP1 under acidic condition

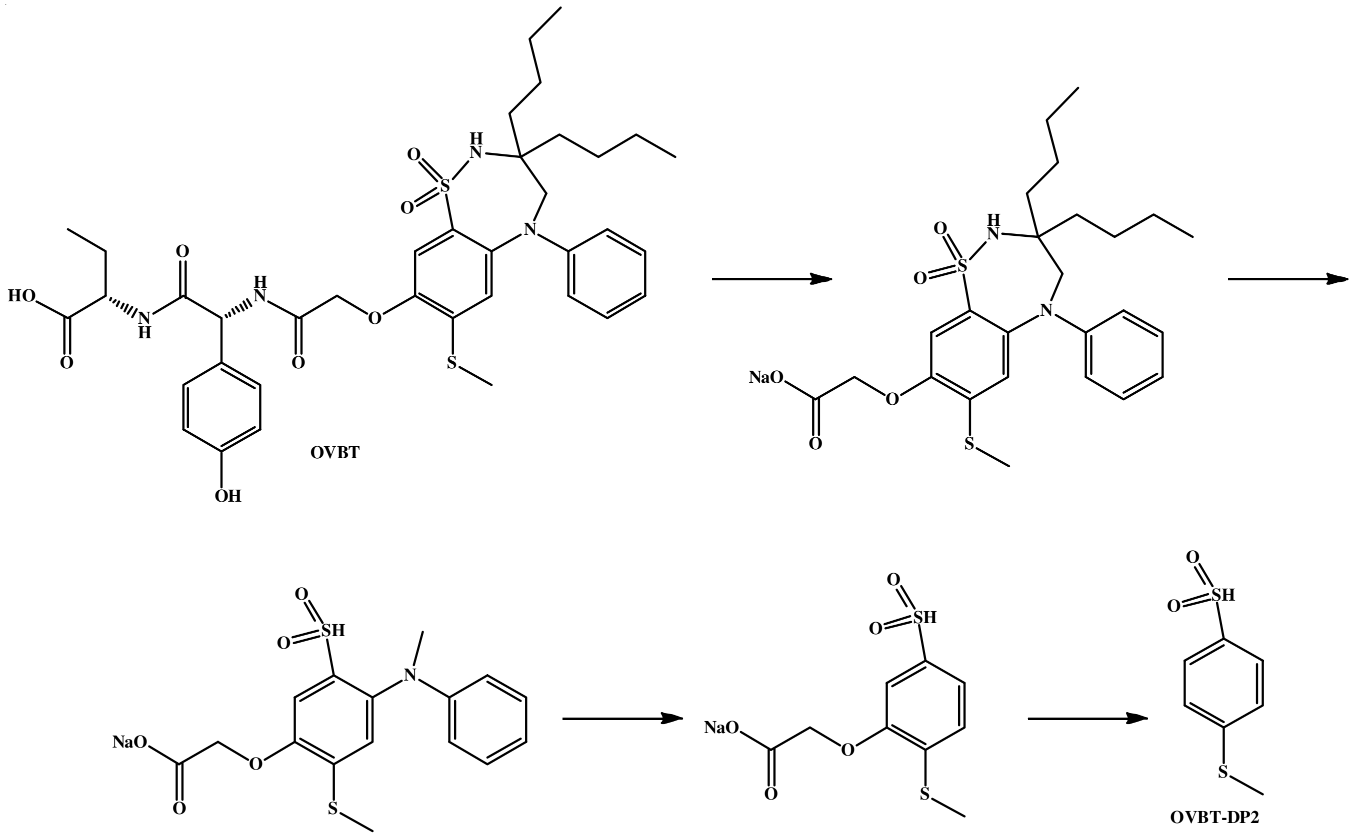

Fig. 9. Degradation of odevixibat to OVBT-DP2 under alkaline condition

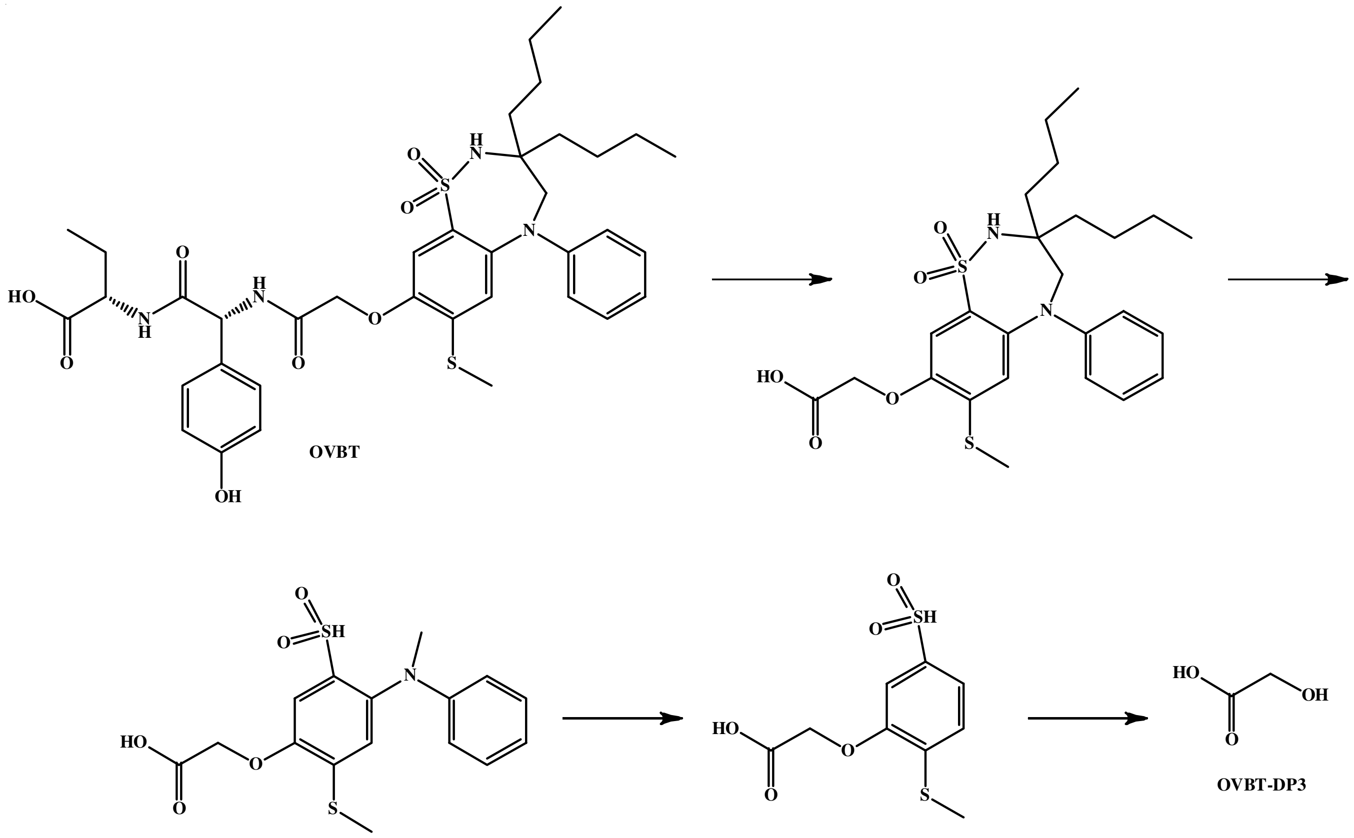

Fig. 10. Degradation of odevixibat to OVBT-DP3 under peroxide condition

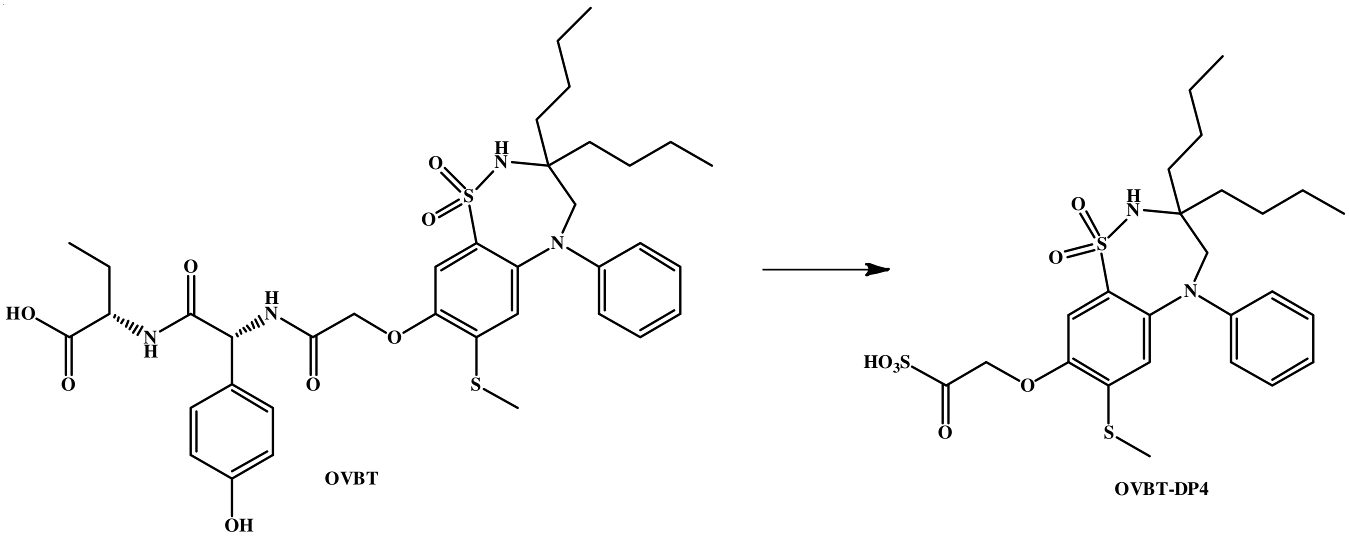

Fig. 11. Degradation of odevixibat to OVBT-DP4 under reducing condition

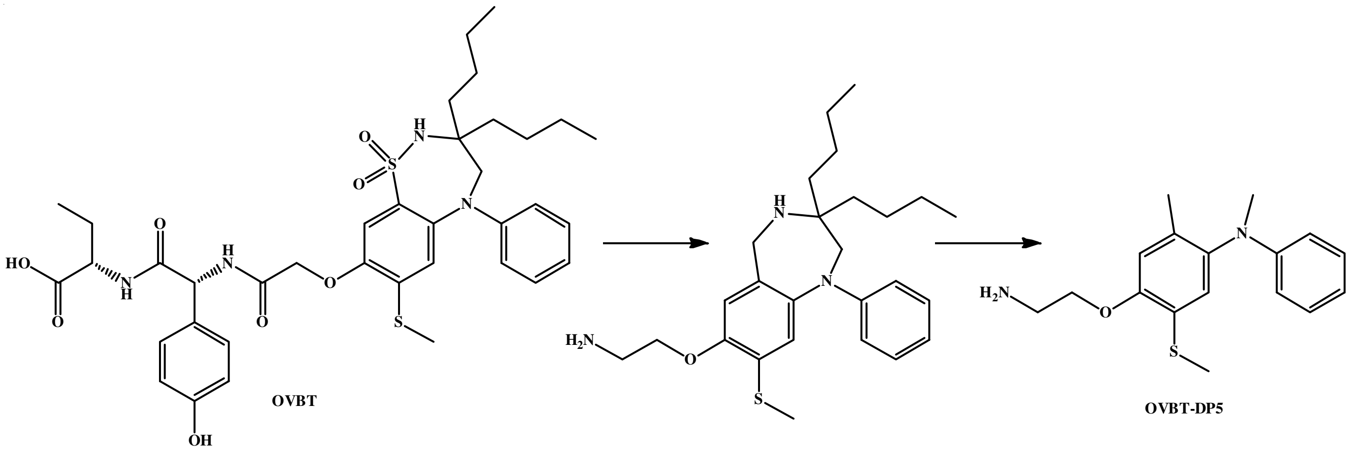

Fig. 12. Degradation of odevixibat to OVBT-DP5 under thermal condition

3. U. Baumann, E. Sturm, F. Lacaille, E. Gonzalès, H. Arnell, B. Fischler, M.H. Jørgensen, R.J. Thompson, J.P. Mattsson, M. Ekelund, E. Lindström, P.G. Gillberg, K. Torfgård and P.N. Soni, *Clin. Res. Hepatol. Gastroenterol.*, **45**, 101751 (2021); https://doi.org/10.1016/j.clinre.2021.101751
4. R.J. Thompson, H. Arnell, R. Artan, U. Baumann, P. Czubkowski, P.L. Calvo, B. Dalgic, L. D'Antiga, Ö. Durmaz, B. Fischler, E. Gonzalès, T. Grammatikopoulos, G. Gupte, W. Hardikar, R.H.J. Houwen, B.M. Kamath, S.J. Karpen, L. Kjems, F. Lacaille, A. Lachaux, E. Lainka, C.L. Mack, J.P. Mattsson, P. McKiernan, H. Özen, S.R. Rajwal, B. Roquelaure, M. Shagrani, E. Shteyer, N. Soufi, E. Sturm, M.E. Tessier, H.J. Verkade and P. Horn, *Lancet Gastroenterol. Hepatol.*, **7**, 830 (2022); https://doi.org/10.1016/S2468-1253(22)00093-0
5. P. Mikus and L. Novotny, *Res. & Rev.: J. Pharma. Anal.*, **4**, 13 (2015).
6. C.K. Zacharis and C.K. Markopoulou, *Molecules*, **25**, 3560 (2020); https://doi.org/10.3390/molecules25163560
7. M.R. Siddiqui, Z.A. AlOthman and N. Rahman, *Arab. J. Chem.*, **10**, S1409 (2017); https://doi.org/10.1016/j.arabjc.2013.04.016
8. W. Misiuk, *J. Pharm. Bioallied Sci.*, **2**, 88 (2010); https://doi.org/10.4103/0975-7406.67007
9. A.Y. Abdin, P. Yeboah and C. Jacob, *Int. J. Environ. Res. Public Health*, **17**, 1030 (2020); https://doi.org/10.3390/ijerph17031030
10. B. Ramachandra, *Crit. Rev. Anal. Chem.*, **47**, 24 (2017); https://doi.org/10.1080/10408347.2016.1169913
11. B. Nikolin, B. Imamovic, S. Medanhodzic-Vuk and M. Sober, *Bosn. J. Basic Med. Sci.*, **4**, 5 (2004); https://doi.org/10.17305/bjbms.2004.3405
12. F. Chen, B. Fang, P. Li and S. Wang, *Int. J. Anal. Chem.*, **2021**, 5533646 (2021); https://doi.org/10.1155/2021/5533646
13. L.G. Martins, N.M. Khalil and R.M. Mainardes, *J. Pharm. Anal.*, **7**, 388 (2017); https://doi.org/10.1016/j.jpha.2017.05.007
14. M. Hollá, A. Bílková, P. Jakubec, S. Košková, H. Koèová Vlèková, D. Šatínský, F. Švec and H. Sklenáøová, *Molecules*, **26**, 3246 (2021); https://doi.org/10.3390/molecules26113246
15. A.M. Ahmed, M.W.I. Nassar, A. El-Olemy and M.S. Emara, *Egypt. J. Chem.*, **65(10)**, 203 (2022); https://doi.org/10.21608/EJCHEM.2022.113638.5160
16. ICH, International Conference on Harmonization, Harmonized Tripartite Guideline Q1A (R2), Stability Testing of New Drug Substances and Products, Geneva (2003).
17. ICH, International Conference on Harmonization (ICH), Q2 (R1): Validation of Analytical Procedures—Text and Methodology, Geneva (2005).